

Development and Validation of a Gas-Liquid Two-Phase Model for Industrial Computational Fluid Dynamics Applications

Von der Fakultät für Maschinenbau, Elektro- und
Energiesysteme der Brandenburgischen Technischen
Universität Cottbus–Senftenberg zur Erlangung des
akademischen Grades eines

Doktor-Ingenieur
genehmigte Dissertation

vorgelegt von

Diplom-Ingenieur (FH)
Mario Nowitzki

geboren am 22.07.1980 in Zossen,
Deutschland

Vorsitzender: Prof. Dr.-Ing. Georg Möhlenkamp (BTU Cottbus-Senftenberg)
1. Gutachter: Prof. Dr.-Ing. Fabian Mauß (BTU Cottbus-Senftenberg)
2. Gutachter: Prof. Dr.-Ing. Hans-Joachim Krautz (BTU Cottbus-Senftenberg)
3. Gutachter: Prof. Dr.-Ing. Udo Hellwig (ERK Eckrohrkessel GmbH)

Tag der mündlichen Prüfung: 10. November 2020

DOI: <https://doi.org/10.26127/BTUOpen-5413>

for my family

Abstract

A local algebraic simulation model was developed, to determine the characteristic length scales for dispersed phases. This model includes the Ishii-Zuber drag model, the lift, the wall lubrication force and the turbulent dispersion force as well. It is based on the Algebraic Interface Area Density (AIAD) model from the Helmholtz Zentrum Dresden Rossendorf (HZDR), which provides the morphology detection and the free surface drag model. The developed model is in agreement with the current state of knowledge based on an examination of the theory and of state of science models for interface momentum transfer.

This new simulation model was tested on three different experiments. Two experiments can be found in the literature, the Fabre, Masbernat, and Suzanne (1987) and the Hewitt and Owen (1987) experiment. And the third simulation is based on a steam drum experiment. This steam drum experiment is designed with ERK Eckrohrkessel GmbH internals and was developed to examine the droplet mass flow out of the turbulent separation stage.

The implementation of all models and tests was performed using Ansys CFX. The first analysis was carried out to reproduce a wavy stratified flow to examine the effects of different simulation model set-ups according to the velocity and kinetic energy profiles, as well as the pressure drop gradient and the water level measured by Fabre, Masbernat, and Suzanne (1987). The second analysis was a proof on concept for reproducing the vertical flow pattern by an experiment from Hewitt and Owen (1987). The third simulation analysed the water distribution in the steam drum and feeding pipes system as well as the droplet carryover into the gas phase in the turbulent separation region of the drum.

These simulations have shown, that the accuracy of the particle distribution model in interaction with the drag and non-drag forces is able to reproduce horizontal and vertical flow patterns. Higher deviations are recognised for the liquid volume fraction close above the interface. Generally, simulations can now be performed to optimise industrial steam drum designs.

Zusammenfassung

Ein algebraisches Simulationsmodell, basierend auf lokalen Variablen, wurde entwickelt, zur Berechnung von charakteristischen Längen von dispersen Phasen. Dieses Modell beinhaltet das Ishii-Zuber Widerstandsmodell, die „lift“, die „wall lubrication“ und die „turbulent dispersion“ Kraft. Das Modell baut auf das „Algebraic Interface Area Density“ (AIAD) Modell, vom Helmholtz Zentrum Dresden Rossendorf (HZDR) auf, welches die Detektion der Morphologie der Strömung und das Widerstandsmodell der freien Oberfläche bereitstellt. Das entwickelte Modell basiert auf dem Stand der Technik, auf die Begutachtung der Theorie und auf Modelle für den Impulstransport an der Phasengrenzfläche, die Stand der Wissenschaft sind. Auf drei verschiedenen Experimenten wurde das Simulationsmodell angewendet. Die Experimente von Fabre, Masbernat und Suzanne (1987) und Hewitt und Owen (1987) wurden aus der Literatur entnommen. Das dritte Experiment war eine Dampftrommel, die entwickelt wurde, um den Tröpfchenmassenstrom zu ermitteln, der aus der turbulenten Abscheidungszone mitgerissen wurde. Diese Dampftrommel basiert auf ein Design von ERK Eckrohrkessel GmbH. Die Implementierung und Erprobung wurde mit Ansys CFX durchgeführt. In der ersten Analyse sollte der Einfluss der verschiedenen Modelle auf das Geschwindigkeits-, das kinetische Energieprofil, den Druckgradienten und die Höhe der Phasengrenzfläche bezüglich einer Wellenströmung im Fabre, Masbernat und Suzanne (1987) Experimente untersucht werden. Die zweite Analyse war ein Machbarkeitsnachweis bezüglich eines vertikalen Zweiphasenströmung-Experimentes von Hewitt und Owen (1987). In einer dritten Analyse wurde die Wasserverteilung in einer Dampftrommel und den Zulaufrohren, sowie der mitgerissene Massenstrom an Tröpfchen aus der turbulenten Abscheidungszone, untersucht. Diese Simulationen haben gezeigt, dass die Genauigkeit des Partikelverteilungsmodells, den „drag“ und „non-drag“ Kräften ausreicht, um horizontale und vertikale Strömungsformen zu reproduzieren. Bei der Phasenverteilung über der Phasengrenzfläche sind größere Abweichungen zu erkennen. Generell eignet sich das Simulationsmodell, um eine Optimierung von Dampftrommeln jetzt durchzuführen.

The source code can be provided on request

Mario_SourceCode@gmx.de

Contents

Abstract	ii
Zusammenfassung	iii
Contents	v
1 Introduction	1
2 State of the Art and Theoretical Basics	4
2.1 Two-Phase Flow	5
2.1.1 Two-Phase Flow in Vertical Pipes	5
2.1.2 Two-Phase Flow in Horizontal Pipes	6
2.1.3 Flow Maps	7
2.2 Steam Water Separation in Eckrohrkessel Steam Boilers	13
2.2.1 Eckrohrkessel Boiler	13
2.2.2 Steam Quality	17
2.2.3 Separation Devices	18
2.3 Multiphase Flow Models in Ansys CFX	26
2.3.1 Ansys CFX Basics for Single Phase Flows	28
2.3.2 Multiphase Formulation in Ansys CFX	32
2.3.3 The Inhomogeneous Model	34
2.3.4 Interfacial Momentum Transport Inhomogeneous Model	38
2.4 Algebraic Interface Area Density Model	47
2.4.1 Morphology Detection	47
2.4.2 Drag Modelling	49

2.4.3	Turbulence Modelling	54
2.5	Non-Drag Forces	57
2.5.1	Lift Force	57
2.5.2	Wall Lubrication Force	62
2.5.3	Turbulent Dispersion Force	63
2.6	Conclusion State of the Art and Motivation	66
3	Particle Information Reconstruction from Euler Phase	69
3.1	Particle Size Distribution	72
3.1.1	Sauter Mean Diameter and Mass Specific Particle Surface	72
3.1.2	Derivation Sauter Mean Diameter for Uniform Distri- bution	75
3.1.3	Derivation Sauter Diameter for Triangle Distribution .	76
3.1.4	Derivation Sauter Diameter for RRSB Distribution . .	77
3.2	Minimum and Maximum Particle Diameter Estimation	79
3.2.1	Shape Regimes for Fluid Particles	79
3.2.2	Maximum Stable Particle Diameter	81
3.2.3	Minimum Diameter	94
3.3	Summary Particle Reconstruction	95
4	Implementation of Developed Model in CFX	97
4.1	Interfacial Area Density Implementation	98
4.2	Drag Coefficient Correlation Implementation	100
5	Validation with Horizontal Test Case	101
5.1	Fabre Model	104
5.1.1	Fabre CFD Geometry and Mesh	106
5.1.2	Fabre Boundary Conditions	107
5.1.3	Fabre Physics Set-Up	108
5.1.4	Fabre Initial Conditions	110
5.1.5	CFX Solver Issues Notes For Transient Simulations . .	111
5.2	Mesh Study	112
5.3	Distribution Function Comparison	118
5.4	Validation with Horizontal Channel Experiment	123

5.5	Fabre Conclusion	144
6	Proof of Concept with Vertical Test Case	145
6.1	Hewitt Model	146
6.1.1	Hewitt CFD Geometry and Mesh	148
6.1.2	Hewitt Boundary Conditions	151
6.1.3	Hewitt Initial Conditions	152
6.2	Vertical Pipe Simulation	153
6.3	Hewitt Conclusion	157
7	Proof of Concept with Steam Drum Experiment	158
7.1	Steam Drum Experiment	161
7.1.1	Steam Drum CFD Geometry and Mesh	167
7.1.2	Steam Drum Simulation Boundary Conditions	171
7.1.3	Steam Drum Simulation Initial Conditions	173
7.2	Steam Drum Simulation	174
7.3	Steam Drum Simulation Conclusion	178
8	Conclusion and Discussion	182
	Nomenclature	194
	List of Figures	201
	List of Tables	203
	Bibliography	212
	Acknowledgements	213
	Appendices	214
A	Interface Area Density Implementation Flowchart	215
B	Ishii Zuber Drag Model Implementation Flowchart	218
C	Proof of Concept Hewitt Experiment	225

Chapter 1

Introduction

Two-phase flow regimes are occurred in many applications, such as power systems, heat transfer systems, process systems, transport systems and geomeeteorological phenomena. The fluid dynamics in all of the above applications are essentially governed by similar physical laws, i.e. the momentum and mass balance equations. Those balance equations can be solved with computationally intensive numeric algorithms. In addition to the balance equations, in multiphase simulations closure models are needed. Those closure models are not yet well-developed and there are a lot of research going on in this field. The driving force for the multiphase flow model development is the nuclear power industry, which need more reliable simulation models to decrease the risk of a core meltdown.

But due to the increase in processing speed of (modern) computers, the multiphase flow simulation increasingly comes into the focus of non-nuclear boiler engineers. Rapid advances in engineering technology, new and stricter operating conditions and new designs require an increasing design accuracy are the main reasons for this development. Hence a new approach is in progress, turning from designs, based on static experimental correlations, to ones based on dynamical mathematical models. Thereby the multiphase flow has an immense importance for the boiler design, because it allows the prediction of operational limits, process stability, product quality or damage prevention.

One specific problem is the steam/water separation in a steam drum. This technology was mainly developed in the 1970s. At this time, there were fewer demands on boiler efficiency than nowadays. Hence the development and measurements of separation equipment within the drum (drum internals) are adjusted to these conditions. Today, conditions like pressure, and temperature are changing to always higher values, so that older design data is out of range. To ensure a good steam quality for new and stricter operating conditions, more time will have to be dedicated to this topic. Hence a computational fluid dynamics (CFD) model is developed in this thesis in order to examine the two-phase flow in steam drums.

Due to new, faster computers, modelling of such a two-phase flow is carried out by researchers more often. From those studies came new CFD models, which modelling two-phase flows more accurately. One of the institutions, which developing CFD multiphase models is the Helmholtz Zentrum Dresden Rossendorf (HZDR). The HZDR has developed the Algebraic Interfacial Area Density (AIAD) model, cf. [Porombka and Höhne 2015](#). This AIAD model uses the volume fraction parameter to differentiate between two-phase regimes. Luckily for CFD, all used parameters in the AIAD model belong to the macroscopic scale and thus it is independent of system scale length. But mesoscopic and microscopic scale information was left out in order to efficient determine interface properties.

The characteristic length scales for each dispersed phase is still needed as an input parameter in the AIAD model to calculate the drag coefficient and the interfacial area density. In case of steam drums, the characteristic length scales strongly depends on the location, fluctuate during operation and should not be set as constant. Hence, a mesoscopic scale statistical particle size estimation model for droplets and bubbles has been developed by the author to extend the AIAD model.

In the following thesis a new submodel in order to calculate particle characteristic length scales for two-phase gas/liquid mixtures is developed. This CFD submodel is specifically for industrial usage. The developing submodel will be implemented exemplarily into the software Ansys CFX. To examine

drum internals and the behaviour of steam-water separation at high pressures and high temperatures, that new submodel should be used.

To test this CFD model, a steam drum experiment is carried out. Eckrohrkessel (ERK) drum internals are used for the experiment drum. An air/water mixture is used to feed the experiment drum. In that experiment especially the gas/liquid separation due to turbulence will be examined. But before the simulation model is applied to the steam drum experiment, it is tested and enhanced for horizontal and vertical two-phase flows by experiments taken from the literature. In these test cases the correct implementation of the submodels, a analyse of the impact of the submodels on the pressure field, velocity fields and phase distribution, as well as the reproduction of flow pattern is examined and subsequently a parameter fit is carried out.

Chapter 2

State of the Art and Theoretical Basics

In this section the crucial basics of two-phase flows and steam water separation in boilers are described and an overview of drum separation devices, as well as the theoretical CFD equations, which are used in this thesis, is given. In section [2.6](#) the state of the art and lacks of knowledge are discussed, which results to the motivation to develop a new multiphase model.

2.1 Two-Phase Flow

Generally in multiphase flows more than one fluid occur in the same flow system but with different state of matter. A two-phase flow is a special case of multiphase flow with only two fluids. Consequently these two fluids in two-phase flow are at different state of matter, where in multiphase flow only one fluid has to be at different state of matter. In the most cases a homogeneous mixture can be treated as single phase, like air. Hence a falling raindrops in air can be treated as a two-phase flow, air as continuous phase and rain drops as dispersed phase. Mainly in steam boilers the working fluid should be taken only two of the four state of matters, namely liquid and gaseous. Hence in the following sections only gaseous-liquid two-phase flows are considered.

2.1.1 Two-Phase Flow in Vertical Pipes

Two-phase flows can be divided into certain base flow pattern. Between these basic flow pattern transition states can be occurred. In figure 2.1 the two-phase flow pattern for a vertical adiabatic pipe is shown. The volume fraction of the gas phase increased from left to right.

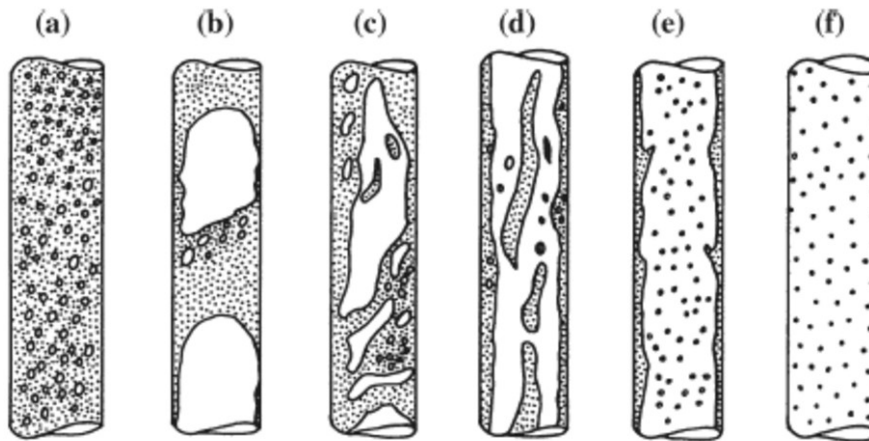


Figure 2.1: Two-phase flow pattern for a liquid-gaseous-flow in adiabatic vertical pipe. a) bubble flow; b) plug flow; c) churn flow; d) wispy-annular flow; e) annular flow; f) spray or drop flow; Baehr and Stephan 2016

In bubble flows, see figure 2.1a, the gas phase is dispersed in the continuous phase. This flow pattern occurs when gas volume fraction is small. In plug flows, see figure 2.1b, large bubbles fill almost the whole pipe cross section. Between these large bubbles liquid with small bubbles is flowing. For higher gas volume fractions some bubbles are concatenated and the bubble structure is disappeared, see 2.1c. The churn flow consists of irregular gas wisps and has a highly transient behaviour. This flow pattern is developed particular in large pipe diameters with high pressures. In wispy-annular flows, see figure 2.1d, consists of a relative large liquid film thickness at the wall, but even with a high amount of liquid in the gas core of the flow. The liquid film consists of small bubbles and the liquid phase in the gas core consists of large droplets, which can be concatenated to larger liquid wisps. An frequently occur flow pattern is the annular flow, see figure 2.1e. The characteristic of the flow pattern is that the main mass of the liquid is located at the wall and the gas flow with increased velocity in the pipe core with some droplets. Due to evaporation and particular on high gas velocity the liquid film at the wall is broke up and a drop flow is developed, see figure 2.1f. The drop flow occur particular at high pressurised evaporation. During the liquid evaporation in a vertical pipe, the two-phase flow pattern mentioned above are occurred consecutively more or less pronounced. Baehr and Stephan 2016

2.1.2 Two-Phase Flow in Horizontal Pipes

In horizontal adiabatic pipes the liquid flow is almost at the bottom of the pipe in contrast to the gas which is more in the upper part of the cross sectional pipe area, due to the gravity. In case of low velocities the inertia force is small compared to the gravity force and in a horizontal pipe flow pattern occur which can not be observed in vertical pipes, see figure 2.2.

If bubbles are collected in the upper part of the pipe, it correspond to bubble flow, see figure 2.2a. The bubbles in a bubble flow can be merged together if the gas fraction is increased and a plug flow can be developed, see figure 2.2b. For low velocities the two phases are complete separated which correspond to stratified flow, see figure 2.2c. If the gas velocity is increasing, waves develop

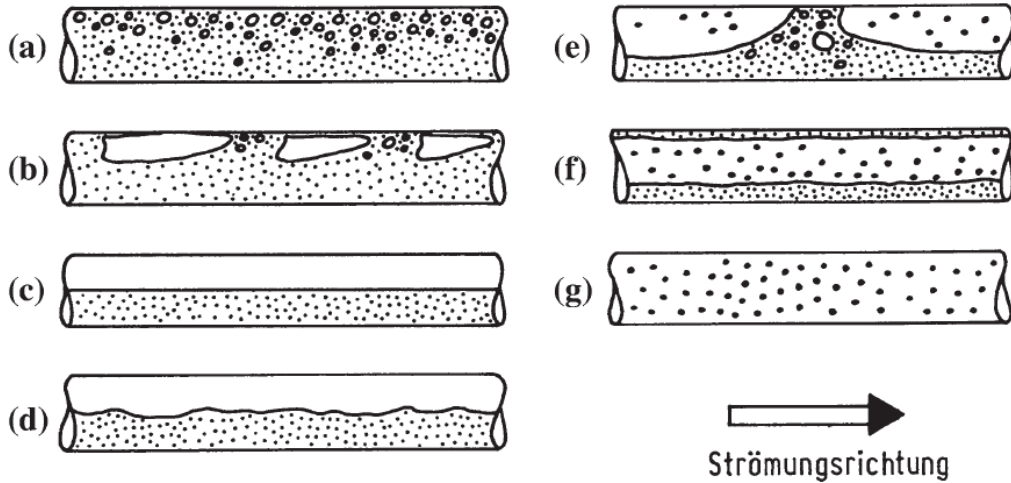


Figure 2.2: Two-phase flow pattern for a liquid-gaseous-flow in adiabatic horizontal pipe. a) bubble flow; b) plug flow; c) stratified flow; d) wavy flow; e) slug flow; f) annular flow; g) spray or drop flow Baehr and Stephan 2016

at the gas-liquid interface and a wavy flow is developed, see figure 2.2d. In the slug flow, see figure 2.2e, the gas velocity is increased regarding the wavy flow, so that wave crests are became higher and are wetted in irregular intervals the upper wall. For still higher velocities, regarding the slug flow, a annular flow is developed, see figure 2.2f. The film thickness at the wall of an annular flow in horizontal pipes is usually higher at the lower and thinner at the upper pipe cross section. A spray or drop flow is developed if the gas velocity is increased further, see figure 2.2g. Baehr and Stephan 2016.

2.1.3 Flow Maps

Horizontal Pipes

Pressure drop, heat transfer rates, volume fractions, interfacial stability, residence time distribution, etc. and all other factors of interest behaviour are expected to be different with different two-phase flow pattern, see Dukler and Taitel (1986) chapter 1 or Baker (1954). Hence it is needed to predict the flow pattern to determine the required necessary properties. Formerly, before the CFD simulation was used, flow maps were widely used to choose

the correct flow pattern for a problem. Until now these flow maps are used to design two-phase flow applications.

Generally two types of flow pattern maps can be distinguished:

- Specific flow pattern maps
- General flow pattern maps

The specific flow maps are for a particular set of conditions. In contrast general flow maps can be represented flow pattern for a wide range of properties, like tube diameter, etc.

In the literature there are many empirical specific mapping without any basis of physical mechanisms. Each result is thus valid for certain experiment conditions. [[Dukler and Taitel 1986](#)]

Baker was one of the first researcher, who published a specific flow map to predict the type of flow pattern in horizontal pipelines to estimate the flow pattern. He applies the modified calculation method proposed by [Lockhart and Martinelli \(1949\)](#), in the form of a separate equation for each type of flow pattern. In [figure 2.3](#) the Baker (1958) flow map is shown.[[Baker 1954](#)]
On the y-axis in [figure 2.3](#) is plotted the gas mass velocity G divided by a correction factor λ . On the x-axis is plotted the ratio of mass velocities of the liquid L and gas phase G , corrected by a λ function and a ψ function. Details of used variables in [figure 2.3](#) are in [table 2.1](#).

All these flow patterns are shown in the [figure 2.2](#) and in the [figure 2.3](#) as well. [Baker \(1958\)](#) uses slightly different names. The [table 2.2](#) shows the assignment of all different horizontal flow patterns for both cases.

The appearing flow pattern depends on the water content in the pipe, see x-axis [figure 2.3](#), and the mass velocity of the gas phase, see y-axis [figure 2.3](#).

Baker's flow map has been modified by some researchers such as [Govier and Omer \(1962\)](#), to advance the original Baker flow map, such as the inclusion of the effects of pipe diameter.

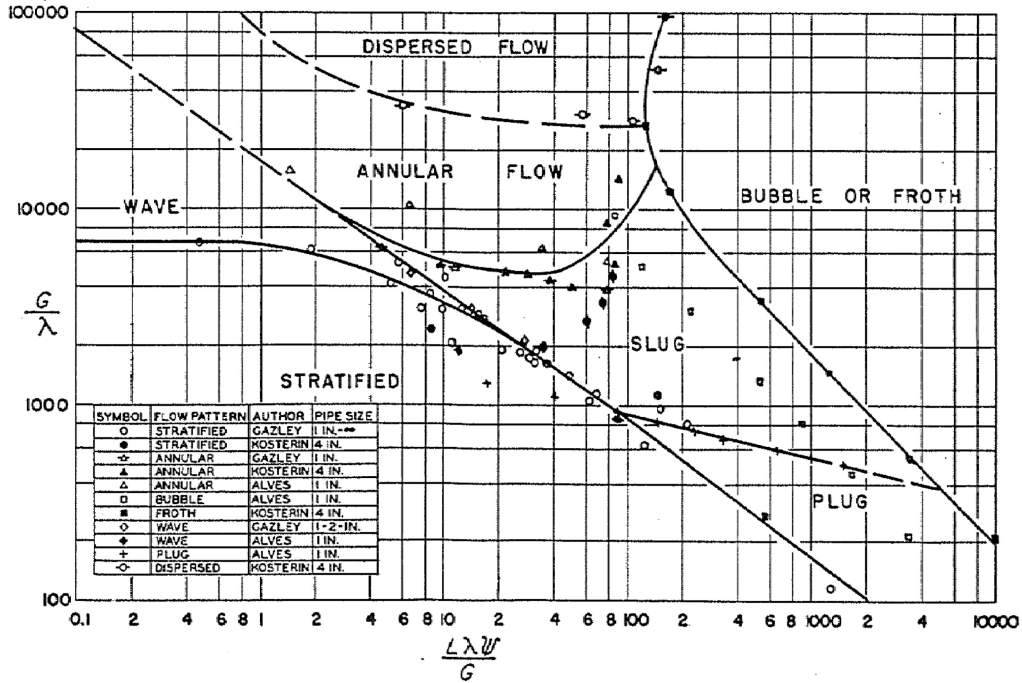


Figure 2.3: Flow pattern regions in two-phase flow, mass velocity of gas phase above ratio of liquid and gas mass velocities Baker 1958

Table 2.1: Part of the nomenclature in Baker (1958)

G	mass velocity of the gas phase	pounds per hour per square foot
L	mass velocity of the liquid phase	pounds per hour per square foot
ρ_g	density of gas phase	lb. per cu. ft.
ρ_l	density of liquid phase	lb. per cu. ft.
γ	surface tension of liquid phase	dynes per centimetre
μ_l	viscosity of liquid phase	centipoise
λ	$\left[\left(\frac{\rho_g}{0.075} \right) \left(\frac{\rho_l}{62.3} \right) \right]^{1/2}$	
ψ	$\left(\frac{73}{\gamma} \right) \left[\mu_l \left(\frac{62.3}{\rho_l} \right)^2 \right]^{1/3}$	

Because of the dimensional coordinate system in figure 2.3, extending it to other conditions of pipe size or inclination, fluid properties, and flow rates would introduce an unknown error or may give completely wrong results. Hence some researchers such as Griffith and Wallis (1961) and later

Table 2.2: Comparison of Baehr and Stephan (2016) horizontal flow pattern (figure 2.2) and Baker (1958) flow map (figure 2.3)

flow pattern figure 2.2	flow map figure 2.3
(a) bubble flow	BUBBLE OR FROTH region
(b) plug flow	PLUG region
(c) stratified flow	STRATIFIED region
(d) wavy flow	WAVE region
(e) slug flow	SLUG region
(f) annular flow	ANNULAR FLOW region
(g) spray or droplet flow	DISPERSED FLOW region

Al-Sheikh, Saunders, and Brodkey (1970) have tried to find dimensionless numbers for the axis of the flow map in order to generalise the flow map.

Taitel and Dukler (1976) developed a theoretical model, that predicts the relationship between the gas and liquid mass flow rates, the properties of the fluids, the pipe diameters and the angle of inclination, see figure 2.4.

The Taitel flow map is based on five dimensionless numbers, see Taitel and Dukler (1976):

$$X = \sqrt{\frac{\left| \left(\frac{dp}{dx} \right)_{l,s} \right|}{\left| \left(\frac{dp}{dx} \right)_{g,s} \right|}}, \quad T = \sqrt{\frac{\left| \left(\frac{dp}{dx} \right)_{l,s} \right|}{(\varrho_l - \varrho_g) g \cos(\alpha)}}$$

$$Y = \frac{(\varrho_l - \varrho_g) g \sin(\alpha)}{\left| \left(\frac{dp}{dx} \right)_{g,s} \right|}, \quad F = \sqrt{\frac{\varrho_g}{\varrho_l - \varrho_g} \frac{|\vec{U}_{g,s}|}{\sqrt{d g \cos(\alpha)}}} \quad (2.1)$$

$$K = F \sqrt{\frac{d |\vec{U}_{l,s}|}{\nu_l}} = F \sqrt{Re_{l,s}}$$

All of these dimensionless numbers given in equation 2.1 can be determined from the operating conditions. The transitions are shown in figure 2.4 are controlled by the following dimensionless numbers, see Taitel and Dukler (1976):

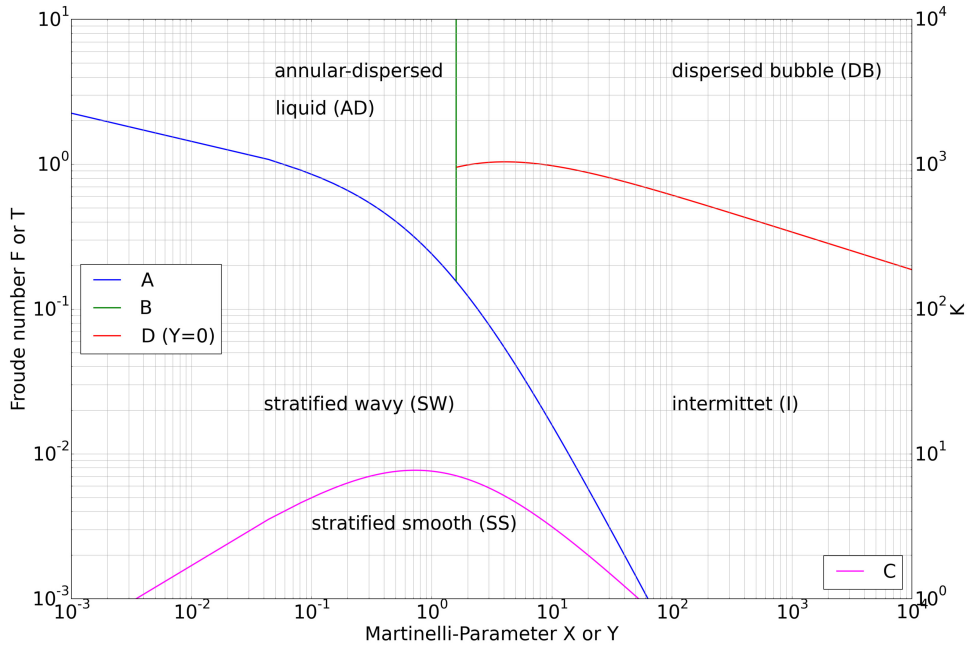


Figure 2.4: Generalised Taitel and Dukler (1976) flow map for horizontal two-phase flow; figure by the author

Stratified to annular	X, F, Y
Stratified to intermittent	X, F, Y
Intermittent to dispersed bubble	X, T, Y
Stratified smooth to stratified wavy	X, K, Y
Annular dispersed liquid to dispersed bubble	X, Y
Annular dispersed liquid to intermittent	X, Y

The remarkable achievement of Taitel and Duckler is that their model is based on a theoretical description of two-phase flows. In Barnea et al. 1980 one can see the good correlation of this model with earlier measurements. All parameter used in the Baker (1958) flow map are dimensional, whereas Taitel and Dukler (1976) uses in his model non-dimensional parameters. This allowing Taitel and Dukler (1976) to be applied to many different pipe diameters, fluids and inclinations. The development of the equations in 2.1 and a detailed explanation can be found in Taitel and Dukler (1976).

Vertical Pipes

For vertical pipes there are much more flow maps available. Hence Wu et al. (2017) examine the most used flow maps for vertical pipes with the up to date measurement techniques. It can be seen, that no flow map exist which is the best overall for upward co-current flows. Following there is a short overview of the Wu et al. (2017) results, which shows the best flow map for specific flow pattern transitions:

- Barnea (1987) best for dispersed bubble to bubble flow regime transition
- Taitel, Bornea, and Dukler (1980) best for bubble to slug flow regime transition
- Barnea (1987) best for slug to churn flow regime transition
- Mishima and Ishii (1984) best for churn to annular flow regime transition

2.2 Steam Water Separation in Eckrohrkessel Steam Boilers

In this section the basics of an Eckrohrkessel boiler is given and the importance of the steam/water separation for the water circulation and the damage prevention of superheaters and turbines. And a briefly overview of separation devices in boiler applications follows.

2.2.1 Eckrohrkessel Boiler

The goal of a steam boiler is to produce steam by feeding with thermal energy. The boiler consists of evaporator, often superheater and economiser heat exchangers. Sometimes an air preheater is added to heat up the combustion air. In evaporators the saturated water is partial evaporated, which have to be separated after to feeding the superheater with dry steam. The superheater heat up the steam to the desired steam temperature. When only saturated steam is needed, the superheater can be cancelled out. The boiler is fed with water, which temperature is less than the saturated temperature usually. But for a better boiler performance, it is recommended to heat up the feed water close to the saturation temperature. This latter task take over the economiser.

Many boiler types exist, though this work focuses on an Eckrohrkessel type. The Eckrohrkessel is a part of the water tube boiler family with natural circulation. Water tube boiler means, that the water flow inside the pipes in contrast to shell boilers. Natural circulation boilers working without a circulation pump. All natural circulation boilers are limited up to about 180 bar, see [Mayr and Gritsch \(1997\)](#), because this technique needs different densities to be working. A schematic drawing of an Eckrohrkessel natural circulation can be seen in figure [2.5](#).

The natural circulation is caused by different densities in the downcomers and return pipes compared to the riser pipes. This can be achieved if riser pipes are heated up and downcomers not. Due to the heating of the riser pipes evaporation is started. This results to a steam/water mixture with

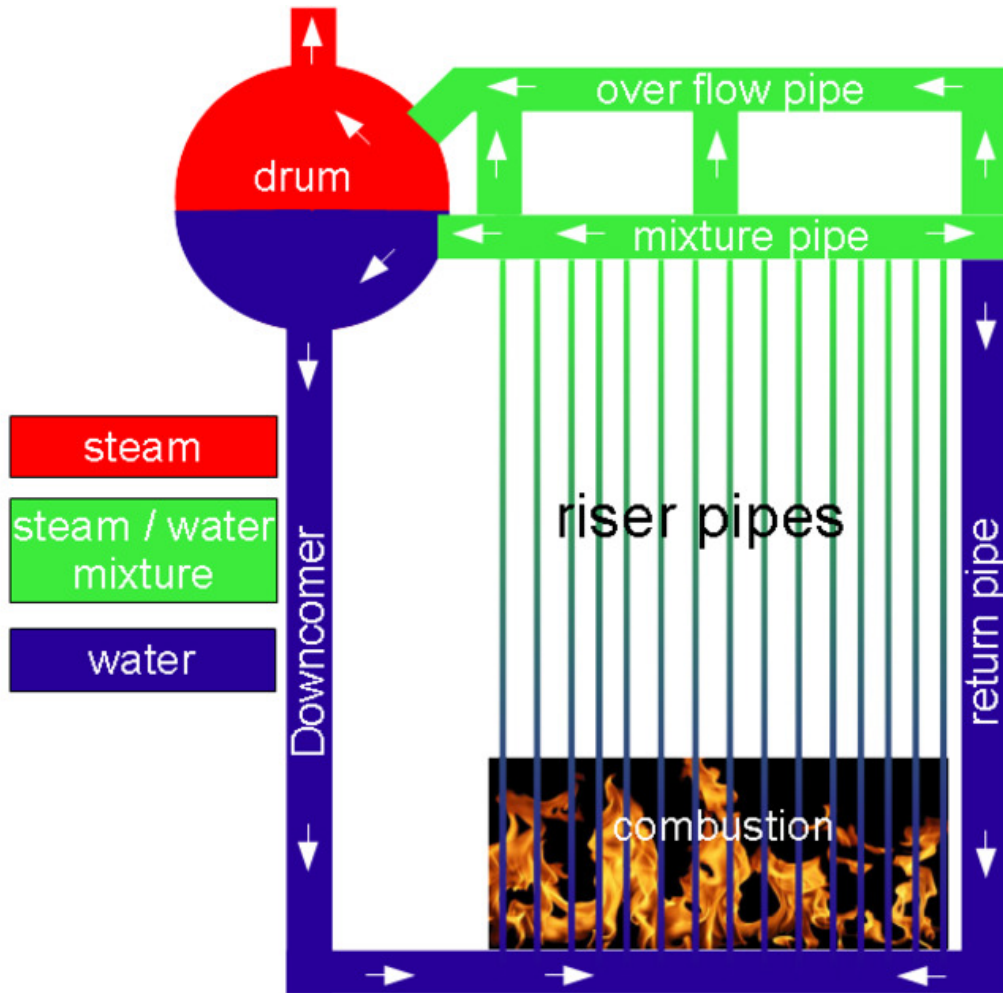


Figure 2.5: Schematic drawing of an Eckrohrkessel steam boiler; figure by the author

less density in the riser pipes and the steam/water mixture rise upwards in the gravity field, whereas the saturated water in the downcomers move downwards. For the natural water circulation it is necessary that there is no steam contamination in downcomers, because this would reduce the density there and results to a lower density difference, which would reduce the water circulation.

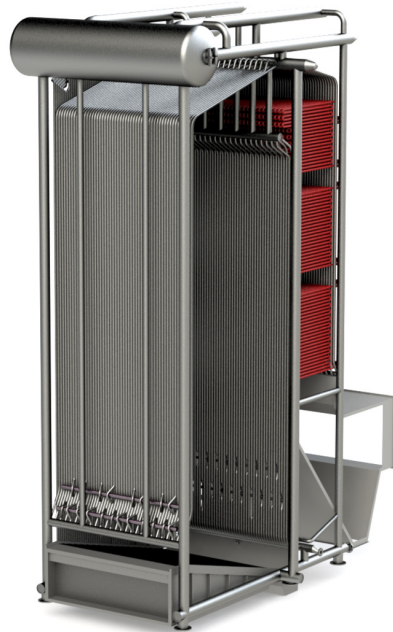
When the water circulation of a running boiler stops, there is no cooling of the heated riser pipes and could lead to a damage. Hence a stopped or very slow water circulation have to be avoided. To ensure a high liquid

purity in the downcomers, there is a drum above downcomers which separate the steam/water mixture to ensure that only water is fed in downcomers. To increase the steam/water mixture separation in drums the Eckrohrkessel boiler have a pre-separation device, see mixture and overflow pipe in figure 2.5. Before the steam/water mixture reach the drum, the steam is mostly flowing in the overflow pipes, whereas the water is mostly flowing in the mixture pipes to the drum.

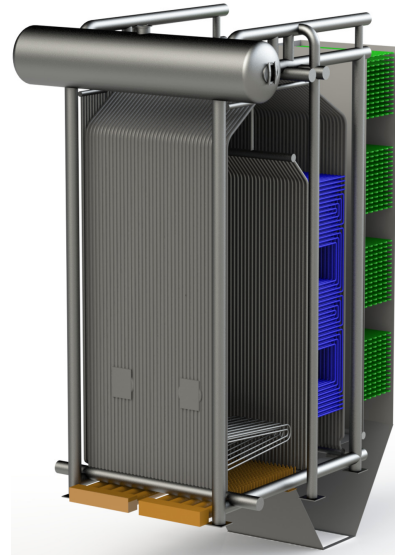
Additionally only an Eckrohrkessel provide return pipes. In the return pipes the water is moving down to feed the riser pipes. It is not such effective like the downcomers, because there is no steam/water mixture separation at the return pipe inlet and steam can suck into the return pipes. But the return pipes advance the water circulation. The big downcomers and return pipes in the boiler corners form a self supporting framework. Types of Eckrohrkessel boilers can be seen in figure 2.6.

For a deeper insight of boiler types and operation principles the book of [Mayr and Gritsch \(1997\)](#) is recommended. The book of [Kitto and Stultz \(2005\)](#) is recommended for someone which is interested in steam production and handling, as well as boiler equipment.

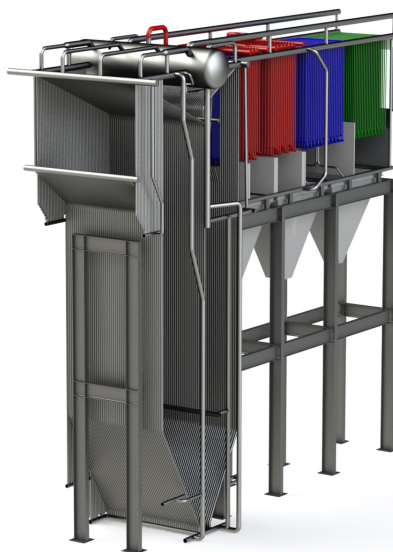
A stable and sufficient water circulation is important for a good boiler operation. To avoid unnecessary boiler operation conditions, it is needed to take into account the flow pattern in mixture and overflow pipes, in the steam drum, and downcomers. Today the Eckrohrkessel is mostly designed as a vertical pipe boiler. Hence the riser, downcomer, and return pipes are vertical pipes. And the flow maps for vertical pipes, see section 2.1.3 vertical pipes, can be used to estimate the flow pattern in these pipes. Overflow pipes, mixture pipes, and the steam drum are horizontal pipes and flow maps for horizontal pipes can be applied, see section 2.1.3 horizontal pipes. One example of unnecessary boiler operation condition is when only one riser pipe is in drop flow regime, see figure 2.1 f. This would result to a damage, because there is no water at the pipe wall and therefore the cooling decrease compared to all other flow regimes, see figure 2.1. Another example are unwanted flow pattern inside the steam drum. In the steam drum a separation



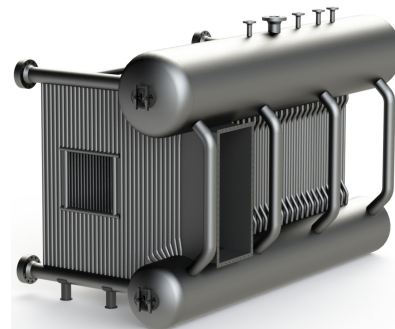
(a)



(b)



(c)



(d)

Figure 2.6: Eckrohrkessel boiler types: (a) grate firing system single drum boiler, (b) fluidised bed single drum boiler, (c) tail end single drum boiler for waste incineration, (d) gas/oil burner bi drum boiler; ERK Eckrohrkessel GmbH 2018

of steam/water mixture is wanted. Hence only the stratified or wavy stratified flow pattern are desired, see figure 2.2. All other flow pattern would result to worse steam quality or steam contamination in downcomers. Generally for all boiler pipes a steady state flow are preferable than transient flow pattern.

2.2.2 Steam Quality

In most boiler applications a high efficiency steam/water mixture separation is crucial in order to:

1. prevent water droplet carryover into superheaters where thermal damage can occur,
2. minimise steam carryunder in the water feeding downcomers where residual steam can reduce the water circulation, and
3. prevent the carryover of solids, dissolved in water droplets in steam flow, into superheaters and turbine where damaging deposits may form, see [Kitto and Stultz \(2005\)](#).

Item 3 is the most important. Boiler water contains contaminants, principally in solution. More than 0.6 ppm of these solids in steam can damage the superheaters and turbine. The solubility of these solids is mostly a few orders of magnitude less in steam than in water, except silica acid, see [Mayr and Gritsch \(1997\)](#). Only small amounts of water droplet carryover, greater than 0.25 mass%, can result in substantial carryover of solids and this leads to unacceptable depositions in superheaters and turbines. [Kitto and Stultz 2005](#)

The steam quality can be calculated by dividing the mass of the steam by the mass of the total mixture, which correspond to the steam mass fraction:

$$q = mf_{steam} = \frac{M_{steam}}{M_{tot}} = \frac{M_{steam}}{M_{steam} + M_{water}} = \frac{\Phi_{steam}^M}{\Phi_{tot}^M} \quad (2.2)$$

2.2.3 Separation Devices

Subcritical pressure recirculating steam boilers are equipped with cylindrical vessels called “steam drums”. Steam drums, see figure 2.5, permit separation of the steam/water mixture, see section 2.2.1. The water is recirculated from the drum to the downcomers and feeding the riser pipes for further steam generation. The saturated steam is discharged through the drum outlet nozzles. Additional task of steam drums are:

1. mix the feedwater with saturated water,
2. mix the additional solids for water treatment,
3. purify the saturated steam to remove contaminants and moisture,
4. remove part of the water (blowdown) to control solids content, and
5. provide water storage to accommodate load fluctuations and cooling if blackout happen, see [Kitto and Stultz \(2005\)](#) and [ERK Eckrohrkessel GmbH \(2018\)](#).

General two different approaches exist to permit high efficiency steam/water mixture separation in steam drums. The first is by providing a large steam/water interface and low steam velocities for natural gravity-driven separation. The second approach is by force the separation with additional mechanical separation equipment. Many boiler design companies combine these both approaches in order to reduce the steam drum investment costs with sufficient steam quality at the same time. The steam drum internals and design procedure of these internals are often company secrets, see [ERK Eckrohrkessel GmbH \(2018\)](#).

Natural Gravity-Driven Separation

Regarding [Kitto and Stultz \(2005\)](#), natural steam/water separation looks at the first glance simple but it is quite complex. This separation strongly depends on a lot influencing factors, like:

1. inlet velocities, see figure 2.7, and
2. inlet location, see figure 2.8,
3. average inlet steam quality,
4. flow pattern,
5. downcomer and steam discharge pipe locations, and
6. disengagement of liquid and steam above the nominal water interface.

Due to the complexity of that separation, the performance of these devices have to be determined by experimental evaluations.

In figure 2.7 (a) it can be seen, that a steam velocity leaving the water surface less than 0.9 m/s is sufficient time for steam/water separation. The same arrangement with higher steam velocities, see figure 2.7 (b), there are water droplets carryover in the discharge steam and steam carryunder in the discharge water, due to the insufficient time. Additionally the rising bubbles cause a false water level indication.

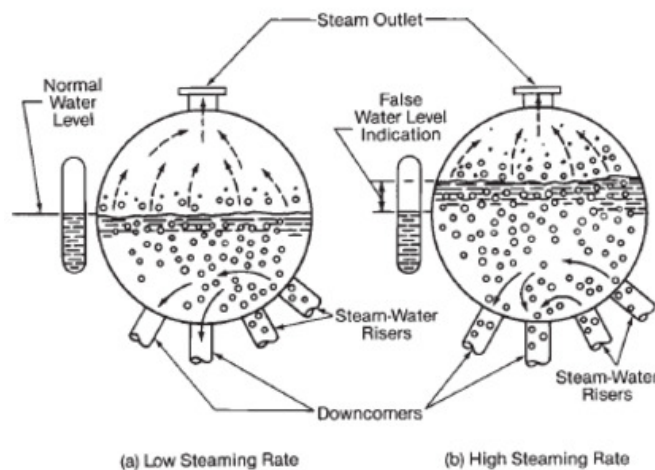


Figure 2.7: Steam drum with natural steam/water separation and different steaming rates; see Kitto and Stultz (2005)

To ensure a sufficient steam drum volume to avoid carryover of water droplets in discharged steam, the “Fachverband Dampfkessel-, Behälter- und Rohrleitungsbau e.V.” (FDBR) published a chart of permitted steam volume strain, see FDBR (2013). This chart is valid for steam boilers mainly natural gravity-driven separation and with subcritical pressure but minimum operation pressure inside the drum greater than 10 bar. The steam volume strain is the saturated steam volume flow divided by the effective steam volume.

$$B_v = \frac{\Phi_{steam}^V}{V_{drum,eff}} \quad (2.3)$$

Whereby the effective drum volume is the volume inside the drum at normal water level which is full applied by the saturated steam.

This chart determine the influence of the permitted steam volume strain to the pressure. If the pressure is increasing the permitted volume strain is decreasing, which results to a bigger effective drum volume. In this easy to use chart it is trying to include effects of all influencing factor, mentioned above. Hence it can be only a rough estimation. For an optimisation of drum volume, above influencing factors and drum internals a detail examination should be carried out by experiments or CFD analyses.

To clarify the complexity of inlet pipe locations, two steam drums with different riser pipe inlet locations are shown in figure 2.8 (a) and 2.8 (b). In both figures one can see a carryover of water droplets in discharged steam and steam bubbles in discharged water. Both arrangements are not sufficient to separate the steam/water mixture only due to the natural gravity-driven separation alone. This effect for example is not included in the FDBR permitted steam volume strain chart. The steam drum design engineer companies have a lot of experience about that pipe connection location but there is no possibility to change the design in order to optimise the steam/water separation without new experiments or CFD analyses.

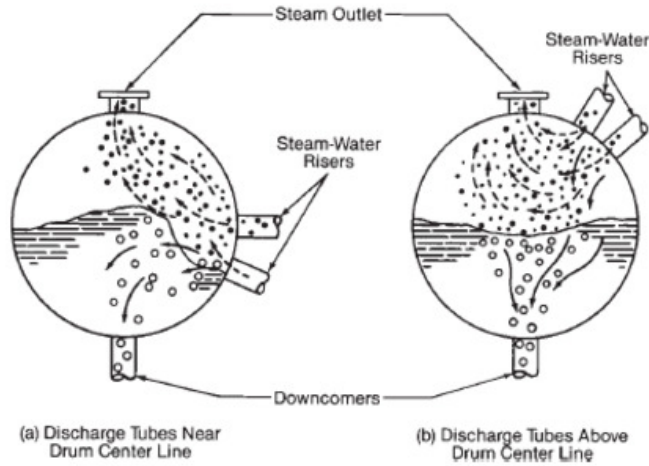
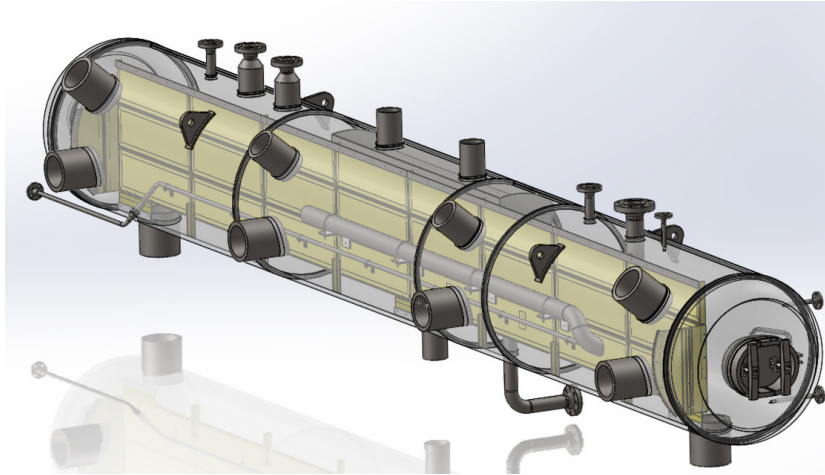


Figure 2.8: Steam drum with natural steam/water separation and different inlet locations of; see Kitto and Stultz (2005)

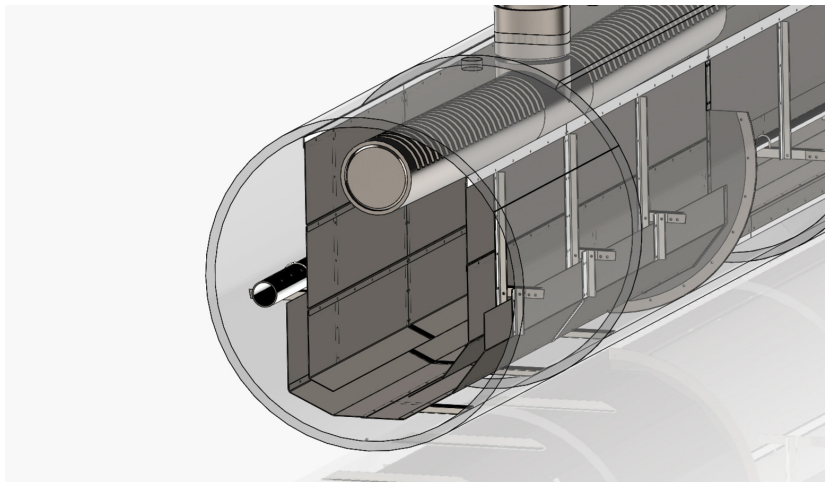
Mechanical Separation Equipment

Mechanical separation equipment can be divided in baffle, screens or scrubbers and centrifugal or radial acceleration forced separators. Baffles provide changes in direction, more even distribution of steam/water mixture, additional flow resistance and increase the steam flow residence time to enhance the gravity-driven separation process. The designs and arrangement of baffles and scrubbers are company secrets, mentioned above. Hence many different arrangements exists. Also Eckrohrkessel have a special design for drum internals, which depending on the pressure, boiler load, drum dimension, single or bi drum boiler and water level. Two exemplary examples of Eckrohrkessel drum internals can be seen in figure 2.9.

In figure 2.9 (a) a single drum baffle arrangement of Eckrohrkessel can be seen in yellow. The inlet pipes located at only one side is nearby the horizontal drum centre line. The steam outlets located at the top and the downcomers at the bottom of the drum, on the vertical centre line. In figure 2.9 (b) a baffle arrangement from Eckrohrkessel can be seen which is often used for bi drum boilers. Like in single drum arrangement the steam outlets and the downcomers located at the top and at the bottom of the drum in the vertical centre line. The riser pipes are located at the lower half of the drum, which



(a)



(b)

Figure 2.9: Eckrohrkessel baffle and scrubber drum internals 3D drawing: (a) Drum baffle internals for single drum boiler, (b) Drum baffle internals for bi drum boilers; ERK Eckrohrkessel GmbH 2018

it is not shown. In some cases Eckrohrkessel put a scrubber before the steam outlet, see the perforated pipe at the top in figure 2.9 (b), to enhance the steam quality. Pictures of single drum Eckrohrkessel drum internals on side can be seen in figure 2.10, which arrangement is comparable with figure 2.9 (a).

Variations of perforated plates have been widely used also, see perforated

pipe at the top of figure 2.9 (b) and 2.10 (b). The last is useful when the boiler load fluctuate a lot or a high purified steam is needed.



(a)



(b)

Figure 2.10: Eckrohrkessel baffle and scrubber drum internals pictures at side: (a) longitudinal and side baffle plate arrangement, (b) side baffle plate and scrubber box for steam outlet at the top of the drum; ERK Eckrohrkessel GmbH 2018

Additional to the baffle plates, there are mechanical separation devices, which used the centrifugal force or the radial acceleration. In figure 2.11 are shown exemplary a conical cyclone 2.11 (a), a curved arm separator 2.11 (b), a

horizontal 2.11 (c) and a vertical cyclone separator 2.11 (d).

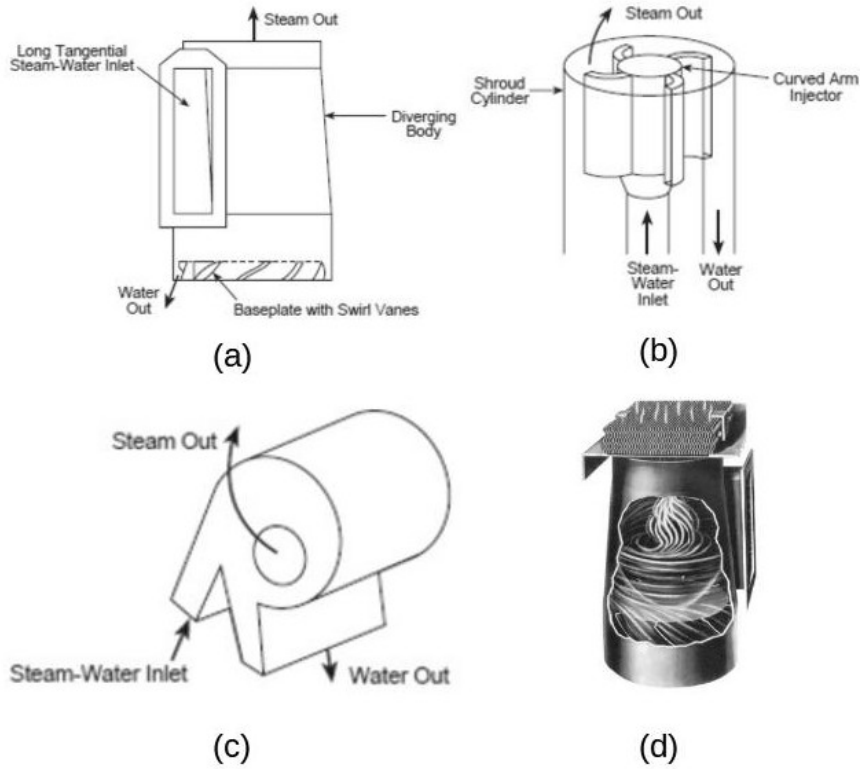


Figure 2.11: Typical steam/water mechanical separators: (a) Conical cyclone, (b) Curved arm, (c) horizontal cyclone separator, (d) vertical cyclone separator; [Kitto and Stultz 2005](#)

All these devices in figure 2.11 are arranged inside the drum often in combination with baffles to force the steam/water mixture through these devices. For example vertical cyclones are placed inside the drum in rows along the length of the drum, see figure 2.12.

In forced separation devices the steam/water mixture is admitted tangentially as shown in figures 2.11. The redirection of the steam/water mixture is caused in figure 2.12 by baffle plates. In this drum internal arrangement from Babcock the purified water leave the vertical cyclones downwards to the downcomers. The steam flow upwards from the cyclones to a first and subsequently to a second scrubber and is discharged through the steam drum outlet nozzle.

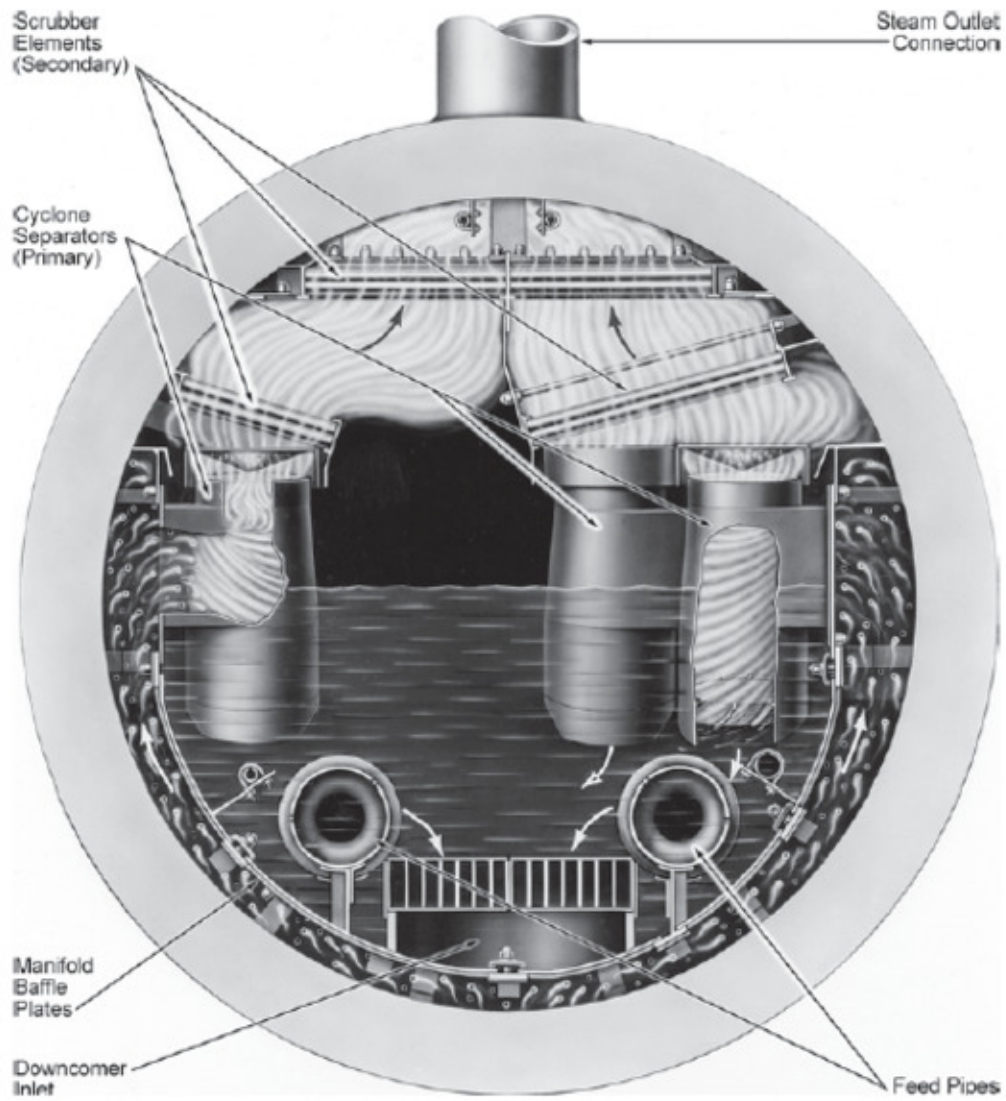


Figure 2.12: Steam drum internals with three rows of cyclone separators; see Kitto and Stultz (2005)

2.3 Multiphase Flow Models in Ansys CFX

Ishii and Hibiki (2006) put it in a nutshell: "At first glance it may appear that various two or multiphase flow systems and their physical phenomena have very little in common". Many researcher tending to develop system specific models and correlations of limited generality and applicability in the last decades. Therefore a fundamental understanding of two-phase flow growing only slowly and the predictive capability is very little. The performance of such a predictive model rises and falls upon both the availability of experimental data and of mathematical models.

But the derivation of multiphase flow equations is compared to single-phase more complicated. The existence of multiple, deformable and moving interfaces and attendant significant discontinuities of fluid properties and complicated flow field next to the interface is the reason why, see Harlow and Amsden (1975) and Prosperetti and Jones (1984). Thus additionally to single-phase field equations the geometric structure of the interface take into account in multiphase flows. The mentioned geometric structure affect the flow pattern in a strong way, which can be seen in multiphase experiments, see Fabre, Masbernat, and Suzanne (1987) for example.

Therefore it is a good idea to classify the two-phase flow systems regarding the interface structure. Like a single-phase flow can be classified into laminar, transitional and turbulent flow a two-phase flow can be classified according to the structure of interface into separated flow, transitional or mixed flow and dispersed flow, see Ishii and Hibiki (2006), Clift, Grace, and Weber (1978), Huhn and Wolf (1975), Kandlikar (1999), Cheremisinoff and Gupta (1983). It can be expected that if the flow regime is the same, the two-phase flow is exhibited similarities.

To put the physics in a mathematical model, generally Ishii and other authors recommend a macroscopic formulation based on proper averaging, which results to a two-phase flow continuum formulation instead of a local instant formulation with explicit moving interfaces, see Ishii and Hibiki (2006), Prosperetti and Jones (1984), Harlow and Amsden (1975), Flügge et al. (1959),

etc. The macroscopic formulation eliminate the interfacial discontinuities and ensure the numerical stability, see [Harlow and Amsden \(1975\)](#). Though this macroscopic formulation has to take into account that a multiphase flow consists of multiple length scales, which multi-scale effects bringing to continuum flow formulations and closure relations. By [Ishii and Hibiki \(2006\)](#) the important length scales of a multiphase flow are

1. system scale
system transients and component interaction are the primary focus
2. macroscopic scale
required for continuum assumption, interface structure, transport of mass, momentum and energy
3. mesoscopic scale
related to local structures, the conservation principles need additional constitutive relations for bulk transfer, interfacial transfer rates based on interfacial flux and interfacial area
4. microscopic scale
wall nucleation or condensation, bubble coalescence and break-up, entrainment and deposition

As mentioned in section [2.1.3](#) in early years researchers developed two-phase specific models, which included variables belonging to system scale. Some example specific models can be founded in [Cheremisinoff and Gupta \(1983\)](#) for a number of two-phase flow applications. There are some publication regarding general flow maps where are trying to predict the two-phase flow pattern, [Taitel and Dukler \(1976\)](#), [Cheremisinoff and Gupta \(1983\)](#). These flow maps are based on empirical system scale properties and were derived from experimental data. Hence this can not be used for a predictive CFD model in which system scale variables are often not available. But these flow maps are useful for validation.

For a description of a two-phase flow the volume fraction and the interfacial area are fundamental parameters. Both parameters belong to the mesoscopic

scale. The volume fraction as well as the interfacial area are closely related to the two-phase flow pattern, see [Ishii and Hibiki \(2006\)](#) and [Ansys \(2016c\)](#).

In the following sections an overview on available multiphase flow models in CFX and belonging mathematical notation is presented. The following section in this chapter is based on the CFX Solver Theory Guide, see [Ansys \(2016c\)](#). Additional sources are also mentioned in the text below.

2.3.1 Ansys CFX Basics for Single Phase Flows

Ansys CFX is a CFD software which based on the unsteady Navier-Stokes equations in there conservative form, see [Versteeg and Malalasekera \(2007\)](#) and [Anderson \(1995\)](#) for advanced informations. Following there are the continuity, momentum and energy equations for a single phase flow in Cartesian coordinate system:

1. The continuity equation

$$\frac{\partial \rho}{\partial t} + \text{div}(\rho \vec{U}) = 0 \quad (2.4)$$

2. The momentum equations

x - component:

$$\frac{\partial(\rho u)}{\partial t} + \text{div}(\rho u \vec{U}) = -\frac{\partial p}{\partial x} + \frac{\partial \tau_{xx}}{\partial x} + \frac{\partial \tau_{yx}}{\partial y} + \frac{\partial \tau_{zx}}{\partial z} + \rho f_x$$

y - component:

$$\frac{\partial(\rho v)}{\partial t} + \text{div}(\rho v \vec{U}) = -\frac{\partial p}{\partial y} + \frac{\partial \tau_{xy}}{\partial x} + \frac{\partial \tau_{yy}}{\partial y} + \frac{\partial \tau_{zy}}{\partial z} + \rho f_y \quad (2.5)$$

z - component:

$$\frac{\partial(\rho w)}{\partial t} + \text{div}(\rho w \vec{U}) = -\frac{\partial p}{\partial z} + \frac{\partial \tau_{xz}}{\partial x} + \frac{\partial \tau_{yz}}{\partial y} + \frac{\partial \tau_{zz}}{\partial z} + \rho f_z$$

Where the stress tensor τ is related to the strain rate regarding Stokes

by:

$$\begin{aligned}
\tau_{xx} &= \lambda(\operatorname{div}\vec{U}) + 2\mu\frac{\partial u}{\partial x} \\
\tau_{yy} &= \lambda(\operatorname{div}\vec{U}) + 2\mu\frac{\partial v}{\partial y} \\
\tau_{zz} &= \lambda(\operatorname{div}\vec{U}) + 2\mu\frac{\partial w}{\partial z} \\
\tau_{xy} = \tau_{yx} &= \mu\left(\frac{\partial v}{\partial x} + \frac{\partial u}{\partial y}\right) \\
\tau_{zx} = \tau_{xz} &= \mu\left(\frac{\partial u}{\partial z} + \frac{\partial w}{\partial x}\right) \\
\tau_{yz} = \tau_{zy} &= \mu\left(\frac{\partial w}{\partial y} + \frac{\partial v}{\partial z}\right)
\end{aligned} \tag{2.6}$$

The momentum source term can be written to:

$$S_M = \varrho\vec{f} \tag{2.7}$$

3. The total enthalpy equation

$$\begin{aligned}
\frac{\partial(\varrho h_{tot})}{\partial t} + \operatorname{div}(\varrho h_{tot}\vec{U}) &= \operatorname{div}(k \operatorname{grad}T) + \frac{\partial p}{\partial t} \\
&+ \left[\frac{\partial(u\tau_{xx})}{\partial x} + \frac{\partial(u\tau_{yx})}{\partial y} + \frac{\partial(u\tau_{zx})}{\partial z} \right. \\
&+ \frac{\partial(v\tau_{xy})}{\partial x} + \frac{\partial(v\tau_{yy})}{\partial y} + \frac{\partial(v\tau_{zy})}{\partial z} \\
&\left. + \frac{\partial(w\tau_{xz})}{\partial x} + \frac{\partial(w\tau_{yz})}{\partial y} + \frac{\partial(w\tau_{zz})}{\partial z} \right] + S_h
\end{aligned} \tag{2.8}$$

Where h_{tot} is the total enthalpy, related to static enthalpy $h(T, p)$ by

equation 2.9:

$$h_{tot} = h + \frac{1}{2}\vec{U}^2 = h + \frac{1}{2}(u^2 + v^2 + w^2) \quad (2.9)$$

and the static enthalpy related to equation 2.10:

$$h = e + \frac{p}{\varrho} \quad (2.10)$$

Additionally to the Navier-Stokes equations, equations of state are needed in order to solve the equation system. At this point, it is referred to the literature, see Anderson (1995), Versteeg and Malalasekera (2007), Ansys (2016c) and Bošnjaković and Knoche (1988).

Buoyancy effects are deactivated in CFX by default. For simulations involving multicomponent flow, multiphase flow or a fluid with variable density, the buoyancy model should be activated. To include buoyancy effects a source term is added to the momentum equation, see equation 2.11:

$$S_{M,buoy} = (\varrho - \varrho_{ref})\vec{g} \quad (2.11)$$

If buoyancy is activated in CFX the pressure in the momentum equation excludes the hydrostatic pressure gradient due to the reference density ϱ_{ref} , see equation 2.12:

$$p_{abs} = p + p_{ref} + \varrho_{ref}\vec{g}(\vec{r} - \vec{r}_{ref}) \quad (2.12)$$

\vec{r}_{ref} is a reference location. The absolute pressure is used for the fluid properties.

The Navier-Stokes equations are coupled non-linear partial differential equations and have to be discretised with numerical methods to be solved by computers. Most of the available CFD software use the Finite-Volume-Method (FVM) discretisation which is described in Anderson (1995) or Versteeg and Malalasekera (2007). Ansys CFX differ from these method. It uses an

element-based FVM. A detailed description can be found in [Ansys \(2016c\)](#). Hence, CFX stores all unknowns at the nodes instead on center points. This procedure results to a control volume which has more balance faces than the geometric mesh cell and look likes a polyhedron. Due to more balance faces and neighboring cells the approximation of gradients are much better, see [Versteeg and Malalasekera \(2007\)](#) and [Ansys \(2016c\)](#). Hence gradients like at the interface are solved with more accuracy and stabilise the numeric solution process. This latter fact advantage Ansys CFX for simulation with high gradients like appearing in multiphase flow.

In most CFD software there are a couple of solvers with different pressure-velocity coupling procedures but not in Ansys CFX. CFX provide only the implicit pressure based coupled algorithm to solve the set of linear coupled system of equations. The difference to the segregated algorithm and other density based solver with advantages and disadvantages can be seen in [Ansys \(2016d\)](#). The coupled algorithm offers some advantages over the segregated, see [Ansys \(2016d\)](#) and [Ansys \(2016c\)](#)

- more robustness if mesh is poor or large time steps are used,
- higher efficiency, and faster convergence.

The drawback of the coupled algorithm is the higher memory waste than the segregated one, see [Ansys \(2016c\)](#). In multiphase flows with large interfaces the segregated algorithm has significant problems to solve the pressure field due to high gradients at the interface. Spurious velocities can arise rather with segregated algorithm and destabilise the simulation. Hence Ansys CFX is recommended for multiphase flows.

Important for implementation of own models, Ansys CFX provides two interfaces. Firstly, one can insert new models as "Expressions". This can be carried out easily but with some restrictions. The second interface assume, that the CFX user is familiar with the programming language Fortran77. The second interface is more powerful than the first one but more error prone and time consuming. For more information above CFX interfaces see [Ansys \(2016a\)](#).

2.3.2 Multiphase Formulation in Ansys CFX

Currently two different approaches for the numerical calculation of multiphase flows are available

- the Euler-Lagrange approach
- the Euler-Euler approach

The Euler-Lagrange Approach

In General the fluid phase is treated as a continuum with the complete set of Navier-Stokes equation mentioned above. This phase is called the Euler phase, because the continuum based on fixed in space coordinate system. While the dispersed phase is solved by tracking a number of particles through the Euler phase like in Lagrange balance model with moving coordinate systems, see [Anderson \(1995\)](#). The particle trajectories are computed individually at specified intervals. "This makes the model appropriate for the modelling of spray dryers, coal and liquid fuel combustion, and some particle-laden flows, but inappropriate for the modelling of liquid-liquid mixtures, fluidized beds, or any application where the volume fraction of the second phase cannot be neglected", see [Ansys \(2016d\)](#). Due to the Euler-Lagrange approach resolves informations on the level of a single particle it is quite computationally expensive. The computational effort can be decreased if a number of single particles are pooled to clusters and then track clusters. Though to track clusters cause a high computational effort furthermore and is increased if the number of particles is increased too.

The Euler-Euler Approach

In the Euler-Euler approach, all phases treated as interpenetrating continua. Since the volume of a phase cannot be occupied by the other phase a new variable the volume fraction is introduced, see [Ansys \(2016c\)](#). The Euler-Euler Approach is appropriate for separated flows as well as restricted for dispersed flows. Dispersed flows can be simulated with that Euler-Euler approach if the overall motion of the particles is of interest instead than tracking

individual particles. All equations are averaged in each cell to obtain mean fields, as describe in section 2.3.3. Source terms in the momentum equation have to be modelled to achieve coupling between the different phases, see section 2.3.4.

Additionally to the single phase notation lowercase Greek letters, α , β , γ introduced to distinguish different fluids. In one cell, in multiphase flow, all fluids exist at the same time. The volume fraction is the volume which is occupied by one phase in one cell volume, like a weighting factor. For example the volume which the phase α is occupied V_α divided by the Cell Volume V equals

$$vf_\alpha = \frac{V_\alpha}{V} \quad (2.13)$$

These volume fractions are assumed to be continuous functions. The sum of all volume fractions in one cell is equal one.

Then the density of a bulk fluid in one cell is given by

$$\varrho_{mix} = \sum_{\alpha} \varrho_{\alpha} vf_{\alpha} \quad (2.14)$$

The total pressure in a multiphase simulation is defined as

$$p_{tot} = p_{stat} + \sum_{\alpha} \frac{1}{2} vf_{\alpha} \varrho_{\alpha} \vec{U}_{\alpha}^2 \quad (2.15)$$

This Thesis deals with a steam drum in which all multiphase flow pattern can arise. Hence the Euler-Lagrange approach is inappropriate because high volume fractions of a phase can not be neglected, see 2.3.2 "The Euler-Lagrange Approach" and the Euler-Euler model is used.

In Ansys CFX two different sub-models are available for the Euler-Euler approach

- the homogeneous model
- and the inter-fluid transfer (inhomogeneous) model.

The main distinction of the homogeneous and inhomogeneous model is that the common flow field is shared by all fluids in the homogeneous model and is separate in inhomogeneous model. Hence a homogeneous flow field allows some simplifications. The homogeneous model correspond to the volume of fluid (VOF) model, see [Ansys \(2016c\)](#) and [Ansys \(2016d\)](#).

In case of a wavy stratified two fluid flow the homogeneous model result in a wrong geometric interface structure. Due to the shared flow field the velocities for the heavier and the lighter fluid are the same at the interface. There are some experiments, like in [Fabre, Masbernat, and Suzanne \(1987\)](#), where a slip velocity of both phases at the interface was measured. Such an wavy stratified flow regime is the most common regime in ERK steam drums inlet pipes. Because of the importance of the slip velocity and the importance of geometric interface structures for droplet prediction, the homogeneous model is discarded and the inhomogeneous model is used. Ansys recommend the homogeneous model for well defined distinct interface. If the interface not well defined, for example one phase is entrained in the other and behaves as a disperse phase, the inhomogeneous model may be more appropriate which underpin the choice, see [Ansys \(2016c\)](#).

2.3.3 The Inhomogeneous Model

For each phase the Navier-Stokes equation have to be solved. Coupling is achieved through the pressure and interface transfer of momentum, heat and mass. A detailed derivation can be seen in [Ishii and Hibiki \(2006\)](#) and an overview in [Ansys \(2016c\)](#). For the sake of completeness the most important relations are stated here. Ishii obtained the macroscopic balance equations by time averaging the local formulation of the Navier-Stokes equations. The time averaging eliminate the drastically change at one point in all properties. The averaging is to transform two phases, alternately occupying a point with discontinuities at the interface, into two simultaneous continua. Because of turbulence and rapidly variable fluctuations (discontinuities) in vicinity of the interface, see figure [2.13](#), the local instant formulation are inaccessible. This procedure is equal to turbulence handling in single phase flow.

First we take a fixed time interval Δt that is large enough to smooth out the local variations of properties but small compared to macroscopic time scales of the bulk flow, see figure 2.14.

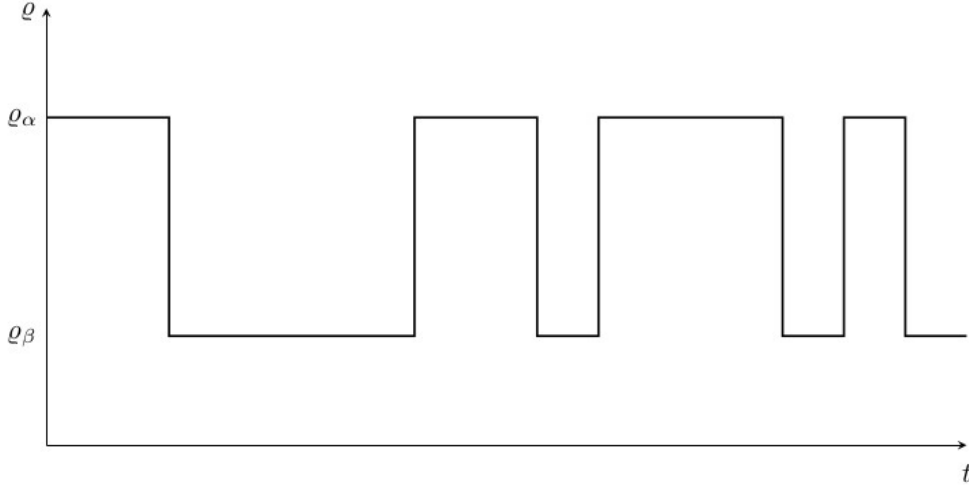


Figure 2.13: Local instant formulation of fluid density in time; figure by the author

In figure 2.14 we can identify different time intervals

- $\Delta t_\alpha =$ phase α occupied point \vec{r}_0 [s]
- $\Delta t_\beta =$ phase β occupied point \vec{r}_0 [s]
- $\Delta t_{fs} =$ characteristic of the interface dominates at point \vec{r}_0 [s]

The overall time interval Δt equals the sum of all different time intervals

$$\Delta t = \sum_i \Delta t_{fs,i} + \sum_k \sum_i \Delta t_{k,i}, \text{ for } k = \alpha, \beta \quad (2.16)$$

Regarding figure 2.14 we can assign indicator functions M_α , M_β and M_{fs} to distinguish three states

1. $M_\alpha(\vec{r}, t) = 1$, $M_\beta(\vec{r}, t) = 0$, $M_{fs}(\vec{r}, t) = 0$, a point occupied by phase α
2. $M_\alpha(\vec{r}, t) = 0$, $M_\beta(\vec{r}, t) = 1$, $M_{fs}(\vec{r}, t) = 0$, a point occupied by phase β
3. $M_\alpha(\vec{r}, t) = 0$, $M_\beta(\vec{r}, t) = 0$, $M_{fs}(\vec{r}, t) = 1$, a point occupied by interface

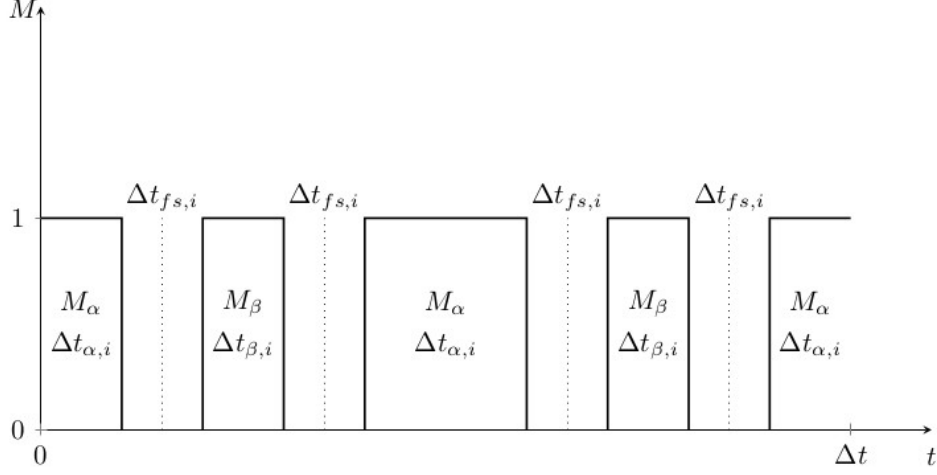


Figure 2.14: Local instant formulation of arbitrary variable with various time intervals; figure by the author

Thus a general function of k^{th} -phase ϕ_k at the point of averaging \vec{r}_0 is defined as

$$\phi_k(\vec{r}_0, t) = M_k(\vec{r}_0, t)\phi \quad (2.17)$$

With the assumption of a singular interface thickness $\delta \rightarrow 0$ we can write $\Delta t_{fs} = 0$. Hence we can find the time average phase density function vf_k as

$$vf_k(\vec{r}_0, t_0) \equiv \lim_{\delta \rightarrow 0} \frac{1}{\Delta t} \int_{\Delta t} M_k(\vec{r}_0, t) dt = \frac{\Delta t_k}{\Delta t}, \text{ for } k = \alpha, \beta \quad (2.18)$$

vf_k is a fundamental parameter in time averaged field equations. The physically meaning of that parameter is the probability of finding the k^{th} -phase. This parameter is namely the *local time fraction* or *void fraction* or *volume fraction* of the k^{th} -phase.

Following Ishii and Hibiki (2006) the Eulerian time average of an general function of the k^{th} -phase ϕ_k is given by

$$\overline{\phi_k}(\vec{r}_0, t_0) \equiv \lim_{\delta \rightarrow 0} \frac{1}{\Delta t} \int_{\Delta t} \phi_k(\vec{r}_0, t) dt \quad (2.19)$$

The phase average of an general function of k^{th} -phase $\overline{\overline{\phi_k}}$ can be defined by the indicator function M_k and the time average of the general function $\overline{\phi_k}$

$$\overline{\overline{\phi_k}} = \frac{\overline{M_k \phi_k}}{\overline{M_k}} = \frac{\overline{\phi_k}}{v f_k} = \frac{1}{\Delta t_k} \int_{\Delta t_k} \phi_k dt \quad (2.20)$$

Mass specific quantities should be weighted by the densities

$$\widehat{\phi_k} = \frac{\overline{\rho_k \phi_k}}{\overline{\rho_k}} \quad (2.21)$$

With the previous definitions the time average of local instant continuum equation yields to a macroscopic continuum equation for each phase

$$\frac{\partial v f_k \overline{\overline{\rho_k}}}{\partial t} + \text{div} \left(v f_k \overline{\overline{\rho_k}} \widehat{\vec{U}_k} \right) = S_{Mass,k}, \text{ for } k = \alpha, \beta \quad (2.22)$$

and

$$\sum_k S_{Mass,k} = 0 \quad (2.23)$$

If phase change appearing on the interface the mass source terms $S_{Mass,k}$ are unequal zero.

The macroscopic momentum balance equation for each phase is

$$\begin{aligned} \frac{\partial v f_k \overline{\overline{\rho_k}} \widehat{\vec{U}_k}}{\partial t} + \text{div} \left(v f_k \overline{\overline{\rho_k}} \widehat{\vec{U}_k} \widehat{\vec{U}_k} \right) &= -\text{grad} \left(v f_k \overline{\overline{p_k}} \right) \\ + \text{div} \left[v f_k \left(\overline{\overline{\tau_k}} + \tau_{turb,k} \right) \right] &+ v f_k \overline{\overline{\rho_k}} \vec{g} + S_{Mom,k} \end{aligned} \quad (2.24)$$

with the pressure p , the gravity acceleration vector \vec{g} , the viscous τ and the turbulent τ_{turb} stress tensor. The term $S_{Mom,k}$ denote the k^{th} -phase momentum source which form the interfacial transfer.

The momentum balance equations are coupled by the condition

$$\sum_k S_{Mom,k} - S_{st} = 0 \quad (2.25)$$

with the mixture momentum source due to surface tension S_{st} .

For each phase a transport equation for the volume fraction is solved, additionally to the regular transport equations, to obtain a transported volume conservation equation. Divide the phasic density from equation 2.22 and sum

over all phases yields to

$$\sum_k \frac{1}{\overline{\varrho_k}} \left[\frac{\partial}{\partial t} (v f_k \overline{\varrho_k}) + \text{div} (v f_k \overline{\varrho_k} \vec{U}_k) \right] = \sum_k \frac{1}{\overline{\varrho_k}} (S_{Mass,k}) \quad (2.26)$$

Equation 2.26 can be simplified for an incompressible flow to

$$\frac{\partial v f_k}{\partial t} + \text{div} (v f_k \vec{U}_k) = 0 \quad (2.27)$$

Equation 2.26 or 2.27 is required to ensure the volume flows to have zero divergence.

2.3.4 Interfacial Momentum Transport of Inhomogeneous Model

The exact form of momentum interfacial transport term $S_{Mom,k}$ is expressed in local instant variables. Thus it is not possible to use them as the constitutive law in the average field equations. Furthermore not all the characteristics inherent to the local instant two-phase flow can be brought into the time-average model, see Ishii and Hibiki (2006). Hence we have to make some assumptions in order to distinguish the dominant transfer mechanisms and also eliminate some of the complicated terms that have insignificant effects in the macroscopic field. Generally the momentum transport term is modelled as

$$\begin{aligned} S_{Mom,k} &= \frac{v f_k}{V_{sphere}} \left(\vec{F}_k^D + \vec{F}_k^V + \vec{F}_k^B + \vec{F}_k^L + \vec{F}_k^W + \vec{F}_k^T \right) \\ &= S_{Mom,k}^D + S_{Mom,k}^V + S_{Mom,k}^B + S_{Mom,k}^L + S_{Mom,k}^W + S_{Mom,k}^T \end{aligned} \quad (2.28)$$

- $S_{Mom,k}$: combined generalized interfacial drag force
- $S_{Mom,k}^D$: Drag force
- $S_{Mom,k}^V$: Virtual mass force; force which is required to accelerate the apparent mass of the surrounding phase

- $S_{Mom,k}^B$: Basset force; effect of the acceleration on viscous drag and boundary-layer development
- $S_{Mom,k}^L$: Lift force normal to the relative velocity; due to rotation of fluid
- $S_{Mom,k}^W$: Wall-lift or wall-lubrication force; due to velocity distribution change near a wall
- $S_{Mom,k}^T$: Turbulent dispersion force; due to concentration gradient

Especially the drag force is significant to form the free surface and all other forces can be neglected, see [Porombka and Höhne \(2015\)](#). But if one phase dispersed all these forces should take into account see [Lucas and Krepper \(2007\)](#). For more information also regarding the other forces can be seen in [Ishii and Hibiki \(2006\)](#).

Generally the standard drag force under steady-state condition acting on a particle is based on the drag coefficient C_D and the relative velocity \vec{U}_{rel}

$$\vec{F}_{disp}^D = -C_D \frac{\rho_c}{2} \vec{U}_{rel} |\vec{U}_{rel}| A_{proj} \quad (2.29)$$

- C_D drag coefficient [-]
- ρ_c density of continuum [kg/m³]
- $\vec{U}_{rel} = \vec{U}_{disp} - \vec{U}_c$ relative velocity [m/s]
- A_{proj} projected Area of a particle [m²]

The drag force is related to interfacial drag force as

$$S_{Mom,disp}^D = \frac{v f_{disp} \vec{F}_{disp}^D}{V_{sphere}} = - \left(v f_{disp} \frac{A_{proj}}{V_{sphere}} \right) C_D \frac{\rho_c}{2} \vec{U}_{rel} |\vec{U}_{rel}| \quad (2.30)$$

where

$$A_{\alpha\beta} = \frac{A_{proj}}{V_{sphere}} \quad (2.31)$$

represent the interfacial area per unit volume and called interfacial area density (IAD).

This interfacial transfer depends directly from the unknown contact surface area per unit volume between the two phases namely the interfacial area density $A_{\alpha\beta}$ and drag coefficient C_D . Currently there are three algebraic models to prescribe $A_{\alpha\beta}$ and C_D in CFX either the particle model or the mixture model or the free surface model.

Interface momentum transfer implementation in Ansys CFX will be described to understand the implementation of interfacial length scale and drag coefficient functions. Interface momentum transfer, $\vec{M}_{\alpha\beta}$, occur by the interaction of phase β on phase α . The total force on phase α due to interaction with other phases \vec{M}_α is.

$$\vec{M}_\alpha = \sum_{\beta \neq \alpha} \vec{M}_{\alpha\beta} \quad (2.32)$$

Interfacial forces between two phases are equal an opposite, so that the net interfacial forces sum to zero:

$$\left(\vec{M}_{\alpha\beta} = -\vec{M}_{\beta\alpha} \right) \curvearrowright \sum_{\alpha} \vec{M}_\alpha = 0 \quad (2.33)$$

Like in equation 2.28 there are several physical effects which have to sum up to total interfacial force:

$$\vec{M}_{\alpha\beta} = \vec{M}_{\alpha\beta}^D + \vec{M}_{\alpha\beta}^V + \vec{M}_{\alpha\beta}^B + \vec{M}_{\alpha\beta}^L + \vec{M}_{\alpha\beta}^W + \vec{M}_{\alpha\beta}^T + \dots \quad (2.34)$$

In Ansys CFX the following form is used to model interface drag force acting on phase α due to phase β

$$\vec{M}_\alpha^D = c_{\alpha\beta}^D \left(\vec{U}_\beta - \vec{U}_\alpha \right) \quad (2.35)$$

The coefficient $c_{\alpha\beta}^D$ can be computed from dimensionless drag coefficients:

$$C_D = \frac{\left| \vec{F}_{disp}^D \right|}{\frac{1}{2} \rho_\alpha \left| \vec{U}_\beta - \vec{U}_\alpha \right|^2 A_{proj}} \quad (2.36)$$

The Inhomogeneous MUSIG Model

The inhomogeneous multiple bubble size group model (iMUSIG) can handle polydispersed multiphase flows. The iMUSIG model is based on the Population balance equation (PBE), what provide the opportunity that the dispersed phase has a large variation in size. Such a population balance model (PBM) is an advanced model that can take into account mechanisms of breakup, coalescence, etc. The iMUSIG model is a well validated model for bubbly flows, see [HZDR and Ansys \(2016\)](#). Due to many additional transport equations PBM is computational intensive. In the iMUSIG model PBE's are solved for each size fraction

$$\frac{\partial n(m, t)}{\partial t} + \text{div}(\vec{U} n(m, t)) = B_B - D_B + B_C - D_C \quad (2.37)$$

In equation [2.37](#) $n(m, t)$ denotes the number density of particles of mass m at time t , B_B is the birth rate due to breakup of larger particles and D_B the death rate due to breakup into smaller particles, B_C and D_C respectively represent the birth rate due to coalescence of smaller particles, and the death rate due to coalescence with other particles.

Currently it is possible to set only one phase as dispersed. Hence iMUSIG is not considered any further. [Ansys 2016c](#) But there are some research to advance the iMUSIG model that the gas phase can be dispersed and continuous. Currently, see [HZDR and Ansys \(2016\)](#), the liquid phase is still continuous. This research at HZDR is in progress and can be find under the keyword GENTOP. It is to be expected that the GENTOP model is very computational intensive, because three phases have to be solved for a two-phase flow. For further information about iMUSIG implementation in CFX see [Ansys \(2016c\)](#) and information about GENTOP see [HZDR and Ansys \(2016\)](#).

The Particle Model

The particle model assumes that one of the phases is continuous (phase α) and the other is dispersed (phase β). The dispersed phase is assumed consist of spherical particles of mean diameter d_β . With that assumption,

the interface area density is

$$A_{\alpha\beta} = \frac{6 v f_{\beta}}{d_{\beta}} \quad (2.38)$$

see Ansys theory [Ansys \(2016c\)](#). The equation 2.38 correspond to the Sauter diameter equation see 3.3. Some interface transfer models need non-dimensional numbers like particle Reynolds number and fluid Prandtl number.

$$Re_{\alpha\beta} = \frac{\varrho_{\alpha} |\vec{U}_{\beta} - \vec{U}_{\alpha}| d_{\beta}}{\mu_{\alpha}} \quad (2.39)$$

$$Pr_{\alpha\beta} = \frac{\mu_{\alpha} cp_{\alpha}}{k_{\alpha}} \quad (2.40)$$

- ϱ_{α} = density of continuous phase [kg/m³]
- $v f_{\beta}$ = volume fraction of dispersed phase [–]
- d_{β} = diameter of dispersed phase [m]
- $A_{\alpha\beta}$ = interfacial area density [1/m]
- $\vec{U}_{\beta} - \vec{U}_{\alpha}$ = relative velocity [m/s]
- μ_{α} = dynamic viscosity of continuous phase [Pa · s]
- cp_{α} = specific heat capacity of continuous phase [J/(kg · K)]
- k_{α} = thermal conductivity of continuous phase [W/(m · K)]

For the dispersed phase the correlations of the particle model are needed. For example for droplets the interface area density is calculated by equation 2.38.

In the particle model particles assumed to be spherical. Hence the coefficient $c_{\alpha\beta}^D$ from equation 2.35 can be derived analytically. The projected area A_{proj} and the volume of a single particle V_{disp} are:

$$A_{proj} = \frac{\Pi d_{mean}^2}{4} \quad (2.41)$$

$$V_{disp} = \frac{\Pi d_{mean}^3}{6}$$

And the number of particles per unit volume n_{disp} :

$$n_{disp} = \frac{vf_{\beta}}{V_{disp}} = \frac{6vf_{\beta}}{\Pi d_{mean}^3} \quad (2.42)$$

Regarding equation 2.29 the drag by a single particle act on the continuous phase is:

$$\vec{F}_p^D = \frac{1}{2} C_D \varrho_{\alpha} A_{proj} |\vec{U}_{\beta} - \vec{U}_{\alpha}| (\vec{U}_{\beta} - \vec{U}_{\alpha}) \quad (2.43)$$

Thus the total drag per unit volume exerted on the continuous phase α is:

$$\vec{F}_{\alpha\beta,par}^D = n_{disp} \vec{F}_p = \frac{3}{4} \frac{C_D}{d_{mean}} vf_{\beta} \varrho_{\alpha} |\vec{U}_{\beta} - \vec{U}_{\alpha}| (\vec{U}_{\beta} - \vec{U}_{\alpha}) \quad (2.44)$$

Equalise interface drag force per unit volume equation 2.35 with the total drag force per unit volume from equation 2.44

$$M_{\alpha}^D = \vec{F}_{\alpha\beta} \quad (2.45)$$

and rearrange to $c_{\alpha\beta}^D$ yields to:

$$c_{\alpha\beta}^D = \frac{3}{4} \frac{C_D}{d_{mean}} vf_{\beta} \varrho_{\alpha} |\vec{U}_{\beta} - \vec{U}_{\alpha}| \quad (2.46)$$

With the interface area density $A_{\alpha\beta}$ from equation 2.38 the final form which is implemented for the particle model in Ansys CFX is:

$$c_{\alpha\beta}^D = \frac{C_D}{8} A_{\alpha\beta} \varrho_{\alpha} |\vec{U}_{\beta} - \vec{U}_{\alpha}| \quad (2.47)$$

For particles several empirical correlations exist to determine the drag coefficient, see table 2.3.

Table 2.3: Drag coefficient correlations for particle model available in Ansys CFX; see [Ansys 2016c](#)

Flow Regime	Model
sparsely distributed solid particles	Schiller Naumann drag model
densely distributed solid particles	Wen Yu drag model Gidaspow drag model
sparsely distributed fluid particles	Ishii-Zuber drag model Grace drag model
densely distributed fluid particles	Ishii-Zuber drag model Grace drag model

The Mixture Model

The mixture model treats both phase α and β symmetrically, see [Ansys \(2016c\)](#). This is the most general approach for calculating the interfacial area density. Here the interfacial area density can be calculated with

$$A_{\alpha\beta} = \frac{vf_{\alpha} vf_{\beta}}{d_{\alpha\beta}} \quad (2.48)$$

$d_{\alpha\beta}$ is an interfacial length scale, which have to specify manually. In CFX it is possible to write a function or equation to calculate $d_{\alpha\beta}$.

Non-dimensional numbers like mixture Reynolds number and mixture Prandtl number are defined as

$$Re_{\alpha\beta} = \frac{\varrho_{\alpha\beta} |\vec{U}_{\beta} - \vec{U}_{\alpha}| d_{\alpha\beta}}{\mu_{\alpha\beta}} \quad (2.49)$$

$$Pr_{\alpha\beta} = \frac{\mu_{\alpha\beta} cp_{\alpha\beta}}{k_{\alpha\beta}} \quad (2.50)$$

Property variables with subscript $\alpha\beta$ regarding the mixture are calculated, for example

$$\begin{aligned} \varrho_{\alpha\beta} &= vf_{\alpha} \varrho_{\alpha} + vf_{\beta} \varrho_{\beta} \\ \mu_{\alpha\beta} &= vf_{\alpha} \mu_{\alpha} + vf_{\beta} \mu_{\beta} \end{aligned} \quad (2.51)$$

- $\varrho_{\alpha\beta}$ = density of mixture [kg/m³]

- vf_α = volume fraction of α phase [-]
- vf_β = volume fraction of β phase [-]
- $d_{\alpha\beta}$ = interfacial length scale [m]
- $A_{\alpha\beta}$ = interfacial area density [1/m]
- $\vec{U}_\beta - \vec{U}_\alpha$ = relative velocity [m/s]
- $\mu_{\alpha\beta}$ = dynamic viscosity of mixture [Pa · s]
- $cp_{\alpha\beta}$ = specific heat capacity of mixture [J/(kg · K)]
- $k_{\alpha\beta}$ = thermal conductivity of mixture [W/(m · K)]

The interface drag for the mixture model is slightly different compared to the particle model. It uses the mixture density $\varrho_{\alpha\beta}$ and a different expression for the interface area density, see equation 2.48:

$$\vec{F}_{\alpha\beta,mix}^D = C_D \varrho_{\alpha\beta} A_{\alpha\beta} |\vec{U}_\beta - \vec{U}_\alpha| (\vec{U}_\beta - \vec{U}_\alpha) \quad (2.52)$$

The value for C_D and $d_{\alpha\beta}$ have to be defined as a constant value or a function.

The Free Surface Model

If no dispersed phase exist the interfacial area density of just two phases is

$$A_{\alpha\beta} = |\text{grad}(vf_\alpha)| \quad (2.53)$$

If more than two phases exist the interfacial area density can be generalised as

$$A_{\alpha\beta} = \frac{2 |\text{grad}(vf_\alpha)| \cdot |\text{grad}(vf_\beta)|}{|\text{grad}(vf_\alpha)| + |\text{grad}(vf_\beta)|} \quad (2.54)$$

- vf_α = volume fraction of α phase [-]
- vf_β = volume fraction of β phase [-]

- $A_{\alpha\beta}$ = interfacial area density [1/m]

The interface drag for the free surface model is calculated in the same way as for the mixture model but with other expression for the interfacial area density, see equation 2.54:

$$\vec{F}_{\alpha\beta,fs} = C_D \varrho_{\alpha\beta} A_{\alpha\beta} |\vec{U}_\beta - \vec{U}_\alpha| (\vec{U}_\beta - \vec{U}_\alpha) \quad (2.55)$$

Conversion of Particle Drag Model to Mixture Drag Model

The drag coefficient can be calculated for the particle drag model but if it implemented in the mixture model some modification have to be carried out, due to different implementation, see equations 2.44 and 2.52:

$$C_{D,mix} = \frac{C_{D,par}}{8} \frac{\varrho_\alpha}{\varrho_{\alpha\beta}} \quad (2.56)$$

2.4 Algebraic Interface Area Density Model

Separate multiphase models are necessary to describe the two-phase coupling for each morphology namely separated flow, transitional or mixed flow and dispersed flow, see [Ishii and Hibiki \(2006\)](#). The reason why is the different momentum transfer physics, which take into account the different interfacial area density calculations, see section [2.3.3](#). The mixture model in Ansys CFX, see [2.3.4](#), is a modelling infrastructure, which can be used for multiphase flow of such complex morphology. Unlike the particle model for dispersed two-phase flows, the mixture model does not include ready-to-use equations for different flow regimes but user-defined function can be implemented easily, see [Egorov \(2004\)](#). The Algebraic Interface Area Density Model (AIAD) was developed to capture the morphological formations such as small bubbles, droplets and free surface, if the grid is not sufficiently small for such fine structures. In the broadest sense the AIAD model is a library which holds some additional functions for morphology detection and turbulence treatment based on the Ansys CFX mixture model. Egorov proposed this procedure in his work [Egorov \(2004\)](#) and Höhne adopted this model and implemented it in Ansys CFX via CFX command expression language (CEL) interface. A detail description is given in [Porombka and Höhne \(2015\)](#) and [Höhne and Vallée \(2010\)](#). Therefore only the most important relations are stated here.

2.4.1 Morphology Detection

Based on the gas and liquid volume fractions the AIAD model can be distinguish between three different morphologies

- Bubbles in continuous liquid phase (dispersed regime)
- Droplets in continuous gas phase (dispersed regime)
- Free surface (separated regime)

Two versions of blending functions are introduced by Höhne and compared in his study, see [Porombka and Höhne \(2015\)](#). Both versions are based only

on gas and liquid volume fraction vf_g and vf_l . The first set of blending functions are

$$\begin{aligned} f_b &= \left[1 + e^{a_b(vf_g - vf_{b,lim})} \right]^{-1} \\ f_d &= \left[1 + e^{a_d(vf_l - vf_{d,lim})} \right]^{-1} \\ f_{fs} &= 1 - f_b - f_d \end{aligned} \quad (2.57)$$

In equations 2.57 Höhne recommend for the AIAD model constants, see Porombka and Höhne (2015) and Höhne and Vallée (2010)

- $a_b = a_d = 50$ and
- $vf_{b,lim} = vf_{d,lim} = 0.3$

In this present work the above recommended constants for the AIAD model are used too, see figure 2.15.

The second set of blending functions also taken into account the gradient of the volume fraction

$$\begin{aligned} f_b^* &= \left[1 + e^{a_b(vf_g - vf_{b,lim})} \right]^{-1} \cdot \left[1 + c_g \cdot |\text{grad}(vf_g)| \right]^{-1} \\ f_d^* &= \left[1 + e^{a_d(vf_l - vf_{d,lim})} \right]^{-1} \cdot \left[1 + c_g \cdot |\text{grad}(vf_l)| \right]^{-1} \\ f_{fs}^* &= 1 - f_b^* - f_d^* \end{aligned} \quad (2.58)$$

c_g is a new parameter and Höhne set it to $c_g = 0.05$, see Porombka and Höhne (2015). The other constants are the same mentioned above.

Höhne showed in his paper Porombka and Höhne (2015) that discontinuities revealed for the free surface function with the first set of blending functions, see 2.57. Set 2, see 2.58 is continuous. Hence the present work blending function set 2 see 2.58 is used.

Densely distributed particles are taken into account by the AIAD model. Particles touch each other if the maximum particle packing is reached. Above a volume fraction 0.74 for non oscillating particles the maximum packing

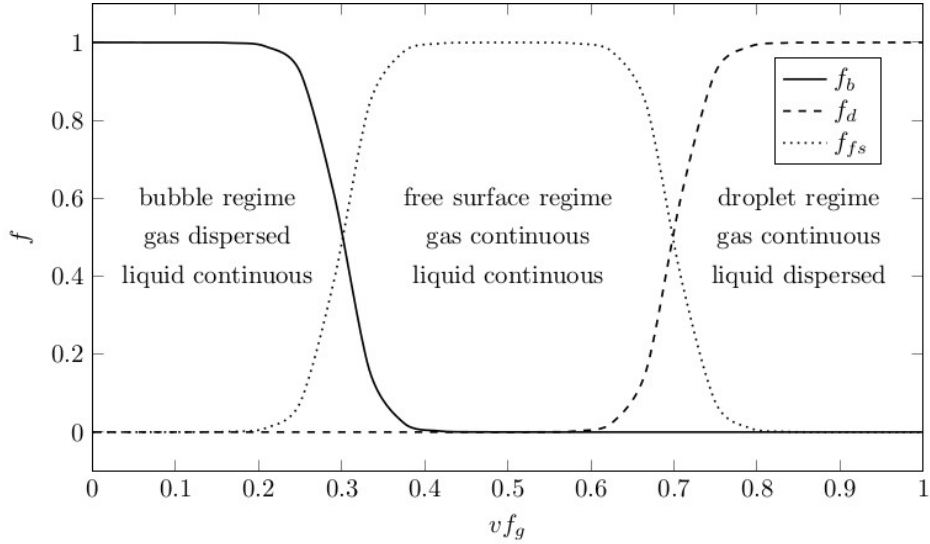


Figure 2.15: Blending functions f_b , f_d and f_{fs} regarding to 2.57; figure by the author

density is reached and can be assumed to be continuous, see Kolev (2012). Hence a bubble flow cannot exist for $vf_g > 0.74$ or droplet flow cannot exist for $vf_g < 0.26$. Particles start to oscillating if the flow pattern is turbulent and the particles touch each other earlier. Hence the maximum packing density volume is smaller in turbulent case than in laminar case. Kolev estimate the volume fraction for turbulent flows up to $vf_g > 0.7$ to 0.74. Hence the AIAD parameter $vf_{b,lim}$ and $vf_{d,lim}$ can vary a little bit in range of 0.26 for laminar flow to 0.3 for turbulent flows. Additional it can be seen in Brocchini and Peregrine (2001) that a fully connection between the two-phases are in range $0.3 < vf_g < 0.7$, see figure 2.16. The most occurring flow pattern in steam drums and pipes is turbulent and the recommended range for the free surface volume fraction from Brocchini, $vf_{b,lim}$ and $vf_{d,lim}$ is set to 0.3 for this work.

2.4.2 Drag Modelling

The most important two-phase momentum transfer force is the drag force, see discussion in section 2.3.4.

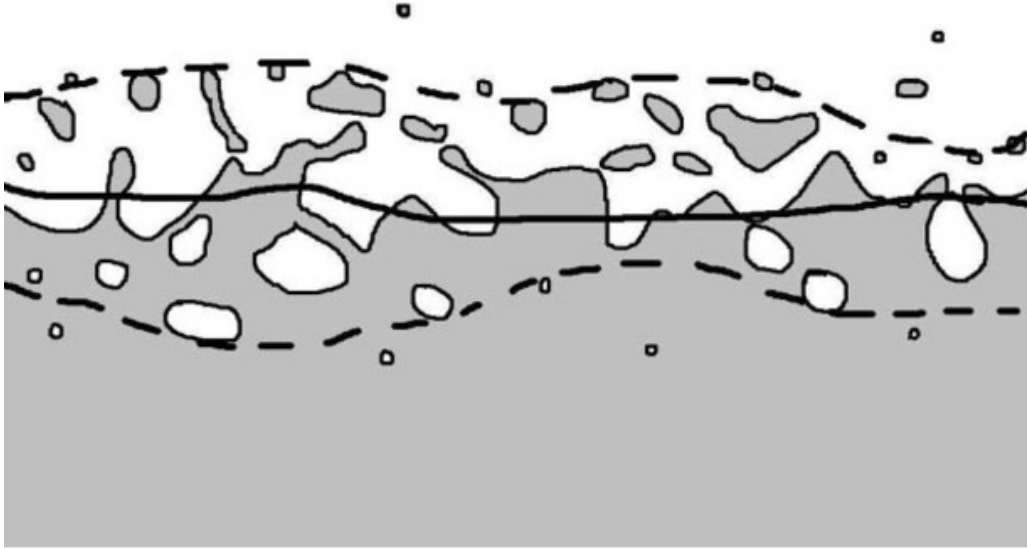


Figure 2.16: Two-phase surface layer; upper and lower bounds are indicated with dashed lines; mean free surface is given with a solid line; Brocchini and Peregrine 2001

There are two unknown variables in the drag force, the drag coefficient and the interfacial area density (IAD), see equation 2.30. Generally the drag coefficient and the IAD depends on the morphology of the flow. Due to the morphology detection in AIAD model it can be distinguished between dispersed phase flow and free surface flow morphology and for these two morphologies the drag coefficient will be handled separately.

Fluid Particle Drag Force

In the AIAD model, for the dispersed phase a constant spherical diameter of the particles is assumed, as well as a constant drag coefficient, see Porom-bka and Höhne (2015). A constant drag coefficient can be expected, if the particle Reynolds number is in the turbulent region. In turbulent flows with $Re_{p,solid} > 1000$ a drag coefficient of 0.44 can be assumed, see figure 3.2. Hence the droplet and bubble drag coefficients, which often used, are

$$C_{D,b} = 0.44 \quad (2.59)$$

$$C_{D,d} = 0.44 \quad (2.60)$$

With constant drag coefficients 2.59 and 2.60, it is not possible to take into account different Reynolds number for bubbles and droplets within the system boundaries. For a well defined experiment it is possible to hold the flow regime constant and a constant drag coefficient can be assumed. But for an industrial application case not. Hence it is needed to have a variable particle sizes to include drag force models, in order to determine the corresponding drag coefficients.

Particle drag models can be divide in drag models for solid and fluid particles. In this thesis only fluid particle drag models come into consideration. Fluid particle drag models can be subdivided into sparsely and densely distributed drag models. Most drag models for densely distributed fluid particles have been included the drag correlations for the sparsely distributed regimes as well. So that drag models regarding the densely distributed regime are more general or for a wider range of fluid particle volume fractions.

Ansys (2016c) provide the Ishii-Zuber and Grace drag model for the densely distributed fluid particles. The Ishii and Zuber (1979) drag model, see Ishii and Hibiki (2006) also, use the Schiller Naumann drag model for spherical particles in the viscous regime

$$C_{D,p,sphere} = \frac{24}{Re_{mix}} \left(1 + 0.15 Re_{mix}^{0.687}\right) \quad (2.61)$$

with a modified Reynolds number, to take into account densely distributed fluid particles

$$Re_{mix} = \frac{\rho_c |\vec{U}_p - \vec{U}_c| d_p}{\mu_{mix}} \quad (2.62)$$

which based on the mixture viscosity

$$\frac{\mu_{mix}}{\mu_c} = \left(1 - \frac{vf_p}{vf_{p,max}}\right)^{-2.5 vf_{p,max} \mu^*} \quad (2.63)$$

In equation 2.63 $v f_{p,max}$ is the maximum packing value and μ^* is the dimensionless viscosity defined as follows

$$\mu^* = \frac{\mu_d + 0.4\mu_c}{\mu_d + \mu_c} \quad (2.64)$$

In the dense distorted particle regime Ishii and Hibiki (2006) use a correction factor multiplied with the single particle drag coefficient

$$C_{D,p,ellipse} = E_{rp} C_{D,ellipse,\infty} \quad (2.65)$$

The single particle drag coefficient depends in this regime only on the particle radius and fluid properties, see Harmathy (1960) and equation 3.36.

$$C_{D,ellipse,\infty} = \frac{2}{3} \sqrt{Eo_{fc}} \quad (2.66)$$

The correction factor depends only on viscosities and particle volume fraction

$$E_{rp} = \left[\frac{(1 + 17.67 f_{rp}^{6/7})}{18.67 f_{rp}} \right]^2 \quad (2.67)$$

with

$$f_{rp} = \frac{\mu_c}{\mu_{mix}} \sqrt{1 - v f_p} \quad (2.68)$$

How it is discussed later in section 3.2.2 Particle Acceleration for Flowing Fluids, the inertia force in Eo number in equation 2.66 is modified for this present work, to make this equation available for forced convective multiphase flow

$$Eo_{fc} = \frac{\rho_c |\vec{a}_{rel}| d_p^2}{\sigma} \quad (2.69)$$

Like in the distorted regime Ishii and Zuber (1979) uses a correction factor for the single particle drag coefficient for the churn-turbulent-flow regime

$$C_{D,p,cap} = C_{D,cap,\infty} (1 - v f_p)^2 \quad (2.70)$$

with the single particle drag

$$C_{D,cap,\infty} = \frac{8}{3} \quad (2.71)$$

Ansys (2016c) provide an automatic regime selection for the Ishii Zuber drag model

$$\begin{aligned} & \text{if } C_{D,p,sphere} \geq C_{D,p,ellipse} \\ & \text{then } C_D = C_{D,p,sphere} \\ & \text{else } C_D = \min(C_{D,p,ellipse}, C_{D,p,cap}) \end{aligned} \quad (2.72)$$

The Grace drag model is formulated for flow past a single bubble and in densely distributed fluid particle regime there exist a power law correction. Due to the fact that the Grace model is developed for bubble flows the Ishii and Zuber (1979) drag correlation is used in this work, because estimate the distribution of water droplets in a steam drum is the overall goal. Hence it is assumed that the Ishii and Zuber (1979) drag correlation performance is better for this work compared to the Grace model for different fluid particles.

Free Surface Drag Coefficient

The drag coefficient correlation of a free surface flow differs to drag coefficient correlation of a dispersed flow. The free surface drag coefficient based on the assumption of no-slip condition. Because the free surface is acting like a wall, the free surface drag coefficient correlation can be written as

$$C_{D,fs} = \frac{2(vf_l \tau_{fs,l} + vf_g \tau_{fs,g})}{\rho_l |\vec{U}_{slip}|^2} \quad (2.73)$$

where τ_{fs} represent the viscous stress on the free surface, see Höhne and Vallée (2010). Improvements of free surface drag was carried out and published in Porombka and Höhne (2015), which yield to a modified $C_{D,fs}$

$$C_{D,fs}^* = \max \left(0.01, \frac{2(vf_l |\vec{t}_{fs,l}| + vf_g |\vec{t}_{fs,g}|)}{\rho_{mix} |\vec{U}_{slip}|^2} \right) \quad (2.74)$$

In equation 2.74 the tangential shear stress at the free surface is used instead of the magnitude of the viscous stress, like in equation 2.73, see Porombka and Höhne (2015). The stress vector can be calculated by

$$\vec{t} = \tau \vec{n} \quad (2.75)$$

Additional in equation 2.74 the mixture density is used, because of the consistency with the mixture model, see equation 2.52. The free surface drag coefficient should be limited to ensure numerical stability. Porombka and Höhne 2015

2.4.3 Turbulence Modelling

The turbulence modelling is one of the important issue to simulate phase interactions. In order to predicting the interfacial area densities of a dispersed phase, the breakup and coalescence is important, which primarily depends on the average velocity difference of phases and on the turbulence.

In Ansys CFX there are two different approaches for turbulence modelling for Eulerian-Eulerian multiphase flows, the homogeneous and the inhomogeneous. The inhomogeneous model can only be used in conjunction with the inhomogeneous multiphase model, see section 2.3.3. Whereas the homogeneous turbulence model can used for both multiphase models, the homogeneous and inhomogeneous.

According Ansys (2016c) in the inhomogeneous turbulence model a turbulence field is solved for each phase separately. In contrast to this, the homogeneous turbulence modelling solve only one turbulence field, which is shared by all phases. Except that the mixture density and mixture viscosity is used, the homogeneous turbulence model is solved in the same way like as the single phase equations. For single phase flow turbulence modelling Versteeg and Malalasekera (2007) is recommended for the basics and Ansys (2016c)

is recommended for Ansys CFX implementation.

Regarding the Ansys support and [Ansys \(2016b\)](#) a homogeneous turbulence model should be chosen for separated flow, stratified flow and situations where the phases tend to separate out. In all cases which will be examined in this thesis a separated flow primarily is assumed. Hence the inhomogeneous multiphase model with homogeneous turbulence is recommended for all following simulations.

Turbulence Enhancement

Additional turbulence enhancement should be taken into account. Large particles increase turbulence in the continuous phase due to wakes behind the particles. Regarding [Ansys \(2016c\)](#) in Ansys CFX the particle induced turbulence is calculated by an additional eddy viscosity term from the Sato turbulence transfer model, as a beta feature

$$\mu_{t,c} = \mu_{t,hear} + \mu_{t,p} \quad (2.76)$$

where $\mu_{t,hear}$ is the usual shear induced eddy viscosity from the turbulence model, and $\mu_{t,p}$ is the additional eddy viscosity:

$$\mu_{t,p} = C_{\mu,p} \rho_c v f_d d_p |\vec{U}_d - \vec{U}_c| \quad (2.77)$$

The value of $C_{\mu,p}$ is 0.6 per default.

Turbulence Interface Damping

In [Höhne and Vallée \(2010\)](#) and [Porombka and Höhne \(2015\)](#) a discussion of turbulence models can be found. They use an approach from [Egorov \(2004\)](#). This [Egorov \(2004\)](#) approach based on the $k - \omega$ turbulence model with a symmetric wall damping procedure near the interface. Damping the turbulence near the interface is necessary, because it acts like a wall boundary and for walls a damping procedure is needed for the $k - \omega$ model. The damping nearby the interface is introduced by an additional dissipation source term

$$S_{damping,k} = f_{fs}^* A_{\alpha\beta} \beta \Delta y \frac{1}{\rho_k} \left(B \frac{6 \mu_k}{\beta \Delta n^2} \right)^2 \quad (2.78)$$

Here the f_{fs}^* , $A_{\alpha\beta}$, β , Δy , Δn and B is the free surface blending function, the interfacial area density, $k - \omega$ model constant of 0.075, the typical grid spacing normal to the interface, the typical grid cell size at the interface and the model parameter B . According [Porombka and Höhne \(2015\)](#) is $B=100$ and according [Ansys \(2016d\)](#) B is per default 10. In [Ansys \(2016d\)](#) it can be seen, that Δy is set equal to Δn , what can be assumed for low cell aspect ratios in the interface region. This latter assumption is used in the following simulations too. The grid spacing can be approximated with:

$$\Delta y = \Delta n = \sqrt[3]{V_{cell}} \quad (2.79)$$

In order to add this turbulence source term [2.78](#) to the right-hand side of the ω equation, a CEL expression have to be created and assigned to an user fluid source in Ansys CFX.

2.5 Non-Drag Forces

Additionally to the drag force, which acts in flow direction, some other interface momentum transfer forces are occurred in multiphase. This latter forces called non-drag forced and acting perpendicular to the flow direction. In equation 2.28 it can be seen, that the drag and the non-drag forces added linearly. There are an controversial discussion whether non-drag forces can be added linearly, because for example a wake behind a bubble change the liquid turbulence structures completely and thus the non-drag forces may strong coupled. That is one reason why it is so difficult to identify each force experimentally. Until nowadays constitutive equations for such lateral forces are not well-developed, because there is lack of relevant experimental data. Nevertheless, all interface momentum forces are of great importance for the prediction of void fraction distribution in multiphase-flows. Ishii and Hibiki 2006; Tomiyama 2002

2.5.1 Lift Force

Consider a fluid particle moving in a laminar shear flow, see figure 2.17.

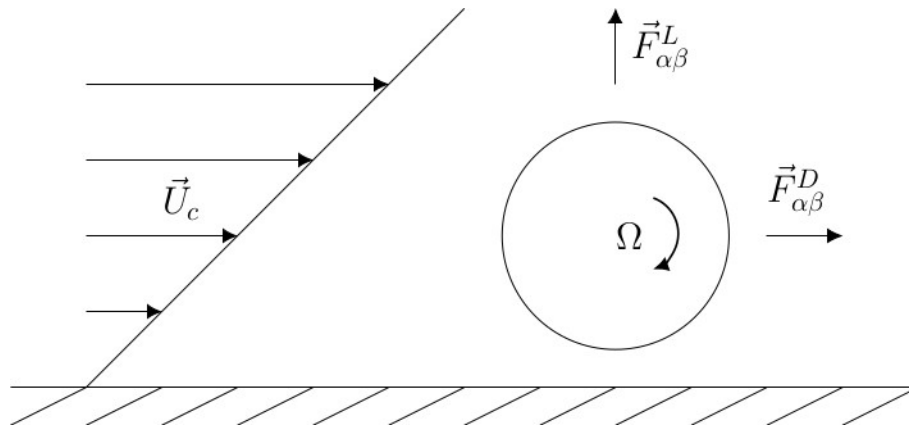


Figure 2.17: Schematic drawing of sphere in simple shear flow; figure by the author

The velocity gradients of continuous fluid yields to different velocities on the particle surface, which results to different rotating vortices around the

particle. This results to a pressure distribution and a net force perpendicular to the flow direction arise, which called lift force as introduced in Saffman (1965). A newer correlation for the lift force can be found in Drew and Lahey (1987)

$$\vec{F}_{\alpha\beta}^L = -C_L v_{fp} \varrho_c (\vec{U}_p - \vec{U}_c) \times rot(\vec{U}_c) \quad (2.80)$$

The Drew and Lahey correlation is often used nowadays and is included in Ansys CFX for some multiphase models.

Classical the lift coefficient C_L is positive and acts in the direction of decreasing continuous phase velocity. This fact is guilty if someone deals with rigid sphere particles. Ervin and Tryggvason (1997) showed numerical that deformable fluid particles change the sign of the lift force and are deflected in the opposite direction. Tomiyama et al. (2002b) has validated the numerical results from Ervin and Tryggvason (1997) experimental. Further Tomiyama derived from his experiments the following correlations for the lift coefficient

$$C_L = \begin{cases} \min [0.288 \tanh(0.121 Re), f(Eo_{d,fc})] & Eo_{d,fc} < 4 \\ f(Eo_{d,fc}) & 4 \leq Eo_{d,fc} < 10 \\ -0.27 & Eo_{d,fc} \geq 10 \end{cases} \quad (2.81)$$

with

$$f(Eo_{d,fc}) = 0.00105 Eo_{d,fc}^3 - 0.0159 Eo_{d,fc}^2 - 0.0204 Eo_{d,fc} + 0.474 \quad (2.82)$$

Eo_d is a modified Eötvös number, which is defined by using the maximum horizontal dimension of a particle as a characteristic length

$$Eo_d = \frac{g \Delta \varrho d_H^2}{\sigma} \quad (2.83)$$

The inertia force in equation 2.83 will be modified in the same way like equation 2.69.

$$Eo_{d,fc} = \frac{\rho_c |\vec{a}_{rel}| d_H^2}{\sigma} \quad (2.84)$$

Equation 2.81 is an empirical correlation and C_L depends slightly on Morton number M in the Eo_d range, see Tomiyama (2002). Despite of equation 2.81 and 2.83 is deduced from glycerol-water solution, Tomiyama et al. (2002b) have showed good coincidence with air-water bubbly upflow experimental data.

Tomiyama use the correlation from Wellek, Agrawal, and Skelland (1966) for the fluid particle aspect ratio

$$E = \frac{d_V}{d_H} = \frac{b + \beta' b}{2a} = \frac{1}{1 + 0.163 Eo_{fc}^{0.757}} \quad (2.85)$$

An overview of distorted fluid particle dimensions following Tomiyama et al. (2002a) can be seen in figure 2.18. The maximum horizontal dimension d_H , which is needed for equation 2.84 can be calculated

$$d_H = 2a = d_p \left(\frac{\gamma}{E_f} \right)^{1/3} \quad (2.86)$$

see Tomiyama et al. (2002a), where γ is the distortion factor

$$\gamma = \frac{2}{1 + \beta'} \quad (2.87)$$

and E_f is the fluid particle frontal part aspect ratio

$$E_f = \gamma E \quad (2.88)$$

With the parameter β' it is possible to express different particle shapes like dimpled hemispheroidal-cap ($-1 < \beta' < 0$), hemispheroidal-cap ($\beta' = 0$), distorted spheroid ($0 < \beta' < 1$, $\beta' > 1$) and spheroid ($\beta' = 1$).

Ansys assume spherical particles with $\beta' = 1$. In order that the distortion factor γ becomes one and combining equation 2.85, 2.88 and 2.86 yields to

$$d_{H,Ansys} = d_p \sqrt[3]{1 + 0.163 Eo_{fc}^{0.757}} \quad (2.89)$$

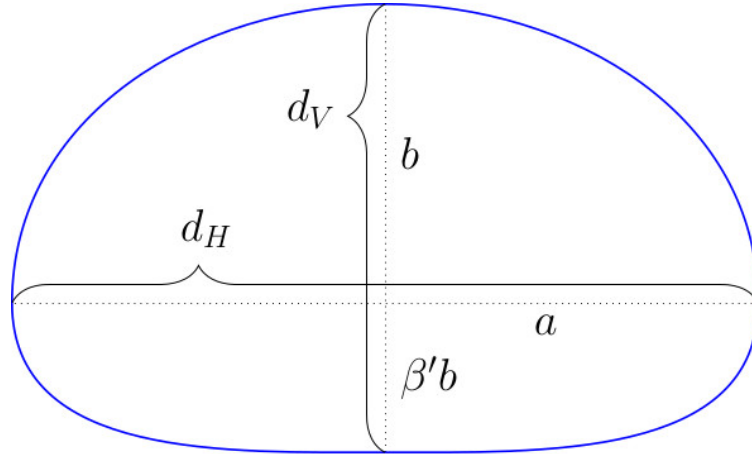


Figure 2.18: Distorted fluid particle with dimensions following Tomiyama et al. (2002a)

In figure 2.19 the aspect ratio E over the Eötvös number is plotted.

To bring all the different experiments in the chart 2.19, Clift, Grace, and Weber (1978) adjust the Eötvös number with the viscosity ratio $\kappa = \mu_p/\mu_c$.

An adjusted Eötvös number lower than 0.5, the scatter of the aspect ratios are small compared to the higher adjusted Eötvös numbers. That fact is guilty for bubbles, see A5 Aybers and Tapucu (1969) and drops in liquid, see W8 Winnikow and Chao (1966). Additional Clift, Grace, and Weber (1978) draw the mentioned above correlation 2.85 from Wellek in this chart, see Eq.(7-20) in figure 2.19. The particle aspect ratio differences regarding the Wellek correlation and the experimental results are increased with increased Eötvös numbers. Hence the particle deformation of fluid particle in purified systems is stronger than Wellek calculated. In the present work purified water and air is used, so that the Wellek correlation would results to a larger error.

Pellacani (2012) has derived a correlation for purified air/water mixture regarding the Aybers and Tapucu (1969) results

$$E = 0.3971 E_{ofc}^{-0.418} \quad (2.90)$$

which fit the aspect ratios better than Wellek and hence this correlation is

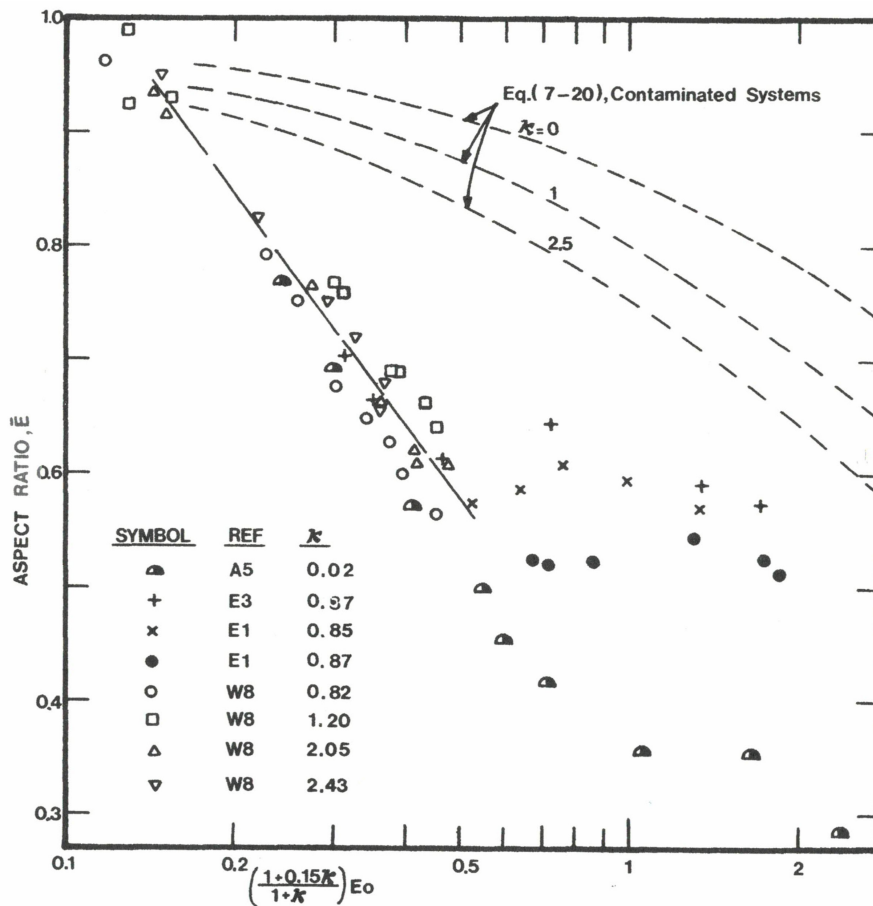


Figure 2.19: Deformation of drops and bubbles in pure Water; Clift, Grace, and Weber 1978

used for this work.

To calculate the maximal horizontal particle dimension a β' value of 0.5 is used in order to obtain the distorted spheroid regime which is rather close to the experimental data base how it can be seen in figure 2.19. That $\beta' = 0.5$ correspond to distorted spheroid regime in cooperation with the equation 2.90, which yields to a larger deformed particle in purified fluids and larger maximum horizontal dimensions are obtained than Wellek, Agrawal, and Skelland (1966) with spheroid particle shape.

2.5.2 Wall Lubrication Force

Particles in infinite media have a symmetrical drainage of the fluid around, in laminar flows. The drainage around the particle is changed in vicinity of a wall, see figure 2.20.

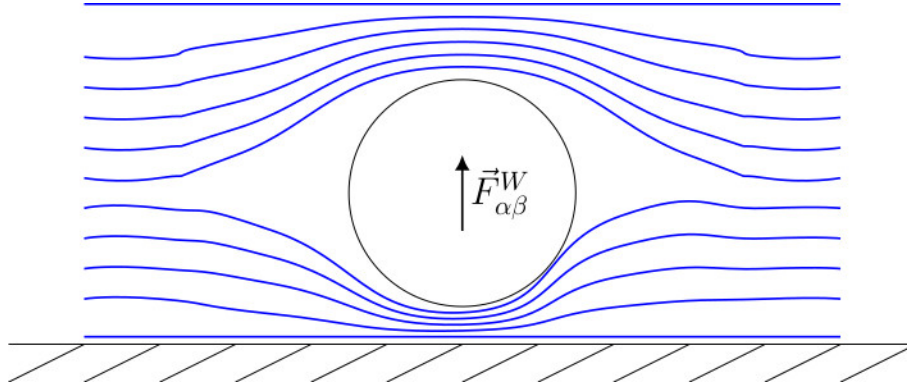


Figure 2.20: Schematic drawing of drainage around a sphere near the wall; figure by the author

Due to the no-slip condition at the wall, the drainage is slowed between particle and wall and the drainage rate is increased on the opposite site. This asymmetric drainage cause a force on the particle, which tends to move the particle away from the wall. Ishii and Hibiki 2006

This force $F_{\alpha\beta}^W$ was investigated by Antal, Lahey, and Flaherty (1991) and called wall-lift force

$$\vec{F}_{\alpha\beta}^W = -C_{WL} v f_p \varrho_c |\vec{U}_c - \vec{U}_p|^2 \vec{n}_{wall} \quad (2.91)$$

with

$$C_{WL} = \max \left\{ 0, \frac{C_{W1}}{d_p} + \frac{C_{W2}}{y_W} \right\} \quad (2.92)$$

The non-dimensional coefficients are $C_{W1} = -0.01$ and $C_{W2} = 0.05$ according Antal, Lahey, and Flaherty (1991). Other authors changed these values for example Krepper (1999) to $C_{W1} = -0.0064$ and $C_{W2} = 0.016$. There is a lack of experimental and numerical database according the wall-lift force for droplets. Due to Antal, Lahey, and Flaherty (1991) had investigated a

spherical bubble in laminar flow analytically and numerically it is assumed, that the coefficients from [Antal, Lahey, and Flaherty \(1991\)](#) are better for a general approach and will be used in this work. In equation 2.91 $|\vec{U}_c - \vec{U}_p|$ is the relative velocity between the dispersed and the continuous phase normal to the wall.

Further wall-lift force models are from Tomiyama or Frank, see [Ansys \(2016c\)](#) and [Lucas and Krepper \(2007\)](#). However the Tomiyama model contain the pipe diameter, because this model is developed for pipe flows. Due to the complex drum design the there is no constant diameter and the Tomiyama model is discarded. As well the Frank model is discarded, because of the uncertainty of choosing good model parameters.

The wall-lift force prevents that particles touch the wall and is important to predict the observed void profile for co-current laminar upward and downward flows. For further reading see [Antal, Lahey, and Flaherty \(1991\)](#), [Lucas and Krepper \(2007\)](#) and [Ishii and Hibiki \(2006\)](#).

2.5.3 Turbulent Dispersion Force

Turbulent dispersion means particles will tend to get caught up in continuous phase turbulent eddies and be carried from regions of high concentration to regions of low concentration. [Burns et al. \(2004\)](#) present a general framework for the modelling of turbulent dispersion for an arbitrary number of phases with arbitrary morphologies. With some simplifications the Favre Averaged Drag turbulent dispersion force model can be written as

$$\vec{F}_c^T = -\vec{F}_p^T = C_{TD} C_{D,p} \frac{\nu_{turb,c}}{\sigma_{turb,c}} \left(\frac{grad(vf_p)}{vf_p} - \frac{grad(vf_c)}{vf_c} \right) \quad (2.93)$$

[Burns et al. \(2004\)](#) have compared different turbulent dispersion force models with the Favre Averaged Drag (FAD) model. [Burns et al. \(2004\)](#) have assumed, that the multiplier C_{TD} and the turbulent Schmidt number $\sigma_{turb,c}$ is equal to unity.

In [Ansys \(2016c\)](#) there is a discussion about the multiplier C_{TD} . The assumption of equality to unity of the latter multiplier is only valid for short

particle relaxation time compared to turbulent time-scales, which implies low turbulent Stokes numbers. Low turbulent Stokes numbers are appeared in cases where the dispersed phase is light relative to the continuous phase, like in bubbly flows. But for heavier dispersed phases than the continuous phase, for small Stokes numbers the particle diameters have to be very small.

$$St_{turb} = \frac{\tau_R}{t_E} \quad \text{with} \quad \tau_R = \frac{\rho_p d_P^2}{18 \mu_c} \quad \text{and} \quad t_E = 0.3 \frac{k_c}{\epsilon_c} \quad (2.94)$$

Hence the value of C_{TD} of one overestimate the dispersion force for heavy large particles, like bigger droplets. Ansys (2016c) recommend to making a decreasing function, that is equal to unity at $St_{turb} = 0$ and tending to zero as $St_{turb} \rightarrow \infty$. The following correlation for C_{TD} is used

$$C_{TD} = \frac{1}{exp(0.01 St_{turb})} \quad (2.95)$$

Equation 2.95 is plotted over the turbulent Stokes number in figure 2.21.

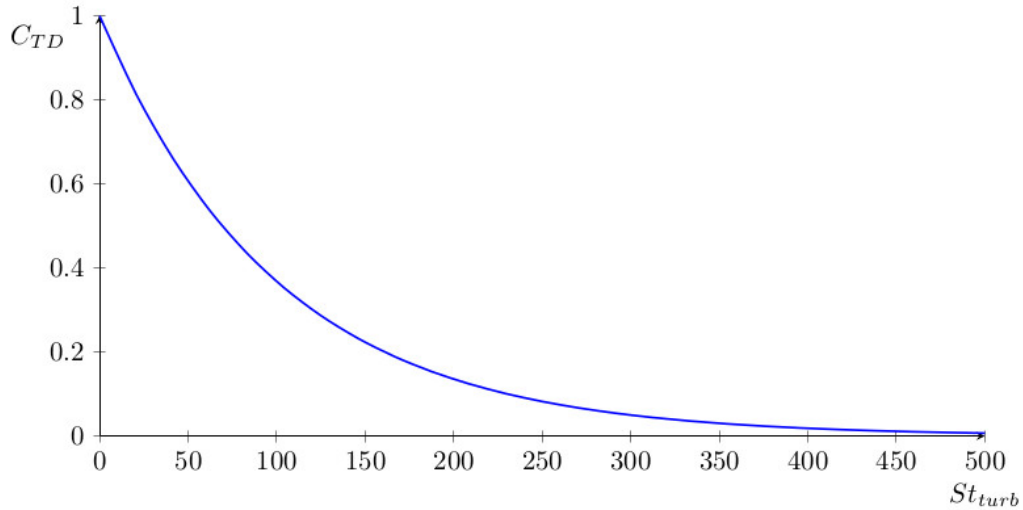


Figure 2.21: FAD multiplier decreasing function; figure by the author

Equation 2.95 is verified with the Fabre channel case in chapter 5 but is not validated. A Validation of equation 2.95 with different experiments are highly recommended. Within the function 2.95 for C_{TD} the FAD turbulence model can be used for bubbles and droplets, what is carried out in all the

following simulations.

2.6 Conclusion State of the Art and Motivation

Increasing production of renewable energies set pressure on the flexibility of conventional energy suppliers and thereby also on the boiler design. This causes an increasing interest in better knowledge of two-phase flows. Due to the fluctuating wind and solar energy, the stability of the electricity grid reduces. Today new boilers are supposed to be very flexible and react quickly on grid power fluctuations in order to counteract the reducing grid stability by the renewable energies. However, more flexible boiler designs need better prediction of the steam/water separation to ensure the water circulation. The acceleration of the transition in energy production causes shorter cycles in new boiler designs. Boiler producers react on this demand by replacing elaborated and costly experiments by CFD simulations.

Other industries are also concerned with multiphase flow phenomena. For example, mixing tasks in the chemical, biological, and food industry increase the number of cases in which a CFD model as introduced in this thesis can help optimise processes.

The section 2.2 describes the separation of steam/water mixture inside steam drums. The importance of separation for superheaters and turbines is shown in the section 2.2.2. But, it becomes clear that there are no closed mathematically procedures or algorithms for designing a highly efficient steam/water separation steam drum and internals. Rather, the design of steam drums is based on companies know-how and companies own semi empirical models, see [ERK Eckrohrkessel GmbH \(2018\)](#). One reason is the complexity of steam/water separation. In the section 2.1 there is an overview of the two-phase flow pattern under well-defined operating conditions. Nevertheless, the determination of two-phase flow patterns under well-defined conditions is affected by large errors until today. Additionally, large flow fluctuations occur in steam drums, which increase the errors of the well-defined experimental data. To enhance or optimise the steam/water separation in a steam drum, an experiment or a CFD analysis can be carried out. Experiments including

each specific case under many different conditions are costly. Hence, CFD simulations are the most efficient tool for improving or optimising steam/water separation applications.

To obtain sufficiently accurate results from CFD simulations, an appropriate multiphase model is needed. The driving force for the development of multiphase flow models is the nuclear power industry, which needs more reliable simulation models to reduce the risk of a core meltdown. With increasing computing power, the multiphase flow models improve their predictive performance.

Due to the large number of problems where multiphase flow models can increase the process performance, there is a lot of research and development of multiphase simulation models, because it is a difficult task to predict the local two-phase behaviour. One of these R&D institutions is the Helmholtz Zentrum Dresden Rossendorf (HZDR), which develops and validates multiphase flow models for CFD software.

Such improved multiphase flow models are needed to describe the flow phenomena in a steam drum. The main focus of the current development is the Euler-Lagrange model, which predicts particle behaviour better than the Euler-Euler model. But, mentioned in section 2.3, a multiphase flow model which can handle water as well as steam and both as dispersed and continuous phase simultaneously, is needed for a steam drum simulation.

Solely the AIAD multiphase model from the HZDR is able to treat a gas and a liquid as dispersed and continuous. But till today, the particle size is a constant parameter in the AIAD model. Due to the different flow regimes in a steam drum, the constant particle size is insufficient.

However, the AIAD model can be used as a base model for further development and the needed physics extension can be added, see section 2.4. These latter extension models are developed in this thesis and are described in chapter 3.

The author received the AIAD model as source code from the HZDR, which was not yet coupled to commercial CFD.

In addition, most of the new available Euler-Lagrange multiphase models

are so complex that the computation time increases tremendous compared to single phase flows, except the AIAD model. The AIAD model does not depend on the number of individual particles or clusters and is therefore suitable for industrial CFD applications.

When developing the model extension, computational time should be taken into account as it should be developed for industrial applications and should treat a dispersed phase more realistically to allow better prediction of carry-over of the dispersed phase into the continuous phase and the phase distribution.

Chapter 3

Particle Information Reconstruction from Euler Phase

The Inhomogeneous and the homogeneous model, see section [2.3.2](#), exist for the Euler-Euler approach in CFX. In the homogeneous model a common flow field is shared by all fluids as well as other relevant field variables such as temperature and turbulence. This allows some simplifications which increase the robustness and reduce the solution time. The limit of the homogeneous model is, it can only be used for strong coupled phases and phases at the same velocity, because it assume a local equilibrium over short spatial length, see [Ishii and Hibiki \(2006\)](#) and [Ansys \(2016d\)](#). In the steam drum high slip velocity between phases will be expected. Thus only the inhomogeneous model is appropriated for steam drum simulations and is further considered. In order to calculate the interfacial area density or drag coefficient, CFX distinguish between three submodels for the inhomogeneous model.

- Free surface model
- Particle model
- Mixture model

When the steam/water mixture in the steam drum are separated and the flow pattern is only in the separated flow regime, the free surface model can be used. Because of forced convective two-phase flow inside tanks and pipes all flow patterns in figure 2.2 and 2.1 can occur and the assumption of free surface model is for such devices inappropriate.

The Particle Model, see 2.3.2 has a detail mathematical description of the interface structure and forces. Good results can be achieved in heated two phase flows. The drawback at the moment is, that this particle model when the dispersed and the continuous phase are set, it cannot be changed. Hence, for devices in which simultaneously the light fluid (bubble region) and the heavy fluid are dispersed (droplet region) in the same flow domain, this particle model is not applicable. In steam drums and the pipings before the steam drum, bubble and droplet regimes exist simultaneously and the particle model can not be applied.

The mixture Model, see 2.3.4, which is a more general CFD model can handle such systems with more than one dispersed fluid. But this model provide less informations about the interfacial area and is less accurate. Today, the mixture model needs user values for the interfacial length scales and drag coefficients. CFX allows the latter two parameters as a user function. Accordingly user functions for interfacial length scales and drag coefficients in the mixture model, a submodel is derived to reconstruct the interfacial length scale for dispersed phases, because a model does not exist at the moment. The interfacial length scale and drag coefficient for free surface flow regime coming from AIAD model, as well as the morphology detection, see 2.4.

The interfacial area is very important for heat and mass transfer, as well as particle transport, see Ishii and Hibiki (2006), Vallée et al. (2008), Cheremisinoff and Gupta (1983), and Clift, Grace, and Weber (1978). In state of the art CFD simulations the grid size is not small enough to resolve the interfacial areas in most cases. Hence a submodel is needed. This to be developed submodel should use only the void fraction and already existing field variables. The interfacial area is calculated from a local Sauter mean diameter, which is based on a local particle size distribution, see 3.1 and 3.2.

The to be developed submodel should be system scale independent. This means it should be based only on local variables and for example not on pipe diameters. Transient as well as steady state simulations should be possible. For the use in industry it is important that the model accuracy is good enough to predict the microscopic behaviour generally but doesn't depend on microscopic variables to save computational time. The submodel should not be very sensitive to the mesh to ensure good results also on a coarse mesh.

There are some experiments which can be used for validation of this above mentioned submodel. But those experiments are concentrated often on a special flow pattern and for a general model validation not expedient. Because of the complex two-phase separation in a steam drum and pipes, a steam drum experiment is needed which reflects the flow pattern behaviour like in steam drums. This steam drum experiment is carried out specially for the CFD model validation, see section 7.1 and chapter 7.

In this section the theoretical background regarding the submodel to be developed is given and the assumptions are discussed. As mentioned above the local particle size distribution is needed to calculate the mean Sauter diameter. To estimate such a local particle size distribution a minimum and maximum particle diameter is needed. A state of the art particle size distribution overview and discussion about minimum and maximum particle sizes in steam drums are discussed too.

3.1 Particle Size Distribution

Discussion about particle size distributions in multiphase flows can be seen in [Brodkey \(2005\)](#), [Reitz and Beale \(1999\)](#) and [Luo and Svendsen \(1996\)](#). Brodkey mentioned that for the overall system the distribution is important and should be selected very carefully. Against Luo mentioned that the choice of the particle size distribution has been more or less arbitrary by previous authors despite reliable results. [Reitz and Beale \(1999\)](#) had shown that even with a uniform distribution acceptable predictive model results can be achieved compared with experiments. Additionally Reitz used a Rosin, Rammler, Sperling and Bennet (RRSB) distribution to enhance the model results and has shown that with a good choice of appropriate parameters the model accuracy can be increased.

Hence the Sauter mean diameter is derived for uniform, triangle and RRSB distribution following Reitz. The Triangle distribution is additionally to Reitz. This distribution can be vary by one parameter and the integral is easy to compute. All those three distributions need less computational effort to calculate the integral in common, whereby for the RRSB distribution integral an approximation is used.

In the following section the Sauter mean diameter is introduced, following by the derivative of the Sauter mean diameter for the uniform, triangle and RRSB distribution. For more detail information see [Stieß \(2009\)](#) or [Zogg \(1993\)](#).

3.1.1 Sauter Mean Diameter and Mass Specific Particle Surface

An equivalent diameter is a diameter of a sphere which have the same properties as the irregular real particle. This equivalent diameter is more convenient for modelling. Regarding the particle surface operations a surface specific diameter is important for the transport processes like heat and mass transfer as well as momentum transfer, see [Stieß \(2009\)](#). One important surface specific diameter is the Sauter mean diameter SMD or d_{32} . The SMD is an average

of swarm particle sizes. It replaced the original particle swarm with uniform spheres, which have overall the same volume and same surface area as the original particle swarm.

The overall particle volume can be calculated with

$$V_p = N_p \cdot \frac{\Pi}{6} \cdot d_{32}^3 \quad (3.1)$$

- N_p = sphere count
- d_{32} = Sauter mean diameter
- V_p = overall particle swarm volume

and the overall Sauter particle surface area equals original particle swarm area A_p

$$A_p = N_p \cdot \Pi \cdot d_{32}^2 \quad (3.2)$$

Hence the Sauter diameter results to:

$$d_{32} = \frac{6 \cdot V_p}{A_p} \quad (3.3)$$

or with $V_p = M_p / \varrho_p$

$$d_{32} = \frac{6}{\varrho_p} \cdot \frac{M_p}{A_p} \quad (3.4)$$

The mass of particle fraction equals

$$\Delta M_{p,i} = N_{p,i} \cdot \varrho_p \cdot \frac{\Pi}{6} \cdot d_{p,i}^3 \quad (3.5)$$

- $N_{p,i}$ = sphere count of particle fraction i
- $d_{p,i}$ = mean particle diameter of particle fraction i
- ϱ_p = particle density

- M_p = mass of particles

Rearrange equation 3.5 to sphere count $N_{p,i}$, we get the sphere count of particle fraction mass

$$N_{p,i} = \frac{6 \cdot \Delta M_{p,i}}{\rho_p \cdot \Pi \cdot d_{p,i}^3} \quad (3.6)$$

The surface of all spheres in this particle fraction is the product of surface of a single sphere times sphere count

$$\Delta A_{K,i} = N_{p,i} \cdot \Pi \cdot d_{p,i}^2 = \frac{6 \cdot \Delta M_{p,i}}{\rho_p \cdot d_{p,i}} \quad (3.7)$$

- $\Delta A_{K,i}$ = surface of all spheres in a particle fraction

The exactly mean diameter per particle fraction is not known, why equation 3.7 can be a rough estimation only. This latter error disappears if the particle fraction width approaching zero. Thus the mass of particle fraction shrinking down to an infinitesimal small value dM_p .

$$dA_K = \frac{6 \cdot dM_p}{\rho_p \cdot d_p} \quad (3.8)$$

The mass specific surface [$m^2 \text{ kg}^{-1}$] of the above mentioned particle fraction is

$$\frac{dA_K}{M_p} = \frac{6 \cdot dM_p}{\rho_p \cdot d_p \cdot M_p} \quad (3.9)$$

The term dM_p/M_p is by definition the relative frequency times the gradient of particle diameter.

$$\frac{dA_K}{M_p} = \frac{6 \cdot yH}{\rho_p \cdot d_p} \cdot d(dp) \quad (3.10)$$

- yH = probability density function, relative frequency

Finally the sphere mass specific surface of any particle distribution between minimal $d_{p,min}$ and maximal sphere diameter $d_{p,max}$ are the integral of equation 3.10

$$\frac{A_K}{M_p} = \frac{6}{\rho_p} \cdot \int_{d_{p,min}}^{d_{p,max}} \frac{yH}{d_p} d(dp) \quad (3.11)$$

3.1.2 Derivation Sauter Mean Diameter for Uniform Distribution

The probability density function of the continuous uniform distribution is, see Hayter (2007):

$$y_H = f(dp) = \begin{cases} \frac{1}{d_{p,max} - d_{p,min}} & d_{p,min} \leq dp \leq d_{p,max}, \\ 0 & dp < d_{p,min} \text{ or } dp > d_{p,max}, \end{cases} \quad (3.12)$$

where $d_{p,min}$ is the minimum particle diameter of the particle size distribution (PDF) and $d_{p,max}$ is the maximum particle diameter of the PDF. The cumulative distribution function (CDF) is:

$$Y_H = F(dp) = \begin{cases} 0 & dp < d_{p,min} \\ \frac{dp - d_{p,min}}{d_{p,max} - d_{p,min}} & d_{p,min} \leq dp \leq d_{p,max}, \\ 1 & dp > d_{p,max}, \end{cases} \quad (3.13)$$

Substituting equation 3.12 in equation 3.11

$$\begin{aligned} \frac{A_p}{M_p} &= \frac{6}{\rho_p} \cdot \int_{d_{p,min}}^{d_{p,max}} \frac{1}{d_{p,max} - d_{p,min}} \frac{d(dp)}{dp} \\ &= \frac{6}{\rho_p \cdot (d_{p,max} - d_{p,min})} \cdot \int_{d_{p,min}}^{d_{p,max}} \frac{d(dp)}{dp} \end{aligned} \quad (3.14)$$

and solve the integral

$$\begin{aligned} \frac{A_p}{M_p} &= \frac{6}{\rho_p \cdot (d_{p,max} - d_{p,min})} \cdot \left[\ln(dp) \right]_{d_{p,min}}^{d_{p,max}} \\ &= \frac{6}{\rho_p \cdot (d_{p,max} - d_{p,min})} \cdot \left(\ln(d_{p,max}) - \ln(d_{p,min}) \right) \end{aligned} \quad (3.15)$$

Put equation 3.15 into the Sauter diameter definition, see 3.4 yields to

$$d_{32,uniform} = \frac{(d_{p,max} - d_{p,min})}{\left(\ln(d_{p,max}) - \ln(d_{p,min})\right)} \quad (3.16)$$

3.1.3 Derivation Sauter Diameter for Triangle Distribution

The probability density function of the triangle distribution is, see Kotz and van Dorp (2004):

$$y_H = f(dp) = \begin{cases} 0 & d_p < d_{p,min}, \\ \frac{2(d_p - d_{p,min})}{(d_{p,max} - d_{p,min})(d_{p,m} - d_{p,min})} & d_{p,min} \leq d_p \leq d_{p,m}, \\ \frac{2(d_{p,max} - d_p)}{(d_{p,max} - d_{p,min})(d_{p,max} - d_{p,m})} & d_{p,m} < d_p \leq d_{p,max}, \\ 0 & d_p > d_{p,max}, \end{cases} \quad (3.17)$$

where $d_{p,m}$ is the mode of the triangle distribution.

The cumulative distribution function is:

$$Y_H = F(dp) = \begin{cases} 0 & d_p \leq d_{p,min}, \\ \frac{(d_p - d_{p,min})^2}{(d_{p,max} - d_{p,min})(d_{p,m} - d_{p,min})} & d_{p,min} < d_p \leq d_{p,m}, \\ 1 - \frac{(d_{p,max} - d_p)^2}{(d_{p,max} - d_{p,min})(d_{p,max} - d_{p,m})} & d_{p,m} < d_p < d_{p,max}, \\ 1 & d_p \geq d_{p,max}, \end{cases} \quad (3.18)$$

Substituting equation 3.17 in equation 3.11

$$\frac{A_p}{M_p} \Big|_{d_{p,min} \rightarrow d_{p,m}} = \frac{6}{\varrho_p} \cdot \int_{d_{p,min}}^{d_{p,m}} \frac{2(d_p - d_{p,min})}{(d_{p,max} - d_{p,min})(d_{p,m} - d_{p,min})} \frac{d(dp)}{dp} \quad (3.19)$$

$$\frac{A_p}{M_p} \Big|_{d_{p,m} \rightarrow d_{p,max}} = \frac{6}{\varrho_p} \cdot \int_{d_{p,m}}^{d_{p,max}} \frac{2(d_{p,max} - d_p)}{(d_{p,max} - d_{p,min})(d_{p,max} - d_{p,m})} \frac{d(d_p)}{d_p} \quad (3.20)$$

and solve the integral

$$\begin{aligned} \frac{A_p}{M_p} \Big|_{d_{p,min} \rightarrow d_{p,m}} &= \left[\frac{6 \cdot 2 \cdot (d_p - d_{p,min} \ln(d_p))}{\varrho_p \cdot (d_{p,min} - d_{p,max})(d_{p,min} - d_{p,m})} \right]_{d_{p,min}}^{d_{p,m}} \\ &= \frac{6 \cdot 2 \cdot \left(d_{p,m} - d_{p,min} + d_{p,min} \ln\left(\frac{d_{p,min}}{d_{p,m}}\right) \right)}{\varrho_p \cdot (d_{p,min} - d_{p,max})(d_{p,min} - d_{p,m})} \end{aligned} \quad (3.21)$$

$$\begin{aligned} \frac{A_p}{M_p} \Big|_{d_{p,m} \rightarrow d_{p,max}} &= \left[\frac{6 \cdot 2 \cdot (d_p - d_{p,max} \ln(d_p))}{\varrho_p \cdot (d_{p,min} - d_{p,max})(d_{p,max} - d_{p,m})} \right]_{d_{p,m}}^{d_{p,max}} \\ &= \frac{6 \cdot 2 \cdot \left(d_{p,max} - d_{p,m} + d_{p,max} \ln\left(\frac{d_{p,m}}{d_{p,max}}\right) \right)}{\varrho_p \cdot (d_{p,min} - d_{p,max})(d_{p,max} - d_{p,m})} \end{aligned} \quad (3.22)$$

Put equation 3.21 and 3.22 into the Sauter diameter definition, see 3.4 yields to

$$\boxed{d_{32,triangle} = \frac{(d_{p,min} - d_{p,max})(d_{p,min} - d_{p,m})}{2 \cdot \left(d_{p,m} - d_{p,min} + d_{p,min} \ln\left(\frac{d_{p,min}}{d_{p,m}}\right) \right)} + \frac{(d_{p,min} - d_{p,max})(d_{p,max} - d_{p,m})}{2 \cdot \left(d_{p,max} - d_{p,m} + d_{p,max} \ln\left(\frac{d_{p,m}}{d_{p,max}}\right) \right)}} \quad (3.23)$$

3.1.4 Derivation Sauter Diameter for RRSB Distribution

The Rosin, Rammler, Sperling and Bennet distribution (RRSB) is a specific particle size distribution in mechanical process engineering. The RRSB dis-

tribution is called Weibull distribution in probability theory and statistic. This distribution is an empirical distribution and often used for many crushing products and dusts, see [Zogg \(1993\)](#) and [Hayter \(2007\)](#). One advantage of this distribution is that an approximation of the integral from Kiesskalt and Matz exist. The maximal deviation of this approximation is about $\pm 2.5\%$, see [Zogg \(1993\)](#).

Two parameters are needed to determine the RRSB distribution, the scale parameter $d'_{p,RRSB}$ and shape parameter n_{RRSB} .

The probability density function of the RRSB distribution is

$$y_H = f(d_p) = \frac{n_{RRSB}}{d'_{p,RRSB}} \left(\frac{d_p}{d'_{p,RRSB}} \right)^{n_{RRSB}-1} \cdot \exp \left[- \left(\frac{d_p}{d'_{p,RRSB}} \right)^{n_{RRSB}} \right] \quad (3.24)$$

Kiesskalt and Matz approximate the integral of the RRSB with

$$\frac{A_K}{M_p} = \left(\frac{6.39}{\varrho_p \cdot d'_{p,RRSB}} \right) \cdot \exp \left(\frac{1.795}{n_{RRSB}^2} \right) \quad (3.25)$$

Put equation [3.25](#) into the Sauter diameter definition, see [3.4](#) yields to

$$d_{32,RRSB} = 0.938967 \cdot \exp \left(- \frac{1.795}{n_{RRSB}^2} \right) \cdot d'_{p,RRSB} \quad (3.26)$$

3.2 Minimum and Maximum Particle Diameter Estimation

The minimum and maximum Limits for the integrals, see [3.1.2](#), [3.1.3](#) and [3.1.4](#), provide the basis together with a distribution function in order to estimate the Sauter mean diameter. In this section some considerations are presented to find the best minimum and maximum diameters for reconstruction particle distributions for droplets and bubble regimes.

The diameter of particles, namely droplets and bubbles, depends major on interfacial tension, viscous and inertia forces. Regarding that tension and inertia force ratio the particles develop a different shape. The following section [3.2.1](#) give an short overview about particle shapes. For detail information see for example [Clift, Grace, and Weber \(1978\)](#).

3.2.1 Shape Regimes for Fluid Particles

Particles in free motion under the influence of gravity can be grouped in three categories:

1. "spherical" Generally, particles are closely approximated by spheres if interfacial tension are much more important than inertia forces. Fluid particles will be termed "spherical" if the minor to major axis ratios lies within 10% of unity, for our purposes.
2. "Ellipsoidal": Generally "ellipsoidal" is used to refer bubbles and drops which are oblate with a convex interface, viewed from outside, around the entire surface. Furthermore, ellipsoidal bubbles and drops commonly undergo periodic random wobbling motions which make characterisation of shape difficult.
3. "Spherical-cap" or "ellipsoidal-cap": Larger fluid particles tend to adopt flat. Such particles may look very similar to segments cut from spheres or from oblate spheroids, why these terms "spherical-cap" and "ellipsoidal-cap" are used. If an indentation at the rear of a fluid particle exist, it is often called "dimpled". After some large spherical- or

ellipsoidal-caps may also trail thin envelopes of dispersed fluid assigned to as "skirts".

In Clift, Grace, and Weber (1978) a generalised graphical correlation in terms of Eötvös number Eo or Bond number Bo , Morton number Mo and Reynolds number Re_p can be found, see figure 3.1.

$$Eo = Bo = \frac{\Delta\rho \cdot g \cdot d_{K, Veq}^2}{\sigma} \approx \frac{\text{buoyancy / volume or inertia force}}{\text{capillary / surface force}} \quad (3.27)$$

$$Mo = \frac{g \cdot \mu_c^4 \cdot \Delta\rho}{\rho_c^2 \cdot \sigma^3} \approx \frac{\text{volume or viscosity force}}{\text{interface / surface force}} \quad (3.28)$$

$$Re_p = \frac{\rho_c \cdot d_{K, Veq} \cdot u_{rel}}{\mu_c} \approx \frac{\text{volume or inertia forces}}{\text{viscous forces}} \quad (3.29)$$

- $\Delta\rho$ = density difference of the two phases [$kg\ m^{-3}$]
- g = gravitational acceleration magnitude [$m\ s^{-2}$]
- $d_{K, Veq}$ = volume equivalent sphere diameter [m]
- σ = surface tension [$N\ m^{-1}$]
- μ_c = viscosity of surrounding continuum fluid [$Pa\ s$]
- ρ_c = density of surrounding continuum fluid [$kg\ m^{-3}$]
- u_{rel} = velocity of particle with respect to surrounding fluid [$m\ s^{-1}$]

If we can assume, that the Eötvös and particle Reynolds numbers are small, we can expect that the particles are spherical, see figure 3.1. Particle Reynolds numbers become small if the relative velocity of both phases or the particle diameter is small, see equation 3.29. In a separated flow the highest relative velocities are nearby the interface. Far away from this interface the phase velocities adjust each other. Both regions are far away from the

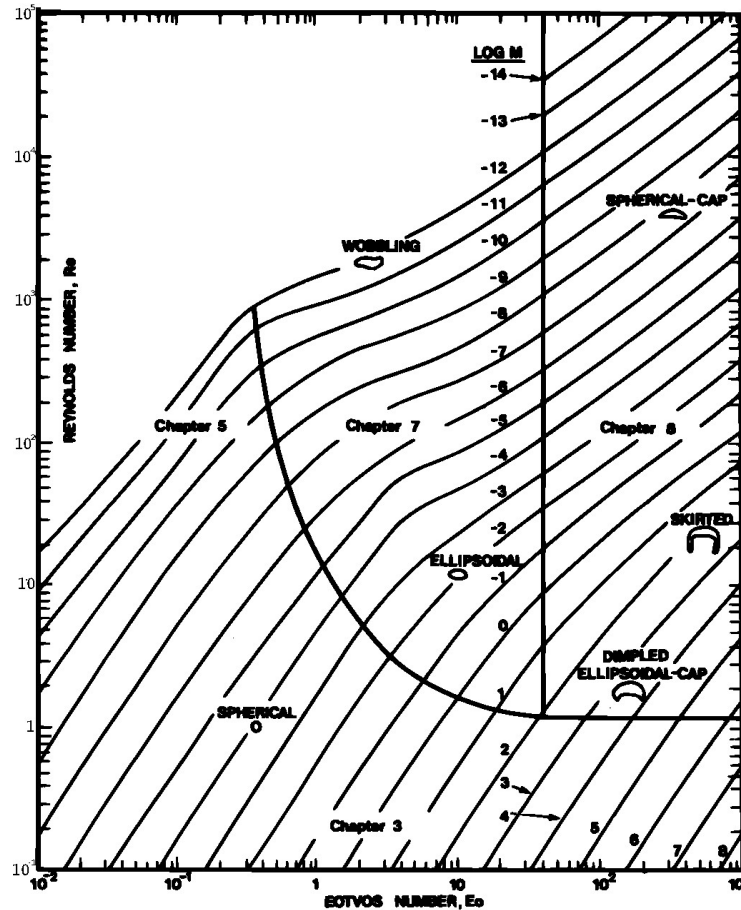


Figure 3.1: Shape regimes for bubbles and drops in unimpeded gravitational motion through liquids; Clift, Grace, and Weber 1978

interface and fulfil the requirements for a small particle Reynolds number. In the same manner a small Eötvös number can be assumed in the bubble and droplet region, because the relative velocities are small and thus the relative acceleration too, see equation 3.27. For this reason spherical particles are assumed and a shape factor equal to 1 is used. Hence following particle diameter are concerning spheres.

3.2.2 Maximum Stable Particle Diameter

The prediction of bubbles and droplets maximum sizes goes hand in hand with the perturbation of interfaces. Perturbation coming from inertia forces

and destabilise the interface in contrast to surface tension and viscous forces which slow the rate of growth of unstable surface waves, see [Ishii and Hibiki \(2006\)](#) and [Clift, Grace, and Weber \(1978\)](#).

There is a wholly branch of researchers which deal with interface perturbation. They develop breakup and coalescence models to predict particle sizes for example in sprays. The breakup models can be used to determine the maximum stable diameter d_{max} of the particle. At a critical diameter d_{crit} just the smallest perturbation cause a particle breakup. Particles which bigger diameter than the critical diameter can be exist but they break into some child particles after the breakup time is reached. If initial perturbation has a sufficiently large deflection, the breakup takes place immediately and hence the breakup time approaching zero, see [Avdeev \(2016\)](#). Due to the short breakup time compared to the time scale of the simulation and the assumed sufficiently large deflection, the occurrence of bigger particle above the critical one is neglected. Hence the maximum stable diameter equals the half of the critical diameter and is chosen for the upper PDF limit, see for example equation 3.34. This latter assumption is conservative, because smaller particles leads to a higher number of particles in the continuous phase. This fact tends to a particle mass flow, which always higher than in reality, to ensure a safety margin. The conservativeness is required for designing industrial pressurised parts.

Regarding the breakup models we have to distinguish between closed theoretical or semi theoretical models and empirical models. Empirical models can be found for nearly every experiment which was done to determine the particle sizes. Unfortunately these models are only valid for a short branch of flow regimes and fluids. Until now there are a lack of multiphase experiments to develop predictive models, which needs a wide experimental basis.

A short overview of state of the art and validated secondary breakup models which are used frequently in the CFD can be seen in Fluent theory guide [Ansys \(2016d\)](#). Four droplet breakup models: the Taylor Analogy Breakup (TAB) model, the Wave model, the Kelvin-Helmholtz Rayleigh-Taylor (KHRT) model, and the Stochastic Secondary Droplet (SSD) model

often used. In general, breakup models can be divided in primary and secondary breakup models, where the primary breakup models determine the initial particle diameters those leave the nozzle. The focus in this work is to find the maximum particle diameter in a free stream, why the secondary breakup models are mainly of interest, because those secondary breakup describe the particle breakup depends on acting forces. To develop a predictive model for particle sizes, it is necessary to choose a secondary breakup model, that is valid for a wide range of particle sizes or Weber numbers.

The above models can be divided according to the Weber number. A high Weber number represent an big particle size and a small Weber number a small particle size, if we assume a constant velocity field and constant fluid properties. The TAB model is recommended for low-Weber-number in contrast to the Wave model which is suitable for Weber number greater than 100, see [Ansys \(2016d\)](#). The SSD model is developed for large Weber numbers, see [Apte, Gorokhovski, and Moin \(2003\)](#).

The Tab model, the Wave model as well as the SSD model are rather suitable for a small range of Weber number. The KHRT model is an hybrid model which is placed between the low and high Weber numbers, see [Reitz and Beale \(1999\)](#). Regarding the range of Weber numbers the KHRT model is preferred.

Those models mentioned above are applicable for a Lagrangian discrete phase. Because this work deals with an Euler-Euler approach, those models have to be checked whether they applicable or not for such an Euler-Euler approach.

Some breakup models assume that parent particle sizes are known which is suitable, if the Euler-Euler Particle model is used, see [2.3.4](#). That is not guilty for the Euler-Euler AIAD model which based on the mixture model, see section [2.3.4](#) and [2.4](#). As described in section [3](#) for simulation of a steam drum the mixture model is needed and hence there are no information about the parent particle sizes as well as distribution. Only the KHRT model from Reitz, see [Reitz \(1987\)](#) and [Reitz and Beale \(1999\)](#), which is based on the particle acceleration, is suitable to predict the maximum stable diameter

in this Euler-Euler approach. Additionally the KHRT model is valid for a large range of Weber numbers. Hence the KHRT model is proper for the Euler-Euler mixture model.

Additionally a new model based on Ishii-Zuber drag model is develop to predict d_{max} and is compared with the KHRT model from Reitz.

Reitz Kelvin-Helmholtz Rayleigh-Taylor Breakup Model

The KHRT model consists of a two step mechanism, see [Reitz and Beale \(1999\)](#). The first step is carried out for the primary breakup. In this step the breakup of a liquid core behind an injection is computed with the Kelvin-Helmholtz (KH) instability model. The second step is called the secondary breakup and based on the Rayleigh-Taylor (RT) instability model. Here the breakup of individual particles outside of the liquid core is computed. Keep in mind that a submodel is needed for a dispersed region far away from a free interface, see discussion in section [3.2.1](#). Hence the primary step is not needed to predict d_{max} , only the secondary breakup model. A short overview is given below but for deeper information see [Reitz \(1987\)](#), [Reitz and Beale \(1999\)](#), [XIN, RICART, and REITZ \(1998\)](#), [Ansys \(2016d\)](#) and [Kolev \(2012\)](#). The RT model is like the KH model a wave instability model. The angular wave number corresponding to the fastest growing wave is given in the [Reitz and Beale \(1999\)](#) RT model by,

$$K_{RT} = \sqrt{\frac{-g_t (\rho_p - \rho_c)}{3 \sigma}} \quad (3.30)$$

and λ_{RT} is the corresponding Rayleigh-Taylor wavelength, see [Kolev \(2012\)](#)

$$\lambda_{RT} = \sqrt{\frac{\sigma}{-g_t (\rho_p - \rho_c)}} \quad (3.31)$$

- K_{RT} = Angular wave number [1/m]
- λ_{RT} = Wave length [m]
- g_t = acceleration in the direction of travel; $g_t = \vec{g} \cdot \vec{j} + \vec{a} \cdot \vec{j}$ where g_t is the

droplet acceleration due to gravity vector \vec{g} and droplet acceleration \vec{a} ;
 \vec{j} is the unit vector tangent to the particle trajectory; [m/s²]

- ρ_p = Particle density [kg/m³]
- ρ_c = Continuum density [kg/m³]
- σ = Surface tension [N/m]

In general the angular wave number of radians per unit distance can be converted to the wavelength with the following expression

$$K = \frac{2 \Pi}{\lambda} \quad (3.32)$$

The radius of particles is proportional to the wavelength of the fastest wave growth rate

$$r_{crit} = \lambda_{RT} * C_{RT} = \frac{2 \Pi C_{RT}}{K_{RT}} \quad (3.33)$$

where C_{RT} is an adjustable constant. Reitz and Beale (1999) use $C_{RT} = 0.1$ in his study. Ansys use the same value as default value. Hence in this thesis $C_{RT} = 0.1$ is used. This constant have a direct influence on the particle diameter and a validation is needed.

Reitz assume that particles with a radius above the critical radius r_{crit} break into two particles of the same size. Hence the child particles radius or with other words the maximum stable particle radius can be calculated with

$$r_{p,max} = \frac{\Pi C_{RT}}{K_{RT}} \quad (3.34)$$

Clift / Grace / Weber Maximum Stable Diameter

The Clift, Grace, and Weber (1978) equation is semi theoretical. But Clift, Grace, and Weber (1978) introduce a coefficient to fit some experimental results.

$$d_{max} \approx 4 \sqrt{\frac{\sigma}{g \Delta \rho}} \quad (3.35)$$

The equation is valid for liquid drops falling in unbounded stagnant gases, as well as for bubbles and for many liquid-liquid systems. Clift, Grace, and Weber (1978) assume that the Eötvös number can not exceed a value of about 16, which they justify with stability considerations and a spherical-cap regime is never attained, see figure 3.1.

Development of new Maximum Stable Diameter Approximation

Especially for fluid particles with large size, the shape become unstable under turbulent condition, see section 3.2.1. If those distortions of the fluid shapes increase, the fluid particle break into smaller child particles. Clift, Grace, and Weber (1978) and Ishii and Hibiki (2006) show that it have to be distinguished between

- Bubble in liquid
- Drop in liquid
- Drop in gas
- Solid particle system

For a two-phase flow without contamination inside tanks and pipes bubbles in liquid and drops in gas can occur. For simplicity, instead of droplet in gas and bubble in liquid, it is mentioned droplets and bubbles following. Experiments by Clift show that bubbles can reach the spherical cap regime before breakup which correspond to $Eo > 40$. Drops in gas almost break up before an Eötvös number of 40 is reached. Clift, Grace, and Weber 1978 Hence droplets at maximum diameter can be found in distortion / ellipsoidal regime and bubbles at maximum diameter in the spherical cap regime, see figure 3.1.

In figure 3.2 the various regimes for drag coefficient can be seen. The drag coefficient for solid spherical particles depends of the Reynolds number in the viscous regime, though C_D is independent of Re in the Newton regime. Fluid particles in the viscous regime have a slightly reduced C_D for a clean sphere

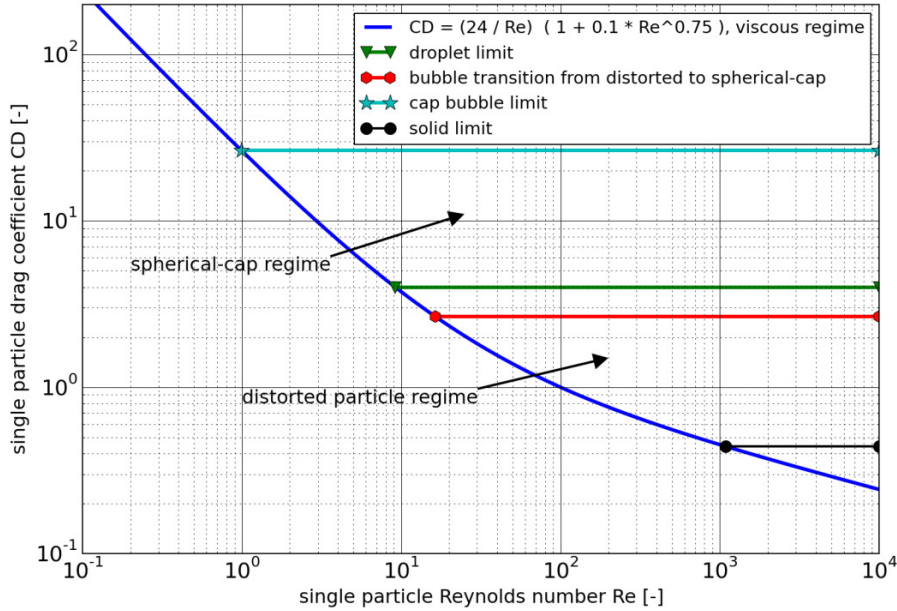


Figure 3.2: Single particle drag coefficient by plotting equation for viscous regime drag coefficient and drag limits; figure by the author

compared with the solid correlation, but irrelevant amounts of impurities eliminate this drag reduction, see Ishii and Zuber (1979). Up to a certain particle size the fluid particle shape is spherical and the solid C_D correlation can be used. Above this particle size the particle interface become unstable. This regime is called the distorted / ellipsoidal regime and spherical-cap regime.

It is well-known that the drag coefficient of solid particle of identical shape is over a wide range practically independent of the Reynolds number under turbulent flow condition, see figure 3.2. For fluid particles the drag coefficient is a superposition of Reynolds number and shape variation. In the region of turbulent flow, the drag coefficient for fluid particles depends only on the shape and not on the Reynolds number. Harmathy introduce a simple method to calculate the drag coefficient and velocity of a fluid particle. This simple method depends mainly on the Eötvös number. But the Harmathy model neglect effects caused by the viscosity. This leads to an increased

damping on the shape oscillation of fluid particles at high Eötvös numbers. Such higher the particle diameter such higher the Eötvös number, see equation 3.27. If the Harmathy model is used to estimate the maximum stable diameter, this oscillation damping effect should be keep in mind. Harmathy 1960

In this distortion or spherical-cap regime the drag coefficient C_D is proportional to the Eötvös number or radius of the particle, see Ishii and Zuber (1979) and equation 2.66

$$C_{D\infty} = \frac{2}{3}\sqrt{Eo} = \frac{4}{3}r_p\sqrt{\frac{g\Delta\rho}{\sigma}} \quad (3.36)$$

In Equation 3.36 the particle size and terminal velocity relation is used, as discussed by Harmathy (1960).

There is a maximum stable diameter for bubbles in spherical-cap regime, see Clift, Grace, and Weber (1978). Ishii introduce an equation for the maximum cap bubble diameter, which is valid for the most practical cases which correspond to a upper drag coefficient of

$$C_{D\infty b} = \frac{80}{3} \quad (3.37)$$

see Ishii and Hibiki (2006). Equalise equation 3.36 and equation 3.37 results to the maximum bubble radius equation

$$r_{\infty max b} = 20\sqrt{\frac{\sigma}{g\Delta\rho}} \quad (3.38)$$

The limit drag coefficient for a liquid drop depends on the droplet interface stability. The stability criterion can be given by the maximum Weber number

$$We = \frac{2\rho_c|\vec{U}_{rel}|^2 r_p}{\sigma} = \begin{cases} 8 & \text{bubble} \\ 12 & \text{droplet} \end{cases} \quad (3.39)$$

see Wallis (1969). Substitution the terminal velocity from Harmathy with a slightly modified proportional factor from Ishii, see Ishii and Hibiki (2006) and Harmathy (1960),

$$|\vec{U}|_{\infty \text{ rel}} = \sqrt{2} \left(\frac{g \sigma \Delta \rho}{\rho_c^2} \right)^{1/4} \quad (3.40)$$

into the We criterion mentioned above, one obtains the maximum stable droplet radius

$$r_{\infty \text{ max } d} = 3 \sqrt{\frac{\sigma}{g \Delta \rho}} \quad (3.41)$$

Combining equation 3.36 and equation 3.41 leads to

$$C_{D\infty d} = 4 \quad (3.42)$$

which can be seen in figure 3.2 as droplet limit.

Equation 3.38 and equation 3.41 are valid for single particles. Though multiphase phase flow inside tanks or pipes, a multiparticle system exists and affect the flow field of adjacent particles. Ishii and Zuber develop a drag coefficient correlation for dispersed two-phase flows of bubbles, drops, and solid particles, see Ishii and Zuber (1979). Those dispersed drag coefficient correlations based on the single particle drag coefficient equations, which are introduced in this section above. A factor, which depends on the volume fraction of the dispersed phase and the mixture viscosity, is used by Ishii to take into account the multiparticle system. For the distorted and spherical-cap regime the drag coefficient in a multiparticle system is

$$C_D = \frac{4}{3} r_p \sqrt{\frac{g \Delta \rho}{\sigma}} Erd \quad (3.43)$$

where Erd is

$$Erd = \left[\frac{1 + 17.67 \{f(vf_p)\}^{(6/7)}}{18.67 f(vf_p)} \right]^2 \quad (3.44)$$

The function $f(vf_p)$ depends on the volume fraction, the continuum phase viscosity and mixture viscosity

$$f(vf_p) = \begin{cases} \sqrt{1 - vf_p} \left(\frac{\mu_c}{\mu_m} \right) & \text{solid particle} \\ (1 - vf_p)^{1.5} & \text{bubble in liquid} \\ (1 - vf_p)^3 & \text{droplet in gas} \end{cases} \quad (3.45)$$

Ishii and Zuber (1979) extend the linear correlation for the mixture viscosity from Taylor, see Taylor (1932), along the power relation for solid particles, see Roscoe (1952),

$$\frac{\mu_m}{\mu_c} = \left(1 - \frac{vf_p}{vf_{p \max}} \right)^{-2.5 vf_{p \max} (\mu_p + 0.4\mu_c) / (\mu_p + \mu_c)} \quad (3.46)$$

$vf_{p \max}$ is the maximum packing. For solid particles the maximum packing in multiparticle systems can vary in range from 0.5 to 0.75. Due to deformation of fluid particles $vf_{p \max}$ can be as high as 0.95 and assumed to be 1 for droplets and bubbles for this work. Ishii and Zuber 1979

Combining equation 3.43, equation 3.37, and equation 3.42 leads to equations for the maximum stable particle diameter in multiparticle systems

For bubbles:

$$r_{\max b} = \frac{20}{Erd} \sqrt{\frac{\sigma}{g \Delta \rho}} \quad (3.47)$$

For droplets:

$$r_{\max d} = \frac{3}{Erd} \sqrt{\frac{\sigma}{g \Delta \rho}} \quad (3.48)$$

If the volume fraction is increasing, the drag coefficient increase too, see figure 3.3. Hence the relative velocities generally decreases for higher volume fraction of the dispersed phase, because of the stronger coupling between phases. That leads to a decreased stable particle diameter with increases in the volume fraction, see figure 3.4.

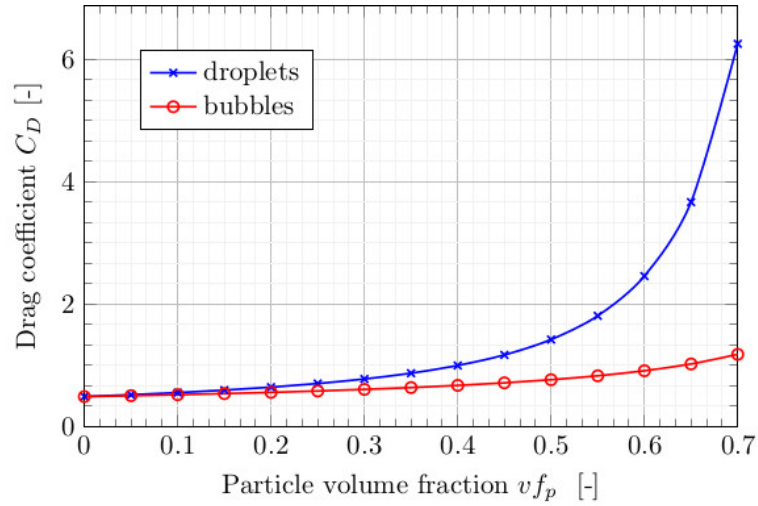


Figure 3.3: Drag coefficient for droplets and bubbles with 2 mm diameter in multiparticle system by plotting equation 3.43; air-water at 25 °C, 1 atm; figure by the author

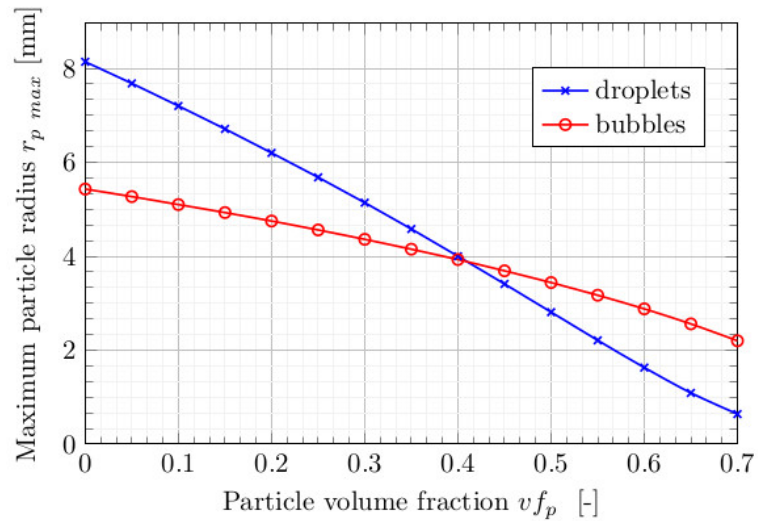


Figure 3.4: Maximum particle radius for droplets and bubbles in multiparticle system by plotting equation 3.48 and 3.47; air-water at 25 °C, 1 atm; figure by the author

Particle Acceleration for Flowing Fluids

Those introduced maximum particle models, see 3.2.2, based on the assumption that particle or particles moving in quasi stationary infinite media, what simplify the momentum equation. Related with that simplification the velocity can be calculated by the gravity force only, see for example Harmathy (1960). This latter assumption is only valid for a few application. The flow in most industrial applications, as well as the present work, are forced convection and more forces cause the fluid acceleration, see section 2.3.4 for the different forces and see equation 2.24. The momentum equation, which is a basic equation for the CFD, is based on the Newton's second law

$$\vec{F} = M \vec{a} \quad (3.49)$$

Hence it is possible to replace the sum of all acting forces on a fluid element with the fluid mass times the acceleration. The acceleration can be calculated from the average velocity field.

The inertia forces acting on the particle interface, caused by the relative velocity of the phases. Hence we can write

$$\vec{F}_{interface} = M \vec{a}_{rel} \quad (3.50)$$

If we examine a bubble flow in stagnant media the only bubble driving force is the gravitational force $\vec{F}_G = \Delta \varrho \vec{g}$. For this special case we can write $M \vec{a}_{rel} = F_G$.

Though for forced convection multiphase flows additional forces have to be taken into account and the term $\Delta \varrho \vec{g}$ have to be substituted by the continuum volume fraction times the continuum density times the relative fluid acceleration, with $\vec{a}_{rel} = D\vec{U}_{rel} \setminus Dt$, see Anderson (1995) or Versteeg and Malalasekera (2007)

$$\Delta \varrho g \hat{=} v f_c \varrho_c \left| \frac{D\vec{U}_{rel}}{Dt} \right| = v f_c \varrho_c \left| \left(\frac{\partial \vec{U}_{rel}}{\partial t} + \vec{U}_{rel} grad(\vec{U}_{rel}) \right) \right| \quad (3.51)$$

where the relative velocity is

$$\vec{U}_{rel} = \vec{U}_c - \vec{U}_p \quad (3.52)$$

The particle shape does not depends on the sign of the acceleration and the norm of the acceleration vector is used. Thus it is not important in equation 3.52 whether the relative velocity is calculated by $\vec{U}_p - \vec{U}_c$ or $\vec{U}_c - \vec{U}_p$.

Reitz take into account the acceleration of a particle along the particle trajectory, see equation 3.31 but this have to be rearrange to the inhomogeneous multiphase model which is used in this work. Thus the Reitz acceleration is substituted with the substantial derivative term like in equation 3.51

$$-g_t(\varrho_p - \varrho_c) \hat{=} v_{f_c} \varrho_c \left| \frac{D\vec{U}_{rel}}{Dt} \right| \quad (3.53)$$

Equation 3.51 and equation 3.53 is the infinitesimal control volume non-conservative form but can rearrange to the infinitesimal control volume conservation form easily, see Anderson (1995). That equation 3.51 and equation 3.53 will be implemented in Ansys CFX software. In CFX there is an interface in which additional equation can be implemented, called Command Expression Language (CEL). In CEL the divergence operator is not available but the gradient operator, thus the gradient form is used. The volume fraction in equations 3.51 and 3.53 is due to the inhomogeneous multiphase model is used, see 2.24.

The acceleration in equation 3.51 in Cartesian coordinates is x-component:

$$\frac{Du_{rel}}{Dt} = \frac{\partial u_{rel}}{\partial t} + u_{rel} \frac{\partial u_{rel}}{\partial x} + v_{rel} \frac{\partial u_{rel}}{\partial y} + w_{rel} \frac{\partial u_{rel}}{\partial z} \quad (3.54)$$

y-component:

$$\frac{Dv_{rel}}{Dt} = \frac{\partial v_{rel}}{\partial t} + u_{rel} \frac{\partial v_{rel}}{\partial x} + v_{rel} \frac{\partial v_{rel}}{\partial y} + w_{rel} \frac{\partial v_{rel}}{\partial z} \quad (3.55)$$

z-component:

$$\frac{Dw_{rel}}{Dt} = \frac{\partial w_{rel}}{\partial t} + u_{rel} \frac{\partial w_{rel}}{\partial x} + v_{rel} \frac{\partial w_{rel}}{\partial y} + w_{rel} \frac{\partial w_{rel}}{\partial z} \quad (3.56)$$

Combining equation 3.54, equation 3.55, and equation 3.56 to calculate the norm of the relative acceleration vector results to

$$|\vec{a}_{rel}| = \sqrt{\left(\frac{Du_{rel}}{Dt}\right)^2 + \left(\frac{Dv_{rel}}{Dt}\right)^2 + \left(\frac{Dw_{rel}}{Dt}\right)^2} \quad (3.57)$$

3.2.3 Minimum Diameter

The theoretical minimum diameter of particles is approaching zero. This is correct when particle interaction can be neglected like drops in atmosphere. In technical devices and containers the particle interaction can't be neglected and coalescence can occur. Hence the minimum diameter should be take into account that interaction and should have an diameter greater than zero.

In the experiment, see section 7.1, observations of droplet in the air flow are done. Some big droplets can be seen nearby the steam window but in the most region no droplets can be seen. But it can be determine a liquid massflow. In other words some droplets exist which the camera or the human eye can't be seen. The dimension of these small particles is below 1 μm . This is in range of aerosols, fog or bubble systems, see Prof. Dr. J. Tomas (2014). Hence the minimum droplet and bubble diameter is assumed to be the minimum diameter of aerosols.

$$d_{p,min} = 1e - 8 \text{ m} \quad (3.58)$$

3.3 Summary Particle Reconstruction

The most important properties for particle impulse and heat transport are the particle swarm surface and the volume. To model particle transport phenomena an equivalent diameter is often used, which takes into account the surface and the volume of the particle swarm. The Sauter mean diameter SMD is such a surface specific parameter of a particle distribution.

In order to determine the SMD the particle density and the mass specific surface of the particle swarm have to be known, see equation 3.4. For this purpose, additional informations are necessary like the minimum and maximum particle diameter and the probability density function, see equation 3.11.

In section 3.1 a discussion about the probability density function PDF can be found. Three different PDF's are chosen for the later simulation model validation.

The minimum particle diameter is chosen as the minimum diameter of aerosols, because it is assumed that in forced convective flow inside pipes, the probability of smaller particles is to be estimated rather low, see section 3.2.3. The maximum particle diameter depends on inertia, viscous, surface tension forces, see figure 3.1. In section 3.2.2 the relations between the particle diameter forces as well as particle properties are presented. All maximum stable particle diameter correlations based on the Harmathy (1960) statement, in which the drag coefficient of a large fluid particle depends only on the shape and not on the Reynolds number, see figure 3.2. Thereby it is possible to estimate the maximum stable diameter in terms of the Eötvös, Weber number and the drag coefficient.

There are some models like the RTB model from Reitz and Beale (1999) and the Clift/Grace/Weber model from Clift, Grace, and Weber (1978), which can be found in the literature. But all models neglect the fluid viscosity, which stabilises the fluid interface and the particle number, and destabilises the interface. The steam drum experiment can demonstrate that there are many fluid particles which interact with each other. Hence, the neglect of the particle number and the viscosity introduces a large error.

Thus a new model to estimate the maximum fluid particle for a multi-particle system is developed. This model includes the Eötvös and Weber number, the drag coefficient, the fluid viscosities and the particle volume fraction, see equation 3.47 and 3.48. It is the only model that considers the different maximum particle sizes for droplets and bubbles, see figure 3.4. To include a correction for a multi-particle system, is a novelty and extend the range for volume fraction of the dispersed phase.

The forced convection inside pipes introduces parameter, other than the potential energy, which influences the acceleration of the fluid particle. However, the Eötvös number only accounts for the potential energy as inertia force. Forces, not considered by the the Eötvös number are not discussed in the literature. Hence in section 3.2.2 "Particle Acceleration for Flowing Fluid" a new approach is developed to calculate the fluid particle acceleration including all forces.

With the multi-particle model and the fluid acceleration model it is possible to simulate a multi-particle system like the steam drum with a forced convection flow.

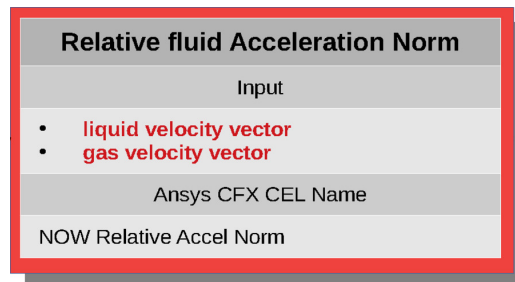
Chapter 4

Implementation of Developed Model in CFX

In this section the implementation of the new developed multiphase CFD model in Ansys CFX is shown. General two parameters for the mixture model are needed, the "Interface Length Scale" (ILS) and the "Drag Coefficient" (Drag). For both parameters a number of functions in Ansys CFX command expression language (CEL) are implemented. General there are functions for ILS, Drag and solver. Solver functions provide for example monitoring tasks and for initialisation and will not be described further. The ILS functions are presented in section [4.1](#) and Drag functions in section [4.2](#). The CEL functions include parts of the AIAD model and the new developed model. Due to distinguish between the AIAD and the new developed model the CEL function have suffixes. AIAD model have the suffix "AIAD" and the new developed model the suffix "NOW". The new developed model will be named "NOW" further.

4.1 Interfacial Area Density Implementation

For better understanding an overview flowchart can be seen in figure 4.3. In Appendix A there is the same figure on A3 format. This flowchart show the implementation of the AIAD model and the NOW model. The AIAD model functions coloured in orange and the NOW model coloured in red. Purple means the input functions for the mixture model, in figure 4.3. Rectangles with a grey coloured table mean a function. An example of a NOW model function is shown in figure 4.1.

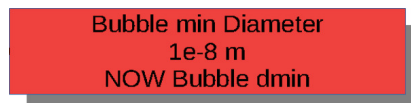


Relative fluid Acceleration Norm
Input
<ul style="list-style-type: none">• liquid velocity vector• gas velocity vector
Ansys CFX CEL Name
NOW Relative Accel Norm

Figure 4.1: Example of NOW model CEL function; by the author

In the header row the function name can be seen, followed by the input variables. On the end of the table one can see the CEL function name. Red highlighted variable names in the input parameter list are variables which are provided from the Ansys CFX field variables. Black input variables are given by another CEL function as output.

Some constants have to be defined, which have an unique colour. An example constant of NOW model can be seen in figure 4.2.



Bubble min Diameter
1e-8 m
NOW Bubble dmin

Figure 4.2: Example of NOW model CEL constant; by the author

The header row of this rectangle shows the name of that constant, the second row is the value with dimension and the last row is the CFX CEL name. Only the velocity fields, the volume fractions and the densities are needed to provide the local interface length scale of the gas-liquid mixture.

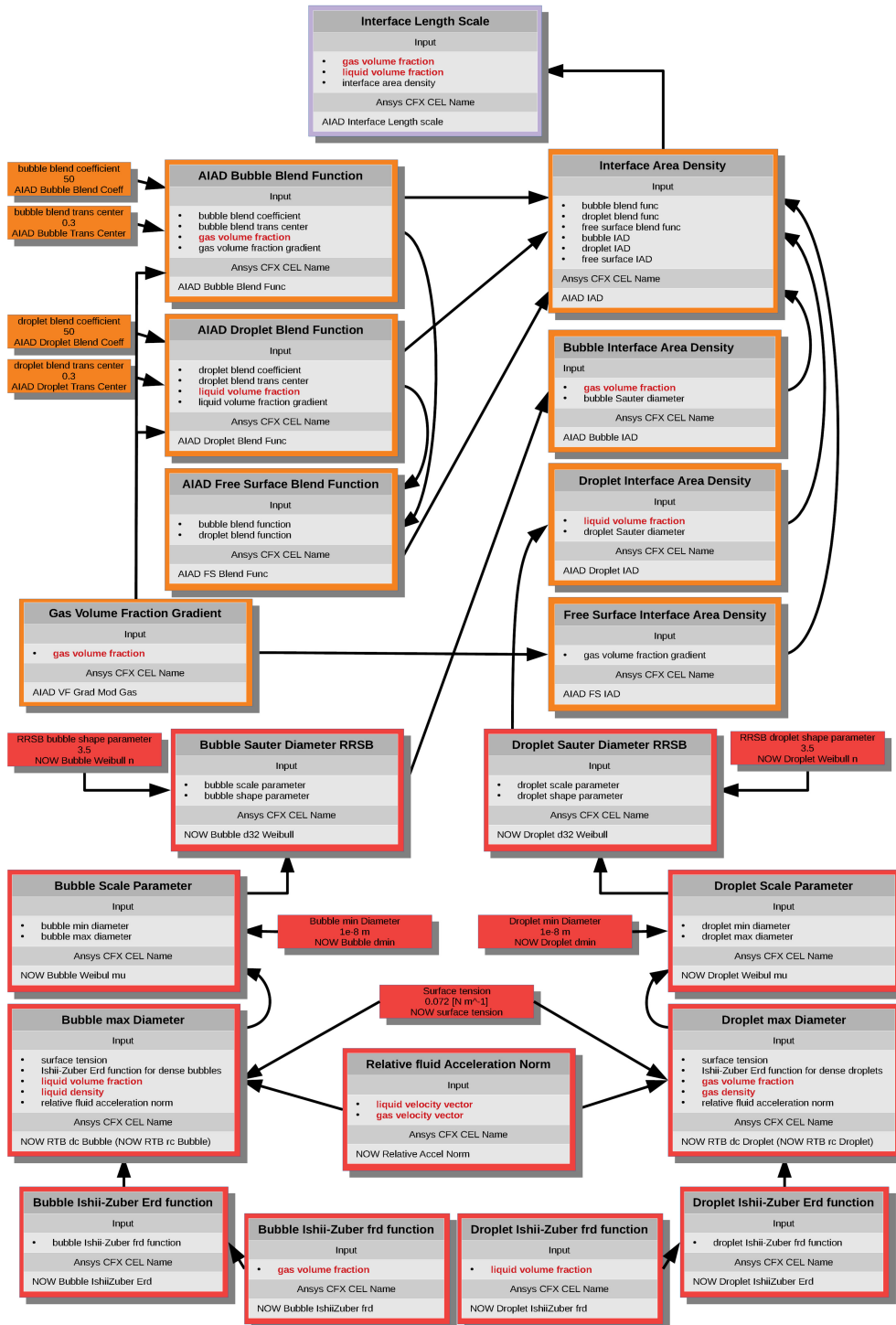


Figure 4.3: Interfacial Area Density Implementation with RRSB distribution in Ansys CFX Mixture Model; by the author

4.2 Drag Coefficient Correlation Implementation

In appendix B flowcharts for the Ishii-Zuber drag model implementation in the CEL can be seen. The Ishii-Zuber drag model provide two functions. One function for the bubble drag coefficient and one for the droplet drag coefficient. Thereby the constant drag coefficients in the AIAD model are replaced. The flowchart is structured like the flowchart which is described in section 4.1. It can be noticed that the ILS affect the drag model, because the ILS is used to calculate the Eötvös and the Reynolds numbers. And hence the drag model is depended on the particle sizes. All functions for the Ishii-Zuber drag model, can be seen in [Ishii and Zuber \(1979\)](#) and [Ishii and Hibiki \(2006\)](#).

Chapter 5

Validation with Horizontal Test Case

Before the new CFD multiphase model is applied to a steam drum, it should be examined in simpler test cases, which are representative key issues. The advantage of such a procedure is, to tune the model parameter of the CFD model before it is applied to the more computationally intensive steam drum simulation. So as not to be too far away from the steam drum simulation two test cases are chosen which represent the predominant flow patterns in a drum.

As described in section 2.2.1, in steam drums a stratified flow is the predominant flow pattern, see figure 5.1. Hence, the new CFD model, which should reproduce the flow pattern in the steam drum, has to be validated with an stratified flow experiment in particular. Due to the steam drum experiment, described in section 7.1, is under isothermal condition and with an air/water mixture as working fluid, an isothermal stratified flow experiment with air/water mixture is chosen. Fabre, Masbernat, and Suzanne (1987) have examined wavy stratified flows in a horizontal duct with the above mentioned conditions. Hence this Fabre experiment data are used to validate horizontal flow regions of a steam drum and feeding pipes. Additional horizontal and vertical feeding pipes play an important role regarding flow pattern in the steam drum and the connected gas liquid separation. The horizontal and

vertical feeding pipes can be seen in figures 2.5 and 2.6. Hence a second test case simulation is carried out with a vertical pipe experiment from Hewitt and Owen (1987).

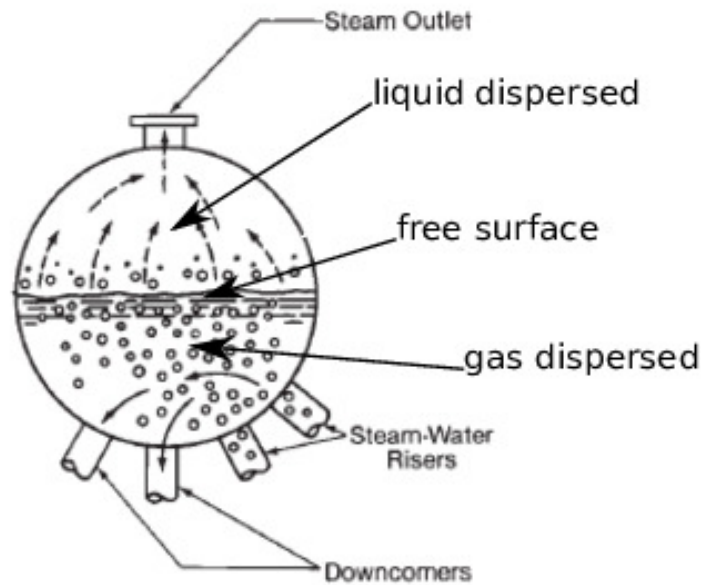


Figure 5.1: Steam drum flow pattern with natural steam/water separation; see Kitto and Stultz 2005

The HZDR had carried out some validations for horizontal two-phase flows, for example Vallée and Höhne (2006), Vallée et al. (2008), Höhne (2009) and Höhne and Vallée (2010). This already several times validated AIAD model, which is introduced in section 2.4, is the basis of the new CFD two-phase model.

Subsequently the validated CFD model, should be applied on the Hewitt and Owen (1987) vertical pipe experiment as a proof of concept, to emphasise the general character of the to be developed two-phase flow model. Especially the general character of the new simulation model is one of the key features, because only with a two-phase model, which cover a wide flow pattern range, it is even possible to simulate such a complex application like a steam drum.

This validation is needed, because the particle Sauter mean diameter reconstruction from relative acceleration based on a predefined distribution function, see section 3.1. Additionally the physical behaviour of the included non-drag forces, which each by itself are at the highest grade in development, shall be tested.

Before to start with the validation, it is important to know the mesh size of mesh independency. Hence the first step is to carry out a mesh study for the Fabre, Masbernat, and Suzanne (1987) experiment, which is based on the RRSB distribution function. Regarding the best mesh, a comparison of distribution functions, as well as a parameter analysis with Fabre, Masbernat, and Suzanne (1987) experiment, see section 3.1, will be carried out.

5.1 Fabre Model

The schematic drawing of the experiment set-up can be seen in figure 5.2. The test section is rectangular with 20 cm width and 10 cm height. The channel is 1260 cm long and consists of Plexiglass. Air and water is recirculate in separate loops. The channel is equipped with a horizontal Plexiglass plate at the inlet, to avoid mixing. The water flow inlet is at the bottom below the inlet plate behind the tranquillisation tank. The air centrifugal fan pump the air above the inlet plate into the channel. Along the channel a water level is developed. The height of the Plexiglass inlet plate can be adjusted to ensure the smallest disturbance, when the water and air touch together. This height depends on the volume flow rates and is changed with experiment cases. On the end of this channel there is an outlet tank for phase separation. Fabre carried out this experiment at 4 different gas velocities. Interesting measured values for the validation are the pressure gradients, interface heights, turbulent kinetic energy profiles and velocity profiles. If someone interested in the detail arrangement, measuring methods and all result, it can be seen in Fabre, Masbernat, and Suzanne (1987).

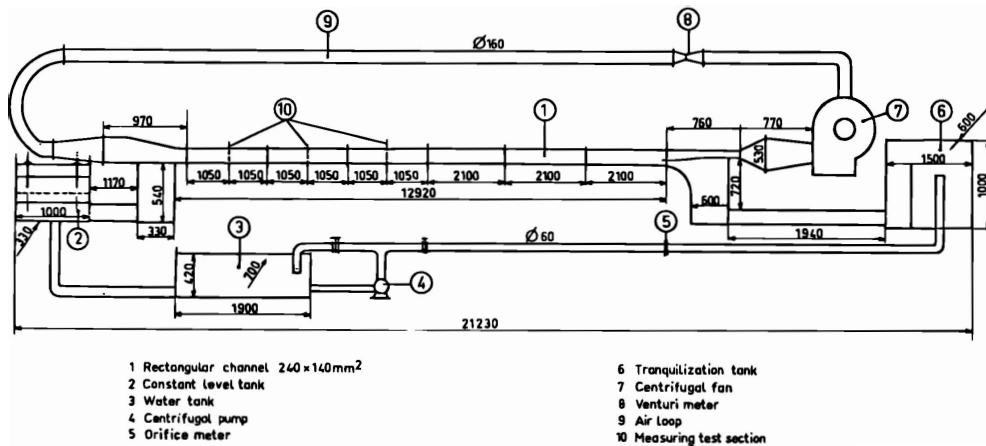


Figure 5.2: Fabre channel general experiment set-up scheme, see Fabre, Masbernat, and Suzanne (1987)

In tables 5.1, 5.2 and 5.3 a selection of measured values is shown, which are important for the CFD model validation. Special attention is paid to run

reference 400, because it is a slightly wavy stratified flow and it is assumed to be occur in steam drums often.

Table 5.1: Fabre channel experiment general data; Fabre, Masbernat, and Suzanne 1987

Run reference	000	250	400	600
Water flow rate [L/s]	3.0	3.0	3.0	3.0
Air flow rate [L/s]	0.0	45.4	75.4	118.7
Bulk velocity of water [m/s]	0.387	0.395	0.476	0.698
Bulk velocity of air [m/s]	0.00	0.3.66	5.50	7.56
Mean water depth [mm]	38.8	38.0	31.5	21.5
Pressure gradient [Pa/m]	0.00	2.10	6.70	14.80

Table 5.2: Fabre channel experiment water velocity and turbulence energy profile run reference 400 data (table 5.1); Fabre, Masbernat, and Suzanne 1987

height [mm]	Velocity [m/s]	turbulence energy [m²/s²]
0.0	0.000	0.000
1.2	0.365	5.135e-3
2.7	0.470	3.880e-3
4.2	0.504	2.790e-3
8.6	0.546	2.180e-3
14.6	0.549	1.820e-3
18.6	0.545	1.266e-3
22.2	0.540	1.270e-3
26.0	0.534	1.442e-3
29.6	0.532	1.791e-3
31.1	0.570	2.490e-3
32.8	0.616	3.090e-3

Table 5.3: Fabre channel experiment air velocity and turbulence energy profile run reference 400 data (table 5.1); Fabre, Masbernat, and Suzanne 1987

height [mm]	Velocity [m/s]	turbulence energy [m ² /s ²]
40.0	5.070	0.948
45.0	5.390	0.874
51.0	5.580	0.759
57.0	5.660	0.670
63.0	5.720	0.604
69.0	5.820	0.560
75.0	5.930	0.489
81.0	6.050	0.429
86.0	6.150	0.368
90.0	6.210	0.337
92.0	6.140	0.345
94.0	5.960	0.388
96.0	5.500	0.531
100.0	0.000	0.000

5.1.1 Fabre CFD Geometry and Mesh

The CFD model geometry is slightly different. Due to the symmetry of the rectangular channel, the CFD geometry can be approximated by a 2D model. Additionally the length of the CFD model channel is 4.5 m long, compared to 12.6 m in the experiment.

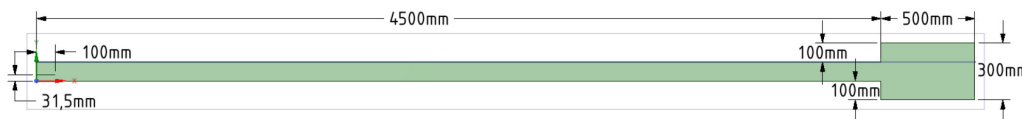


Figure 5.3: Fabre channel CFD 2D geometry with dimensions for run reference 400 data (table 5.1); figure by the author

In figure 5.3 the CFD geometry can be seen with dimensions. Ansys CFX can not solve a 2D model, thus the the geometry in figure 5.3 is in 3D with 2mm thickness. The 2D mesh can extruded with one cell layer along the 2mm thickness. Hence a quasi 2D mesh occur, with one cell layer thickness, which can be solved by a finite volume method solver, see figure 5.4.

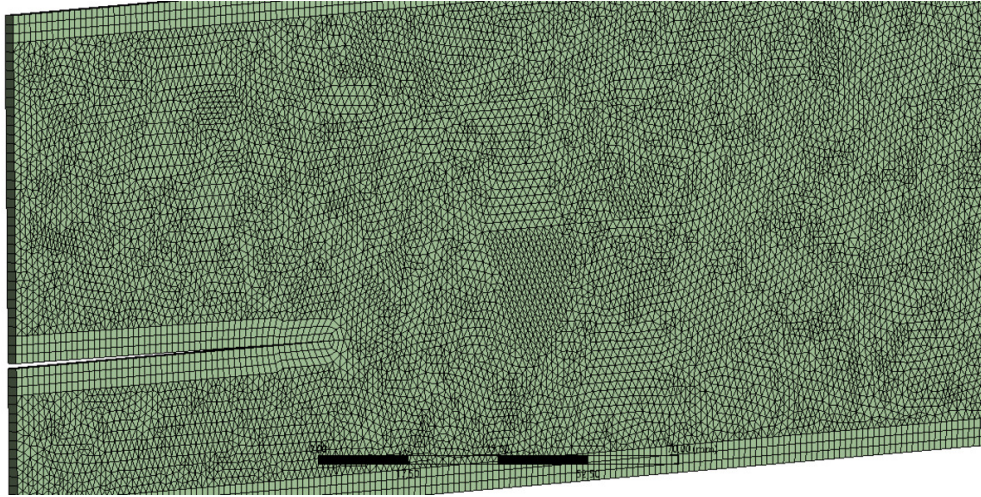


Figure 5.4: Fabre channel CFD 2D mesh; figure by the author

The mentioned above horizontal Plexiglass plate at the inlet, to avoid mixing, is used in the CFD model too. Thereby the inlet is divided in two separate inlets, see figure 5.3 and 5.5. The plate distance from the bottom is the water surface height which can be seen in table 5.1.

The mesh size will be determined in the mesh study, though the boundary layer is constant with 3 layers and a wall y^+ value of above 30.

5.1.2 Fabre Boundary Conditions

In general, the values for the boundary conditions corresponds to the run reference 400 data (table 5.1).

An overview of all boundaries of Fabre channel can be seen in figure 5.5.

Two separate velocity inlets are used in the simulation. One for the air flow and one for the water flow. The corresponding velocities of the experiment volume flow can be seen in table 5.1. The location of both inlets can be seen in figure, 5.5.

Both outlets are modelled as openings. For the air outlet a relative pressure of “0 Pa” is used. At the water outlet the hydrostatic pressure have to be added to a relative pressure of “0 Pa”. The hydrostatic pressure height is determined

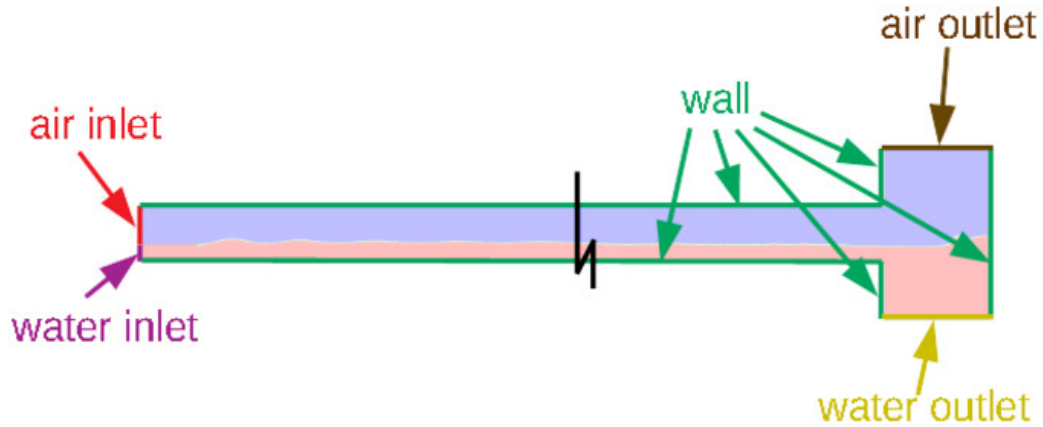


Figure 5.5: Fabre channel CFD model boundary conditions; figure by the author

by the mean water depth from table 5.1 plus the water outlet box depth, see figure 5.3. The water density of 997 kg/m^3 used in the simulation corresponds to the Fabre, Masbernat, and Suzanne (1987) experiment parameter of 1 atm and 25°C . If an recirculation at the outlet occur, only air at air outlet and water at water outlet can flow inside the domain. Due to that the outlets are far away enough from the location of interest, the boundary conditions are sufficient. In Figure 5.5 the outlet positions can be seen.

The front and back sides in figure 5.5 are symmetry boundary condition.

All other boundary condition are hydraulic smooth walls with a wall contact angle of 65° , see figure 5.5.

5.1.3 Fabre Physics Set-Up

The simulations in the mesh study, like the most of the Fabre Channel simulations, are steady state. Transient simulations are only done regarding validation of the steady state model. Due to the constant temperature and small pressure difference in the experiment, the air and water is modelled in simulations with constant properties for 1 atm and 25°C . The inhomogeneous mixture model is used, so that both fluids are defined as continuous. The experiment is under atmospheric condition, so the reference pressure in the simulation is 1 atm. The buoyancy reference pressure is set equal to the

air density of 1.185 kg/m^3 . The gravity vector is set in the same way as in the experiment.

Due to the better performance of the *SST* $k - \omega$ model compared to the standard $k - \omega$ model the SST model is used [Mahaffy et al. 2015], but with the $k - \omega$ interface wall damping function and turbulence enhancement, see section 2.4.3. For the fluid buoyancy model the “Density Difference” is chosen. The interaction between air and water have to be defined. For interface momentum transfer the “Mixture Model” with the “Interface Length Scale” function from the AIAD model is used. An overview can be found in section 2.3.4, 2.4 and 4.1. For this analysis the Sauter mean diameter based on a RRSB distribution is used to calculate the interfacial area density, where the shape parameter is set to 40 and the mean parameter is calculated by the geometric mean.

It is assumed that there is a large range of fluid particle diameters and hence a drag model is needed for the dispersed phases. For fluid particle the Grace model as well as the Ishii-Zuber drag model are possible, see section 2.3.4. Due to the more sophisticated Ishii-Zuber drag model, this is added as CEL functions in Ansys CFX by the author to replace the constant drag coefficient values of the AIAD model, see section 4.2.

It is needed to set “Standard” for the “Free Surface Model” in order to activate the wall adhesion model. The wall contact angle is assumed to be 65° . Liquid is chosen for the primary fluid in the surface tension model with a surface tension coefficient of 0.072 N/m . To take into account a increased turbulence in the continuous phase the “Turbulence Source Terms (Beta)” is chosen for “Turbulence Transfer”.

All Simulations are run with double precision because of stability reasons and accuracy. The simulations run with “High Resolution” for the advection scheme and “High Resolution” for the turbulence numerics too. The “Physical Timescale” of $4\text{e-}3 \text{ s}$ is used. The mass imbalances should be below 1%, which can be determine in the “Conservation Target”. In the advanced option tab, switch from “Segregated” to “Coupled” in “Volume Fraction Coupling” is recommended, because it reduce the mass and momentum imbalances de-

spite higher “Physical Timescale”. Additionally the “Volume-Weighted” option for “Initial Volume Fraction Smoothing” is chosen in order to stabilise the solver during the first iterations.

Sometimes numerical errors are arisen, which needed additional modifications in CFX Pre. Nearby the free surface, large gradients occur in some field variables. If such simulation run in parallel mode a floating point exception occur sometimes but not after restarting the simulation. Reducing the value of the expert parameter “overlap relaxation fluids” from its default value of 1 may be helpful. In most simulation with such a behaviour an “overlap relaxation fluids” value of 0.75 run for this thesis simulations without this error.

In steady state simulations for free surface flows convergence is often hard to achieve in a residual sense. Instead use some global quantity to check if the solution is changing. Failure to converge residuals is often recognisable as small spurious waves on the free surface interface. These waves may be reduced in magnitude if the timestep for the volume fraction equation is an order of magnitude smaller than for the momentum equation [Ansys \(2016b\)](#). Hence for all steady state simulations the volume fraction time scale will be set a magnitude smaller than the overall timescale.

The minimum volume fraction for the dispersed phases is important for the solver stability and results. Overall the minimum volume fraction should be zero, but the solver will be diverged. Hence a value of $1e-6$ for single precision and $1e-12$ for double precision has shown a stable solver behaviour. Hence a value minimum volume fraction of $1e-12$ is used.

5.1.4 Fabre Initial Conditions

The initial conditions are chosen in that way, that initial condition is preferably close to the final solution, because it stabilise the solver during the first iterations and reduce the overall iterations. Hence the water phase is initialised at the channel bottom with the height see in table [5.1](#). Above the water phase the air phase is initialised. Therefore the pressure initialisation

is needed too. A relative pressure of 0 Pa is assumed in the air phase. Due to the gravity force the water phase will be initialised with the hydrostatic pressure. The initial upstream velocity is set to inlet bulk velocity, see table 5.1 individual for every phase.

5.1.5 CFX Solver Issues Notes For Transient Simulations

In transient simulation the local time derivative of velocity is needed to calculate the acceleration. If the time derivative is calculated in CFX CEL language the time derivative values are available at vortices. But the drag model need that derivatives in centre points and the solver produce the following error in CFX Solver:

“Error in CFX-Solve:

*Error in subroutine GET_VAREL :

*Locale BELG1 with entity ICENTRE is illegal for time derivatives

*GETVAR originally called by subroutine cal_CAB_MOM”

Hence the time derivatives are calculated by an user Fortran subroutine, which ensure the time derivatives location at centre points.

For all transient simulation the Courant number of approximately 1.5 are used to ensure mass and momentum imbalances are in between +/- 1%, what cause a stable run without floating point exception errors.

5.2 Mesh Study

The goal of a mesh study is to find a mesh size, where results do not change significant after mesh refinement. The simulation model set-up is described in section 5.1.2, 5.1.3 and 5.1.4 and based on the Fabre Channel run reference 400 data (table 5.1), see table 5.1. To calculate the maximum particle diameter the correlations based on Ishii Zuber model are used as well as the RRSB distribution for Sauter mean diameter. The drag coefficient is calculated by Ishii Zuber model for droplets and bubbles. All parameters of the AIAD model are taken unchanged, except the turbulence damping coefficient. The turbulence damping coefficient recommended by Ansys (2016d) is used. A further discussion about that damping coefficient can be read in section 5.4. For this mesh study RRSB parameters, AIAD model parameters as well as size parameters can be seen in table 5.4. The simulation model set-up is described in section 5.1.

Table 5.4: Fabre channel mesh study simulation model parameter

Parameter	Value or Equation
<i>AIAD model parameter</i>	
High Turbulence Coefficient	15
<i>Distribution parameter</i>	
Distribution function	RRSB
bubble shape parameter	40
bubble scale parameter	$\sqrt{d_{b,max} \cdot d_{b,min}}$
droplet shape parameter	40
droplet scale parameter	$\sqrt{d_{d,max} \cdot d_{d,min}}$
<i>Size Parameter</i>	
bubble min diameter	1e-8 m
bubble max diameter	Nowitzki model, see 3.2.2 on page 86
droplet min diameter	1e-8 m
droplet max diameter	Nowitzki model, see 3.2.2 on page 86
surface tension	0.072 N/m

The mesh size is changed in that way, that only the tetrahedral cells at the symmetry face is decreased, whereby the prism layer ratio and height is constant. In CFX Mesh an element face size which can be seen in column 1 in table 5.5 is defined for the left symmetry plane and is extruded to the opposite side. Thus the volume mesh size corresponds to this symmetry face size. The mesh consists of tetrahedral elements and prisms at walls, see figure 5.4.

In order to examine a mesh independent solution one important field variable, which is representative for all other field variables, will be examined. The mesh sensitivity focuses on the deviation between the pressure drop gradient measured by Fabre and the simulated pressure drop gradient. This pressure gradient deviation is normalised afterwards and can be seen in table 5.5. Due to pressure fluctuations in the simulations, the pressure gradient is an average value over 10.000 iterations.

Table 5.5: Fabre channel mesh study pressure gradient and normalised pressure gradient deviation (NPGD); run reference 400 data (table 5.1)

Case	Number of Elements	Elements ratio	pressure gradient Pa/m	NPGD %
tet 15.000 mm	12,080	1	16.023	139.15
tet 7.500 mm	23,623	2	12.520	86.93
tet 3.500 mm	97,736	8	8.944	33.49
tet 1.750 mm	372,288	31	8.583	28.10
tet 0.875 mm	1,642,812	132	8.460	26.27

In table 5.5 the simulated pressure gradient of the corresponding tetrahedral mesh size and number of elements is shown.

The pressure drop gradient is determined by the pressure difference at two points nearby the top wall divided by the length difference, like in the experiment set-up. The normalised pressure gradient deviation (NPGD) is defined as:

$$NPGD = \frac{\sqrt{\left(\frac{\Delta p_{exp}}{\Delta x} - \frac{\Delta p_{sim,ave}}{\Delta x}\right)^2}}{\frac{\Delta p_{exp}}{\Delta x}} \quad (5.1)$$

This NPGD value corresponds to root mean square (RMS) value for a single value divided by the measured pressure gradient. The simulation pressure gradient is an average value over 10.000 iterations.

The curve progression of the NPGD above the number of elements can be seen in the figure 5.6. The x-axis scale is logarithmic.

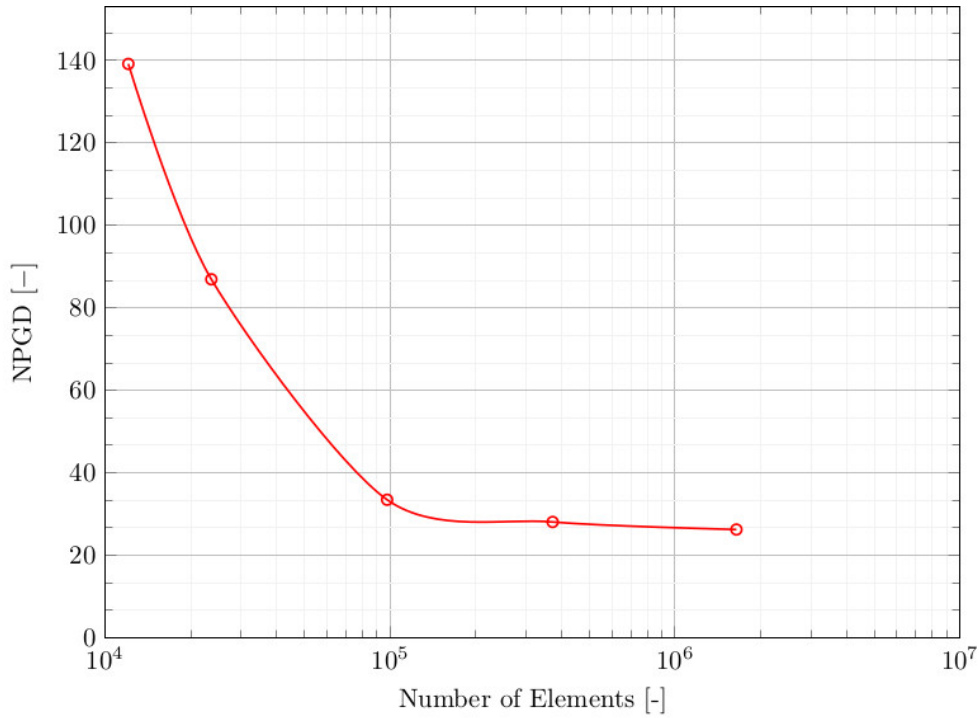


Figure 5.6: Fabre channel run reference 400 data (table 5.1) mesh study; normalised pressure gradient deviation (NPGD) over number of Elements; figure by the author

In figure 5.6 it can be seen, that the NPGD value is decreasing significant until a number of elements of about 1e5 is reached, which correspond to 3.5 mm tetrahedral size. For smaller mesh sizes than 3.5 mm the pressure

drop gradient deviation does not change significantly. The NPGD value difference of the tet 3.5 mm mesh case to the finest is about 7% and the tet 1.75 mm case to the finest mesh about 1%. Hence it will be recommended to use a tetrahedral size of about 1.75 mm. But for a larger parameter study, a mesh size of 3.5 mm is recommended, because of the lower computing time.

To underpin this statement above, additional measurement result are take into account and like in equation 5.1 a normalised deviation of further variables is calculated. The sum of four normalised parameters are shown in figure 5.7.

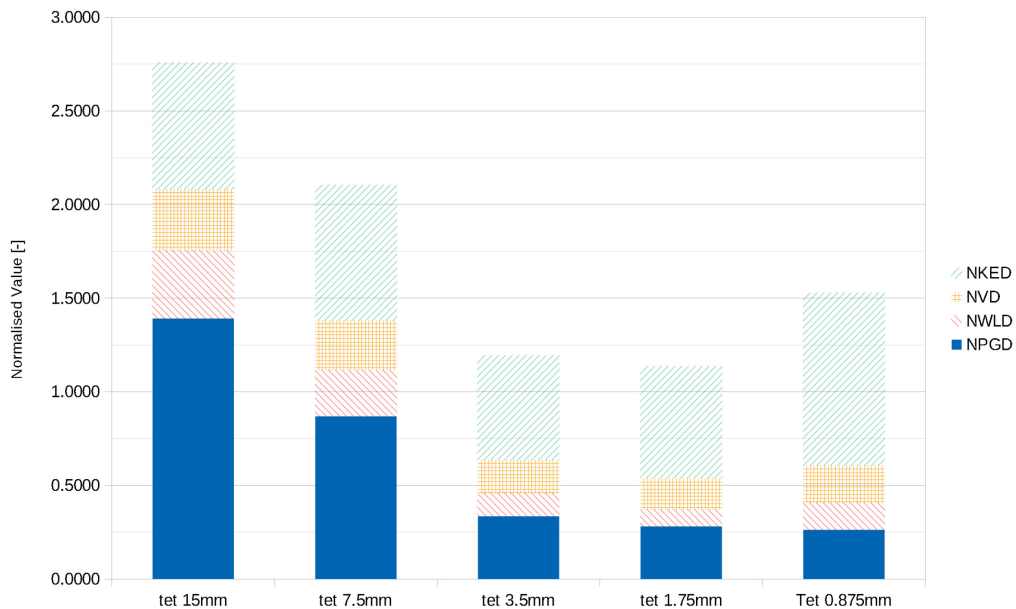


Figure 5.7: Fabre channel run reference 400 data (table 5.1) mesh study; sum of normalised RMS kinetic energy, normalised RMS velocity, normalised water level and normalised RMS pressure gradient value for different mesh sizes; figure by the author

The normalised RMS kinetic energy value (NKED) is the RMS deviation of the Fabre experiment kinetic energy plot, see table 5.2 and 5.3, and the average kinetic energy plot from the simulation divided by the kinetic energy

average value of the experiment data, see equation 5.2:

$$NKED = \frac{\sqrt{\frac{1}{N} \sum_i (ke_{i,exp} - ke_{i,sim,ave})^2}}{\overline{ke_{exp}}} \quad (5.2)$$

In equation 5.2 ke_{exp} , $ke_{sim,ave}$, N and $\overline{ke_{exp}}$ is the kinetic energy from the experiment, the average simulated kinetic energy at a line at $x = 3$ m from top to bottom wall of the Fabre channel, the number of measuring points and the arithmetic average of the measured kinetic energy.

In the same sense like NKED, the normalised RMS velocity (NVD) can be defined as:

$$NVD = \frac{\sqrt{\frac{1}{N} \sum_i (u_{i,exp} - u_{i,sim,ave})^2}}{\overline{u_{exp}}} \quad (5.3)$$

To examine the water level deviation, the water depth from table 5.1 is used as a reference level. The water level in the simulation is calculated by the area average of the height y at an isosurface at a liquid volume fraction value of 0.5. This isosurface represent the interface between air and water. So the normalised water level deviation between the interface in the simulation and the measured water depth is defined as:

$$NWLD = \frac{\frac{\sum_i (y_i - 31.5mm) A_i}{\sum_i A_i}}{31.5mm} \quad (5.4)$$

If one considers in figure 5.7 the RMS value of pressure gradient above the different meshes, the same progress like in figure 5.6 can be recognized. The same behaviour, that the error decreases with a finer mesh, can be seen for the NPGD, NKED, the NVD and NWLD too, except for the finest mesh. At the finest mesh the NPGD value is almost identical to the tet 1.75mm mesh case, but all other error values are increased. This behaviour must not occur for stable numerical algorithms.

The increased error at the finest mesh is probably a consequence of the better interface resolution. The AIAD model uses a blending function to distinguish

between the different morphologies, which depends on the mesh size. Hence, a abrupt change in the morphology regions from the 1.75 mm to the 0.875 mm mesh size can be assumed. This change in morphology causes a non-linear jump in the turbulence model, since the turbulence damping is implement in the free surface region as a jump function. Therefore, it is a difficult task to examine the mesh independence including a non-linear model such as the turbulence damping model.

But apart from this instabilities, the mentioned above recommendation to use the 1.75 mm mesh is confirmed by the figure [5.7](#) also.

5.3 Distribution Function Comparison

It is well known, that the nature of the problem determines which size distribution is appropriate for its analysis. And it is important to be able to recognise which size distribution is appropriate for a particular problem.

Hayter 2007

The most simple continuous distribution, the uniform distribution (UDF), is considered, because it is easy to integrate. That simplicity also applies to the triangle distribution (TDF) too. But the RRSB distribution (RRSB) is not chosen due to the simplicity, rather because of the wide variety of forms, depending on the choice of the two parameter, as well as it is well suited to represent the particle size spectrum of particles sizes which are formed by strong external forces, see Zogg (1993). Additionally the approximation of the integral for the RRSB distribution from Kiesskalt and Matz saves a lot of computing time.

In section 3.1 one can find the derivative of the above mentioned different particle size distributions. Due to the lack of knowledge which distribution function is suited for droplets and bubbles for a air/water mixture, all three distributions are simulated for the same case under the same conditions. The simulation results are compared to the experimental results from Fabre, Masbernat, and Suzanne (1987) run reference 400 data (table 5.1). The UDF does not require any parameter, so that only one simulation is needed. Otherwise the other both distribution functions. The TDF has one scale parameter, whereas the RRSB has a scale and a shape parameter.

Due to the first simulations with the TDF and RRSB, it was decided not to carry out several calculation with TDF and rather examine the scale parameter of the RRSB. The reason is, that the TDF with only one scale parameter is to inflexible to achieve smaller Sauter mean diameter (SMD). Because of the flexibility, the RRSB is given priority, so that a wide range of SMD can be examined.

It is assumed that droplet or bubble breakup and coalescence is a natural process. Natural processes can be directly modelled by the normal distribution.

Additional the central limit theorem is an accurate approximation of identically distributed random variables independent of the distribution of the individual random variables. That means for different probes of Sauter mean diameter at the same location, that the SMD average is normal distributed.

Hayter 2007

In steady state simulations, the field variables correspond to the mean values and hence the a normal distribution is assumed. The RRSB distribution with a shape parameter $n_{RRSB} \geq 3$ is similar a normal distribution and the RRSB distribution with $n_{RRSB} \geq 3$ should be suited to reproduce the particle sizes in steady state simulations for bubbles and droplets. With $1 < n_{RRSB} < 3$ it looks like a logarithmic distribution and will be neglected. Below one the shape of the RRSB distribution looks like root function and will be neglected also.

In table 5.6 all different distribution study simulation cases are presented. The setup of all simulations in this section based on the simulation setup like in the mesh study with a tetrahedral mesh size of 3.5 mm. The mesh study simulation will be called reference and only changes in the distribution function setup are indicated.

The result values of normalised RMS pressure gradient deviation (NPGD), of normalised water level deviation (NWLD), of normalised RMS velocity deviation (NVD), of normalised RMS kinetic energy deviation (NKED) and of mass flow of liquid out of air outlet for all simulation cases from table 5.6, can be seen in table 5.7 and figure 5.8. All data in table 5.7 are calculated with the introduced equations 5.1, 5.4, 5.3 and 5.2, except the liquid mass flow out at air outlet. The latter is a mean value of an expression, which calculate this mentioned mass flow and plot it during the run. Unfortunately this liquid mass flow was not measured by Fabre and is only a simulation result. Hence a normalised value regarding the experiment can not be carried out. Therefore these mass flow results are plotted in figure 5.8 on the second y axis, because the unit is kg/s. But this liquid mass flow value is very important for the air/liquid mixture separation examination. If the liquid mass flow out ot air outlet is small, the air/water separation is strong and

Table 5.6: Fabre channel distribution study simulation cases overview

Case	Reference modification
F_000	Reference
FDF_010	Equal distribution
FDF_020	Triangle distribution
FDF_030	RRSB distribution $d'_{p,RRSB} = (d_{p,max} - d_{p,min})/10; n = 40$
FDF_040	RRSB distribution $d'_{p,RRSB} = (d_{p,max} - d_{p,min})/100; n = 40$
FDF_050	RRSB distribution $d'_{p,RRSB} = (d_{p,max} - d_{p,min})/500; n = 40$
FDF_060	RRSB distribution $d'_{p,RRSB} = (d_{p,max} - d_{p,min})/1000; n = 40$
FDF_070	RRSB distribution $d'_{p,RRSB} = \sqrt{d_{p,max} d_{p,min}} 10; n = 40$
FDF_080	RRSB distribution $d'_{p,RRSB} = \sqrt{d_{p,max} d_{p,min}} 20; n = 40$
FDF_090	RRSB distribution $d'_{p,RRSB} = \sqrt{d_{p,max} d_{p,min}}; n = 4$
FDF_100	RRSB distribution $d'_{p,RRSB} = \sqrt{d_{p,max} d_{p,min}} 20; n = 4$
FDF_110	RRSB distribution $d'_{d,RRSB} = \sqrt{d_{d,max} d_{d,min}} 20; n = 40$
	RRSB distribution $d'_{b,RRSB} = \sqrt{d_{b,max} d_{b,min}}; n = 40$
FDF_120	RRSB distribution $d'_{d,RRSB} = \sqrt{d_{d,max} d_{d,min}}; n = 40$
	RRSB distribution $d'_{b,RRSB} = \sqrt{d_{b,max} d_{b,min}} 20; n = 40$
FDF_130	RRSB distribution $d'_{d,RRSB} = \sqrt{d_{d,max} d_{d,min}} 5; n = 4$
	RRSB distribution $d'_{b,RRSB} = \sqrt{d_{b,max} d_{b,min}}; n = 4$

vice versa. In a separated flow pattern, like in Fabre run reference 400 data (table 5.1), the number of droplets in the air is assumed to be small. Hence the mass flow of liquid out of air outlet in the simulation should be small too.

Due to the air is in contact with the water in the Fabre experiment it is assumed, that the relative humidity is 100 %. And because the air is returned to the inlet in a cycle, the air is in saturated state at the experiment inlet too, see figure 5.2. Hence relative humidity of the air does not change and the amount of steam inside the air, not droplets, can be neglected in the water mass balance equation. Thus a phase change of water can be neglected in the simulation model. In order that the liquid or water mass flow out of the air outlet correspond to the droplets which are carried away from the liquid interface to the air outlet. Like mentioned above a small droplet fraction in

the air is assumed for such a separated flow.

Table 5.7: Distribution function study results of average NPGD, NWLD, average NVD, average NKED, average liquid mass flow out of air outlet and the line average Sauter mean diameter at $x=3.5$ m ; Column minimum value coloured in green and maximum in red; Fabre channel run reference 400 data (table 5.1)

Case	NPGD	NWLD	NVD	NKED	MF Liq	ave SMD
	—	—	—	—	kg/s	mm
F_000	0.3351	0.1858	0.1791	0.5576	1.78e-04	0.2485
FDF_010	0.5255	0.1004	0.2389	0.7762	5.30e-12	13.2800
FDF_020	0.5431	0.1159	0.2719	0.7896	4.71e-11	118.9740
FDF_030	0.5597	0.1173	0.2764	0.7930	9.00e-12	19.8838
FDF_040	0.7012	0.0179	0.1742	0.5687	8.72e-11	2.3503
FDF_050	0.4497	0.0677	0.1343	0.4669	8.25e-09	0.6791
FDF_060	0.2922	0.0921	0.1410	0.4567	2.37e-08	0.4466
FDF_070	0.5616	0.0620	0.1328	0.4989	2.68e-09	0.6330
FDF_080	0.7879	0.0098	0.1501	0.4090	2.52e-09	1.1450
FDF_090	0.7201	0.2201	0.1708	0.7900	4.87e-06	0.2057
FDF_100	0.1364	0.0737	0.1322	0.5009	4.74e-10	1.9030
FDF_110	0.9022	0.0603	0.2057	0.5109	6.00e-08	0.7393
FDF_120	0.2987	0.1972	0.1713	0.5837	5.28e-06	0.6040
FDF_130	0.2884	0.1317	0.1401	0.4846	5.23e-10	0.3286

In table 5.7 the results for the distribution function comparison are shown. To emphasise good values in, they are coloured in green and bad values in red. In figure 5.8 the simulation results from table 5.7 are plotted in a chart.

Considering the figure 5.8, the smallest error overall (lowest bar height) regarding the Fabre run reference 400 data (table 5.1) has produced in simulation case FDF_100. But the physical behaviour of a multiphase flow is more complicated than choosing only the case with the smallest error. Especially the force balance between the phases determine the flow pattern, the velocity fields, as well as the pressure field. Hence the NWLD parameter has a special significance. If the NWLD is small, the simulated phase interface height is equal the interface height from the experiment. That indicates, that drag and non-drag forces nearby the interface in the simulation are approximately

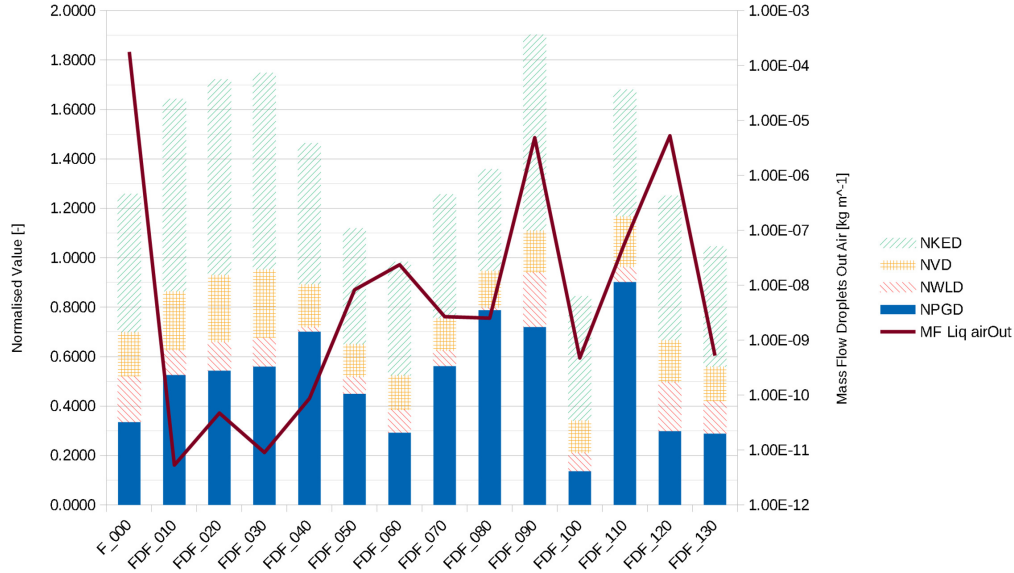


Figure 5.8: Fabre channel run reference 400 data (table 5.1) distribution function study; sum of normalised RMS kinetic energy, normalised RMS velocity, normalised water level and normalised RMS pressure gradient value for different simulation setups; figure by the author

similar to the values from the experiment. Regarding the NWLD minimum, the simulation case FDF_080 is the best. It seems that, when the force balance nearby the interface is close to the experiment, the simulated turbulence kinetic energy is close to the experiment too, see table 5.7.

The air/water separation is strongest in simulation case FDF_010, which correspond to the equilibrium distribution function. That is because of the large SMD. The same behaviour can be seen for cases FDF_020 and FDF_030 too, if one consider the average SMD and the liquid (droplet) mass flow at the air outlet. It is a plausible solution, because larger droplets have a larger inertia than smaller droplets and the air can carry rather more smaller droplets away to the air outlet.

Because of two minimum error values in table 5.7 and the overall minimum error presented in figure 5.8, the case FDF_100 is preferred.

5.4 Validation with Horizontal Channel Experiment

This validation based on the Fabre, Masbernat, and Suzanne (1987) run reference 400 data (table 5.1) experiment data, see table 5.1. As in the distribution function study a tetrahedral mesh size of 3.5 mm is used to ensure a good balance between computational effort and accuracy. In this study the simulation setup as described in section 5.1 is used, except the advection scheme. Due to better comparability an advection scheme with a constant blend factor is used. A constant blend factor of 0.75 is used. The blend factor of 0.75 means, that the first order advection is weighted with 25% and the second order advection is weighted with 75%. A complete second order advection solution was in some cases unstable. For comparability the reference simulation case in section 5.3 is included in this study.

In equation 3.57 a local time derivative is included. This time derivative is only available in transient simulations. Hence a transient U-RANS simulation is carried out to analyse the impact of the transient behaviour with the local time derivative in contrast to a steady state simulation. Here it should be examined whether it is possible to get steady state simulation values close to the experiment values, with a steady state simulation for a slightly transient simulation case.

Briefly a turbulence model impact is examined with a very large eddy simulation (VLES) and with a steady state BSL model simulation. It is assumed that the VLES give a better approximation of the velocity and pressure fields than a two equation model, whereby the BSL turbulence model simulation should be in between the VLES and two equation turbulence model simulation.

Due to different values for the high turbulence damping coefficient (HTC) in the literature, both values are tested.

The Sato advanced turbulence model is included in CFX as a Beta feature. Hence the behaviour of that turbulence transfer model will be tested.

Because of the completely unknown behaviour of non-drag forces in a steady state simulation, a simulation without non-drag forces is carried out. Here the impact on non-drag forces on the simulation result as well as the stability is of interest.

To determine the simulation results differences of a second order and 0.75 times second order simulation, a simulation with forced second order discretisation is carried out.

The AIAD model from HZDR is state of the art and tested well, though the blend coefficient is considered as a fitting parameter and it will be examined too.

Regarding the physical representation of a interface region, see figure 2.16, the question has been raised, whether it is not possible to leave out the free surface drag and IAD calculation and blend the droplet and bubble model with the corresponding volume fraction in this region. Hence one simulation is carried out with a blending procedure inside the free surface region between the droplet and the bubble model.

All other settings are equivalent to the mesh or distribution function study simulations.

Additional some simulation are carried out with different combination with the best particle distribution from section 5.3 and the above described parameters. These simulations have the aim, to find the best setup with the lowest error for this simulation case.

All validation simulation cases can be found in table 5.8.

The result values of normalised RMS pressure gradient deviation (NPGD), of normalised water level deviation (NWLD), of normalised RMS velocity deviation (NVD), of normalised RMS kinetic energy deviation (NKED) and of mass flow of liquid out of air outlet for all simulation cases in table 5.8, can be seen in table 5.9 and figure 5.9.

The analyses is comparable to the distribution function comparison and details can be seen in section 5.3.

Table 5.8: Fabre channel validation simulation cases overview

Case	Reference modification
F_000	Reference
FV_010	Sato advanced turbulence off
FV_020	7 equations BSL turbulence model
FV_030	blend droplet and bubble model in free surface region with volume fraction
FV_040	HTC 10
FV_050	HTC 100
FV_060	transient without local time derivative; Timestep=1e-3 s; 5 maximum inner iterations
FV_070	transient with local time derivative Timestep=1e-3 s; 5 maximum inner iterations
FV_080	switch off all non-drag forces
FV_090	switch off turbulence dispersion force for droplets
FV_100	VLES
FV_110	2nd order
FV_120	AIAD Blend Coeff 100
FV_130	$d'_{p,RRSB} = \sqrt{d_{p,max} d_{p,min}}$ 20
FV_140	$d'_{p,RRSB} = \sqrt{d_{p,max} d_{p,min}}$ 20; HTC 10
FV_150	$d'_{p,RRSB} = \sqrt{d_{p,max} d_{p,min}}$ 20; HTC 10; 2nd order
FV_160	$d'_{p,RRSB} = \sqrt{d_{p,max} d_{p,min}}$ 20; HTC 10; 2nd order; AIAD Blend Coeff 100
FV_170	$d'_{p,RRSB} = \sqrt{d_{p,max} d_{p,min}}$ 20; $n = 40$; HTC 10; 2nd order; switch off turbulence dispersion force for droplets
FV_180	$d'_{p,RRSB} = \sqrt{d_{p,max} d_{p,min}}$ 20; $n = 4$; HTC 100; 2nd order; switch off turbulence dispersion force for droplets
FV_190	$d'_{p,RRSB} = \sqrt{d_{p,max} d_{p,min}}$ 20; $n = 4$; HTC 10; 2nd order; switch off turbulence dispersion force for droplets
FV_200	$d'_{p,RRSB} = \sqrt{d_{p,max} d_{p,min}}$ 20; $n = 4$; HTC 5; 2nd order; switch off turbulence dispersion force for droplets
FV_210	$d'_{p,RRSB} = \sqrt{d_{p,max} d_{p,min}}$ 20; $n = 4$; HTC 50; 2nd order;

All values in table 5.9 are averaged over 5000 iterations for steady state simulations or four times the gas flow-through time for transient simulations, except the NWLD value. The NWLD value is only available in CFX Post and

Table 5.9: Validation results of average NPGD, NWLD, average NVD, average NKED and average liquid mass flow out of air outlet (MF Liq); Column minimum value coloured in green and maximum in red; Fabre channel run reference 400 data (table 5.1)

Case	NPGD	NWLD	NVD	NKED	error sum	MF Liq
	–	–	–	–	–	kg/s
F_000	0.7619	0.2151	0.1672	0.7460	1.8902	4.54e-05
FV_010	0.5237	0.1195	0.1839	0.4608	1.2879	1.73e-04
FV_020	0.8315	0.2205	0.1578	1.2840	2.4938	7.03e-05
FV_030	0.7663	0.2257	0.1804	0.7263	1.8987	1.83e-04
FV_040	0.7396	0.2179	0.1651	0.7660	1.8886	3.14e-06
FV_050	0.5104	0.1858	0.1766	0.5227	1.3955	3.97e-06
FV_060	0.7099	0.2168	0.1681	0.7534	1.8482	2.08e-06
FV_070	0.8124	0.2118	0.1696	0.7506	1.9444	1.10e-04
FV_080	0.8776	0.2045	0.1575	0.8136	2.0532	2.20e-08
FV_090	0.6866	0.2131	0.1672	0.7414	1.8083	1.64e-09
FV_100	0.1451	0.0319	0.3478	-	0.5248	7.71e-07
FV_110	0.3743	0.1486	0.1703	0.5757	1.2689	1.57e-05
FV_120	0.5372	0.1193	0.1747	0.5191	1.3503	1.96e-04
FV_130	0.3133	0.0777	0.1428	0.6617	1.1955	4.76e-13
FV_140	0.2715	0.1176	0.1377	0.6602	1.1870	6.59e-11
FV_150	0.1124	0.0584	0.1240	0.5057	0.8005	1.61e-10
FV_160	0.1144	0.0582	0.1243	0.5034	0.8003	1.79e-10
FV_170	0.1193	0.0574	0.1244	0.5011	0.8022	1.38e-10
FV_180	0.1255	0.0652	0.1425	0.7393	1.0725	6.30e-10
FV_190	0.1534	0.0627	0.1262	0.4732	0.8155	1.42e-10
FV_200	0.1413	0.0568	0.1261	0.4705	0.7947	9.89e-11
FV_210	0.0025	0.0943	0.1367	0.6280	0.8615	9.92e-09

can not be plotted during the simulation run and is therefore an instantaneous value. Instantaneous values are dependent on the current solution field at the specific iteration or time. Hence the NWLD value is more inaccurate than average values.

Sato Advanced Turbulence Model

With the Sato advanced turbulence model, an increased turbulence in the continuous phase is caused, see section 2.4.3. Hence it is to be expected,

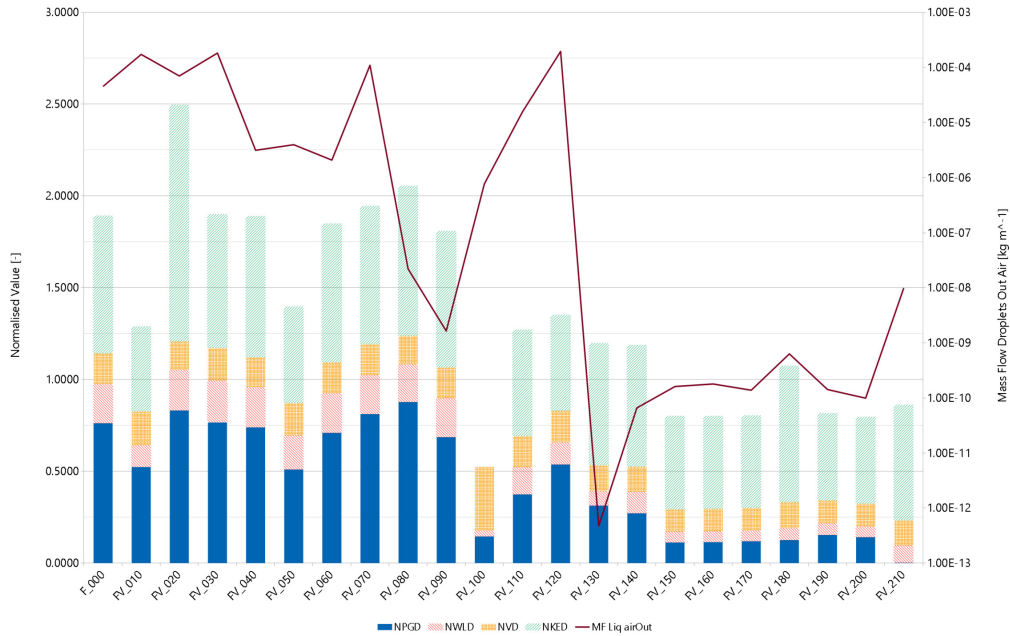


Figure 5.9: Fabre channel run reference 400 data (table 5.1) validation; sum of average normalised RMS kinetic energy, average normalised RMS velocity, normalised water level and average normalised RMS pressure gradient value for different cases; figure by the author

that the pressure drop in the gas phase is increased with this Sato model. This behaviour can be confirmed by the simulation, see in figure 5.9 the increased NPGD value of case F_000 compared to the case without the Sato turbulence transfer model FV_010. Interesting is the effect of the Sato model on the interface height. With the Sato model and thus a continuous fluid with increased kinetic energy, the water level is lower than without the Sato model. Which implies that in saturated flow regimes the turbulence of the lighter phase above the heavier phase have a strong impact of the force normal to the interface in gravity direction.

Despite of better results of the simulation case without the Sato model, the Sato model should be included in the simulation model, since without this Sato model a high droplet mass flow at the air outlet is produced. This is a result of a too high water volume fraction in the air flow above the water surface, see figure 5.10. That could be an effect of droplets with high kinetic energy

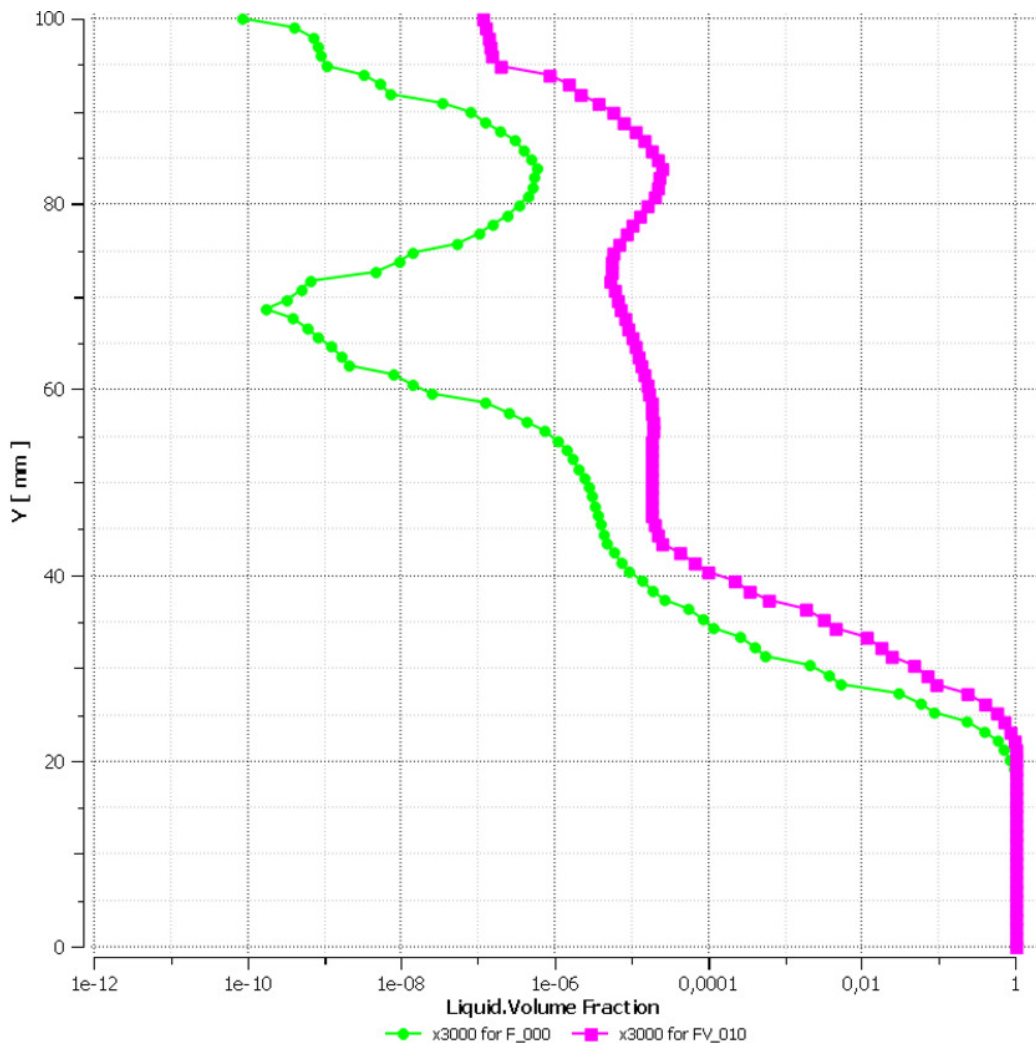


Figure 5.10: Fabre channel run reference 400 data (table 5.1) validation; Liquid volume fraction at $x = 3m$ above the channel height Y for case F_000 and FV_010; figure by the author

and so that with high droplet velocity. Droplets with high kinetic energy can be carried away better from the interface as with less kinetic energy. This yields to an increased volume fraction of water above the interface. With the Sato model, more momentum is needed of the carrier phase air to carry droplets to the air outlet than without the Sato model.

The separation of both fluids are more important for vertical flow pattern. If the separation worse, the flow pattern like slug flow or churn flow do not

occur or only at a wrong volume fraction ratio. Thus in such an intermittent vertical flow a wrong pressure drop is the result. In a horizontal saturated flow this separation is less important. The phase separation in a horizontal flow becomes only again more important for an annular flow.

Turbulence Model

The BSL Reynolds stress turbulence include the effects of "streamline curvature, sudden changes in the strain rate, secondary flows or buoyancy compared to turbulence models using the eddy-viscosity approximation" (Ansys (2016b)). Such secondary flows and free shear flow with strong anisotropy also occurs in the Fabre experiments flow pattern. But except the NVD value the BSL model have increased errors, see table 5.9. Especially the NKED value is too high in the BSL simulation, that this simulation is the worst overall. In the bubble region the kinetic energy has particularly large deviations with the BSL model, see figure 5.11.

Due to the high computational effort and the worse simulation results, the BSL Reynolds stress turbulence model is discarded and the SST turbulence model is preferred.

In general the Large Eddy Simulation (LES) should compute the turbulence more accurate and hence the SMD approximation should be better, see section 4. Hence with a LES the deviation of a steady state SST turbulence model should be figured out.

The LES is applied on a coarse RANS mesh with the wall function approach, which then called Very Large Eddy Simulation (VLES). The mesh which is used in the steady state reference case F_000 is used for the VLES case FV_100 also. Like in the other transient simulations, the Courant number is about 1.5 in the VLES too. To calculate the relative fluid acceleration, the local time derivative is included, like in case FV_070.

The momentum imbalances in case FV_100 are always between +/- 1 %, but the mass imbalances fluctuate in between -30 % and 30 %, but the average is 0. Despite of the same mesh and Courant number the convergence of the

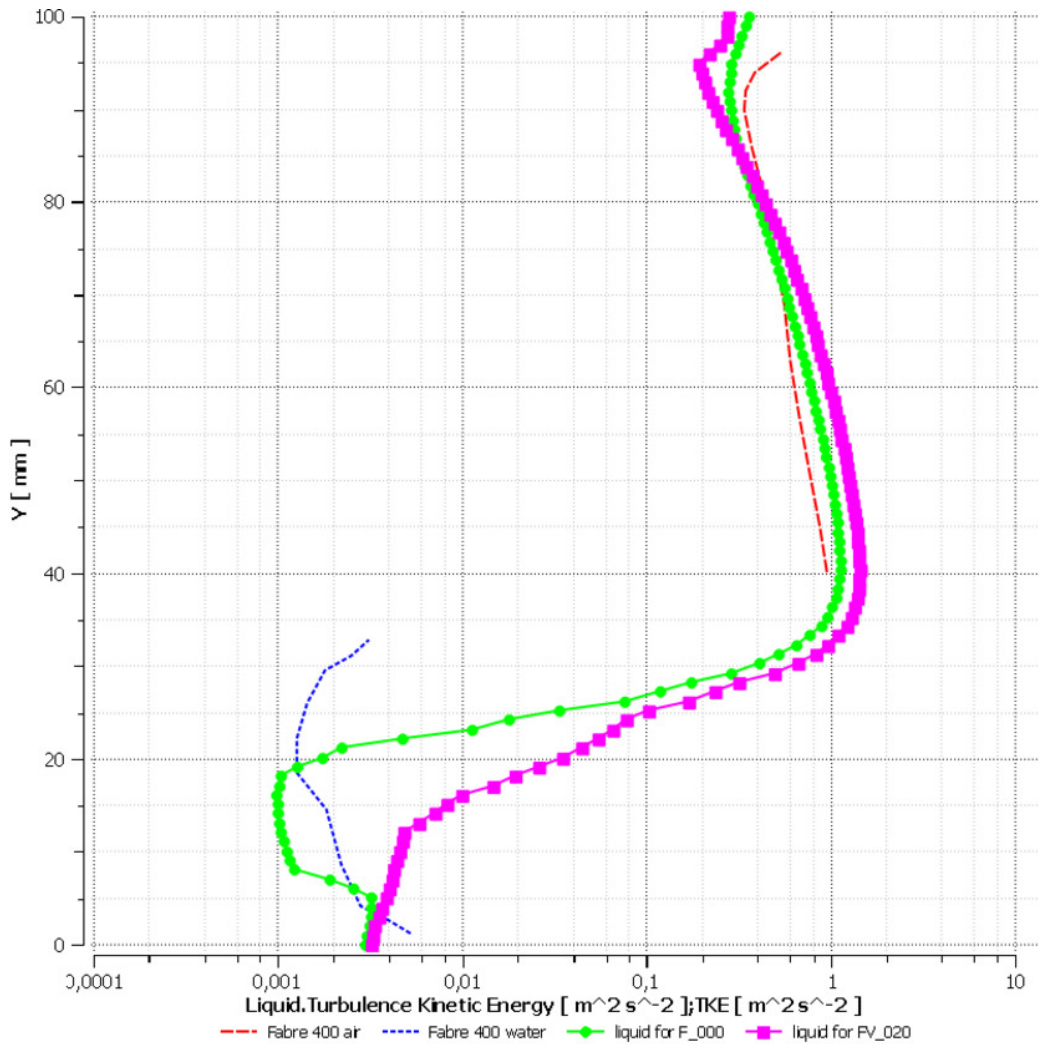


Figure 5.11: Fabre channel run reference 400 data (table 5.1) validation; Kinetic energy at $x = 3\text{m}$ above the channel height Y for case F_{000} and FV_{020} ; figure by the author

pressure field is much slower for the VLES than cases FV_{060} and FV_{070} . The VLES simulation takes about 7.5 times of the simulation time compared to the case F_{000} .

In Fabre, Masbernat, and Suzanne (1987) one can see, that the Fabre reference 400 flow is wavy stratified. The case FV_{100} is the only of all cases in table 5.8, which results to a wavy stratified flow pattern, with a wave length about some 1-5 cm. Whereby the others simulation are rather only a

stratified flow, with a wave length about 1 m. The waves in the VLES could be one of the reasons for the longer convergence.

In figure 5.9 it can be seen, that the VLES case FV_100 has the lowest error overall. Due to the small NWLD and NPGD value of case FV_100 it is assumed, that the forces on the interface are close to the experiment. But the VLES have the worst value for the NVD, see table 5.9. This is probably due to the coarse mesh, because the velocity deviation in the VLES case is more in the droplet region with higher velocities, see figure 5.12. In the water region the VLES simulation results are closer to the Fabre, Masbernat, and Suzanne (1987) results and better than the SST turbulence model velocities. The VLES simulation has a smaller droplet mass flow at air outlet, which reinforces the assumption, that the SST turbulence model have an increased phase diffusion.

Despite of the coarse mesh the VLES showing good results for the pressure drop and phase distribution. Also the VLES is the only simulation which shows a wavy stratified flow. But due to the multiple simulation time compared to a steady state SST simulation, it would take too much time for a large industrial application like a steam drum for the current situation. But with increasing cpu power in future, the VLES could be a good choice for larger applications too.

Free Surface Particle Model

Like mentioned above, the question has occurred, whether it is not possible to replace the drag and IAD calculation for the free surface region and blend the bubble and droplet results with the volume fraction in this region.

Except the droplet mass flow rate at air outlet, all error values are close to the Reference case. The different mass flow is caused by an increased momentum transfer at the interface. This increased momentum transfer can be seen in figure 5.13 at $y = 25$ mm. In this figure the Interface Area Density (IAD) times the drag coefficient (CD) is shown. In equation 2.52 one can see, that the interface drag is increased, if $IAD \cdot CD$ is increased too.

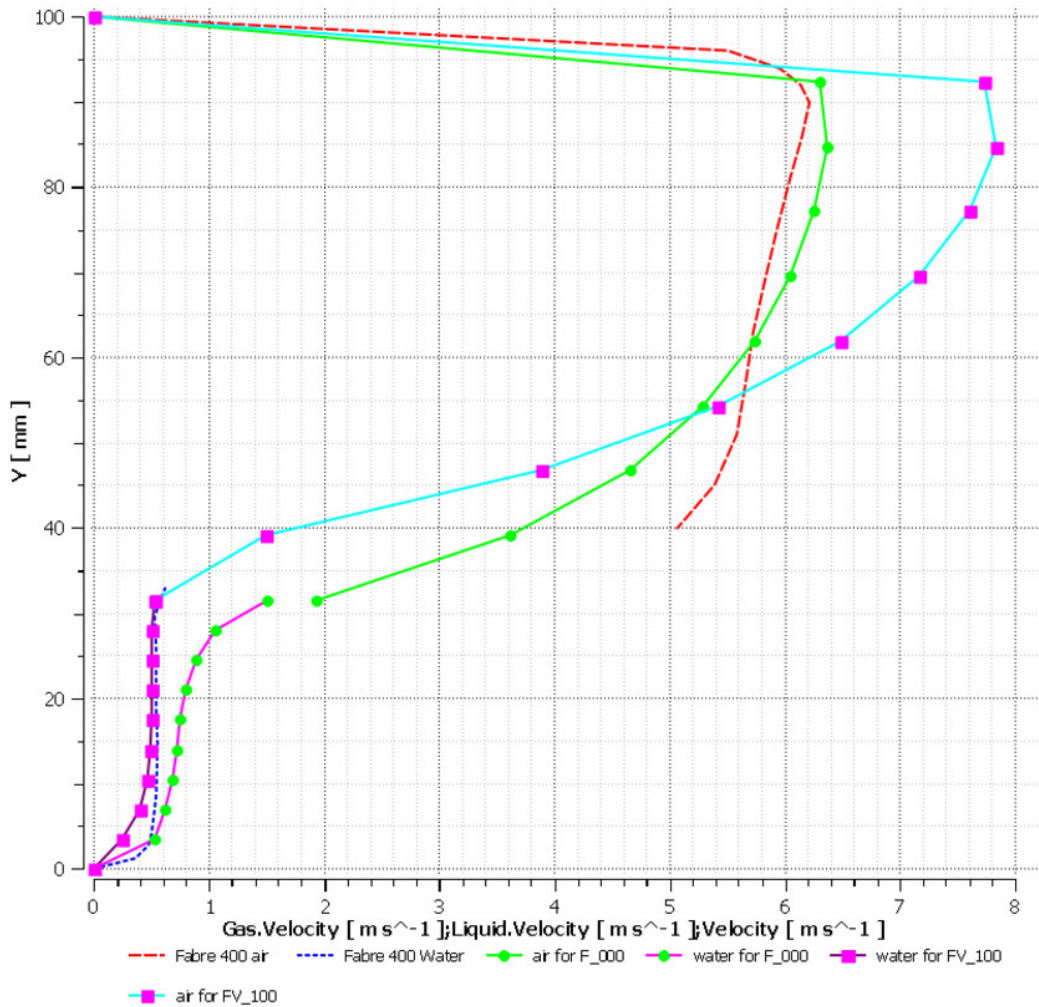


Figure 5.12: Fabre channel run reference 400 data (table 5.1) validation; Velocity at $x = 3\text{m}$ above the channel height Y for case F_000 and FV_100; figure by the author

With this increased momentum drag for case FV_030 the water is pushed stronger against the outlet wall. Therefore more water is redirected to both outlets. Thus the droplet mass flow at air outlet is higher for case FV_030.

The difference IAD and CD values in case FV_030 is a direct result of the replaced free surface model. Hence it is recommended to use the free surface model to calculate the IAD and CD values for the interface region.

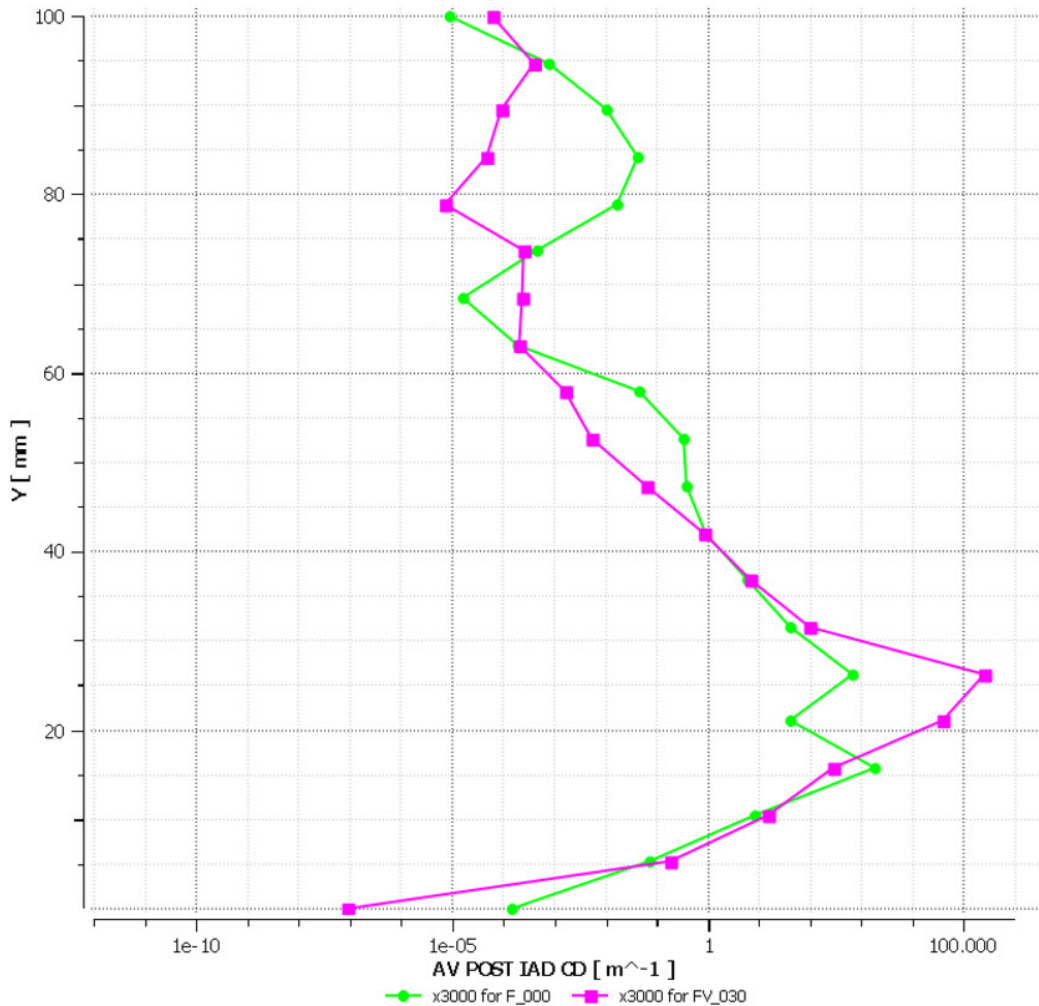


Figure 5.13: Fabre channel run reference 400 data (table 5.1) validation; IAD times CD at $x = 3\text{m}$ above the channel height Y for case F_000 and FV_030; figure by the author

High Turbulence Coefficient Examination

On the one side Porombka and Höhne (2015) recommend a High Turbulence Coefficient (HTC) of about 100. On the other side Ansys (2016d) has a default value of 10. Hence both HTC values will be tested with the Fabre experiment simulation.

The HTC value increase or decrease the turbulence damping in the free surface region, see section 2.4.3. The turbulence damping caused a increasing

ω -value of each phase. Thus the kinetic energy is decreased in this region, see figure 5.14, if the HTC value is increased.

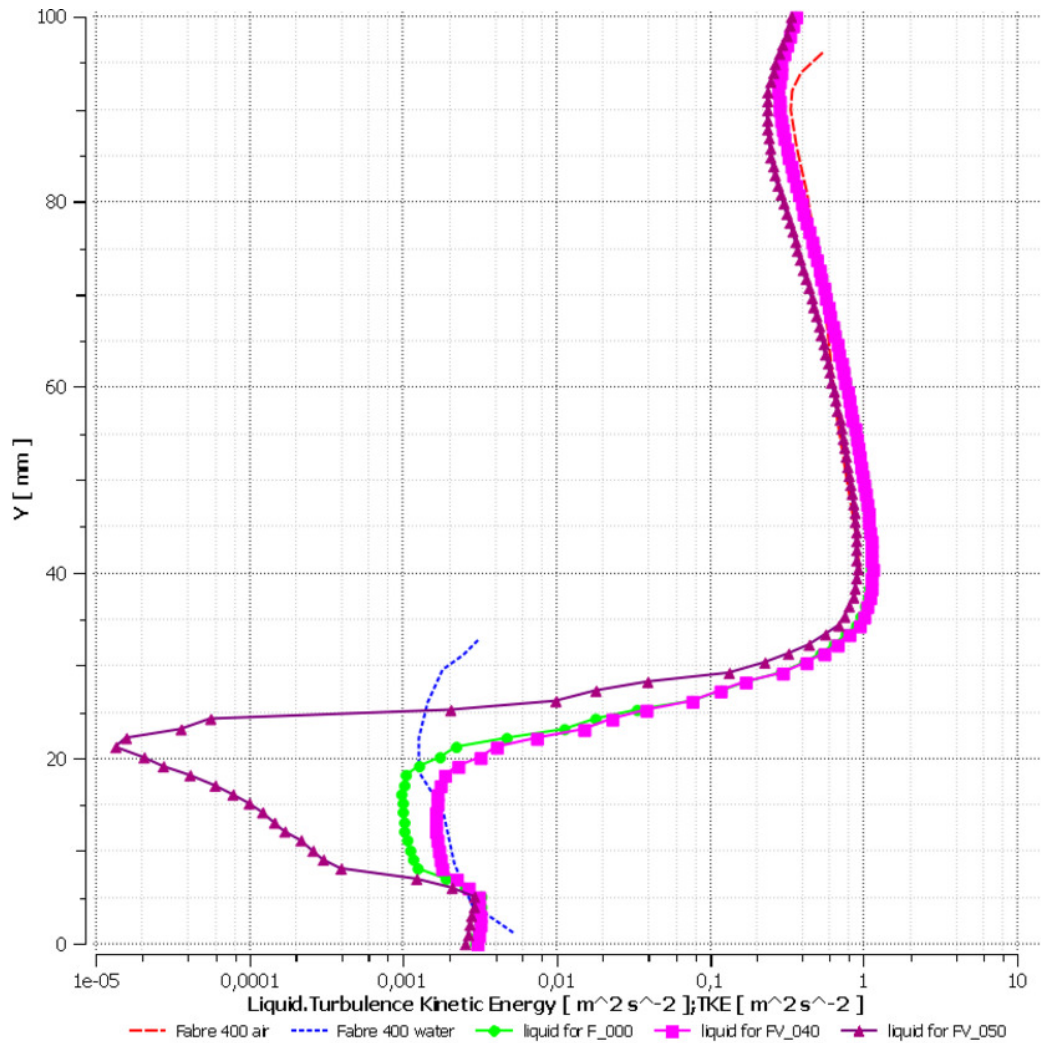


Figure 5.14: Fabre channel run reference 400 data (table 5.1) validation; Kinetic energy at $x = 3\text{m}$ above the channel height Y for case F_000, FV_040 and FV_050; figure by the author

Despite of the large visual deviation of the kinetic energy regarding the case FV_050, this case has the low NKED value. Also the most error values of case FV_050 are smaller than cases with lower HTC values. Thereby the overall error of case FV_050 is the smallest compared to F_000 and F_040. Hence a HTC value of 100 is recommended, but the large kinetic energy

deviation in the water phase is considered critical.

Transient Impact

In general the transient simulations are running 4 times longer than the steady state simulation. The mass and momentum imbalances are below 1%, to ensure stable simulations. The momentum imbalance condition can be satisfied with a Courant number of about 1.5 for the transient simulations, whereby the case FV_060 have much larger mass imbalances than case FV_070, at the same Courant number. In this simulation the drag coefficient depends indirect on the time derivative. This latter cause an error in Ansys CFX. In section 5.1.5 a solution for this CFX error is presented.

In table 5.9 one can see, that the transient simulations FV_060 and FV_070 are close to the reference. Especially the NVD and NKED values are close to each other. The main difference between these simulation cases is the droplet mass flow out of air outlet. The largest droplet mass flow is at case FV_070 and the smallest at case FV_060. The Reference case lies in between. This droplet mass flow behaviour can be explained with figure 5.15.

At Y-value = 100 mm there is the top wall of the channel. Nearby the end of this top wall there is the air outlet. If the drag force increased at the top wall, the water film at this wall is pushed away from the air. Hence the mass flow of droplets at air outlet is increased. In figure 5.15 one can see high drag forces for the case F_000, medium drag forces for FV_070 and the lowest drag forces for the case FV_060 nearby the top wall. This correspond to these different droplet mass flow rates in table 5.9.

We can assume that transient simulations are more accurate than steady state simulations, because the steady state is one special case of a transient simulation without local temporal changes. Then we can suppose that the steady state simulation over predict the drag force in the droplet region, see 5.15. Hence a too high droplet mass flow can be expected, see equation 2.52. And the steady state simulation under predict the drag force nearby the bottom wall in the bubble region, so that less bubbles are carried away nearby the bottom wall. But due to the low liquid volume fraction in the droplet

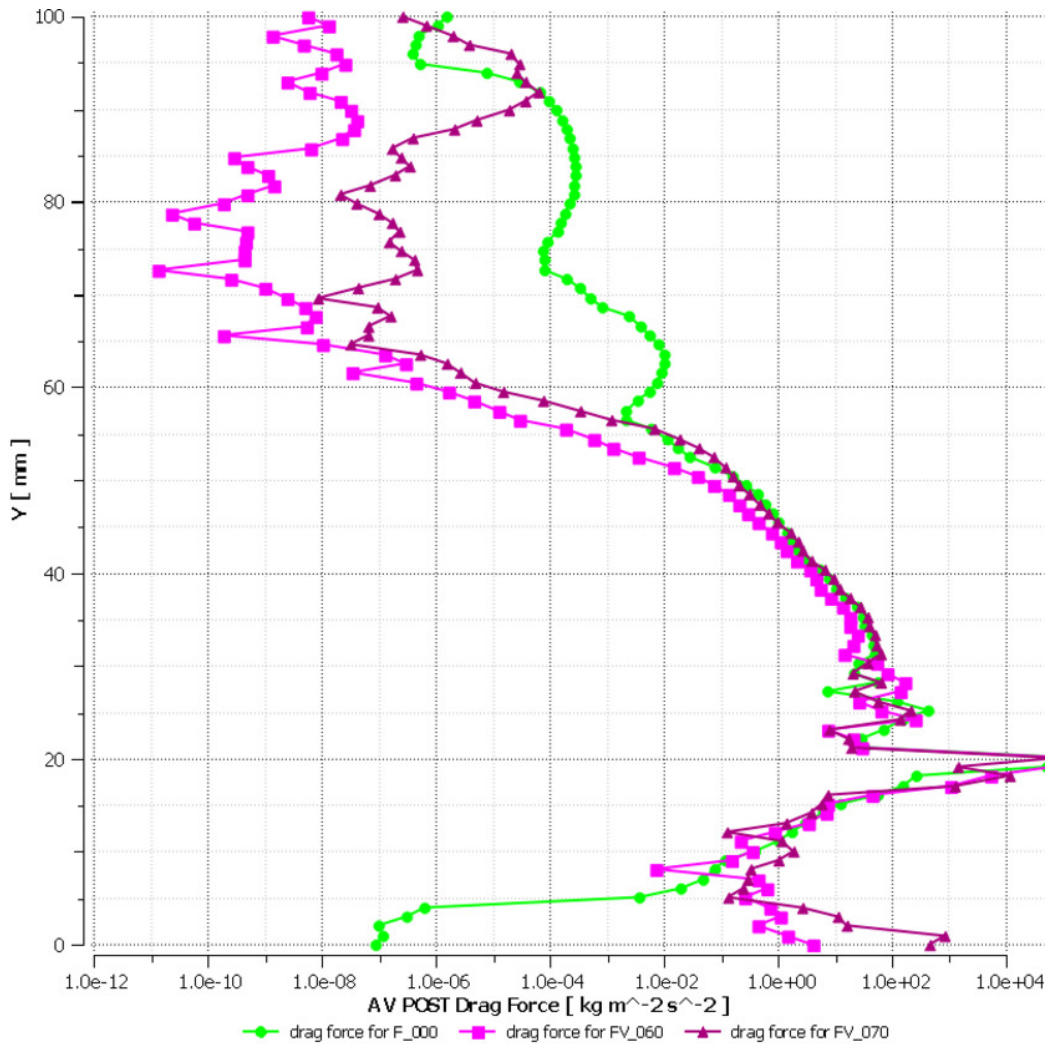


Figure 5.15: Fabre channel run reference 400 data (table 5.1) validation; Drag force at $x = 3\text{m}$ above the channel height Y for case F_000, FV_060 and FV_070; figure by the author

region and low gas volume fraction in the bubble region, the impact of these different drag force curve shapes in these simulations is small regarding the NPGD, NVD and NKED values. This over predicting drag force is caused by a too high IAD which can be seen in figure 5.16, what is again a result of too high liquid volume fractions in the droplet region, see figure 5.17. The relation between IAD and volume fraction for the particle model can be seen in equation 2.38.

Only regarding the phase distribution there are differences between the steady state and transient simulation. Hence it could be possible to correct the IAD or CD value for a steady state case, in order to achieve good results and a decreased computational time at the same time.

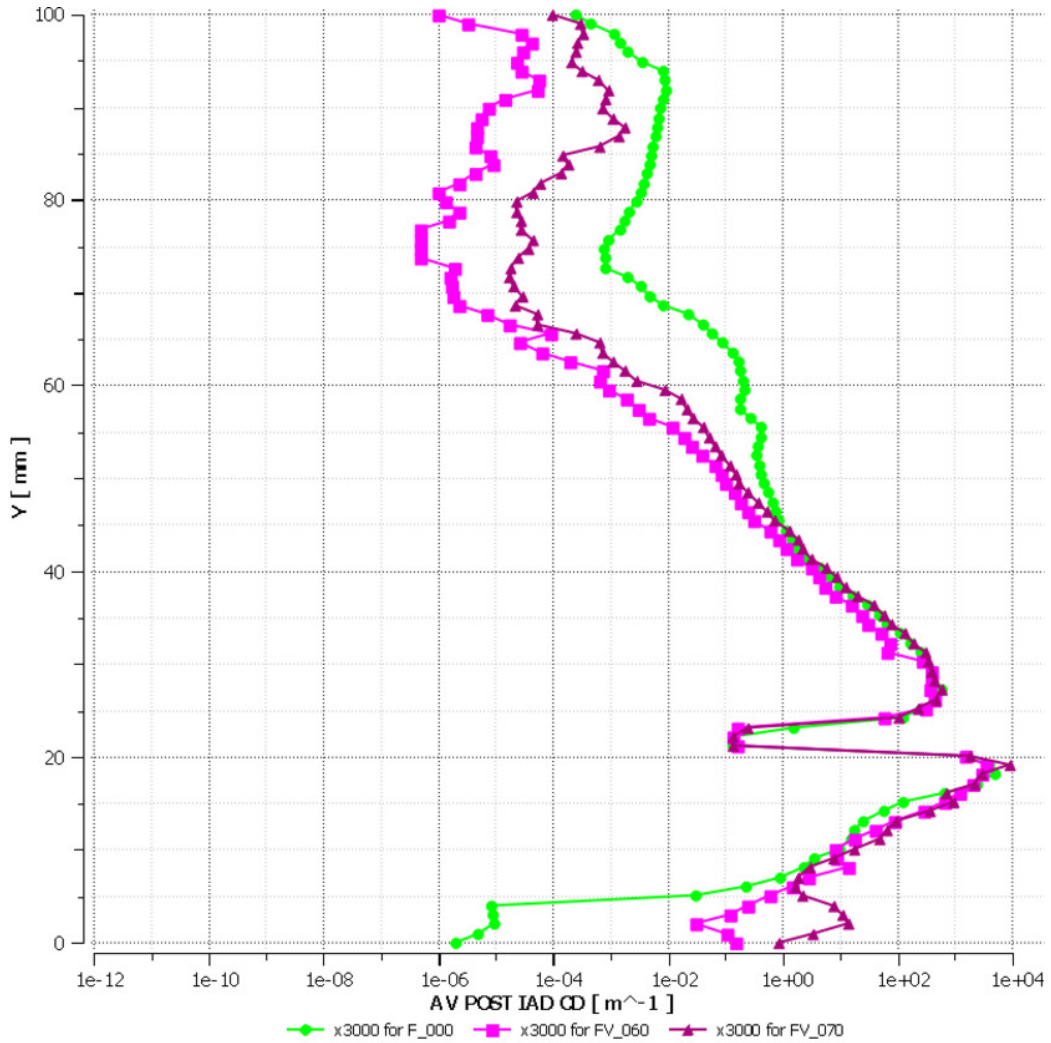


Figure 5.16: Fabre channel run reference 400 data (table 5.1) validation; Interface area density times drag coefficient at $x = 3\text{m}$ above the channel height Y for case F_000, FV_060 and FV_070; figure by the author

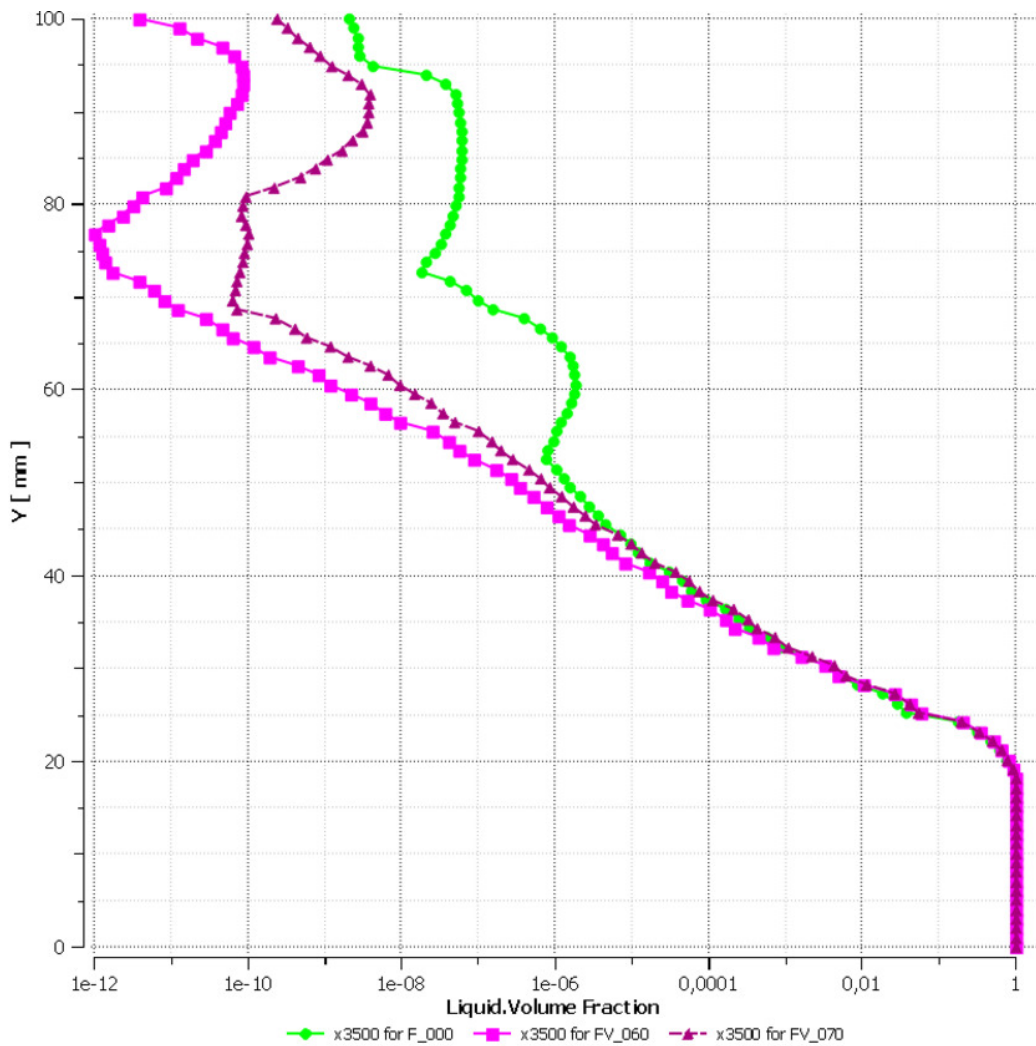


Figure 5.17: Fabre channel run reference 400 data (table 5.1) validation; Liquid volume fraction at $x = 3m$ above the channel height Y for case F_000, FV_060 and FV_070; figure by the author

Impact of Non-Drag Forces

In figure 5.9 it can be seen, that the simulation cases FV_080 and FV_090, which have different non-drag forces than the case F_000, the overall error do not differ so much. The evident difference is the droplet mass flow out of air outlet.

Consequential the non-drag forces increase the droplet transport transverse

to the flow direction. The turbulent dispersion force causes particles from regions of high concentration to low concentration, see section 2.5.3. Hence this force cause mainly a high droplet mass flow at air outlet. In figure 5.9 it can be seen, that the droplet mass flow at air outlet is significantly decreased, if the turbulent dispersion force is switched off for the droplets.

Second Order Advection Scheme

In general the error decrease faster for a second order advection scheme than a first order for more and more smaller cell sizes. So it is recommended to use the second order scheme. But at some simulation model combinations the solution is unstable, why a blending factor of 0.75 between first order and second order is used. With this blending factor of 0.75 all the simulations are run stable. For the reference case F_000, it is possible to run with the second order scheme. The second order case FV_110 have a decreased error for the NPGD, the NWLD and the NKED value. Though both NVD and droplet mass flow at air outlet values are closed together. Hence the overall error of the second order scheme case is smaller than the reference case, see figure 5.9. Hence it is recommended to use the second order advection scheme if possible.

AIAD Blend Coefficient

In the literature the recommended AIAD blend coefficient is 50. But no parameter study can be found that examine this blend coefficient. In case FV_120 the AIAD blend coefficient is increased to 100. This latter has a positive effect on the NPGD, NWLD and NKED value. This is mainly an effect of the decreased drag force nearby the interface, see figure 5.18.

The NVD value is slightly worse but the droplet mass flow at air outlet is much higher. Due to the increased blend coefficient the diffusion of the droplets from the interface is stronger, so that more water is carried away by the air, see figure 5.19.

A final statement can not be made, whether it is better to use an AIAD blend coefficient of 50 or 100. Hence in the following combination of the

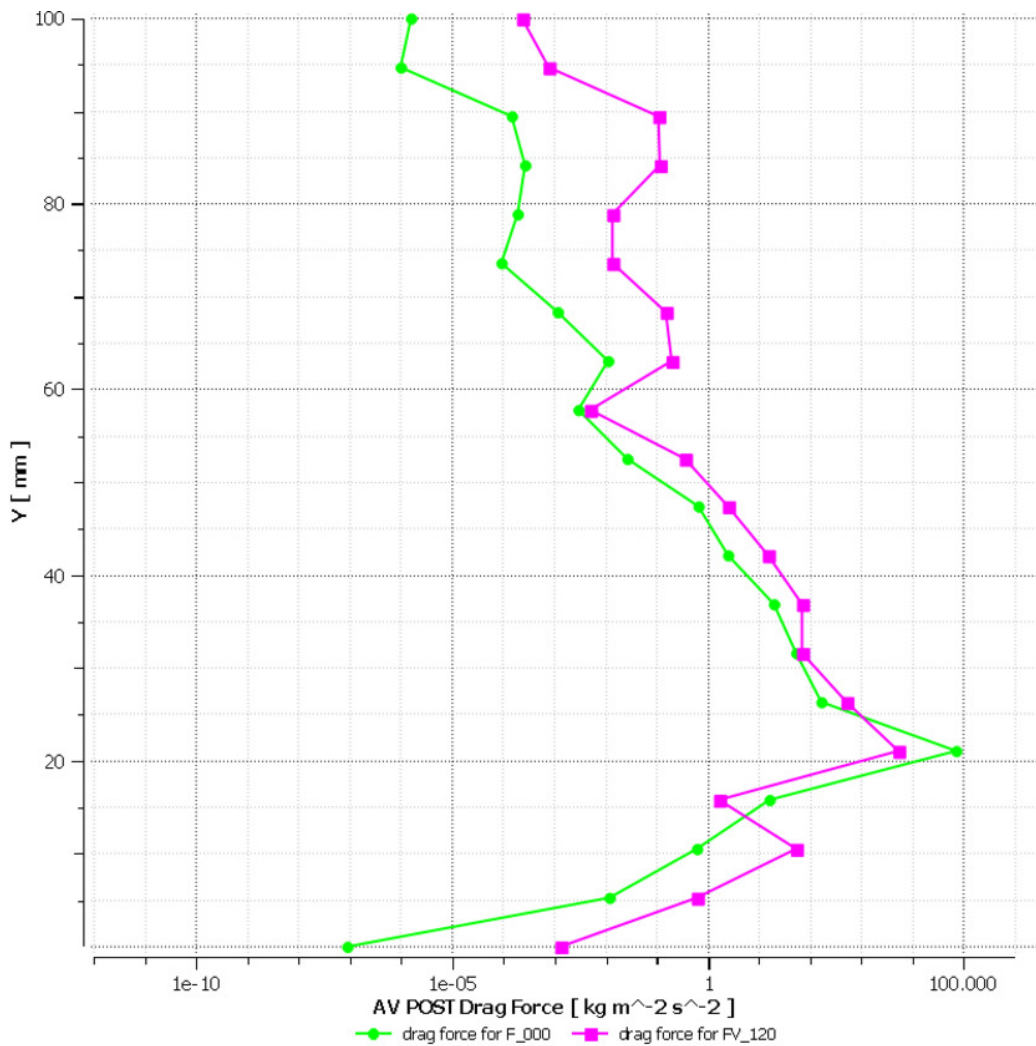


Figure 5.18: Fabre channel run reference 400 data (table 5.1) validation; Drag force at $x = 3\text{m}$ above the channel height Y for case F_000 and FV_120 ; figure by the author

above examined parameter this blend coefficient should be examined in more detail.

Combinations

Following simulations are combinations of the distribution function study results and first results of the validation simulations. Here it is tried to find a good combination of the distribution function, solver and model parameters,

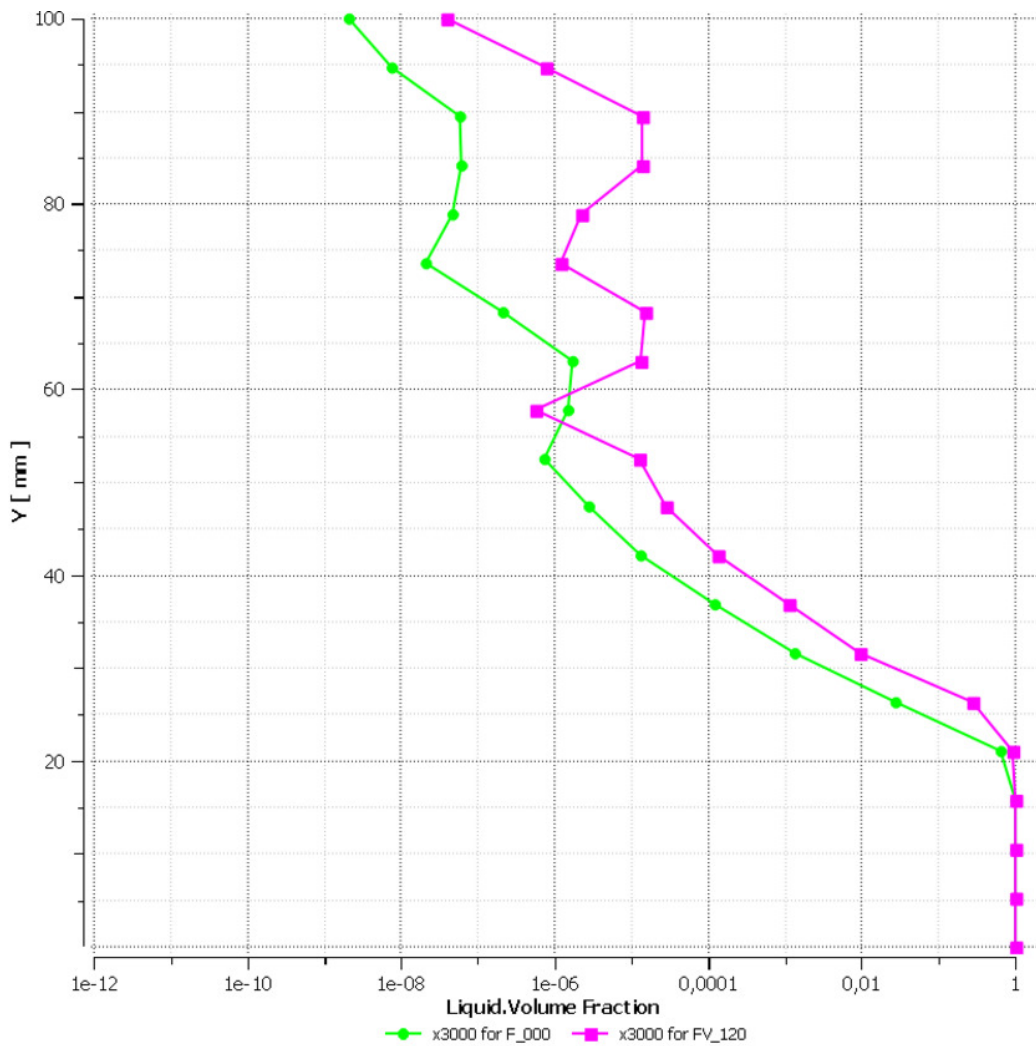


Figure 5.19: Fabre channel run reference 400 data (table 5.1) validation; Liquid volume fraction at $x = 3\text{m}$ above the channel height Y for case F_000 and FV_120; figure by the author

as well as models itself.

From the distribution function study two cases are preferred, see section 5.3. Both cases have a SMD correction factor of 20 overall, but in one of these cases a RRSB shape value of $n=40$ is used and in the other case the RRSB shape value is $n=4$. Both cases are used in the following combinations, see table 5.8.

Keep in mind, that the constant specific blend factor of 0.75 for the advection

scheme is used in the validation study, but the High Resolution model for the advection scheme in the distribution study. Hence case FV_130 and case FDF_080 differ in that point, despite otherwise equal setup.

If we consider all cases with a RRSB shape value of $n=40$ and a SMD geometric mean correction factor of 20, cases from FV_130 to FV_160, we can see that these cases have the strongest phase separation. This strong phase separation is caused by larger particles due to the SMD correction factor, which also can be seen in the distribution study in table 5.7. This statement applies to all cases with larger SMD values. Through additional setup modifications, this effect can be enhanced or reduced, see figure 5.9.

For example a increased HTC value should be reduced the overall error with only a slightly change in the droplet mass flow at air outlet, see paragraph [High Turbulence Coefficient Examination](#). But in case FV_140 it can be seen, that with a decreasing HTC value the simulation errors are decreasing too. Only the phase separation is worse with a decreasing HTC value, what can not be verified in paragraph [High Turbulence Coefficient Examination](#). It may be that some models counteract this decreasing HTC value effect.

There are some positive effects if a second order advection scheme is used, how is described in paragraph [Second Order Advection Scheme](#). This positive effect can be seen in case FV_150 too. Hence the overall error is decreased with a second order advection scheme. Only the mass flow of droplet at air outlet is increased.

As described in paragraph [AIAD Blend Coefficient](#), a AIAD blend factor of 100 reduce the overall error but leads to an increased droplet mass flow at air outlet. In case FV_160 an AIAD blend coefficient of 100 is used, but all differences compared to case FV_150 are go down in the numerical noise. Hence a further analysis of this blend factor is not recommended.

The significantly reduction of the droplet mass flow at air outlet without the Turbulent Dispersion Force (TDF) for the droplets can not be validated with the case FV_170. All differences of cases FV_150 and FV_170 are in the numerical noise. Hence the TDF can be calculated or not for a horizontal separated flow.

Case FV_180 to FV_210 showing the error differences, if the HTC value is changed. When one compare the overall error, it can be seen, that case FV_200 is the simulation with the lowest error, even for all cases in table 5.9.

According to table 5.9 the overall error of cases FV_150, FV_160, FV_170, FV_190 and FV_200 are close together. But case FV_200 has from the latter best cases the smallest droplet mass flow at air outlet. Hence the recommended case in this validation is FV_200.

5.5 Fabre Conclusion

In chapter 3 a new general simulation model is developed, in order to simulate a two-phase flow without the use of global parameters, like pipe diameter. This new model should be fast and robust in order to be applied to large industrial applications. In section 5.2 the impact of the mesh size to the new model is analysed. In the mesh study the normalised pressure gradient deviation (NPGD) is used to examine the mesh independency. Smaller tetrahedra sizes than 3.5 mm causes no large NPGD value deviations. But only from a tet size of 1.75 mm the NPGD error is smaller than 1 % and is recommended.

With the knowledge of the mesh study, a distribution study is carried out. In section 5.3 the best performance is achieved by cases FDF_080 and FDF_100. Later cases are uses the RRSB distribution function with a Sauter mean diameter correction factor of 20.

Due to the complexity of this new simulation model additional simulation are necessary, in order to examine the behaviour of the individual submodels. For this purpose a validation is carried out in section 5.4, where first the impact of the submodels is examined. Afterwards the submodels are modified and combined to reduce the overall error. Here the error could be decreased again. The best combination of submodels is case FV_200. But the error in cases FV_150, FV_160, FV_170 and FV_190 are close to the case FV_200.

Chapter 6

Proof of Concept with Vertical Test Case

Like mentioned in the introduction in section 5, the predominant flow pattern in a steam drum is a stratified flow. But in the feeding pipes of a ERK steam drum, there are some regions with vertical flow pattern. The goal of this thesis is to develop a two-phase simulation model for industrial applications like steam drums, which is independent of the geometry. Hence the vertical flow regimes should be take into account too. Hence subsequently the simulation model was tested for horizontal flows, a proof of concept for a two-phase flow for a vertical pipe is carried out. So this new two-phase model is tested for a broader range of multiphase flow regimes.

The proof of concept test case is the [Hewitt and Owen \(1987\)](#) experiment. In order to compare the results from the horizontal test case, the physical set-up of validation case FV_190 is used in this chapter. For the specific values see section 5.1.3 and table 5.8. Only the different material parameter, see table 6.1, will be changed in those following simulations. The case FV_190 was preferred to case FV_200, because FV_200 yields to unstable simulations sometimes.

6.1 Hewitt Model

In Hewitt and Owen (1987) one can see the complete description of the vertical two-phase flow experiment. The goal of this experiment from Hewitt and Owen (1987) is to predict a fully developed flow in a uniform vertical pipe. The vertical pipe has a 31.8 mm inner diameter and its total length is 23 m. This long pipe ensures a development length of about 570 diameters. The scheme of the experiment set-up can be seen in figure 6.1.

Hewitt and Owen (1987) use air and water as fluids, which corresponds to the Fabre experiment fluids in section 5.1. In this experiment the water mass flux is constant and the air mass flux is increased. In table 6.1 there are the constant parameters of this experiment.

Table 6.1: Hewitt vertical pipe experiment constant parameter; Hewitt and Owen 1987

Water mass flux	297.1 kg/(m ² · s)
Water density	998.5 kg/m ³
Air density	2.9 kg/m ³
Water dynamic viscosity	0.001 Pa · s
Air dynamic viscosity	0.000018 Pa · s
Surface tension	0.0726 N/m

Hewitt and Owen (1987) measure the pressure gradient between the pressure taps in figure 6.1. Furthermore informations about the observed flow pattern is given. The air mass flux is in range of 2.96 to 161.69 kg/(m² · s), which correspond to bubble flow pattern up until annular flow pattern. The pressure gradient and observed flow for two crucial cases can be seen in table 6.2. This restriction to two cases can be done, because mainly bubble and slug flows could be observed in the steam drum experiment in section 7.1.

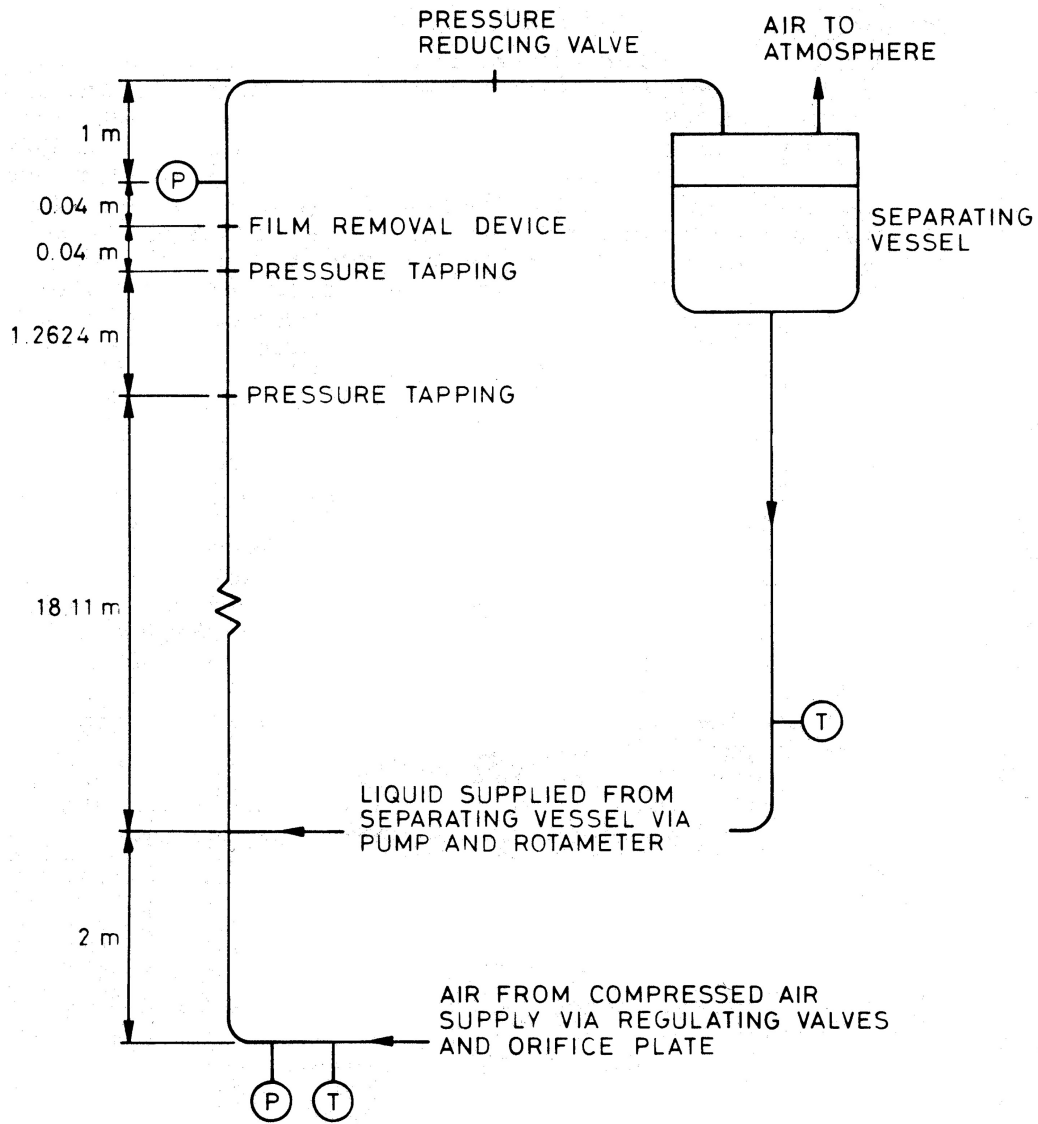


Figure 6.1: Hewitt and Owen (1987) experiment set-up scheme; see Hewitt and Owen 1987

Table 6.2: Extract of Hewitt vertical pipe experiment results; observed flow regime and pressure gradient; Hewitt and Owen 1987

Run No.	Air mass flux [kg/(m ² · s)]	Pressure gradient [Pa/m]	Observed flow regime
1	2.96	9489.0	Bubble
6	8.50	2876.0	Slug

6.1.1 Hewitt CFD Geometry and Mesh

The Hewitt and Owen (1987) experiment is a about 20 m long vertical pipe with a inner diameter of 31.8 mm. In earlier examinations it was tried to reduce the computing time with a quarter and a half part of the vertical pipe compared to a full pipe. In the quarter and half part pipe simulations, the observed flow pattern disagree with the observations of Hewitt and Owen (1987). Only the full pipe simulation show the approximate flow pattern like in the experiment. Hence the computing time can only decreased by a reduction of the pipe length. Therefore only a straight pipe length of 9 m is used in the CFD model, see figure 6.2.

The measure points to calculate the pressure gradient are at the centreline at 7 m and 8 m from the inlet. So that the CFD simulation model have a shorter development length of about 220 diameter than in the experiment.

The mesh consists of parts with hexahedral and tetrahedral cell elements, see figure 6.3.

The outlet box consist of tetrahedral elements. Hexahedral elements can not be used for this section, due to the transition of the pipe to the outlet box.

Due to the rotationally symmetry of the pipe section a 2D mesh can extruded from a start face to a target face of this section. The extrusion length of one step is 12.2 mm.

The start face is the inlet of the pipe, see figure 6.4. This face consist of 3.5 mm large 2D quadrilateral cell elements.

The 3.5 mm size has been taken from the Fabre mesh study, see section 5.2. The three boundary layers are adjusted, that the wall y^+ value is about 30.

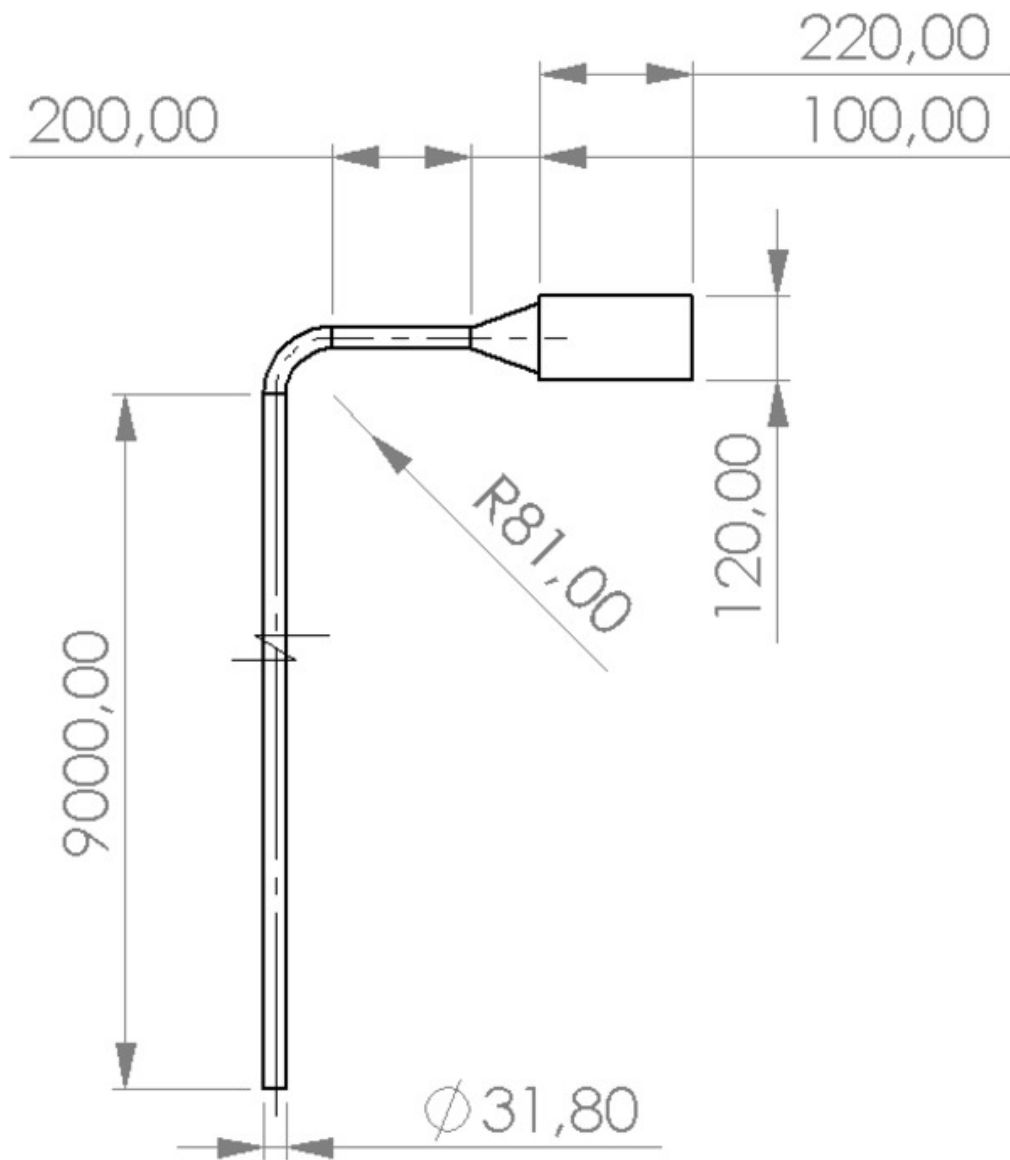


Figure 6.2: Hewitt CFD model drawing with dimensions; figure by the author

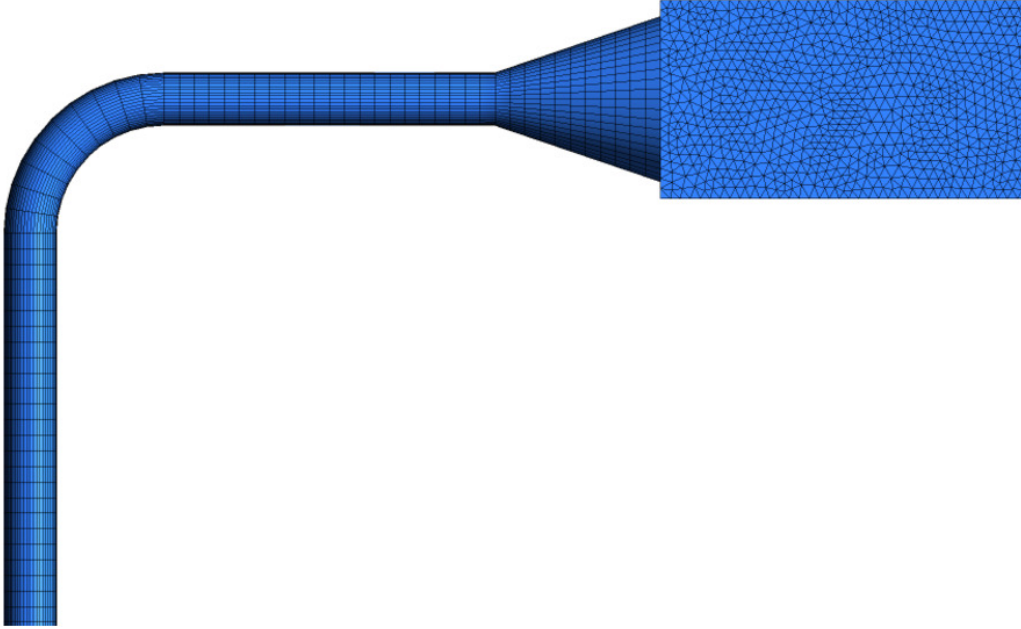


Figure 6.3: Hewitt CFD model; surface mesh; figure by the author

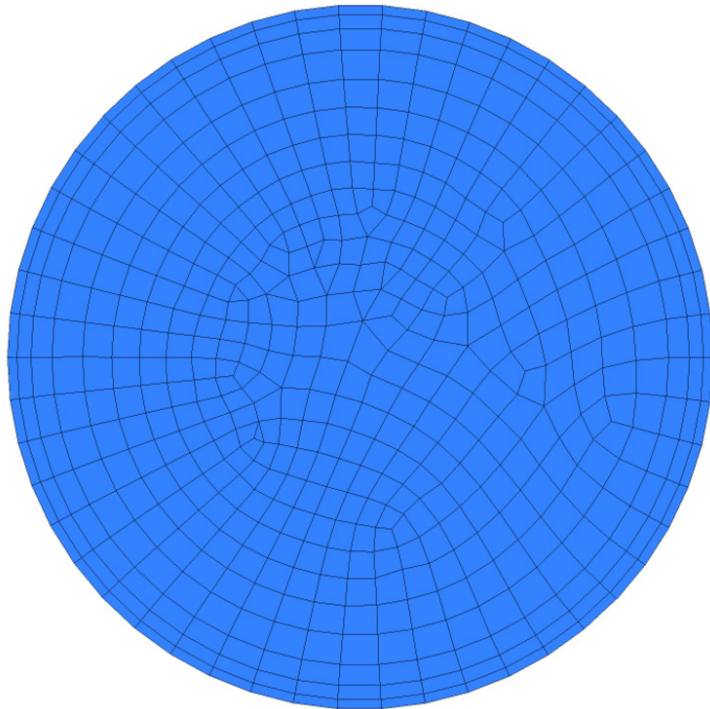


Figure 6.4: Hewitt CFD model; 2D mesh at inlet; figure by the author

6.1.2 Hewitt Boundary Conditions

An overview of the boundary conditions of the CFD model can be seen in figure 6.5.

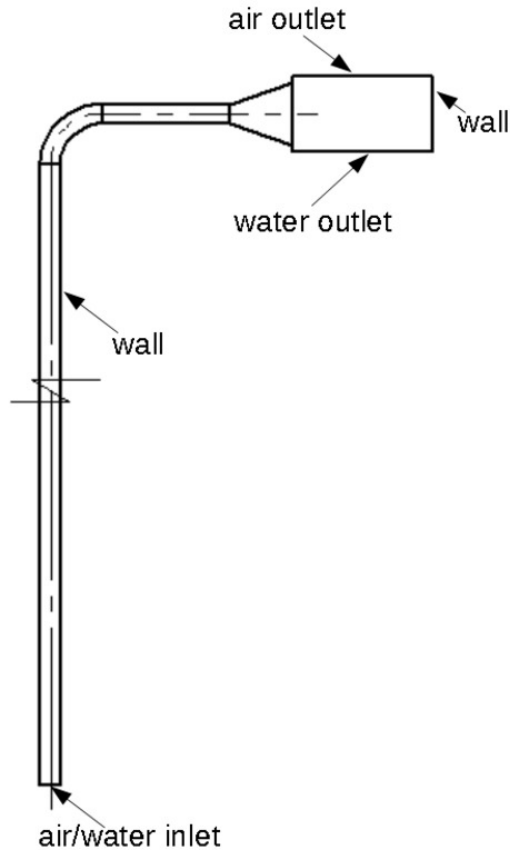


Figure 6.5: Hewitt CFD model; boundary conditions; figure by the author

The inlet condition of this model is changed compared to the experiment. In the CFD it is easier to model a two-phase inlet. Due to this the pipe can be shortened by 2 m, see figure 6.1 and 6.5. The air and water mass flux will be converted with the inlet area to a mass flow. With the corresponding densities the inlet volume fractions can be calculated. The mass flows and the volume fractions are used as input parameter for the inlet boundary condition. The mass fluxes and densities are shown in table 6.1 and 6.2. The air and water outlets are modelled in the same way as the Fabre CFD model, see section 5.1.2. But in this simulation the arbitrary hydrostatic

pressure height is set to 5 mm. Also the wall boundary condition is like in Fabre model, smooth walls with a wall contact angle of 65°.

6.1.3 Hewitt Initial Conditions

The volume fractions on the inlet are calculated in section 6.1.2 and are used for the initial condition. In preliminary simulation it could be seen, that the water hold-up in the pipe is higher than the inlet water fraction. Hence the volume fraction for the the water phase is doubled for the initial conditions and the air volume fraction is the difference from the water volume fraction to one. The simulation instability is increased, if the initial air/water mixture is initialised in the outlet box also. Hence the outlet box is initialised only with air.

Because there is water and air inside the pipe, a initial static pressure value is necessary. Due to both phases are homogeneous distributed at the beginning, the mixture density (equation 2.14) can be used to calculate the hydrostatic pressure with the following equation:

$$p_{init} = (max(y) - y) g \varrho_{mix} \quad (6.1)$$

The initial velocity upwards is set to the superficial phase velocity, calculated by the corresponding phase volume flow and the pipe cross section area. All other initial velocities are set to zero.

6.2 Vertical Pipe Simulation

Generally it can be said, that the vertical flow simulation has higher demands on the numerical solver. To ensure that the mass and momentum imbalance maximum values are in range of $\pm 1\%$ (see section 5.1.3), the physical timescale have to be set about one magnitude lower than in Fabre horizontal flow simulations. With a physical timescale of $5e-4$ s the momentum imbalances in the Hewitt simulations are any time in the specified range. Though due to unsteady flow pattern, the mass imbalances are not balanced but fluctuate with the same curve pattern, see figure 6.6. If these mass imbalance evenly fluctuate around a value and the momentum imbalances are in between $\pm 1\%$, then the simulation can be assumed as converged.

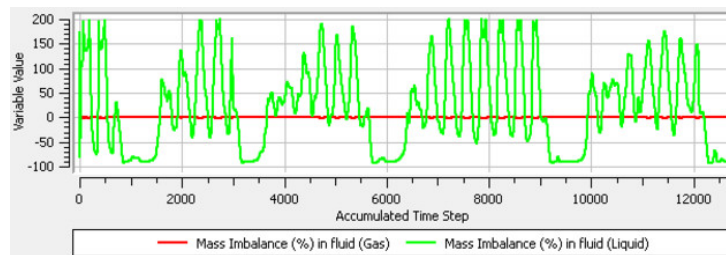


Figure 6.6: Hewitt CFD model, Run No. 6; mass imbalances over iterations; figure by the author

The large deviations higher than 100% in figure 6.6, is caused by the plug flow. A open boundary condition is used for the outlets and fluid can flow in the computational region, which increase the mass inlet flow.

It can be observed, that the physical timescale did not have only an impact on the simulation stability, also the pressure gradient and the flow pattern depend on the timescale. An increased physical timescale yields to a weaker phase separation, which in turn yields to a decreased water hold-up. With less water content in the pipe, the pressure gradient is decreased and the flow pattern is changed.

A better phase separation, caused by a decreased physical timescale in connection with a parallel run, causes sometimes a floating point exception error,

because of to high gradients. If these high gradients occur at the boundary from one partition to the neighbour partition, the linear solver could become unstable. Hence the advection scheme specific blend factor have to reduce to 0.75, in order to run without a simulation solver error. Though this is tested by 56.000 mesh cells per partition. If this latter value is decreased, it could be that the specific blend factor have to be decreased more.

The results of the CFD simulation can be seen in table 6.3.

Table 6.3: Hewitt proof of concept results; Averaged NPGD, observed flow regime from experiment and CFD simulation

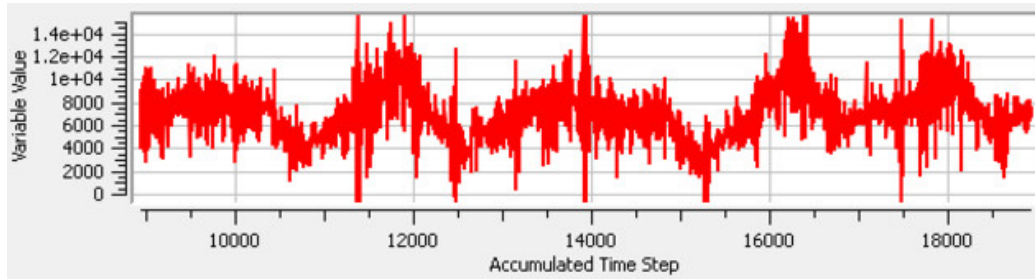
Run No.	NPGD [–]	Flow regime in experiment	Flow regime in CFD simulation
1	0.25	Bubble	Bubble
6	0.13	Plug	Plug

The case FV_190 has a NPGD value of 0.1534. Fortunately the NPGD value for a vertical pipe is close to the horizontal pipe simulation, see table 6.3. Though it can be seen that the NPGD value is increased for a simulation with higher water hold-up. Which could mean that the new CFD simulation model is appropriate to describe flow pattern with larger structures but the NPGD error could increased for flow pattern with small structures like bubble flows or drop flows.

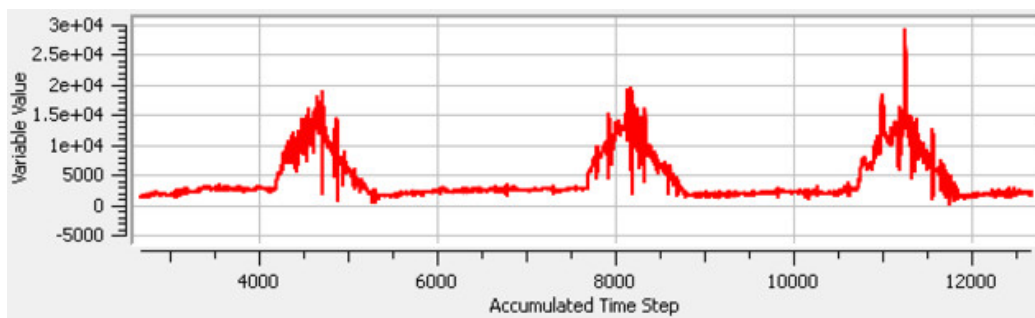
With the shape of the pressure gradient signal, it is possible to derive the flow pattern. The shape of pressure gradient curve of the Hewitt and Owen (1987) CFD simulation, can be seen in figure 6.7.

While the pressure gradient shape of Run No. 1 is roughly sinusoidal shaped, the pressure gradient shape of Run No. 6 is over many iterations constant and followed by a strong increased and decreased pressure gradient in a short period.

The shape of the pressure gradient curve in 6.7 (b) correspond to a plug flow. The pressure gradient curve is constant if no plug reaching the measuring points. If a plug pass the measuring points, the pressure gradient is



(a)



(b)

Figure 6.7: Hewitt CFD model pressure gradient over iterations (a) Run No. 1, (b) Run No. 6; figure by the author

increased and decreased. The iterations between two pressure gradient peaks correspond to the distance between two plugs. An example of a plug flow can be seen in figure 2.1 (b). It is assumed, that Hewitt and Owen (1987) called this last mentioned plug flow slug flow, because a plug flow has some large bubbles surrounded by a continuous phase, so that the bubbles are the plugs. In Hewitt Run No. 6 the water hold-up is lower, so that the air is the continuous phase and the water phase will form the plugs like in figure 2.2 (e). Though the slug flow can only occur in horizontal pipes. Hence the author does not follow Hewitt and Owen (1987) by the naming of the above mentioned flow pattern. Hence the notation plug flow is used in this thesis instead of slug flow introduced by Hewitt and Owen (1987), see table 6.3 column "Flow regime in experiment".

In figure 6.7 (a) the pressure gradient shape is between the bubble flow and plug flow. In an ideal bubble flow the bubbles are equally distributed,

that the pressure gradient shape is constant. Described above the pressure gradient shape of a plug flow is constant with pressure gradient peaks in certain distances. A clear signal when a plug reach the measuring point can not be seen in [6.7 \(a\)](#) and therefore it is rather a bubble flow.

The derivative of the flow pattern is carried out by the pressure gradient signal, because it is assumed, that [Hewitt and Owen \(1987\)](#) are used this signal too, to determine the flow pattern. In [Hewitt and Owen \(1987\)](#) there are no comments how they determine the flow pattern, but visual techniques are excluded due to opaque walls in the experiment and special techniques to measure flow pattern like X-ray tomography would have been explained with certainty in the publication.

With the flow pattern derived from the pressure gradient signal, there is a good agreement of the experiment and simulation, see [table 6.3](#). An overview of some simulation results for a exemplary section of the vertical pipe can be seen in the [appendix C](#).

6.3 Hewitt Conclusion

These proof of concept for a vertical pipe flows should examine the generality of the new CFD two-phase model. In order to achieve this, the NPGD values of the vertical pipe simulations have to be equal with the horizontal pipe simulations.

In section 6.2 a good agreement between the vertical pipe and horizontal channel simulation of the pressure gradient error NPGD can be seen. In the vertical pipe simulation, especially for flow pattern with larger structures, the NPGD value is small. For flow pattern with small structures, like a bubble flow, the pressure gradient deviations are increased. On the basis of this knowledge it is assumed, that the force balance in the free surface region is appropriate, but for a dispersed regions further investigations should be carried out. One possible approach to improve the new CFD model is to use a variable SMD correction factor. It could be, that this correction factor of 20 is appropriate for the large interface structures but not for small ones.

The comparison of the flow pattern is not as accurate as the pressure drop, because no description how Hewitt and Owen (1987) determine the flow pattern can be found. And the author can only assumed, that Hewitt used the pressure signal shape to deduce the flow pattern. But overall good agreements can be shown for the flow pattern.

Due to the good agreement of the CFD simulation with the Hewitt and Owen (1987) experiment and comparable error rates with the Fabre, Masbernat, and Suzanne (1987) simulation FV_190, an appropriate two-phase simulation model for horizontal and vertical flow regimes can be assumed. Due to the complexity of this matter, it is recommended to verify this simulation model with other geometries and fluids. Until the new two-phase model is not based on a broader knowledge basis, it is recommended to carry out a validation every time it is used for a new case.

Chapter 7

Proof of Concept with Steam Drum Experiment

Most of all to prevent the carryover of solids into superheaters or turbines have to be guaranteed by the boiler companies, see section [2.2.2](#). In order to ensure the steam/water separation, there are different separation devices, see section [2.2.3](#). These separation devices are based often on companies know-how or semi empirical models. Because of the complexity of turbulent two-phase flows in the gravity field, it is very difficult to reproduce such a flow with a numerical model. [Epple et al. 2012](#) For the same reason steam drum experiments are expensive, why only some experiments are carried out and not often published.

To overcome the steam/water separation uncertainty, the overall goal of this thesis is to develop a simulation model to reproduce the droplet flow rates in steam drums. Despite of many two-phase experiments in the literature, no experiment for a steam drum can be found. Hence a steam drum experiment, based on the ERK Eckrohrkessel GmbH design, is carried out.

A schematic drawing off a steam drum with ERK drum internals is shown in figure [7.1](#).

In this drawing the drum wall with the most important pipe connections, the baffle plates and water levels are shown.

The steam/water mixture arrive the inner of the steam drum through the

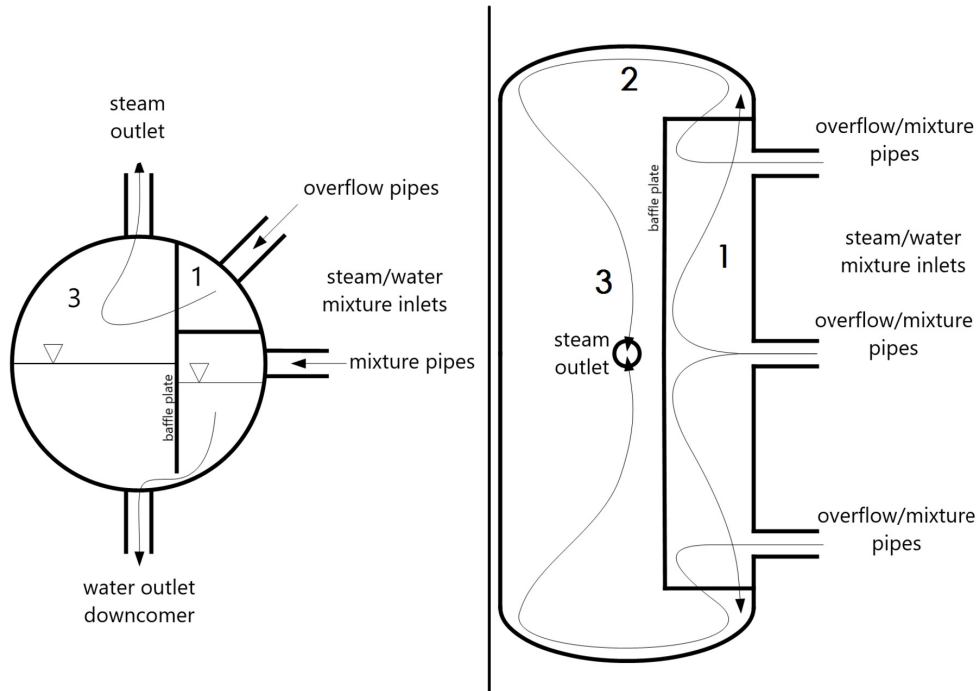


Figure 7.1: ERK steam drum internals schematic drawing; Schreiber, Hellwig, and Nowitzki 2017

overflow and mixture pipes. In the inner of the drum the steam/water separation takes place and water leave the drum through downcomers and the steam through the steam outlet. In order to ensure that the water without bubbles can flow to the downcomers, there is a small opening at the bottom of the baffle plates, that the water can flow underneath. The second opening is the steam window. The steam window is a small open section at the top of the side baffle plates. The steam should only pass the steam window to the steam outlet. The baffle plates delimit the drum inlet region.

Additional the three separation stages are numbered. Stage 1 is nearly enclosed from the drum wall and baffle plates. There the steam/water mixture is separate due to the contact with the baffle plates. A high turbulence increase the contact of the mixture with the walls. Hence region 1 is designed, that the turbulence ensure a good separation and is called “turbulent separation stage”. In separation stage 2, the centrifugal force caused by the redirection at dished heads is used, to push the droplets to the dished head

walls. The separation principle of stage 2 is the same like in a cyclone and is called “centrifugal separation stage” . In stage 3 the velocities have to decreased, in order to separate the steam/water mixture due to the gravity and is called “calm stage” .

The water level position in figure 7.1 is important for the mixture separation too. If is the water level too low, the steam can flow underneath the baffle plate, the separation stage 2 and 3 are not effective and the steam purity is decreased. If is the water level too high, too much water is carried through the steam window and the steam purity is decreased also. Due to always present fluctuations, it is recommended to achieve a half-filled steam drum. Please note that the water level of stage 1 compared to stage 2 and 3 is not the same. Due to the pressure drop of the steam window an increased pressure occurs in stage 1 and pushed down stronger the water level there.

The following CFD simulations of this steam drum experiment should show in a proof of concept, how exact can be a prediction of droplet mass flow out of the turbulent stage. The CFD simulations are based on validation cases FV_170 and FV_190, see section 5.4 and the physics set-up in section 5.1.3. The case FV_200 was neglected, because of unstable behaviour. The complexity of the experiment steam drum simulation is significant increased compared to the Fabre, Masbernat, and Suzanne (1987) and Hewitt and Owen (1987) experiment simulations. Here the CFD model and the physics set-up need a good performance, to limit the computational time to a few hours and ensure a stable run. With an acceptable droplet mass flow prediction and in an acceptable computational time, this simulation set-up should be ready, to be applied to industrial applications.

7.1 Steam Drum Experiment

The steam drum construction and set-up can be seen in [Schreiber, Hellwig, and Nowitzki \(2017\)](#). This experiment is designed for an air/water mixture to determine the droplet mass flow out of the sides, in order to measure the water carry over in the turbulent region in front of the baffle plate (stage 1 in figure 7.1). This experiment steam drum is different to an ERK steam drum, because the carried water droplets from the turbulent inlet region, will be examined only. Hence where in an ERK steam drum a dished head exists, is in the experiment an air outlet. To ensure that all the gas, which pass the steam window, leave the experiment drum at the sides, the rear part (behind the baffle plate) is closed in the experiment drum with extended side baffle plates. Hence the experiment steam outlet has no further task as the pressure regulation only. For comparison ERK steam drums can be seen in figures 2.9 and 2.10.

The experiment steam drum construction is shown in figure 7.2.

The drum wall consist of a polyacrylic pipe, in order to examine the air/water interface and measure the interface position. Two types of inlet pipes exist, mixture and overflow pipes. In both pipes the air/water mixture flow inside the drum, but with different water fraction. Inside the drum the air/water separation takes place, so two types of outlets are needed, one for the water and one for the air. Water is leaving the experiment drum at the three downcomer pipes, whereby the air can leaving the drum at both sides. The baffle plate is to separate the stage 1 from the rest of the steam drum and supports the air/water separation. By this baffle plate, air is forced to flow through the steam windows and the water can only flow through the holes at the bottom of this plate. In order to avoid that air can flow through the baffle plate holes, the water level in this drum have to be higher than the holes, so that the holes are covered with water.

The air/water mass flow ratio, the bulk mass flow, the cross section area of the steam windows as well as the baffle plate position are important parameters for the air flow purity. These parameters are designed by [Schreiber, Hellwig, and Nowitzki \(2017\)](#) for this experiment.

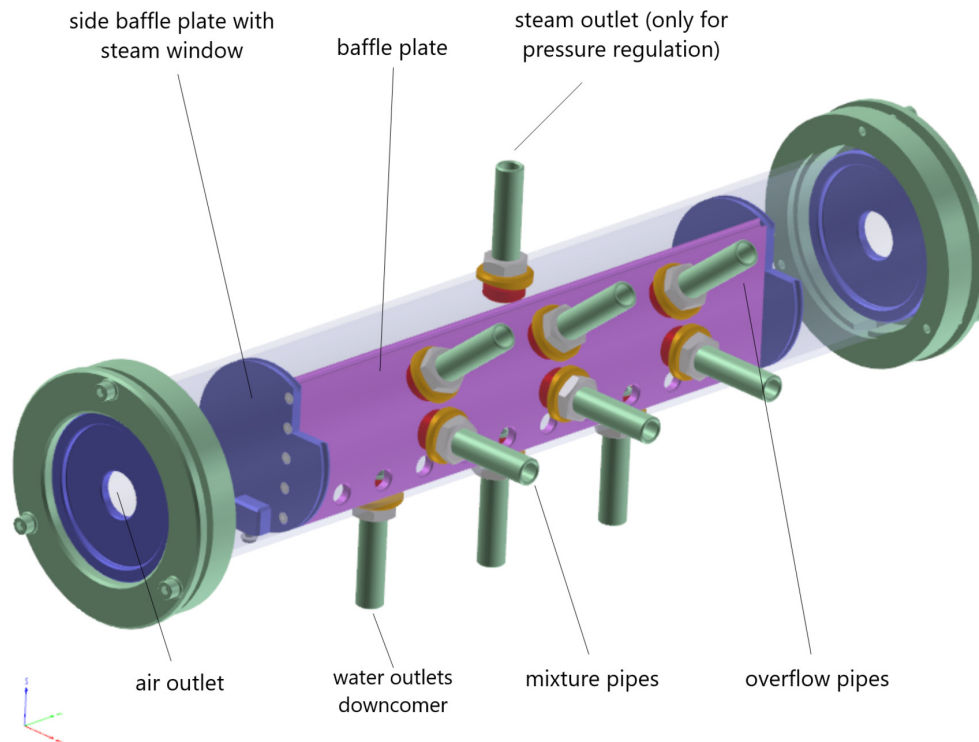


Figure 7.2: Construction of the steam drum experiment; Schreiber, Hellwig, and Nowitzki 2017

To measure the water level height, a marker is stamped on the baffle plate next to the right side baffle plate.

ERK places a pipe network on the top of every boiler, which acts as a pre-separator. This pre-separator pipe network has an effect of the mixture separation inside the steam drum. Hence this pipe network has to be included in the experiment too. How the steam drum and the pre-separator pipes are included in the boiler water circulation is shown in figure 2.5. The experiment pre-separator pipes are shown in figure 7.3.

The three sets of feeding pipes are connected with the three sets of experiment drum inlet pipes. The overflow pipes of the feeding pipes are connected with the overflow inlet pipes on the experiment drum and the mixture pipes respectively. The distributor pipe guide the incoming two-phase mixture to the feeding pipes. Due to the strong mixing in the distributor pipe, it is

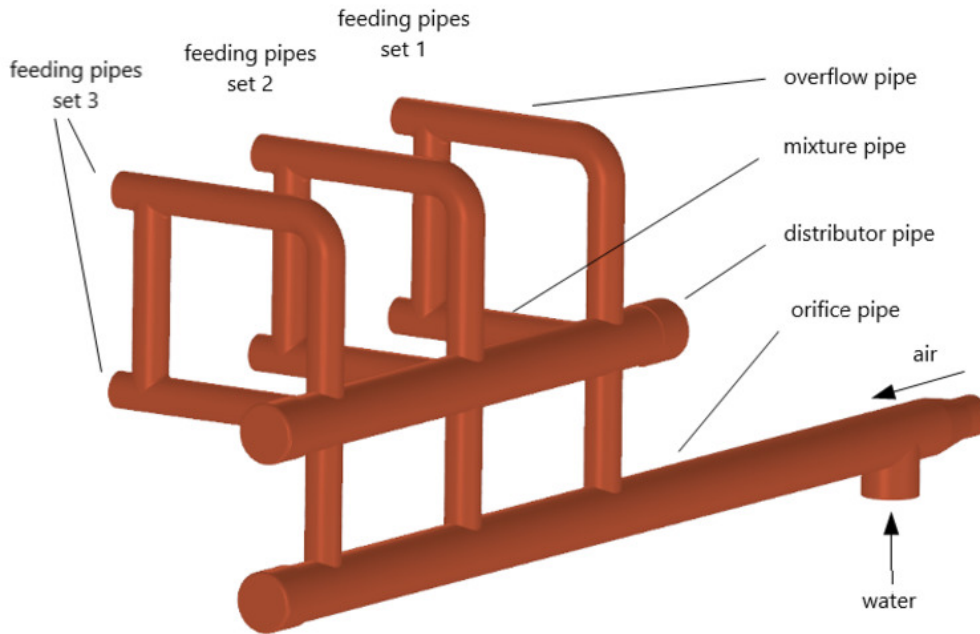


Figure 7.3: Construction of the steam drum experiment feeding pipes; Schreiber, Hellwig, and Nowitzki 2017

assumed that the flow pattern in front of this pipe have only a weak impact of flow pattern in the feeding pipes. Hence it is decided to put the system boundary in front of the distributor pipe.

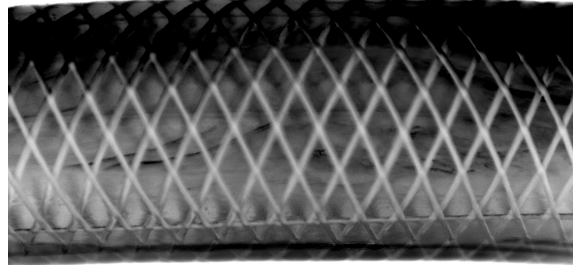
Due to the given conditions an orifice pipe is included in the experiment to feed the distributor pipe with the air/water mixture. The orifice pipe is only a component of the experiment pre-separator. The task of the orifice pipe is to mixing the air with the water and supply the mixture equally to the distributor pipe. Hence there are three orifices in the vertical part of the orifice pipe. This is a design error and does not work, because a two-phase mixture can not be equally distributed with this technique. In order to examine the not equally distributed water fraction in the feeding pipes, the connection pipes between the feeding pipes and the steam drum inlets are realised with transparent tubes.

In the experiment feeding pipes it is assumed that a wavy stratified flow and/or a slug flow can occur. These later flow pattern have an unsteady

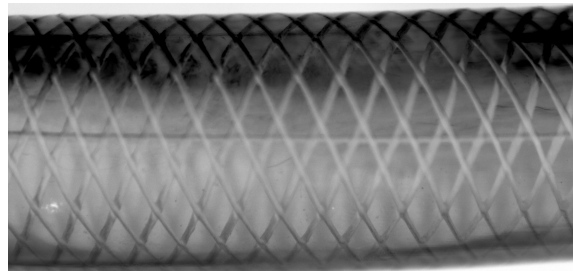
behaviour. Hence to analyse also transient flow pattern, video recordings are carried out. These video recordings showing in every pipe section in set 3 a slug flow regime, but with different water levels and frequencies. A theoretical slug flow can be seen in figure 2.2 (e). But to discuss the water separation in the feeding pipe set 3, only the snapshots in figure 7.4 are needed. The naming of the pipe sections is shown in figure 7.5.

The overflow pipes in sub-figure (c) and (d) have a decreased water level. The air/water mixture is divided partially behind the distributor pipe, so that more water is flowing through the mixture pipe and more air is flowing through the overflow pipe, see figure 7.4 (a) and (c). The following connection pipe between the overflow and mixture pipe cause a further increasing water level in the mixture pipe, see sub-figure (b). Hence the water content of the mixture pipes are higher than in overflow pipes. This different water distribution in overflow and mixture pipe set 3 should be reproduced in the CFD simulation also.

As mentioned above the orifice pipe can not equally distribute the air/water mixture. In Schreiber, Hellwig, and Nowitzki (2017) it can be seen, that in feeding pipes set 3 the water content is much higher than in set 2 and set 2 has a higher water content than in set 1. Those different water levels in the sets cause miscellaneous flow pattern. These miscellaneous flow pattern are a good test for the new CFD model, whether the CFD model can reproduce a wide range of flow pattern.



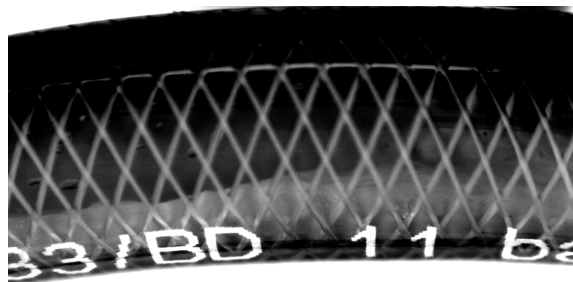
(a)



(b)



(c)



(d)

Figure 7.4: Feeding pipes set 3 visual water level snapshot; case 500 L/h water and 25 m³/h; (a) mixture pipe in front of connection pipe G3.1, (b) mixture pipe behind connection pipe G3.2, (c) overflow pipe in front of connection pipe Ü3.1, (d) overflow pipe behind connection pipe Ü3.2; Schreiber, Hellwig, and Nowitzki 2017

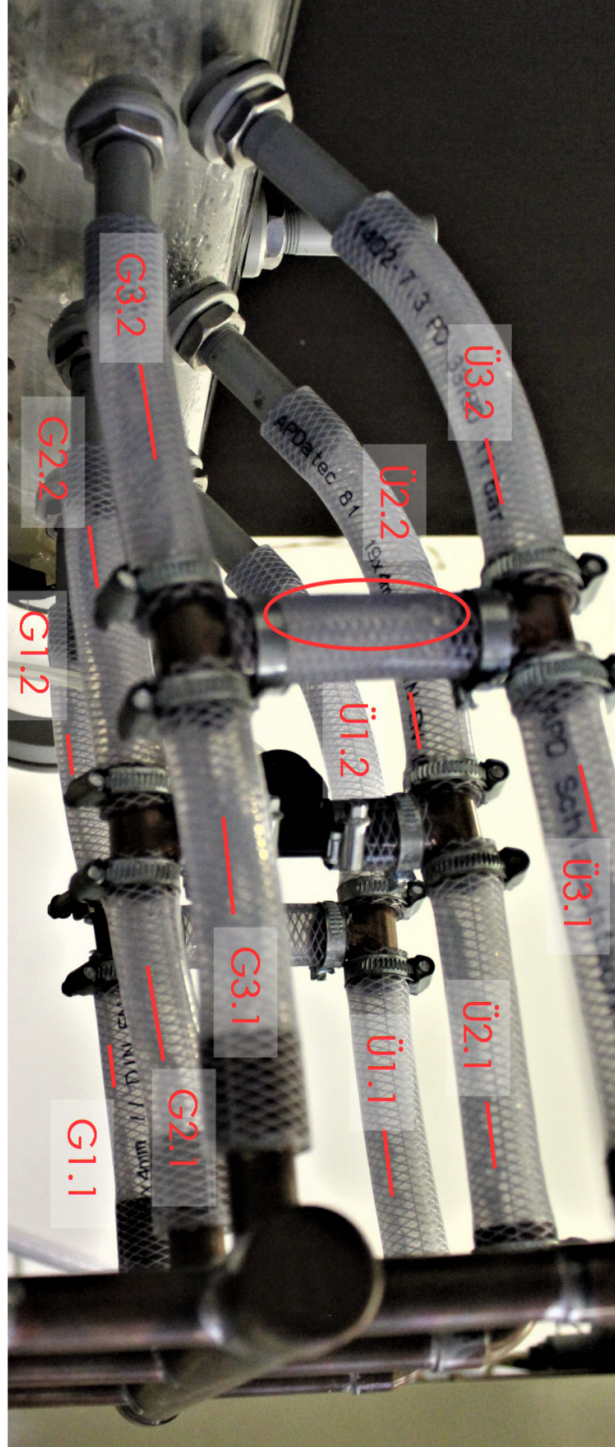


Figure 7.5: Naming of feeding pipes in experiment steam drum regarding water content and flow pattern; Schreiber, Hellwig, and Nowitzki 2017

Due to the transient steam drum inlet behaviour the water interface in stage 1 of the experiment steam drum is unsteady. Because of the flow and water level fluctuation the droplet mass flow fluctuate also. Hence one experiment run should take more than 6 min, in order to overcome this fluctuations. To avoid droplet mass flow deviations due to ambient pressure and temperature changes, the mass flow measurements are repeated on different days. The results of the droplet mass flow at both drum sides is shown in table 7.1.

Table 7.1: Droplet mass flow out of experiment left and right steam drum side

Run	droplet mass flow [kg/s]					
	Day 1		Day 2		Day 3	
	left	right	left	right	left	right
1	1.35e-05	8.88e-08	1.62e-06	1.06e-06	1.75e-06	3.16e-07
2	1.16e-05	8.88e-08	1.10e-06	2.83e-07	3.21e-06	2.50e-07
3	8.21e-06	1.16e-07	4.89e-06	2.61e-07	2.03e-06	1.60e-06
4	1.05e-05	1.77e-07	4.85e-06	1.72e-07	1.27e-06	3.22e-07
5	-	-	1.76e-06	4.44e-07	6.72e-07	3.05e-07
<i>ave</i>	1.09e-05	1.18e-07	2.85e-06	4.44e-07	1.78e-06	5.6e-07

It is trying to hold the conditions for every run constant. These conditions are the air volume flow of 25 m³/h, the water volume flow of 500 L/h and the water level of 21.5 mm below the centreline.

Evident is the difference between the sum of the left side of day 1 in contrast to the others days. It is assumed that at day 1 some discrepancies, regarding the experiment conditions have been occurred, why the measurements at day 1 are discarded. Generally the droplet mass flow out of the right side is smaller than the on the left side. Additional the mass flow fluctuations on the left side are higher than on the right side. That suggests, that on the left side the inlet fluctuations are stronger than on the right side.

7.1.1 Steam Drum CFD Geometry and Mesh

The dimensions of the CFD experiment drum is shown in figure 7.6.

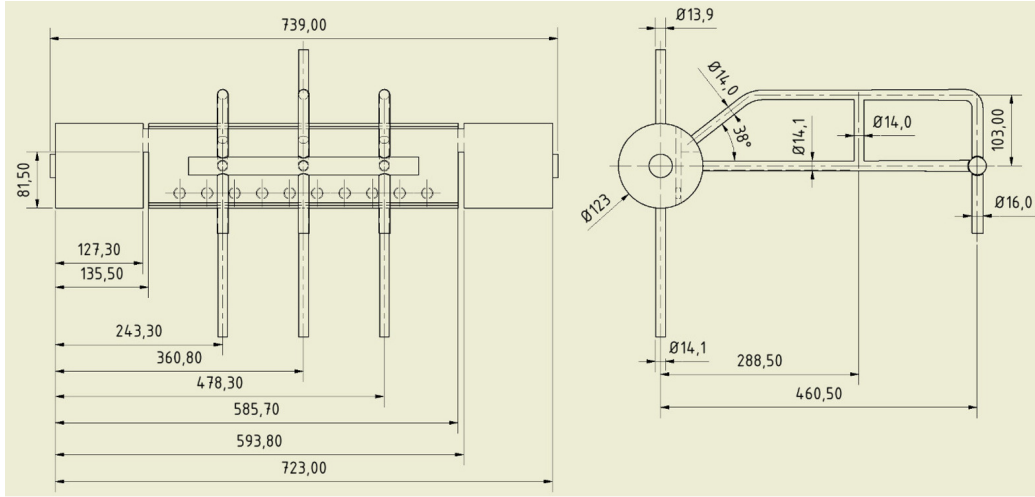


Figure 7.6: CFD Construction of the steam drum experiment with dimensions; Wehner, Hellwig, and Nowitzki 2017

Construction deviations due to production are included in the CFD model, because drum dimensions are determined at the experimental device again and the construction drawing is corrected. The corrected CFD model in 3D can be seen in figure 7.7.

As mesh element type, tetrahedral cells are used. This type provide a fast meshing for complex geometries. Therefore this type is used often in industrial applications. Though the tetrahedral cells have disadvantages by the numerical error in contrast to the hexahedral cell type. To reduce the numerical error a finer mesh of tetrahedral mesh is recommended compared to a hexahedral mesh. Hence global mesh parameters are used for the base mesh, with local refinements. The global mesh parameters for the mesh program "CFX Mesh" can be seen in table 7.2.

Table 7.2: Steam drum experiment global mesh parameters

Size Function	Proximity and Curvature
Min Size	0.3 mm
Proximity Min Size	0.3 mm
Max Face Size	30.0 mm
Max Tet Size	60.0 mm

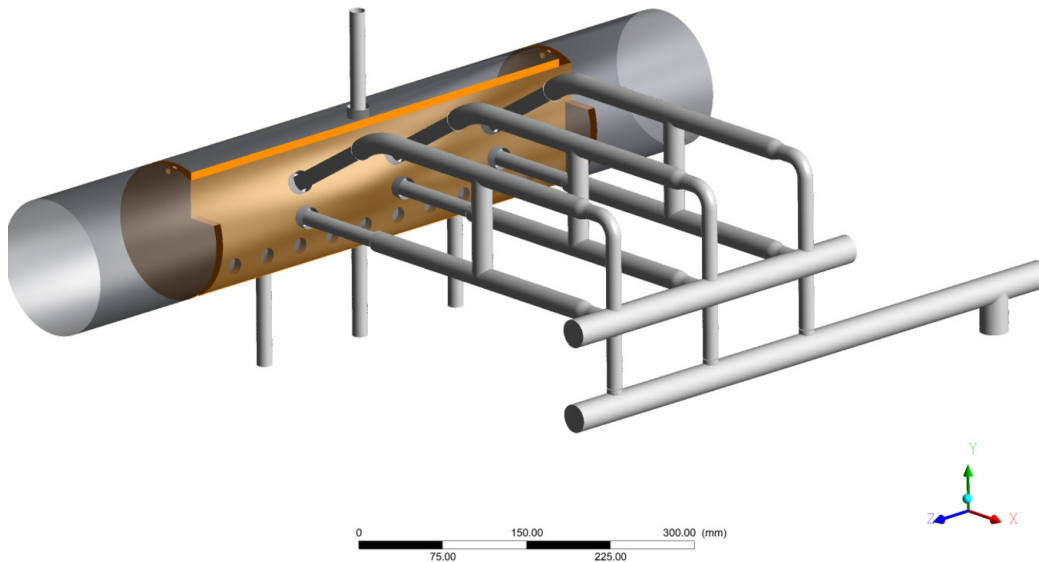


Figure 7.7: 3D drawing of the experiment steam drum; figure by the author

The local refinements are placed at neuralgic positions. At neuralgic positions large gradients of velocities or volume fraction are assumed, who a coarse mesh can cause solver instabilities or are crucial for the accuracy. An overview of the neuralgic positions and the local refinement value is shown in table 7.3.

Table 7.3: Steam drum experiment local refinement mesh parameters

Steam Drum Two-Phase Interface	3.0 mm
Feeding Pipes Wall Surface	1.0 mm
Inner Drum Pipes Surface	1.0 mm
Orifices Edges	0.2 mm
Baffle Plates Surfaces	5.0 mm
Steam Drum Wall Surface	3.0 mm

At steam drum two-phase interface, in the feeding pipes, at the baffle plates and at the steam drum wall especially large volume fraction gradients are assumed. Large velocity gradients are assumed at inner drum pipes (stuck-

through nozzles) and at the orifices.

An overview of the mesh on a cutting plane can be seen in figure 7.8.

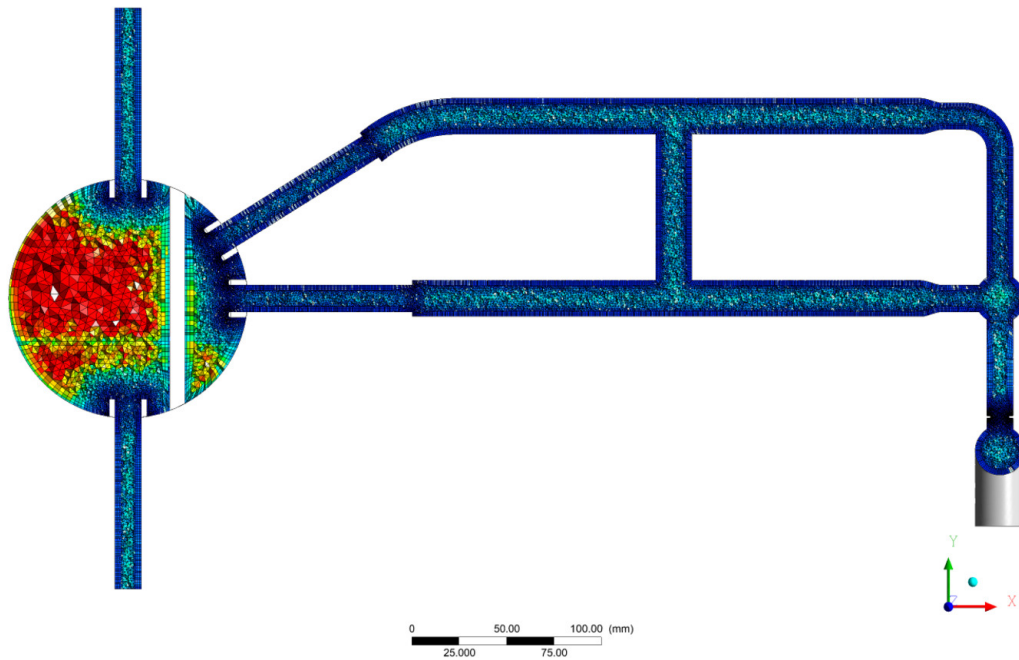


Figure 7.8: Mesh overview of the experiment steam drum cut; Coloured by volume size; figure by the author

For mesh details one can see figure 7.9.

Larger figures of sub-figures in 7.9 can be found in the appendix D.1 - D.4.

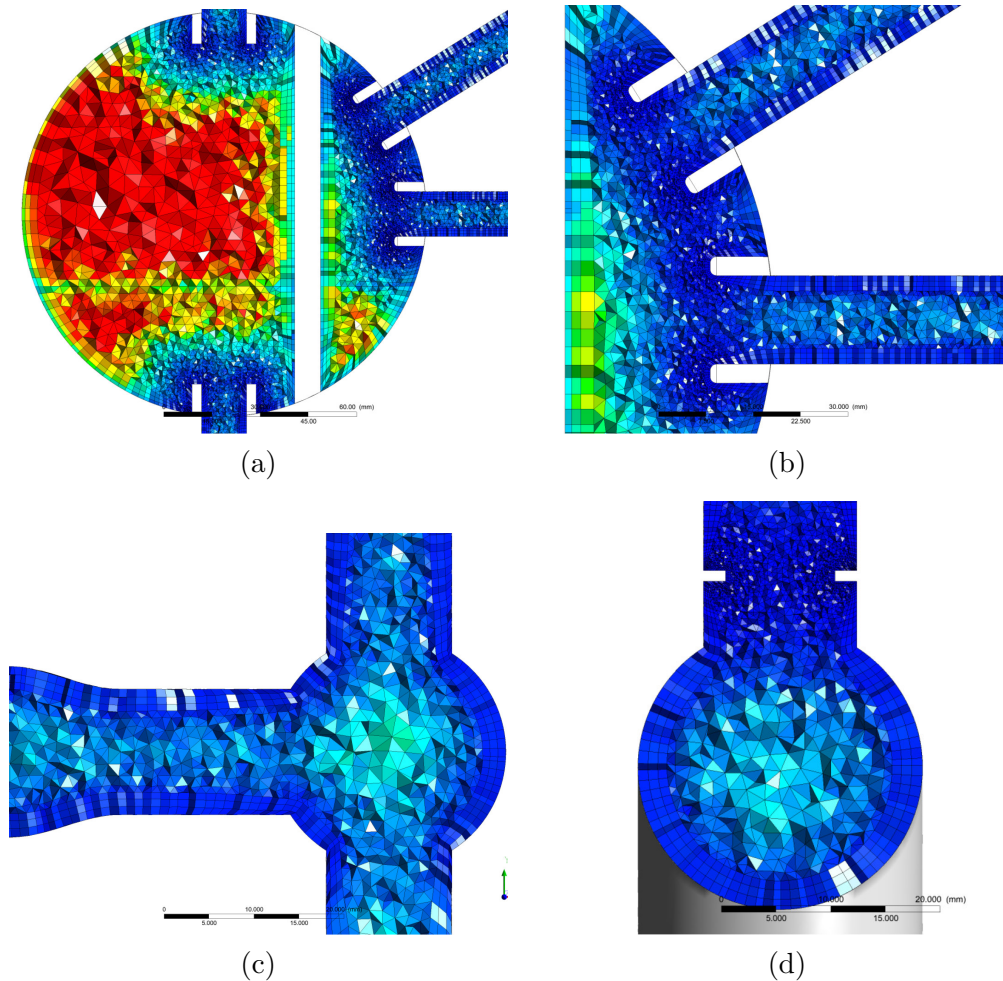


Figure 7.9: Mesh details of the experiment steam drum; Coloured by volume size, (a) steam drum, (b) steam drum stage 1, (c) distributor pipe, (d) orifice pipe; figure by the author

7.1.2 Steam Drum Simulation Boundary Conditions

The experiment steam drum have a water and an air mass flow inlet, see figure 7.3.

The downcomers and the drum sides are pressure outlets. Whereas the side outlet relative pressure is 0 Pa and the relative pressure at the downcomers depends on the water level in the drum. The pressure at downcomers can be calculated by $\Delta p_{downcomer} = \rho_{water} g \Delta h_{waterlevel}$. But during the simulation

run there are different water levels in the turbulent and the calm stage, which is unknown at the beginning. Hence it is an iterative process to find the correct $\Delta h_{waterlevel}$, which correspond to the measured water level in the experiment. Due to the unequal water distribution in the feeding pipes the water level is skewed in turbulent section of the experiment drum. The water level scale is on the right side of the baffle plate, like mentioned above. Hence a filter function in the CFD model is needed which return the water level in stage 1 next to the right baffle plate. In the CFX CEL expression language a volume average of the interface height can be carried out. At first a CEL function is used to return the y values of interface cells on the right of stage 1 based on the free surface blend function:

Listing 7.1: Y values of right side interface cells CEL expression

```
NOW interfaceYCalmed = if( z > -222 [mm] , if( z < -157 [mm] ,
    if( x < 63[mm] , if( x > 30[mm] , if( y > -50[mm] , if(
    Gas.AV AIAD FS Blend Func > 0.8, Y Coordinate , 0[mm]) ,
    0[mm] ) , 0[mm]), 0[mm]), 0[mm]), 0[mm]), 0[mm])
```

and the volume of the corresponding interface cells:

Listing 7.2: Volume of right side interface cells CEL expression

```
NOW interfaceVolumeCalmed = if( z > -222[mm], if( z < -157[mm]
    ], if( x < 63[mm], if( x > 30[mm], if( y > -50[mm], if(
    Gas.AV AIAD FS Blend Func > 0.8, Volume of Finite Volumes
    , 0[m^3]), 0[m^3] ) , 0[m^3]),0[m^3]),0[m^3]),0[m^3])
```

In the second step, both CEL functions in listing 7.1 and 7.2 are defined as additional variables, so that these additional variables can be used in a CEL expression to calculate the volume average interface height:

Listing 7.3: Volume averaged interface height CEL expression

```
NOW waterLevelAve = volumeInt(Gas.AV NOW interfaceY)/fluid /
    sum(Gas.AV NOW interfaceVolume)/fluid
```

Subsequently the CEL expression "NOW waterLevelAve" can be monitored during solver run and should correspond to the experiment water level height.

The steam drum outlet is also included in the experiment steam drum for further experiments, but have no task for this thesis and is closed in experiment and defined in the CFD simulation as a wall.

7.1.3 Steam Drum Simulation Initial Conditions

The water level in the experiment is about 21.5 mm. But the water content in the feeding pipes are transient and unequal distributed. Hence only stage 1 and 3 of the CFD drum is initialised with a water level of 21.5 mm. The feeding pipe region is initialised with a homogeneous volume fraction. These volume fractions correspond to an ideal mixture of the supplied air/water mixture.

For stability reasons an initial hydrodynamic pressure is needed:

$$p_{init} = (y_{waterlevel} - y) g \varrho_{mix} \quad (7.1)$$

whereas p_{init} is only applied in stage 1 and 3 below the water level, else it is set to 0 Pa.

7.2 Steam Drum Simulation

This steam drum simulation comparison based on the Schreiber, Hellwig, and Nowitzki (2017) experiment with an air volume flow of 25 m³/h and a water volume flow of 500 L/h. The water level, as well as the droplet mass flow out of the drum sides is monitored in the simulation. Whereas the water level monitor is necessary to control the downcomer pressure boundary condition, see section 7.1.2. The droplet mass flow at drum sides correspond to the measurement results in table 7.1. Like mentioned above the physical setup is equal validation case FV_170 and case FV_190. Hence there are a consistent comparability of Fabre, Masbernat, and Suzanne (1987), Hewitt and Owen (1987) and steam drum simulations.

In general it can be said that with a physical timescale of 5e-4 s the solver run stable and the momentum imbalances are every time in between +/- 1 %. Sometimes conditions are formed in the simulation, which causes instabilities. These instabilities could not be reconstructed, because within only one iteration the solver crashes. In this short period it is almost impossible to write out a backup file, which can be examined. In addition these instabilities are disappeared after a rerun. It is assumed, that a high gradient value occur on the border between two cpu mesh regions in a parallel run, see keyword "overlap relaxation fluids" in section 5.1.3. But despite of a reduction of the "overlap relaxation fluids" value, the solver crashes again. Only a reduction of the advection scheme specific blend factor to 0.5, the solver runs stable every time. But unfortunately a reduction of the specific blend factor reduce the accuracy of the simulation, see table 5.9.

Before the droplet mass flow can be examined in the simulation, the average water level have to be 21.5 mm below the drum centre line, like in the steam drum experiments. If the water level condition is achieved, the droplet mass flow averaging can be started at this point. As in the other simulations, average values are averaged over 10.000 iterations. The simulated average values of the droplet mass flow out of the sides can be seen in table 7.4.

In Table 7.4 the droplet mass flow at drum sides, the normalised RMS droplet

Table 7.4: Steam drum simulation droplet mass flow at sides; water volume flow 0.5 m³/h, gas volume flow 25 m³/h, 1 atm

		Droplet mass flow	NDMFD	abs deviation
		[kg/s]	[-]	[kg/s]
FV_170	left	1.96e-07	0.92	2.12e-06
	right	7.29e-08	0.85	4.29e-07
FV_190	left	4.39e-08	0.98	2.76e-06
	right	2.09e-07	0.58	2.93e-07

mass flow and absolute deviations are shown for the left and right drum side. The normalised RMS droplet mass flow deviation is defined as:

$$NDMFD = \frac{\sqrt{(\Phi_{d,exp}^M - \Phi_{d,sim,ave}^M)^2}}{\Phi_{d,exp}^M} \quad (7.2)$$

The absolute simulation results are close to the experiment results. This can be seen in table 7.4 column absolute deviation. It is evident, that relative deviations are increased, if simulation values are converged to zero, due to numerical fluctuations. Hence the relative droplet mass flow deviation are high.

Generally one condition in order to use this simulation model in an industrial application is, that the simulation produce every time conservative results. In table 7.4 one can see that this condition is violated. Every simulation result is smaller than the corresponding experiment value.

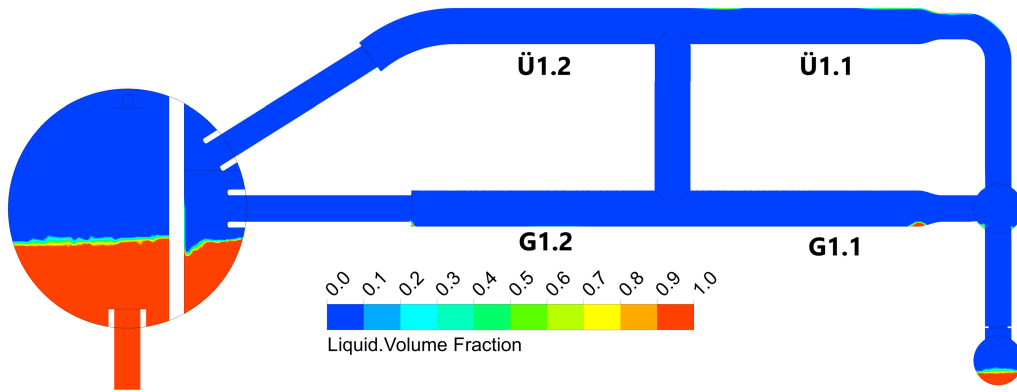
If one compare the different simulation set-ups, the best simulation result is at FV_190 right side, with a NDMFD value of 0.29. But on the other side the worst simulation result is also at FV_190 on the left side, with a NDMFD value of 0.98. But the simulation model FV_170 show the correct ratio between the droplet mass flow at the left and right side. Like mentioned in table 7.1, there is an increased droplet mass flow at the left side compared to the right side. Therefore the simulation model set-up FV_170 is recommended for steam drum simulations.

In order to compare the experiment with the simulation water fraction, cut planes through the centre of all feeding pipe sets are carried out. In figure

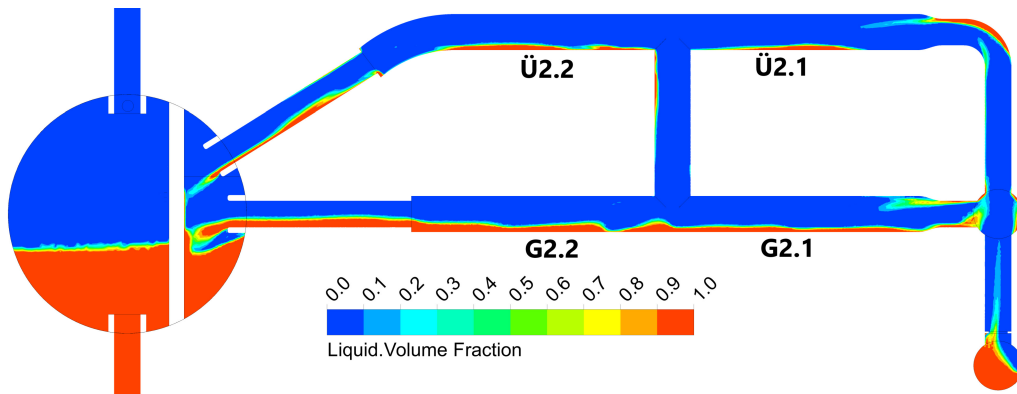
7.10 one can see the cut planes, which are coloured with the liquid volume fraction.

The unequal water content distribution in the experiment can be reproduced by the simulation. In the simulation the water content in the feeding pipes is increased from set 1 to 3 like in the experiment. This is an effect of the inlet condition of the orifice pipe.

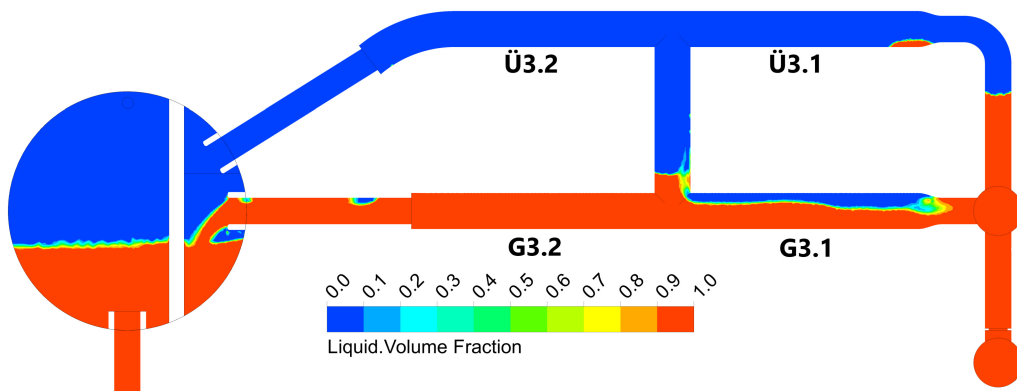
Due to the video recordings it is possible to compare the water content in the feeding pipe set 3 in the experiment and simulation. In order to compare qualitative the water content in the experiment the snapshot in figure 7.4 is edited. In these photos the water phase, in light grey, is highlighted. By comparing figure 7.4 (a) with figure 7.10 G3.1 the flow pattern looks similar. Also the flow pattern in figure 7.4 (b) is similar to the figure 7.10 G3.2. Though in the experiment there is a clearly recognisable water content in the overflow pipes, see figure 7.4 (c) and (d). This water content in the overflow pipes can not be reproduced by the simulation. In figure 7.10 Ü3.1 and Ü3.2 there is no noticeable water.



(a)



(b)



(c)

Figure 7.10: Experiment steam drum simulation; Coloured by liquid volume size, feeding pipe (a) set 1, (b) set 2, (c) set 3; figure by the author

7.3 Steam Drum Simulation Conclusion

Alone if one take a look at the flow pattern in the feeding pipes, it is evident how complex such a two-phase flow in a steam drum is. The feeding pipes and the steam drum form a system of communicating pipes. Local inaccuracies cause changes in the whole pipe system. Also small inaccuracies of the interface momentum balances has a strong impact of the air/water mixture distribution.

It can be seen in the experiment and the simulation, that the flow pattern in the feeding pipes have a strong impact on the droplet mass flow at the drum sides. That is why it is important for the simulation model to reproduce this flow pattern in the feeding pipes. In order to reproduce the flow pattern, the momentum transfer between both phases should be reproduced exactly. A comparison of the flow pattern in the experiment and simulation mixture pipes set 3, show a good agreement. Though the water content in the simulation overflow pipes in set 3 is less than in the experiment. So that to less water is pushed to the overflow pipes.

It is likely, that is in the third vertical orifice pipe branch a too low gas volume fraction. Hence there are not enough larger bubbles to push the water phase upwards, to the overflow pipes. The orifice pipe is responsible for the air/water distribution of the feeding pipe sets. In figure 7.11 one can see the air/water distribution in the orifice pipe and feeding pipe set 3.

The detail in figure 7.11 show the reason why not enough air can reach the feeding pipe set 3. There are only water on the end of the orifice pipe which create an free surface next to the second branch. The air phase can not overcome this free surface, because the kinetic energy is too low in the free surface region. A model of the free surface region is shown in figure 2.16. The kinetic energy in the free surface region depends on the characteristic length scales and the turbulence damping coefficient.

The characteristic length scale for the free surface region include bubble and droplet sizes, as well as the characteristic length of the free surface itself. That the bubble and droplet sizes play a role for the free surface

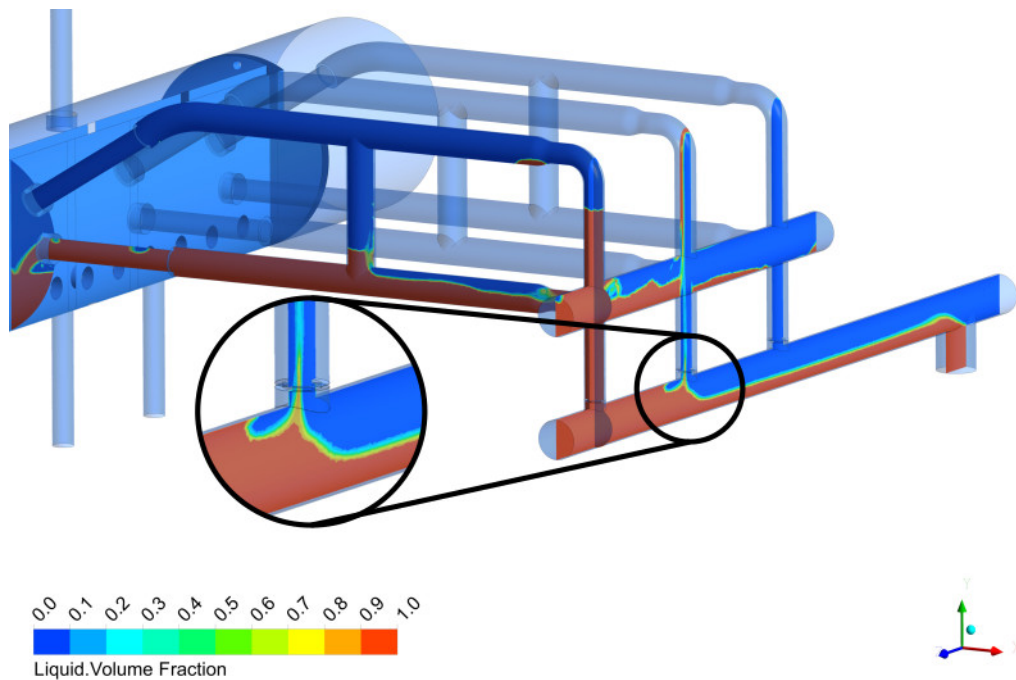


Figure 7.11: Experiment steam drum simulation; Coloured by liquid volume fraction; cut planes through orifice pipes and feeding pipe set 3 and a detail of phase separation in orifice pipe; figure by the author

region is because the blending functions have a slope, see figure 2.15 and the blending function overlap in the free surface region. The free surface region in the simulation is only a model. In reality this region is very thin and it is very hard to measure flow properties and particle distributions close to this free surface. Hence there a lack of experiments and knowledge of characteristic length scales close to the interface. Thus it is difficult to validate the particle size distribution. In the free surface region it could be, that the new particle size prediction model, has an increased deviation, because there are some additional physics, which can be neglected far away from the interface. For example the stronger particle interaction due to the increased density of particles. On the one hand it is possible to include additional models, which take into account these stronger interaction nearby the interface in the algebraic simulation model or a transport equation is used with included particle breakup and coalescence models.

Regarding this transport equation, there are some research approaches to model the phase interaction of a dispersed phase and a continuous phase, namely a mono-dispersed approach with a transport equation for the interfacial area density and a poly-dispersed approach, see [Pellacani \(2012\)](#). In the poly-dispersed approach some additional transport equations are needed and is therefore neglected, due to the high computational time. But the poly-dispersed approach is superior the mono-dispersed approach. The best performance for an industrial simulation could be reached with the interface area density transport equation combined with the mono-dispersed approach. With this latter approach the particle distribution accuracy could be increased, without a significant increase in computing time.

So that the only highly experimental uncertainty is the turbulence damping coefficient, which is not fully understood until today. To overcome this uncertainty more experiments, which examine the turbulence close to a interface is needed. Without a better understanding of the turbulence damping, a validation for every new simulation case is recommended.

Despite of the deviations of the flow pattern in the overflow pipes, the prediction of the mass flow out of the sides are close to the experiment. That implies a good agreement between the modelled droplet behaviour and the experiment. But this determination is only valid for a air/water mixture. But before to use this simulation model as a design tool for industrial steam/water applications, it is necessary to fit some parameter, that the droplet mass flow is every time above the measured values. Recommended fitting parameter are the RRSB scale parameter correction and the turbulence damping coefficient. Further experiments should be carried out with a steam/water mixture to make sure that the simulated steam/water behaviour is close to the experiment also.

Important for industrial application is besides the stability and conservativeness also the computational time. The experiment steam drum simulations takes around 2 days for 9 Mio cells on 40 cores. The reason of this long computational time is mainly the slow adjustment of the water level and thus the mass imbalance convergence. Thus with a better approach to force the

water level adjustment in the steam drum, the overall simulation time will be decreased. Additionally in all simulation a large set of CFL expressions are used. These CFL expressions are easy to use but decelerate the solver speed. An implementation of all functions in CFX subroutines would accelerate the solver. Because "Monitor Statistics" in CFX is used, "Mesh Adaption" must be omitted. If the "Mesh Adaption" can be used, the simulation time can be reduced also. With the three above mentioned improvements, the simulation time could be reduced by about a half.

The steam drum simulation had shown, that such a complex simulation can be carried out within a short time with a prediction of droplets in the gas phase close to the experiment. Though for new applications and fluids, validations are needed, which increase the reliability.

Chapter 8

Conclusion and Discussion

Simulations of two-phase air/water flows have been performed by means of the two-fluid inhomogeneous Euler-Euler approach. With the AIAD model a morphology detection is implemented. The AIAD model use a mono-disperse approach to determine the interfacial area density for the dispersed phases, in which the average particle sizes need to be know a priori. A new model is implemented in Ansys CFX to estimate the particle sizes, without increase the set of differential equations, which replaces the constant particle size diameter of the AIAD model. State of the art and State of science models, to improve the accuracy of the two-phase interaction, have been added to the CFD model. To these additional models belong the Ishii-Zuber drag model for the dispersed phases and non-drag force models.

The CFD model has been applied to the Fabre experiment. In this analysis combinations of different distributions functions as well as different RRSB model parameter have been tested. In the next step, based on the distribution function analysis results, the impact of submodels and different submodel parameters are examined, on the same Fabre experiment. The best model set-up is tested in a proof of concept for a 3D vertical two-phase pipe flow. In the end a CFD simulation has been carried out of a steam drum, with the CFD model set-up tested before. This steam drum experiment was developed to test the capability of droplets prediction of the two-phase CFD model and carried out at the same time as this thesis. The steam drum experiment is

modified regarding a real industrial steam drum, in order to determine the droplet mass flow which carried away by the air, from the turbulent steam drum region.

The main goals of these analyses is to validate the correct implementation of the submodels, analyse the impact of the submodels on the pressure field, velocity fields and phase distribution, as well as the reproduction of the flow phenomena in the steam drum turbulent region. The steam drum simulation should also demonstrate if the CFD model is able to perform an industrial size steam drum simulation.

Generally, despite of the relative coarse mesh and the wall function approach, the CFD model is able to reproduce a stratified flow in horizontal as well as bubble and plug flows in vertical pipes. Relative pressure deviations are in range of about 0.13 in case FV_190 to 0.25 in case Hewitt Run 1.

The Fabre simulations pointed out, that the largest deviations between simulation and experiment is regarding the turbulent kinetic energy, see figure 5.9. That the simulation results strongly depends on the turbulence model, can also be seen by the simulation with different turbulence models. To test the turbulence model dependency, a Very Large Eddy Simulations (VLES) has been carried out. This VLES is closest to the results of the Fabre experiment, without distribution function correction factors. But the VLES has been discarded, because of the strongly increased computing time. Hence correction factors are introduced, to enhance the simulation results. Regarding the SST turbulence model, the largest deviation of the kinetic energy is in the free surface region. Which implies, that the particle diameter and/or the "High Turbulence Damping Coefficient" is not adjusted well. Thus correction factors are introduced to adjust the CFD simulation to the Fabre experiment.

Larger deviations have been occurred for higher water content in vertical pipes. While in Hewitt run 6 good results are achieved, deviations between the simulation and the experiment are greater in Hewitt run 1. This discrepancy is probable an interface structure phenomenon. In Hewitt Run 6 there is a plug flow with large interface structures and in Hewitt Run 1 a bubble

flow occur with small interface structures. Hence it could be that the mixture model can not reproduce very fine flow pattern structures like in bubble flows and the prediction of the interface area density becomes inaccurate.

As mentioned in section 7.3 the kinetic energy is important to reproduce the flow pattern. In the steam drum simulation figure 7.11 one can see the similar problem of too low kinetic energy to reproduce a flow pattern with smaller interface structures. The problem can be traced back probably to the inaccurate reproduction of particle sizes in densely particle regions. The accuracy could be increased by an additional transport equation for the interface area density. In this transport equation particle coalescence and breakup is included, see Pellacani (2012). Validation of this model could be carried out with a new feeding pipe experiment or with a simulation with a poly-dispersed approach for the particle distribution.

Good agreement with the experiment results could be achieved for sparsely particle region like in steam drum turbulent region or Hewitt Run 6 case.

Though if the particle distribution correction factor and turbulence damping coefficient adjust to the kinetic energy profile measured by Fabre, Masbernat, and Suzanne (1987), the water carry over to the air is too high. But with this model set-up, which achieve a good approximation of the kinetic energy in the Fabre channel, the flow pattern in the feeding pipes are closer to the steam drum experiment, compare figure 8.1 with figure 7.4.

This advanced steam drum simulation shows, that a well-chosen combination of particle size and turbulence damping coefficient is suitable to reproduce the flow pattern in the feeding pipes, but a too high liquid volume fraction in the air phase is the consequence. In this advanced simulation the droplet mass flow on the left side is about $2.4e-04$ and on the right side $3.6e-04$. It is probably due to a too strong numerical diffusion of the mixture model approach. To analyse this model diffusion effect the droplet distribution above the interface have to be known. An experiment which provide such a droplet distribution in a pipe or channel is unknown to the author. One possibility to enhance the mono-dispersed approach could be, a validation with the poly-dispersed approach with the Euler-Euler particle model, because this

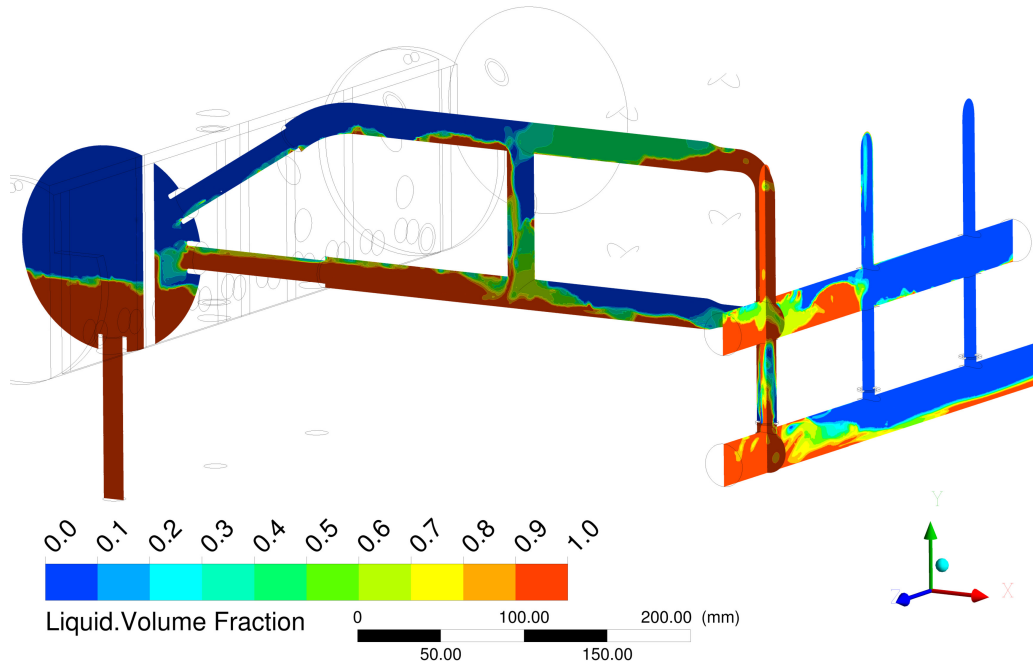


Figure 8.1: Experiment steam drum simulation; Coloured by liquid volume fraction; Cut through orifice pipe and feeding pipe set 3; Advanced interface interaction; figure by the author

poly-dispersed model can better reproduce such droplet distribution above the interface.

To design new or advanced steam drum internals the inlet velocities, inlet steam quality, flow pattern and interface positions have to be known. Until today these mentioned values before are rough estimated or unknown, so that an experiment for every design is needed to examine the separation performance. The simulation model with the Ishii-Zuber drag force and several non-drag forces and with the particle reconstruction model on basis of the AIAD model, can provide these needed values for a separator design process. In the steam drum simulations it can be seen, that the accuracy of the steam quality should be further improved, but the velocities, the flow pattern and the water interface positions can be reproduced with industrial accuracy. Therefore the examination of the steam drum behaviour under worst case scenarios or changing loads is now possible to simulate. Addition-

ally, separator design optimisations can be carried out now on the computer in a shorter time. That allowed the development of new steam drums, which are more suitable for a flexible boiler operation. These new developments would better provide the electrical grid stability with an increased amount of renewable energy technologies.

Future Work

To increase the reliability of the simulation model, tests with a steam/water mixture should be carried out. It is recommended to design an experiment with only the feeding pipe system and a steam/water mixture. So a feeding pipe simulation is much faster for such a system compared to a steam drum simulation, because the slow mass balance convergence of the drum water level would not exist. It becomes apparent that the flow pattern in such a pipe system is very sensitive regarding two-phase interaction inaccuracies and hence it is a good test case for a simulation model phase distribution.

Additional simulations with VLES or LES should be carried out to cancel out turbulence model inaccuracies and adjust the turbulence damping coefficient. Like mentioned above transport equations for the interface area density could be included in the simulation model. This extended model should offer the best compromise between accuracy and computational time.

Like mentioned above, instead of carry out an experiment, it could be possible to build up two simulations based on the Euler-Euler poly-dispersed approach. One simulation with liquid as the dispersed phase and one simulation with gas. This poly-dispersed approach should reproduce the particle distribution in more detail. So the mono-dispersed model can be validated with these poly-dispersed simulations. But an experiment is rather recommended.

Nomenclature

Acronyms

AIAD	Algebraic Interfacial Area Density
CDF	Cumulative distribution function
CEL	Command Expression Language; Interface in Ansys CFX software
CEL	Ansys CFX command expression language; program user interface
CFD	Computational Fluid Dynamics
CFX	CFD software from Ansys
ERK	ERK Eckrohkessel GmbH
FAD	Favre Averaged Drag
FDBR	Fachverband Dampfkessel-, Behälter- und Rohrleitungsbau e.V.
FVM	Finite-Volume-Method
HZDR	Helmholz-Zentrum Dresden Rossendorf
IAD	Interfacial area density
ILS	Interface length scale
iMUSIG	Inhomogeneous multiple bubble size group model
KH	Kelvin-Helmholtz

KHRT	Kelvin-Helmholtz Rayleigh-Taylor Hybrid model
LES	Large Eddy Simulation
NDMFD	Normal Droplet Mass Flow Deviation
NOW	In this thesis developed model
PBE	Population balance equation
PBM	Population balance model
PDF	Particle size distribution
R&D	Research and development
RMSD	Root mean square deviation
RRSB	Rosin, Rammler, Sperling and Bennet Distribution
RT	Rayleigh-Taylor
SMD	Sauter mean diameter
TDF	Triangle distribution function
UDF	Uniform distribution function
VLES	Very Large Eddy Simulation
VOF	Volume of fluid model

Greek Symbols

α	Angle between pipe axis and the horizontal; positive downward	$^{\circ}$
β	$k - \omega$ turbulence model constant, according Ansys (2016c)	—
Δt	Time interval	s
δ	interface thickness	m
ϵ	Turbulence eddy dissipation	m^2/s^3

λ	Second viscosity = $-\frac{2}{3}\mu$ (Stokes hypothesis), see Anderson (1995)	Pa · s
λ	Wave length	m
μ	Dynamic viscosity	Pa · s
ν	Kinematic viscosity	m ² /s
ν_{turb}	Turbulent or eddy kinematic viscosity	m ² /s
Φ^M	Mass flow	kg/s
Φ^V	Volume flow	m ³ /s
σ	Surface tension	N/m
σ_{turb}	Turbulent Schmidt number for volume fraction	—
τ	Viscous stress tensor	Pa
τ_{turb}	Turbulent stress tensor	Pa
Δ	Difference of a variable	—
Π	Pi number	—
ρ	Density	kg/m ³

Roman Symbols

Bo	Bond number, see Eo	—
Eo	Eötvös number or sometimes called Bond number Bo	—
Mo	Morton number	—
Re_p	Particle Reynolds number	—
γ	Distorted fluid particle distortion factor	m
\vec{F}	Force	N

\vec{f}	Mass specific volume force	N/kg
\vec{g}	Gravity acceleration vector	m/s ²
\vec{r}	Position vector	m
\vec{t}	Stress vector normal to free surface	N/m ²
\vec{t}_{fs}	Free surface tangential shear stress vector	N/m ²
\vec{U}	Velocity vector	m/s
A	Area, Surface	m ²
$A_{\alpha\beta}$	Interfacial area density; interfacial area per unit volume between phase α and phase β	1/m
a_b	AIAD model constant for bubble regime	—
a_d	AIAD model constant for droplet regime	—
B	$k - \omega$ interface damping model parameter	—
B_v	Steam volume strain	m ³ /(h · m ³)
C_D	Drag coefficient	—
c_g	AIAD parameter	m
C_{RT}	Adjustable constant for RTB model, see Reitz and Beale (1999)	—
C_{TD}	Multiplier for FAD drag model	—
cp	Specific heat capacity at constant pressure	J/(kg · K)
d	Diameter	m
d_{32}	Sauter mean diameter	m
d_H	Maximum horizontal dimension of a distorted fluid particle	m
$d'_{p,RRSB}$	Scale parameter in RRSB distribution	m

d_V	Maximum vertical dimension of a distorted fluid particle	m
E	Aspect ratio of a distorted fluid particle	—
e	Mass specific internal (thermal) energy	J/kg
E_f	Aspect ratio frontal part of a distorted fluid particle	—
f	Blending function in AIAD model	—
h	Mass specific enthalpy	J/kg
K	Angular wave number	1/m
k	Thermal conductivity coefficient	W/(m · K)
ke	Kinetic energy	—
L	Characteristic length	m
M	Indicator function	—
M	Mass	kg
mf	Mass fraction	—
N	Count	—
n_{RRSB}	Shape parameter RRSB distribution	—
$NKED$	Normalised kinetic energy deviation	—
$NPGD$	Normalised pressure gradient deviation	—
NVD	Normalised velocity deviation	—
$NWLD$	Normalised water level deviation	—
p	Pressure	Pa
q	Steam quality	—
S_h	Volume specific heat source	W/m ³

S_{Mass}	Interfacial mass source	kg/m ³
S_{Mom}	Interfacial momentum source	N/m ³
S_M	Volume specific momentum source	N/m ³
S_{st}	Mixture momentum source due to surface tension	N/m ³
t	Time	s
u	Velocity x component in cartesian coordinate system	m/s
V	Volume	m ³
v	Velocity y component in cartesian coordinate system	m/s
vf	Volume fraction, void fraction	-
w	Velocity z component in cartesian coordinate system	m/s
We	Weber number	-
x	Cartesian coordiante system x coordinate variable	m
y	Cartesian coordiante system y coordinate variable	m
y_W	Nearest wall distance	m
YH	Cumulative distribution function	-
yH	Probability density function, Relative frequency	-
z	Cartesian coordiante system z coordinate variable	m

Superscripts

*	Modified
B	Basset
D	Drag
L	Lift

T	Turbulent dispersion
V	Virtual mass
W	Wall-lift or wall-lubrication

Subscripts

α	Fluid identifier; continous phase
β	Fluid identifier; dispersed phase
γ	Fluid identifier
∞	Single particle in infinite media
<i>abs</i>	Absolute value
<i>ave</i>	Average; in steady state 10.000 iterations; in transient 10 seconds
<i>b</i>	Bubble
<i>c</i>	Continuous phase
<i>crit</i>	Critical
<i>d</i>	Droplet
<i>disp</i>	Dispersed phase
<i>eff</i>	Effective
<i>exp</i>	Regarding experiment
<i>fc</i>	Forced convection
<i>fs</i>	Free surface
<i>g</i>	Gas phase
<i>i, j</i>	Control variable
<i>K</i>	Sphere

<i>k</i>	Control variable for phases
<i>K, Veq</i>	Volume equivalent
<i>l</i>	Liquid phase
<i>lim</i>	Limit
<i>m</i>	Mode of particle distribution
<i>max</i>	Maximum
<i>min</i>	Minimum
<i>mix</i>	Mixture
<i>p</i>	Particle
<i>par</i>	Regarding particle model
<i>proj</i>	Projection
<i>ref</i>	Reference
<i>rel</i>	Relative
<i>RRSB</i>	Regarding RRSB distribution
<i>RT</i>	Rayleigh-Taylor
<i>s</i>	Superficial, for single phase flow
<i>sim</i>	Regarding simulation
<i>sphere</i>	Sphere
<i>t</i>	Turbulence
<i>tot</i>	Total
<i>triangle</i>	Regarding triangle distribution
<i>turb</i>	Turbulence
<i>uniform</i>	Regarding uniform distribution

List of Figures

2.1	Two-phase flow pattern for a liquid-gaseous-flow in adiabatic vertical pipe. a) bubble flow; b) plug flow; c) churn flow; d) wispy-annular flow; e) annular flow; f) spray or drop flow; Baehr and Stephan 2016	5
2.2	Two-phase flow pattern for a liquid-gaseous-flow in adiabatic horizontal pipe. a) bubble flow; b) plug flow; c) stratified flow; d) wavy flow; e) slug flow; f) annular flow; g) spray or drop flow Baehr and Stephan 2016	7
2.3	Flow pattern regions in two-phase flow, mass velocity of gas phase above ratio of liquid and gas mass velocities Baker 1958	9
2.4	Generalised Taitel and Dukler (1976) flow map for horizontal two-phase flow; figure by the author	11
2.5	Schematic drawing of an Eckrohrkessel steam boiler; figure by the author	14
2.6	Eckrohrkessel boiler types: (a) grate firing system single drum boiler, (b) fluidised bed single drum boiler, (c) tail end single drum boiler for waste incineration, (d) gas/oil burner bi drum boiler; ERK Eckrohrkessel GmbH 2018	16
2.7	Steam drum with natural steam/water separation and different steaming rates; see Kitto and Stultz (2005)	19
2.8	Steam drum with natural steam/water separation and different inlet locations of; see Kitto and Stultz (2005)	21

2.9	Eckrohrkessel baffle and scrubber drum internals 3D drawing: (a) Drum baffle internals for single drum boiler, (b) Drum baffle internals for bi drum boilers; ERK Eckrohrkessel GmbH 2018	22
2.10	Eckrohrkessel baffle and scrubber drum internals pictures at side: (a) longitudinal and side baffle plate arrangement, (b) side baffle plate and scrubber box for steam outlet at the top of the drum; ERK Eckrohrkessel GmbH 2018	23
2.11	Typical steam/water mechanical separators: (a) Conical cyclone, (b) Curved arm, (c) horizontal cyclone separator, (d) vertical cyclone separator; Kitto and Stultz 2005	24
2.12	Steam drum internals with three rows of cyclone separators; see Kitto and Stultz (2005)	25
2.13	Local instant formulation of fluid density in time; figure by the author	35
2.14	Local instant formulation of arbitrary variable with various time intervals; figure by the author	36
2.15	Blending functions f_b , f_d and f_{fs} regarding to 2.57; figure by the author	49
2.16	Two-phase surface layer; upper and lower bounds are indicated with dashed lines; mean free surface is given with a solid line; Brocchini and Peregrine 2001	50
2.17	Schematic drawing of sphere in simple shear flow; figure by the author	57
2.18	Distorted fluid particle with dimensions following Tomiyama et al. (2002a)	60
2.19	Deformation of drops and bubbles in pure Water; Clift, Grace, and Weber 1978	61
2.20	Schematic drawing of drainage around a sphere near the wall; figure by the author	62
2.21	FAD multiplier decreasing function; figure by the author	64

3.1	Shape regimes for bubbles and drops in unhindered gravitational motion through liquids; Clift, Grace, and Weber 1978	81
3.2	Single particle drag coefficient by plotting equation for viscous regime drag coefficient and drag limits; figure by the author	87
3.3	Drag coefficient for droplets and bubbles with 2 mm diameter in multiparticle system by plotting equation 3.43; air-water at 25 °C, 1 atm; figure by the author	91
3.4	Maximum particle radius for droplets and bubbles in multiparticle system by plotting equation 3.48 and 3.47; air-water at 25 °C, 1 atm; figure by the author	91
4.1	Example of NOW model CEL function; by the author	98
4.2	Example of NOW model CEL constant; by the author	98
4.3	Interfacial Area Density Implementation with RRSB distribution in Ansys CFX Mixture Model; by the author	99
5.1	Steam drum flow pattern with natural steam/water separation; see Kitto and Stultz 2005	102
5.2	Fabre channel general experiment set-up scheme, see Fabre, Masbernat, and Suzanne (1987)	104
5.3	Fabre channel CFD 2D geometry with dimensions for run reference 400 data (table 5.1); figure by the author	106
5.4	Fabre channel CFD 2D mesh; figure by the author	107
5.5	Fabre channel CFD model boundary conditions; figure by the author	108
5.6	Fabre channel run reference 400 data (table 5.1) mesh study; normalised pressure gradient deviation (NPGD) over number of Elements; figure by the author	114
5.7	Fabre channel run reference 400 data (table 5.1) mesh study; sum of normalised RMS kinetic energy, normalised RMS velocity, normalised water level and normalised RMS pressure gradient value for different mesh sizes; figure by the author	115

5.8	Fabre channel run reference 400 data (table 5.1) distribution function study; sum of normalised RMS kinetic energy, normalised RMS velocity, normalised water level and normalised RMS pressure gradient value for different simulation setups; figure by the author	122
5.9	Fabre channel run reference 400 data (table 5.1) validation; sum of average normalised RMS kinetic energy, average normalised RMS velocity, normalised water level and average normalised RMS pressure gradient value for different cases; figure by the author	127
5.10	Fabre channel run reference 400 data (table 5.1) validation; Liquid volume fraction at $x = 3\text{m}$ above the channel height Y for case F_000 and FV_010; figure by the author	128
5.11	Fabre channel run reference 400 data (table 5.1) validation; Kinetic energy at $x = 3\text{m}$ above the channel height Y for case F_000 and FV_020; figure by the author	130
5.12	Fabre channel run reference 400 data (table 5.1) validation; Velocity at $x = 3\text{m}$ above the channel height Y for case F_000 and FV_100; figure by the author	132
5.13	Fabre channel run reference 400 data (table 5.1) validation; IAD times CD at $x = 3\text{m}$ above the channel height Y for case F_000 and FV_030; figure by the author	133
5.14	Fabre channel run reference 400 data (table 5.1) validation; Kinetic energy at $x = 3\text{m}$ above the channel height Y for case F_000, FV_040 and FV_050; figure by the author	134
5.15	Fabre channel run reference 400 data (table 5.1) validation; Drag force at $x = 3\text{m}$ above the channel height Y for case F_000, FV_060 and FV_070; figure by the author	136
5.16	Fabre channel run reference 400 data (table 5.1) validation; Interface area density times drag coefficient at $x = 3\text{m}$ above the channel height Y for case F_000, FV_060 and FV_070; figure by the author	137

5.17	Fabre channel run reference 400 data (table 5.1) validation; Liquid volume fraction at $x = 3\text{m}$ above the channel height Y for case F_000, FV_060 and FV_070; figure by the author . . .	138
5.18	Fabre channel run reference 400 data (table 5.1) validation; Drag force at $x = 3\text{m}$ above the channel height Y for case F_000 and FV_120; figure by the author	140
5.19	Fabre channel run reference 400 data (table 5.1) validation; Liquid volume fraction at $x = 3\text{m}$ above the channel height Y for case F_000 and FV_120; figure by the author	141
6.1	Hewitt and Owen (1987) experiment set-up scheme; see He- witt and Owen 1987	147
6.2	Hewitt CFD model drawing with dimensions; figure by the author	149
6.3	Hewitt CFD model; surface mesh; figure by the author	150
6.4	Hewitt CFD model; 2D mesh at inlet; figure by the author . .	150
6.5	Hewitt CFD model; boundary conditions; figure by the author	151
6.6	Hewitt CFD model, Run No. 6; mass imbalances over itera- tions; figure by the author	153
6.7	Hewitt CFD model pressure gradient over iterations (a) Run No. 1, (b) Run No. 6; figure by the author	155
7.1	ERK steam drum internals schematic drawing; Schreiber, Hellwig, and Nowitzki 2017	159
7.2	Construction of the steam drum experiment; Schreiber, Hell- wig, and Nowitzki 2017	162
7.3	Construction of the steam drum experiment feeding pipes; Schreiber, Hellwig, and Nowitzki 2017	163
7.4	Feeding pipes set 3 visual water level snapshot; case 500 L/h water and $25\text{ m}^3/\text{h}$; (a) mixture pipe in front of connection pipe G3.1, (b) mixture pipe behind connection pipe G3.2, (c) overflow pipe in front of connection pipe Ü3.1, (d) overflow pipe behind connection pipe Ü3.2; Schreiber, Hellwig, and Nowitzki 2017	165

7.5	Naming of feeding pipes in experiment steam drum regarding water content and flow pattern; Schreiber, Hellwig, and Nowitzki 2017	166
7.6	CFD Construction of the steam drum experiment with dimensions; Wehner, Hellwig, and Nowitzki 2017	168
7.7	3D drawing of the experiment steam drum; figure by the author	169
7.8	Mesh overview of the experiment steam drum cut; Coloured by volume size; figure by the author	170
7.9	Mesh details of the experiment steam drum; Coloured by volume size, (a) steam drum, (b) steam drum stage 1, (c) distributor pipe, (d) orifice pipe; figure by the author	171
7.10	Experiment steam drum simulation; Coloured by liquid volume size, feeding pipe (a) set 1, (b) set 2, (c) set 3; figure by the author	177
7.11	Experiment steam drum simulation; Coloured by liquid volume fraction; cut planes through orifice pipes and feeding pipe set 3 and a detail of phase separation in orifice pipe; figure by the author	179
8.1	Experiment steam drum simulation; Coloured by liquid volume fraction; Cut through orifice pipe and feeding pipe set 3; Advanced interface interaction; figure by the author	185
C.1	Hewitt CFD model, exemplary 2m section of the vertical pipe, Run No. 1; coloured by Eötvös number, interface length scale, bubble blend function and liquid volume fraction; figure by the author	226
C.2	Hewitt CFD model, exemplary 2m section of the vertical pipe, Run No. 6; coloured by Eötvös number, interface length scale, bubble blend function and liquid volume fraction; figure by the author	227
D.1	Mesh of the experiment steam drum cut; Detail Steam Drum; Coloured by volume size; figure by the author	229

D.2	Mesh of the experiment steam drum cut; Detail Steam Drum Stage 1; Coloured by volume size; figure by the author	230
D.3	Mesh of the experiment steam drum cut; Detail Distributor; Coloured by volume size; figure by the author	231
D.4	Mesh of the experiment steam drum cut; Detail Orifice Pipe; Coloured by volume size; figure by the author	232

List of Tables

2.1	Part of the nomenclature in Baker (1958)	9
2.2	Comparison of Baehr and Stephan (2016) horizontal flow pattern (figure 2.2) and Baker (1958) flow map (figure 2.3)	10
2.3	Drag coefficient correlations for particle model available in Ansys CFX; see Ansys 2016c	44
5.1	Fabre channel experiment general data; Fabre, Masbernat, and Suzanne 1987	105
5.2	Fabre channel experiment water velocity and turbulence energy profile run reference 400 data (table 5.1); Fabre, Masbernat, and Suzanne 1987	105
5.3	Fabre channel experiment air velocity and turbulence energy profile run reference 400 data (table 5.1); Fabre, Masbernat, and Suzanne 1987	106
5.4	Fabre channel mesh study simulation model parameter	112
5.5	Fabre channel mesh study pressure gradient and normalised pressure gradient deviation (NPGD); run reference 400 data (table 5.1)	113
5.6	Fabre channel distribution study simulation cases overview . .	120
5.7	Distribution function study results of average NPGD, NWLD, average NVD, average NKED, average liquid mass flow out of air outlet and the line average Sauter mean diameter at $x=3.5$ m ; Column minimum value coloured in green and maximum in red; Fabre channel run reference 400 data (table 5.1)	121
5.8	Fabre channel validation simulation cases overview	125

5.9	Validation results of average NPGD, NWLD, average NVD, average NKED and average liquid mass flow out of air outlet (MF Liq); Column minimum value coloured in green and maximum in red; Fabre channel run reference 400 data (table 5.1)	126
6.1	Hewitt vertical pipe experiment constant parameter; Hewitt and Owen 1987	146
6.2	Extract of Hewitt vertical pipe experiment results; observed flow regime and pressure gradient; Hewitt and Owen 1987	147
6.3	Hewitt proof of concept results; Averaged NPGD, observed flow regime from experiment and CFD simulation	154
7.1	Droplet mass flow out of experiment left and right steam drum side	167
7.2	Steam drum experiment global mesh parameters	168
7.3	Steam drum experiment local refinement mesh parameters	169
7.4	Steam drum simulation droplet mass flow at sides; water volume flow 0.5 m ³ /h, gas volume flow 25 m ³ /h, 1 atm	175

Bibliography

- Al-Sheikh, J. N., D. E. Saunders, and Robert S. Brodkey (1970).
„Prediction of flow patterns in horizontal two-phase pipe flow“.
In: *The Canadian Journal of Chemical Engineering* 48.1, pp. 21–29.
DOI: 10.1002/cjce.5450480105.
- Anderson, John David (1995).
Computational fluid dynamics: The basics with applications.
Internat. ed.
McGraw-Hill series in aeronautical and aerospace engineering.
New York: McGraw-Hill. ISBN: 0070016852.
- Ansys (2016a). *CFX-Pre User Guide 17.2*.
— (2016b). *CFX-Solver Modeling Guide*.
— (2016c). *CFX Theory Guide 17.2*.
— (2016d). *Fluent Theory Guide 17.2*.
- Antal, S. P., R. T. Lahey, and J. E. Flaherty (1991). „Analysis of phase distribution in fully developed laminar bubbly two-phase flow“.
In: *International Journal of Multiphase Flow* 17.5, pp. 635–652.
ISSN: 03019322. DOI: 10.1016/0301-9322(91)90029-3. URL: <http://www.sciencedirect.com/science/article/pii/0301932291900293>.
- Apte, S. V., M. Gorokhovski, and P. Moin (2003). „LES of atomizing spray with stochastic modeling of secondary breakup“.
In: *International Journal of Multiphase Flow* 29, pp. 1503–1522.
ISSN: 03019322.
- Avdeev, Alexander A. (2016). *Bubble Systems*. Mathematical Engineering.
Cham and s.l.: Springer International Publishing. ISBN: 9783319292861.

- DOI: 10.1007/978-3-319-29288-5.
URL: <http://dx.doi.org/10.1007/978-3-319-29288-5>.
- Aybers, N. M. and A. Tapucu (1969). „Studies on the drag and shape of gas bubbles rising through a stagnant liquid“.
In: *Wärme - und Stoffübertragung* 2.3, pp. 171–177. ISSN: 1432-1181.
DOI: 10.1007/BF00751164.
URL: <https://doi.org/10.1007/BF00751164>.
- Baehr, Hans Dieter and Karl Stephan (2016).
Wärme- und Stoffübertragung. 9., aktualisierte Auflage. Lehrbuch.
Berlin and Heidelberg: Springer Vieweg. ISBN: 3662496763.
- Baker, Ovid (1954). „Simultaneous Flow of Oil and Gas“.
In: *Oil and Gas Journal* 53, pp. 185–195.
- (1958). „Multiphase flow in pipelines“. In: *Pipeline News*, pp. 156–167.
- Barnea, D. (1987). „A unified model for predicting flow-pattern transitions for the whole range of pipe inclinations“.
In: *International Journal of Multiphase Flow* 13.1, pp. 1–12.
ISSN: 03019322. DOI: 10.1016/0301-9322(87)90002-4.
- Barnea, Dvora et al. (1980).
„Flow pattern transition for gas-liquid flow in horizontal and inclined pipes. Comparison of experimental data with theory“.
In: *International Journal of Multiphase Flow* 6.3, pp. 217–225.
ISSN: 03019322. DOI: 10.1016/0301-9322(80)90012-9.
- Bošnjaković, Fran and Karl Friedrich Knoche (1988).
Technische Thermodynamik. 7., neubearb. und erw. Aufl. Vol. 11,1.
Wärmelehre und Wärmewirtschaft.
Leipzig: Dt. Verl. für Grundstoffindustrie. ISBN: 3342003189.
- Brocchini, Maurizio and D. H. Peregrine (2001). „The dynamics of strong turbulence at free surfaces. Part 2. Free-surface boundary conditions“.
In: *Journal of Fluid Mechanics* Volume 449, pp. 255–290.
DOI: 10.1017/S0022112001006024.
- Brodkey, Robert. S. (2005). *The Phenomena of Fluid Motions*.
Ohio, USA: Brodkey Publishing. ISBN: 0972663576.

- Burns, Alan et al. (2004).
5th International Conference on Multiphase Flow: The Favre Averaged Drag Model for Turbulent Dispersion in Eulerian Multi-Phase Flows.
 Yokohama, Japan.
- Cheremisinoff, Nicholas P. and Ramesh Gupta, eds. (1983).
Handbook of fluids in motion. Boston: Butterworths. ISBN: 0250404583.
- Clift, Roland, J. R. Grace, and M. E. Weber (1978).
Bubbles, drops, and particles. New York: Academic Press.
 ISBN: 012176950X.
- Drew, D. A. and R. T. Lahey (1987). „The virtual mass and lift force on a sphere in rotating and straining inviscid flow“.
 In: *International Journal of Multiphase Flow* 13.1, pp. 113–121.
 ISSN: 03019322. DOI: 10.1016/0301-9322(87)90011-5. URL: <http://www.sciencedirect.com/science/article/pii/0301932287900115>.
- Dukler, A. E. and Yehuda Taitel (1986). „Flow Pattern Transitions in Gas-Liquid Systems: Measurement and Modeling“.
 In: *Multiphase Science and Technology*. Ed. by Geoffrey Frederick Hewitt, Jean-Marc Delhay, and Novak Zuber.
 Vol. 2. Springer-Verlag Berlin. ISBN: 3-540-16408-1.
- Egorov, Yury (2004). *Validation of CFD codes with PTS-relevant test cases*.
 Ed. by EVOL-ECORA-D07.
- Epple, Bernd et al., eds. (2012).
Simulation von Kraftwerken und Feuerungen. 2., erw. und korr. Aufl.
 Wien: Springer. ISBN: 9783709111819.
- ERK Eckrohrkessel GmbH (2018). *internal raw material*.
- Ervin, E. A. and G. Tryggvason (1997).
 „The Rise of Bubbles in a Vertical Shear Flow“.
 In: *Journal of Fluids Engineering* 119.2, pp. 443–449. ISSN: 0098-2202.
 DOI: 10.1115/1.2819153.
 URL: <http://dx.doi.org/10.1115/1.2819153>.
- Fabre, J., L. Masbernat, and C. Suzanne (1987).
 „Stratified Flow, Part I: Local Structures“.
 In: *Multiphase Science and Technology*. Ed. by

- Geoffrey Frederick Hewitt, Jean-Marc Delhay, and Novak Zuber.
Vol. 3. Springer-Verlag Berlin, pp. 285–301. ISBN: 3-540-17791-4.
- FDBR (2013). *FDBR-Handbuch: Wärme- und Strömungstechnik*.
FDBR Fachverband Dampfkessel-, Behälter- und Rohrleitungsbau e.V.
- Flügge, Siegfried et al. (1959). *Strömungsmechanik I: Fluid dynamics I*.
Vol. Bd. VIII/1. Handbuch der Physik Encyclopedia of physics.
Berlin, Göttingen, and Heidelberg: Springer.
- Govier, G. W. and M. M. Omer (1962).
„The Horizontal Pipeline Flow of Air-Water Mixtures“.
In: *The Canadian Journal of Chemical Engineering* 40, pp. 93–104.
DOI: 10.1002/cjce.5450400303.
- Griffith, Peter and Graham B. Wallis (1961). „Two-Phase Slug Flow“.
In: *Journal of Heat Transfer* 83.3, pp. 307–318.
DOI: 10.1115/1.3682268.
URL: <http://dx.doi.org/10.1115/1.3682268>.
- Harlow, Francis H. and Anthony A. Amsden (1975).
„Numerical Calculation of Multiphase Fluid Flow“.
In: *Journal of Computational Physics* Vol 17, pp. 19–52.
- Harmathy, Tibor Z. (1960). „Velocity of large drops and bubbles in media
of infinite or restricted extent“.
In: *AIChE Journal* Vol. 6.2, pp. 281–288.
- Hayter, Anthony J. (2007).
Probability and statistics for engineers and scientists. 3 ed.
International student edition. Pacific Grove: Duxbury.
ISBN: 9780495108788.
- Hewitt, Geoffrey Frederick and D. G. Owen (1987).
„Pressure Drop and Entrained Fraction in Fully Developed Flow“.
In: *Multiphase Science and Technology*. Ed. by
Geoffrey Frederick Hewitt, Jean-Marc Delhay, and Novak Zuber.
Vol. 3. Springer-Verlag Berlin, pp. 145–154. ISBN: 3-540-17791-4.
- Höhne, Thomas (2009). „Experiments and Numerical Simulations of
Horizontal Two Phase Flow Regimes“. In: *Seventh International
Conference on CFD in the Minerals and Process Industries*.

- Höhne, Thomas and Christophe Vallée (2010).
 „Experiments and Numerical Simulations of Horizontal Two-Phase Flow Regimes Using an Interfacial Area Density Model“.
 In: *The Journal of Computational Multiphase Flows* 2.3, pp. 131–143.
 DOI: 10.1260/1757-482X.2.3.131.
 URL: <https://doi.org/10.1260/1757-482X.2.3.131>.
- Huhn, Jörg and Joachim Wolf (1975).
Zweiphasenströmung: Gasförmig/flüssig. 1. Aufl. Leipzig: Fachbuchverl. HZDR and Ansys, eds. (2016).
14th Multiphase Flow Conference and Short Course.
- Ishii, Mamoru and Takashi Hibiki (2006).
Thermo-fluid Dynamics of Two-Phase Flow. 1. Ed. Berlin: Springer US. ISBN: 0387283218.
- Ishii, Mamoru and Novak Zuber (1979). *Drag coefficient and relative velocity in bubbly, droplet or particulate flows: Drag coefficient and relative velocity in bubbly, droplet or particulate flows*.
 New York: American Institute of Chemical Engineers.
- Kandlikar, Satish G., ed. (1999).
Handbook of phase change: Boiling and condensation.
 Philadelphia, Pa.: Taylor & Francis. ISBN: 1560326344. URL: <http://www.loc.gov/catdir/enhancements/fy0653/99026754-d.html>.
- Kitto, John B. and Stultz, eds. (2005). *Steam: Its generation and use*.
 41. ed., 1. print. Barberton, Ohio: Babcock & Wilcox. ISBN: 0963457012.
- Kolev, Nikolay Ivanov (2012).
Multiphase Flow Dynamics 2: Mechanical Interactions.
 Berlin, Heidelberg: Springer Berlin Heidelberg. ISBN: 9783642205972.
 DOI: 10.1007/978-3-642-20598-9.
 URL: <http://dx.doi.org/10.1007/978-3-642-20598-9>.
- Kotz, Samuel and Johan René van Dorp (2004).
Beyond beta: Other continuous families of distributions with bounded support and applications. Singapore and London: World Scientific.
 ISBN: 9789812561152. URL: <http://search.ebscohost.com/login.aspx?direct=true&scope=site&db=nlebk&db=nlabk&AN=167309>.

- Krepper, Eckhard (1999). *HZDR Annual Report 1999: CFD Simulations of a Bubbly Flow in a Vertical Pipe*. Ed. by F. Weiß and U. Rindelhard. Dresden.
- Lockhart, R. and R. Martinelli (1949). „Proposed correlation of data for isothermal two-phase, two-component flow in pipes“.
In: *Chemical Engineering Progress* 45.1, pp. 39–48.
- Lucas, Dirk and Eckhard Krepper (2007).
CFD models for polydispersed bubbly flows. Vol. 486.
Wissenschaftlich-technische Berichte / FZD, Forschungszentrum Dresden-Rossendorf. Dresden: FZD.
- Luo, Hean and Hallvard F. Svendsen (1996).
Theoretical model for drop and bubble breakup in turbulent dispersions: Theoretical model for drop and bubble breakup in turbulent dispersions.
New York: American Institute of Chemical Engineers.
- Mahaffy, J. et al. (2015). *Best Practice Guidelines for the Use of CFD in Nuclear Reactor Safety Application - Revision: JT03370465; OECD Nuclear Energy Agency (NEA) 2015*.
- Mayr, Fritz and Thomas Gritsch, eds. (1997).
Handbuch der Kesselbetriebstechnik: Kraft- und Wärmeerzeugung in Praxis und Theorie. 7., erg. und verb. Aufl. Gräfelfing: Resch.
ISBN: 3930039133.
- Mishima, Kaichiro and Mamoru Ishii (1984). „Flow Regime Transition Criteria for Upward Two-Phase Flow in Vertical Tubes“.
In: *International Journal of Heat and Mass Transfer* 27.5, pp. 723–737.
- Pellacani, Filippo (2012). *Development and Validation of Bubble Breakup and Coalescence Constitutive Models for the One-Group Interfacial Area Transport Equation*. München.
- Porombka, P. and T. Höhne (2015). „Drag and turbulence modelling for free surface flows within the two-fluid Euler–Euler framework“.
In: *Chemical Engineering Science* 134, pp. 348–359. ISSN: 00092509.
DOI: 10.1016/j.ces.2015.05.029.
- Prof. Dr. J. Tomas (2014). „Mechanical Process Engineering - Particle Technology Disperse Systems - Script“.

- Prosperetti, A. and A.V. Jones (1984).
 „Pressure forces in disperse two-phase flow“.
 In: *International Journal of Multiphase Flow* 10.4, pp. 425–440.
 ISSN: 03019322. DOI: 10.1016/0301-9322(84)90054-5.
- Reitz, Rolf D. (1987).
 „Modeling atomization processes in high-pressure vaporizing sprays“.
 In: *Atomisation Spray Technology* 3, pp. 309–337.
- Reitz, Rolf D. and Jennifer C. Beale (1999).
 „MODELING SPRAY ATOMIZATION WITH THE
 KELVIN-HELMHOLTZ/RAYLEIGH-TAYLOR HYBRID MODEL“.
 In: *Atomization and Sprays* 9.6, pp. 623–650. ISSN: 1044-5110.
- Roscoe, R. (1952). „The viscosity of suspensions of rigid spheres“.
 In: *British Journal of Applied Physics* Volume 3.Issue 8, pp. 267–269.
- Saffman, P. G. (1965). „The lift on a small sphere in a slow shear flow“.
 In: *Journal of Fluid Mechanics* 22.2, pp. 385–400.
 DOI: 10.1017/S0022112065000824.
- Schreiber, Simon, Udo Hellwig, and Mario Nowitzki (2017). *Konstruktion,
 Aufbau und Erprobung zur Trennung von Zweiphasengemischen*.
 Wildau.
- Stieß, Matthias (2009).
Mechanische Verfahrenstechnik - Partikeltechnologie 1.
 3., vollst. neu bearb. Aufl. Springer-Lehrbuch.
 Berlin, Heidelberg: Springer Berlin Heidelberg. ISBN: 9783540325512.
 DOI: 10.1007/978/3-540-32552-9. URL: [http://site.ebrary.com/
 lib/alltitles/docDetail.action?docID=10257925](http://site.ebrary.com/lib/alltitles/docDetail.action?docID=10257925).
- Taitel, Yehuda, Dvora Bornea, and A. E. Dukler (1980). „Modelling flow
 pattern transitions for steady upward gas-liquid flow in vertical tubes“.
 In: *AIChE Journal* 26.3, pp. 345–354. DOI: 10.1002/aic.690260304.
- Taitel, Yemada and A. E. Dukler (1976).
*A model for predicting flow regime transitions in horizontal and near
 horizontal gas-liquid flow: A model for predicting flow regime transitions
 in horizontal and near horizontal gas-liquid flow*.
 New York: American Institute of Chemical Engineers.

- Taylor, G. I. (1932).
 „The Viscosity of a Fluid Containing Small Drops of Another Fluid“.
 In: *Royal Society* Volume 138.issue 834, pp. 41–48.
- Tomiyama, A., ed. (2002). *SINGLE BUBBLES IN STAGNANT LIQUIDS AND IN LINEAR SHEAR FLOWS*.
- Tomiyama, A. et al. (2002a). „Terminal velocity of single bubbles in surface tension force dominant regime“.
 In: *International Journal of Multiphase Flow* 28.9, pp. 1497–1519.
 ISSN: 03019322. DOI: 10.1016/S0301-9322(02)00032-0. URL: <http://www.sciencedirect.com/science/article/pii/S0301932202000320>.
- Tomiyama, Akio et al. (2002b).
 „Transverse migration of single bubbles in simple shear flows“.
 In: *Chemical Engineering Science* 57, pp. 1849–1858. ISSN: 00092509.
- Vallée, Christophe and Thomas Höhne (2006).
 „CFD VALIDATION OF STRATIFIED TWO-PHASE FLOWS IN A HORIZONTAL CHANNEL“. In: *Annual Report 2006*. Dresden, pp. 33–38.
- Vallée, Christophe et al. (2008). „Experimental investigation and CFD simulation of horizontal stratified two-phase flow phenomena“.
 In: *Nuclear Engineering and Design* 238.3, pp. 637–646. ISSN: 0029-5493.
 DOI: 10.1016/j.nucengdes.2007.02.051.
- Versteeg, Henk K. and Weeratunge Malalasekera (2007). *An introduction to computational fluid dynamics: The finite volume method*.
 2. ed., [Nachdr.] Harlow: Pearson/Prentice Hall. ISBN: 9780131274983.
- Wallis, Graham B. (1969). *One-dimensional two-phase flow*.
 New York: McGraw-Hill. ISBN: 0070679428.
- Wehner, Michelle, Udo Hellwig, and Mario Nowitzki (2017).
Numerische Simulation des Stoffgemisches Luft-Wasser im Modell einer technischen Dampftrommel.
- Wellek, R. M., A. K. Agrawal, and A. H. P. Skelland (1966).
 „Shape of liquid drops moving in liquid media“.
 In: *AIChE Journal* 12.5, pp. 854–862. ISSN: 0001-1541.
 DOI: 10.1002/aic.690120506.

- Winnikow, S. and B. T. Chao (1966).
„Droplet Motion in Purified Systems“.
In: *The Physics of Fluids* 9.1, pp. 50–61. ISSN: 0031-9171.
DOI: 10.1063/1.1761532.
- Wu, Benjamin et al. (2017). „A critical review of flow maps for gas-liquid flows in vertical pipes and annuli“.
In: *Chemical Engineering Journal* 326, pp. 350–377. ISSN: 1385-8947.
DOI: 10.1016/j.cej.2017.05.135. URL: <http://www.sciencedirect.com/science/article/pii/S1385894717308938>.
- XIN, J., L. RICART, and R. D. REITZ (1998).
„Computer Modeling of Diesel Spray Atomization and Combustion“.
In: *Combustion Science and Technology* 137.1-6, pp. 171–194.
DOI: 10.1080/00102209808952050.
URL: <https://doi.org/10.1080/00102209808952050>.
- Zogg, Martin (1993). *Einführung in die mechanische Verfahrenstechnik: Mit 29 Tabellen und 32 Berechnungsbeispielen*. 3., überarb. Aufl.
Stuttgart: Teubner. ISBN: 3519163195.

Acknowledgements

I could not have written this thesis without the support from Prof. Dr.-Ing Udo Hellwig and Prof. Thomas Mirre. They gave me inspiration and had my back.

Many thanks to my supervisors Prof. Dr.-Ing. Fabian Mauß and Prof. Dr.-Ing. Hans-Joachim Krautz and all the people in the background who supported me.

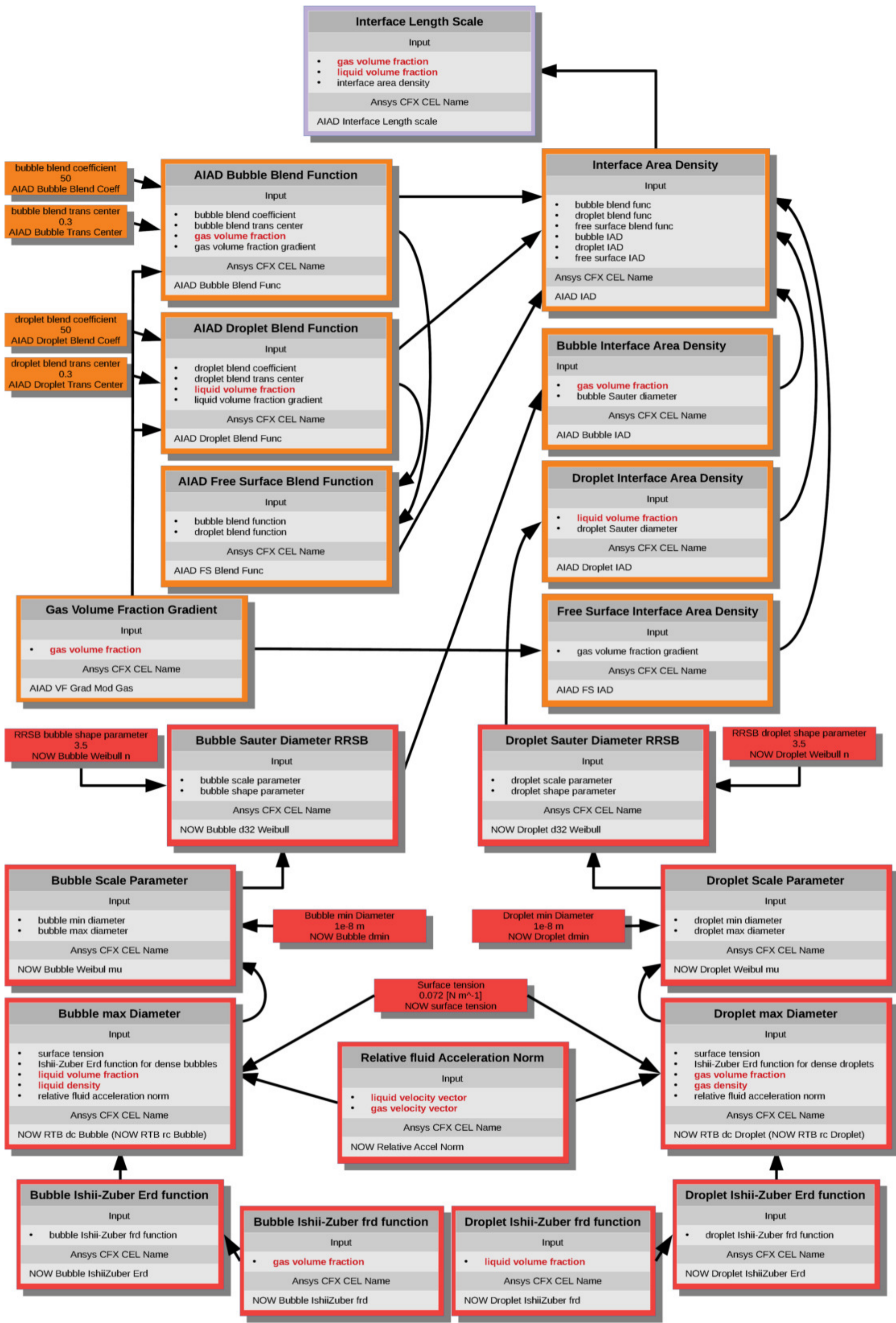
Dr. Thomas Höhne from the HZDR very kindly provided the source code for the AIAD model.

Appendices

Appendix A

Interface Area Density

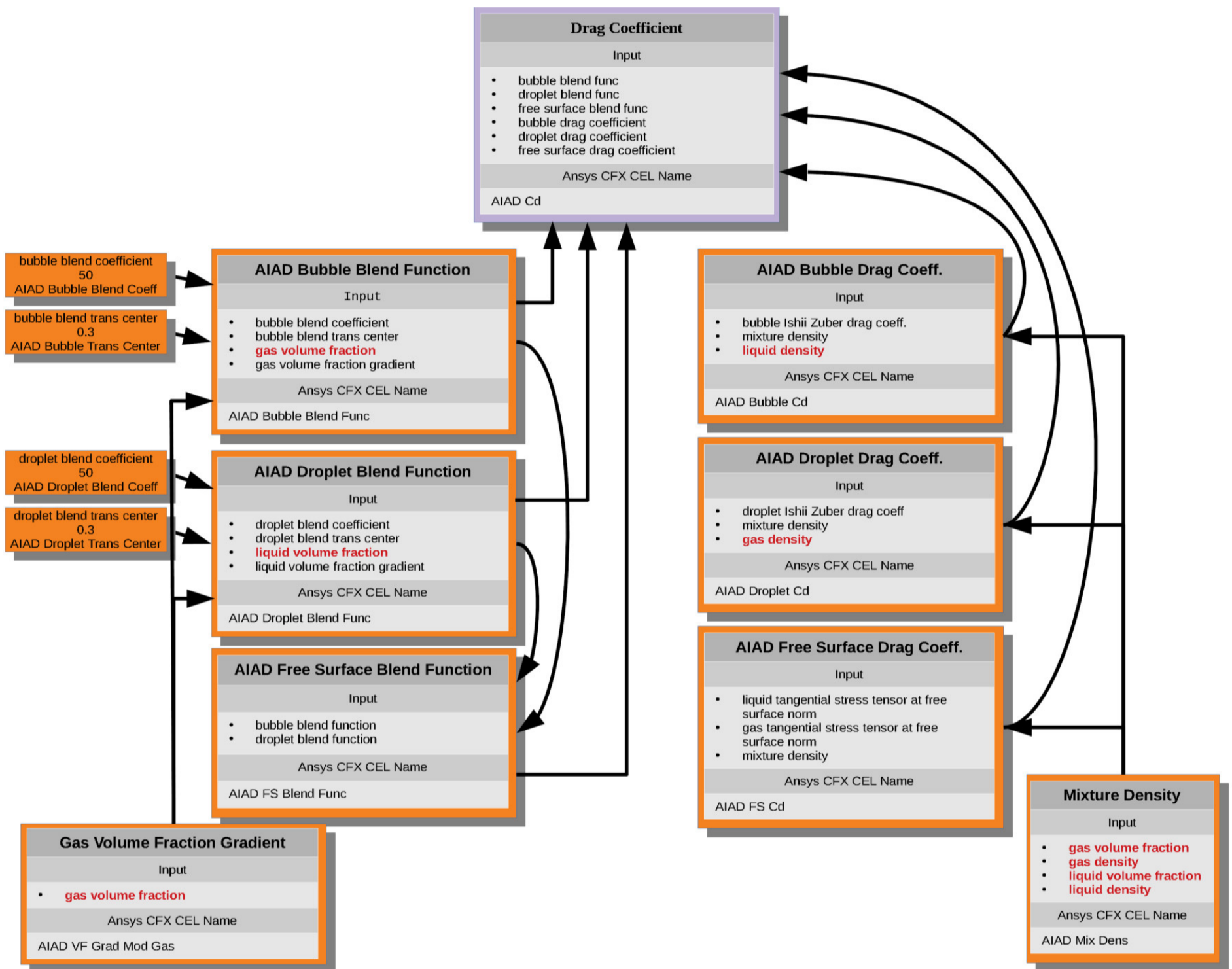
Implementation Flowchart



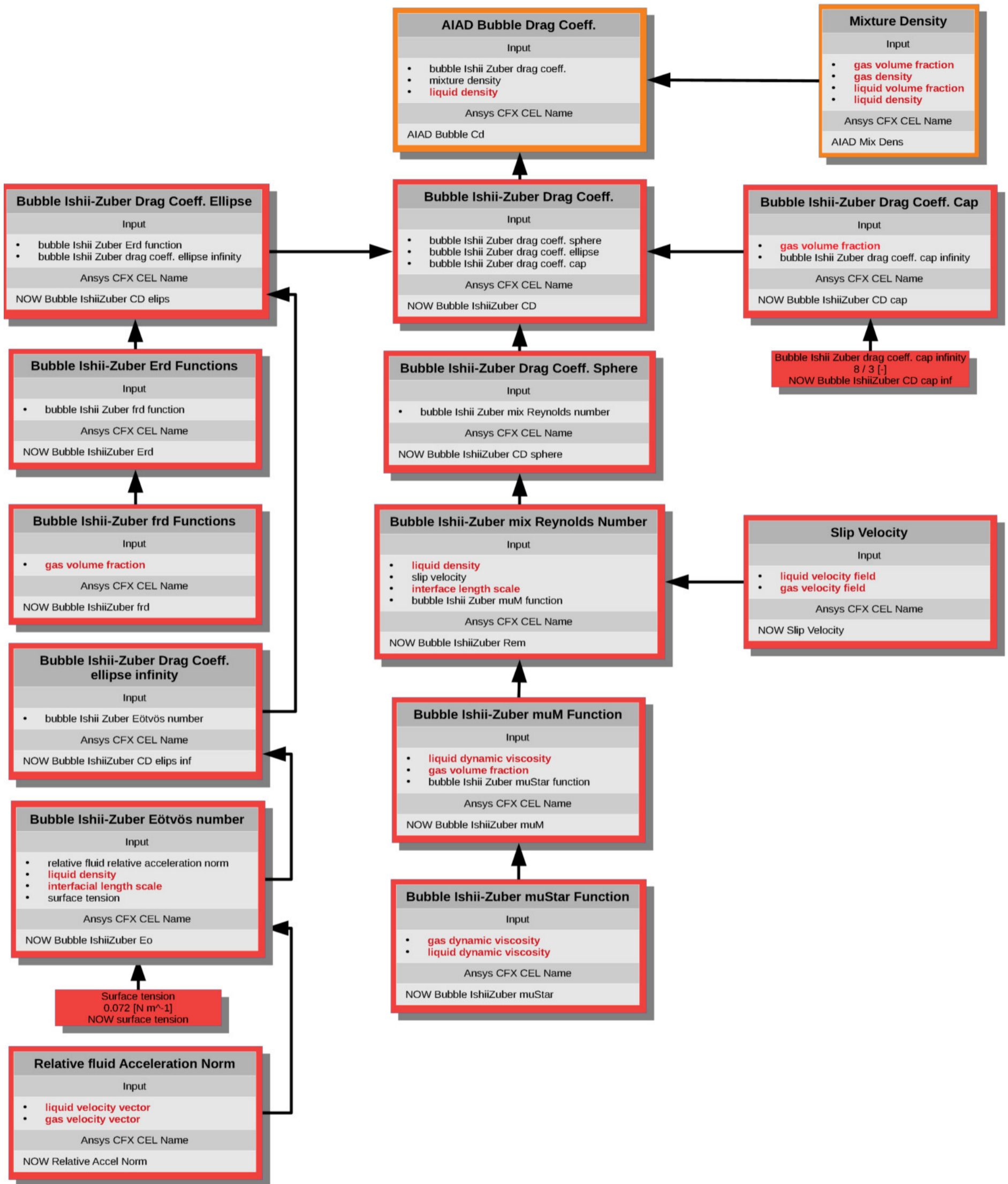
Interfacial Area Density Implementation in Ansys CFX Mixture Model; by the author

Appendix B

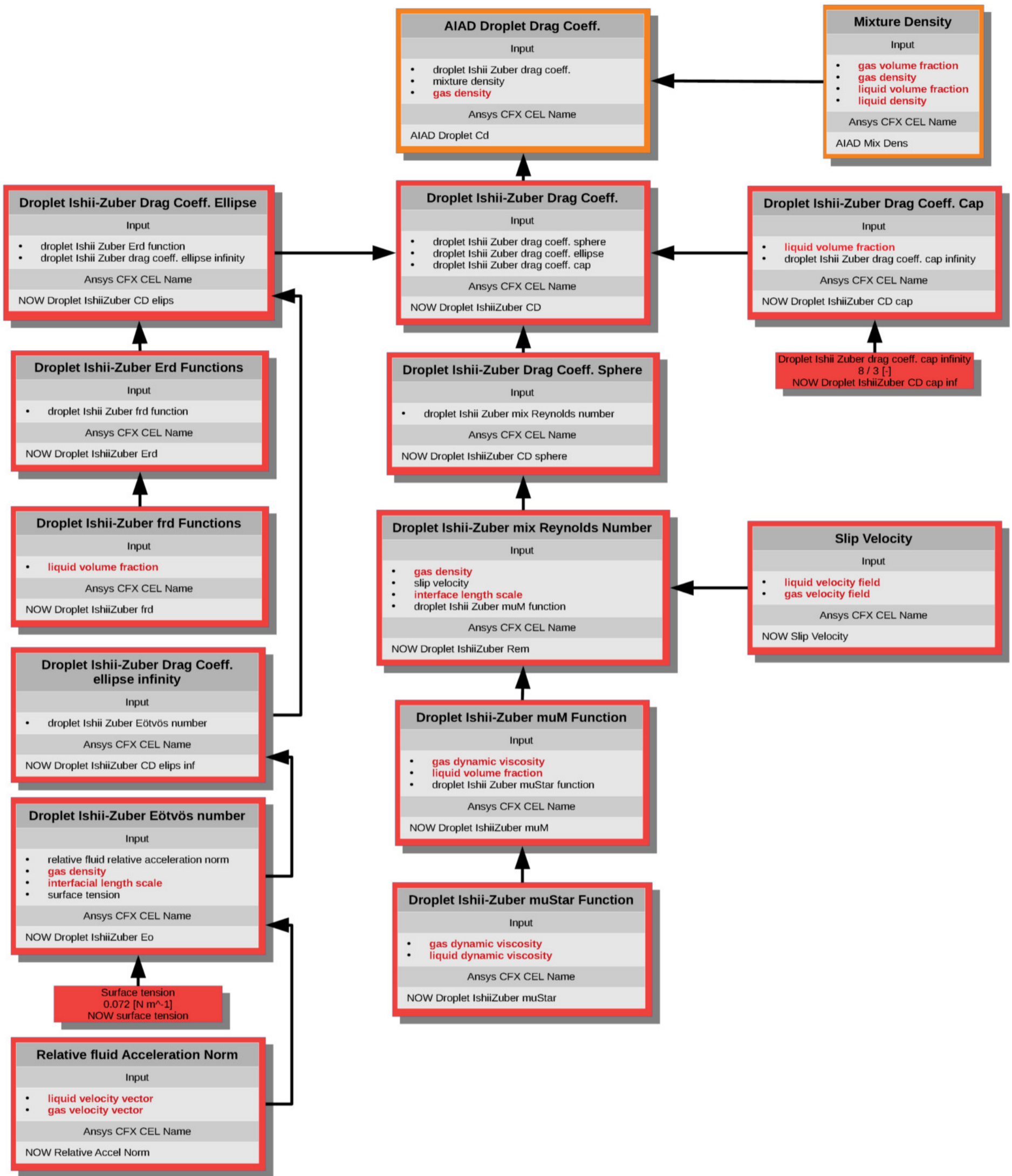
Ishii Zuber Drag Model Implementation Flowchart



Ishii Zuber drag model implementation in CFX Mixture model; overview



Ishii Zuber drag model implementation in CFX Mixture model; for bubbles



Ishii Zuber drag model implementation in CFX Mixture model; for droplets

Appendix C

Proof of Concept Hewitt Experiment

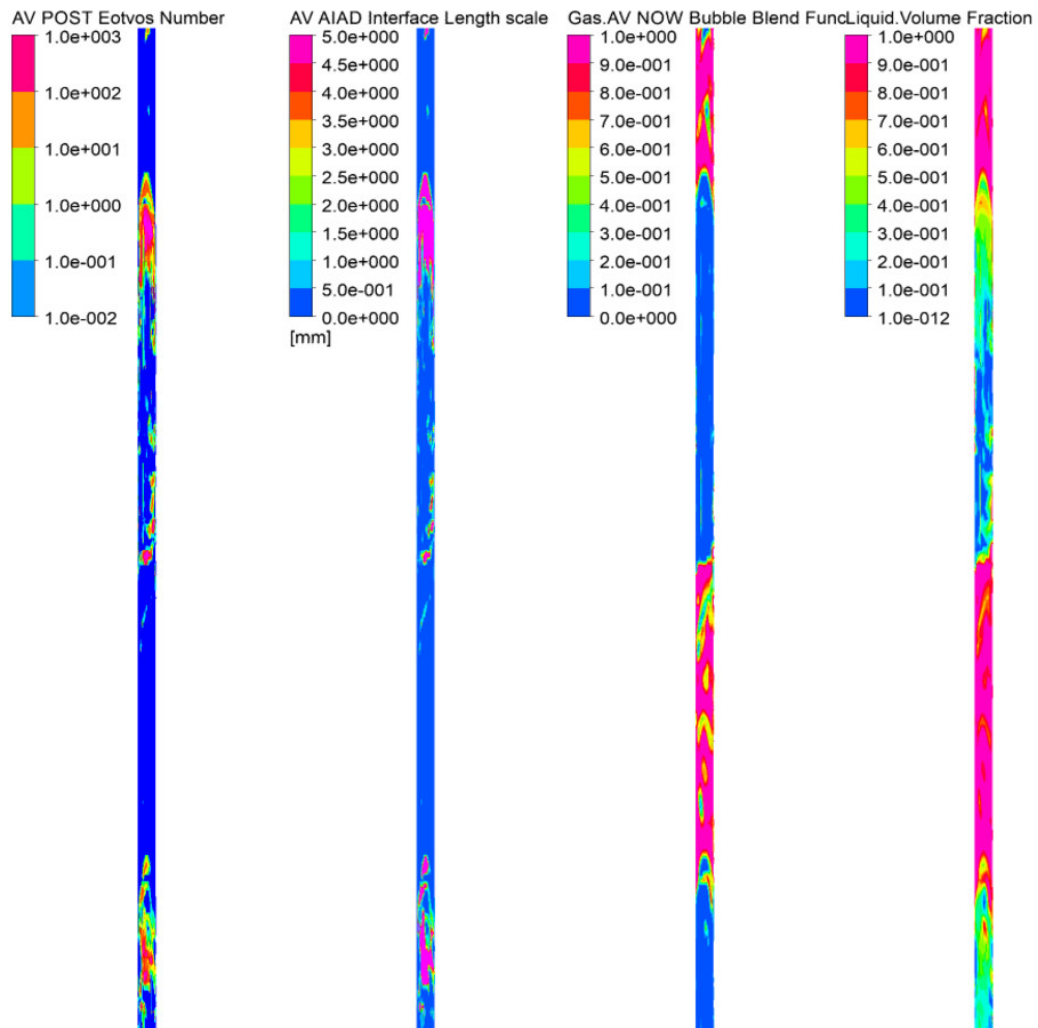


Figure C.1: Hewitt CFD model, exemplary 2m section of the vertical pipe, Run No. 1; coloured by Eötvös number, interface length scale, bubble blend function and liquid volume fraction; figure by the author

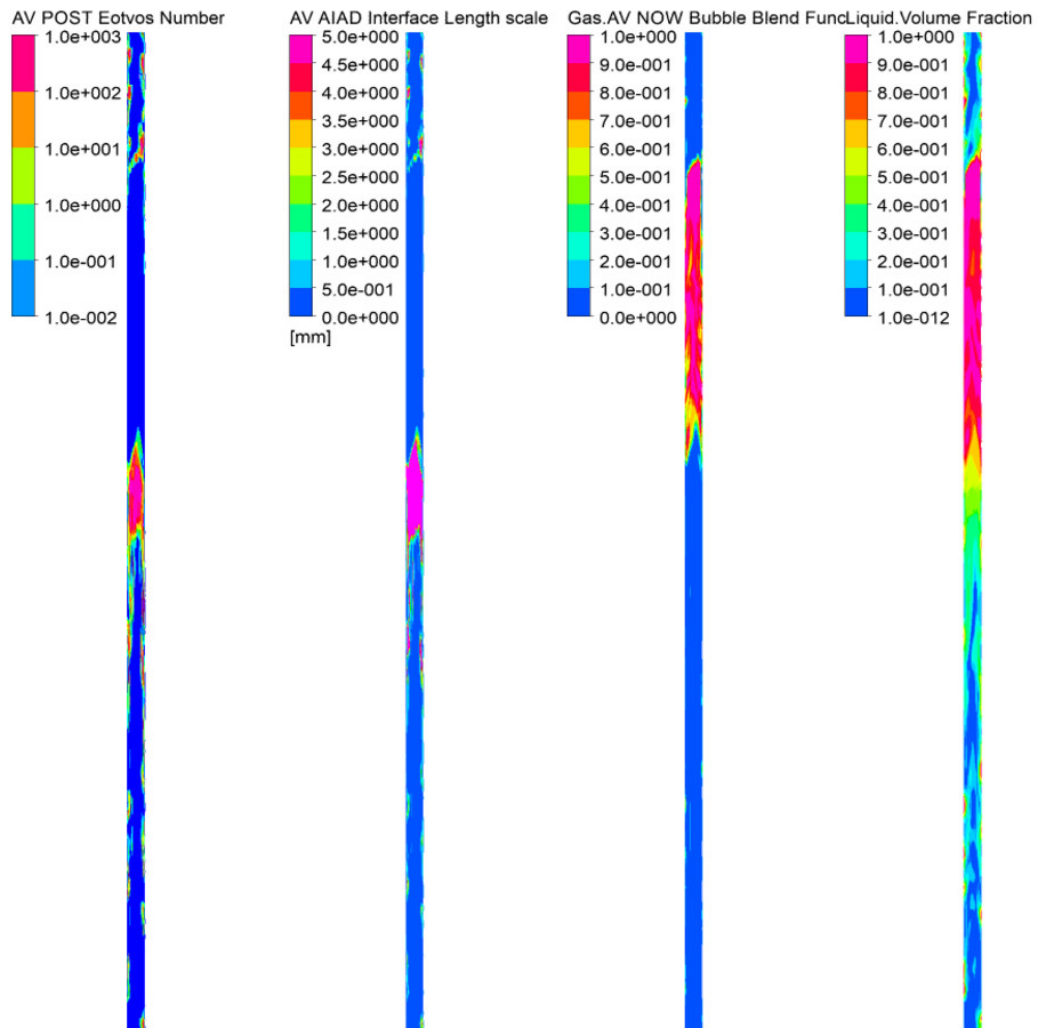


Figure C.2: Hewitt CFD model, exemplary 2m section of the vertical pipe, Run No. 6; coloured by Eötvös number, interface length scale, bubble blend function and liquid volume fraction; figure by the author

Appendix D

Steam Drum Experiment

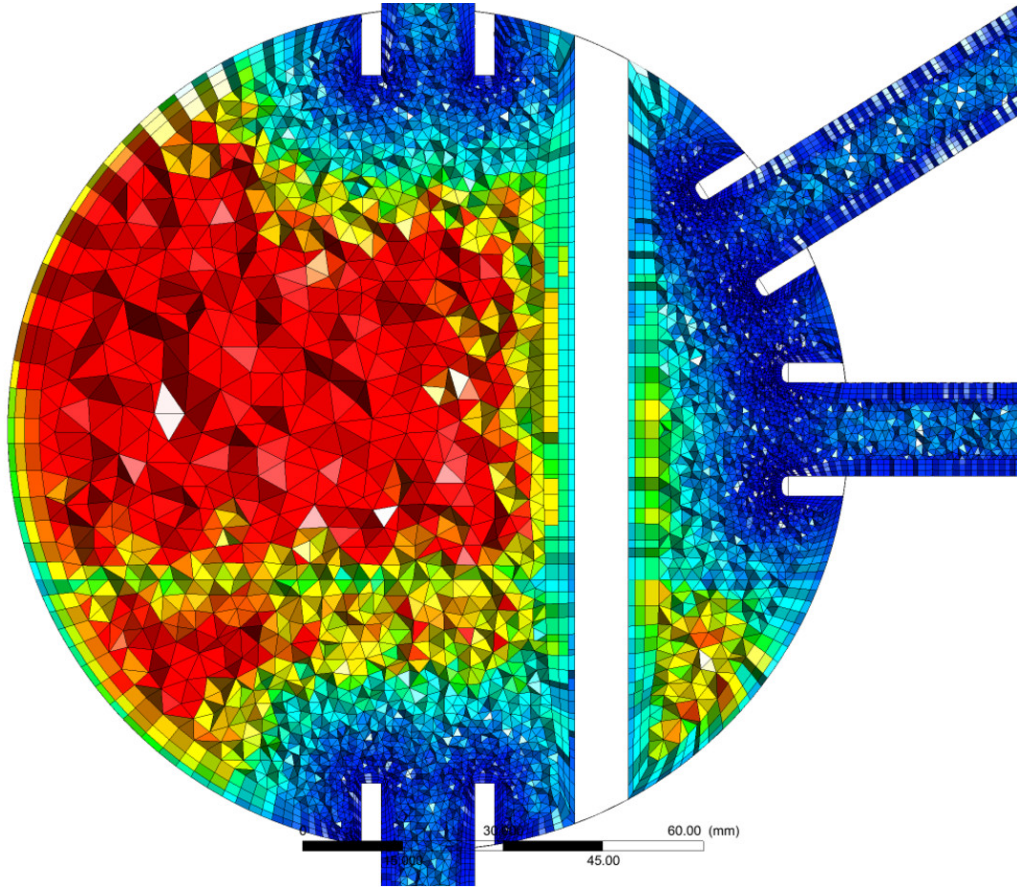


Figure D.1: Mesh of the experiment steam drum cut; Detail Steam Drum; Coloured by volume size; figure by the author

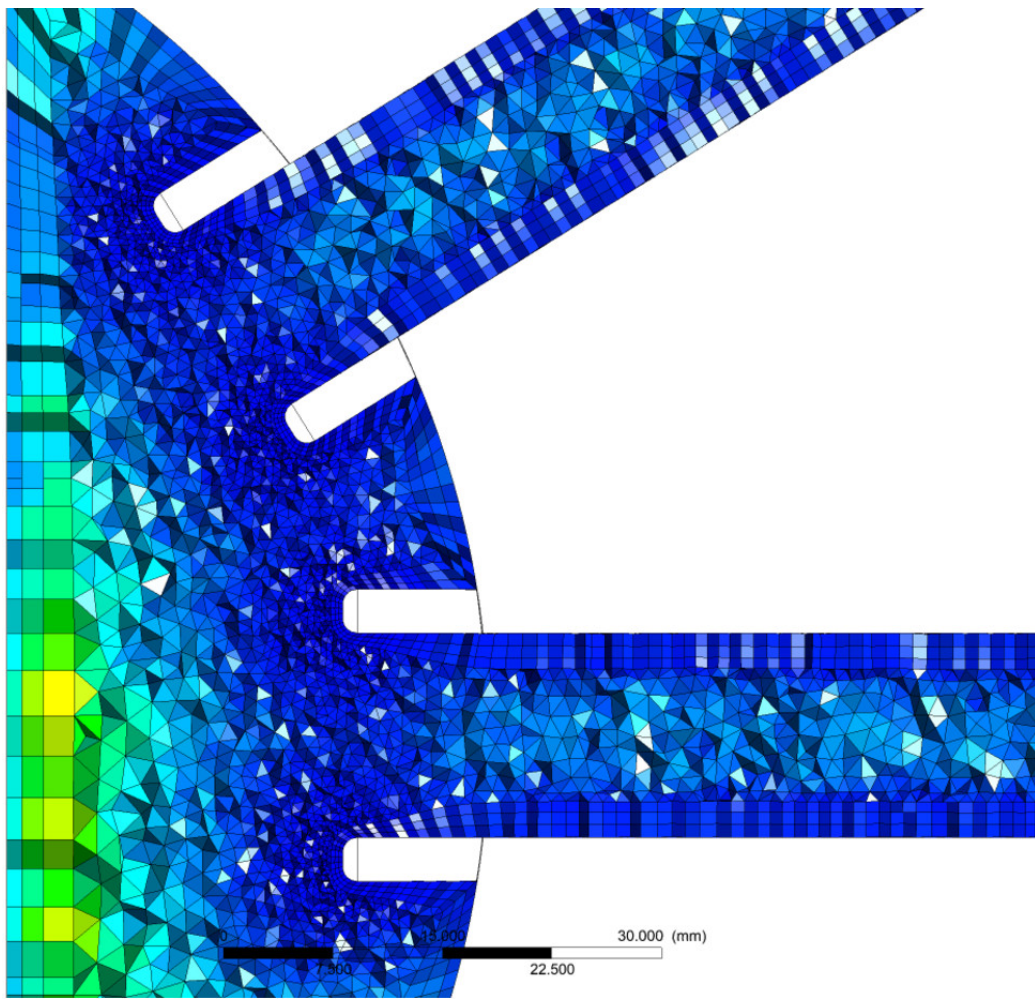


Figure D.2: Mesh of the experiment steam drum cut; Detail Steam Drum Stage 1; Coloured by volume size; figure by the author

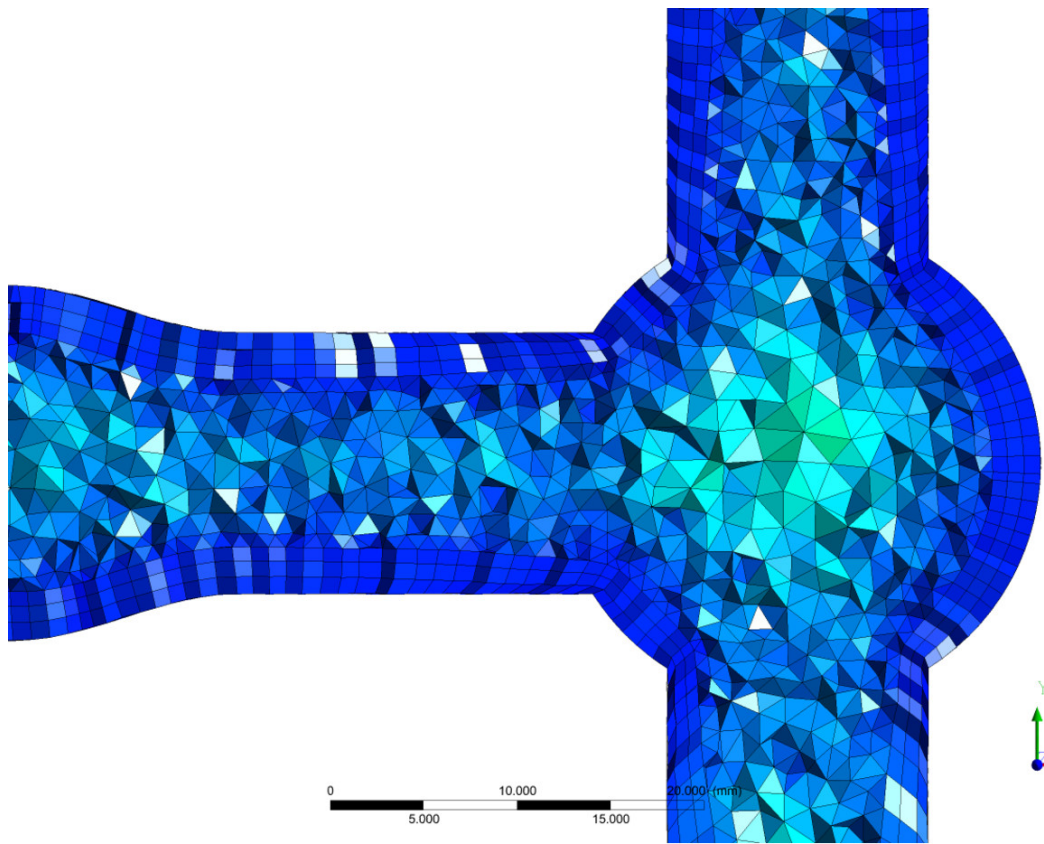


Figure D.3: Mesh of the experiment steam drum cut; Detail Distributor; Coloured by volume size; figure by the author

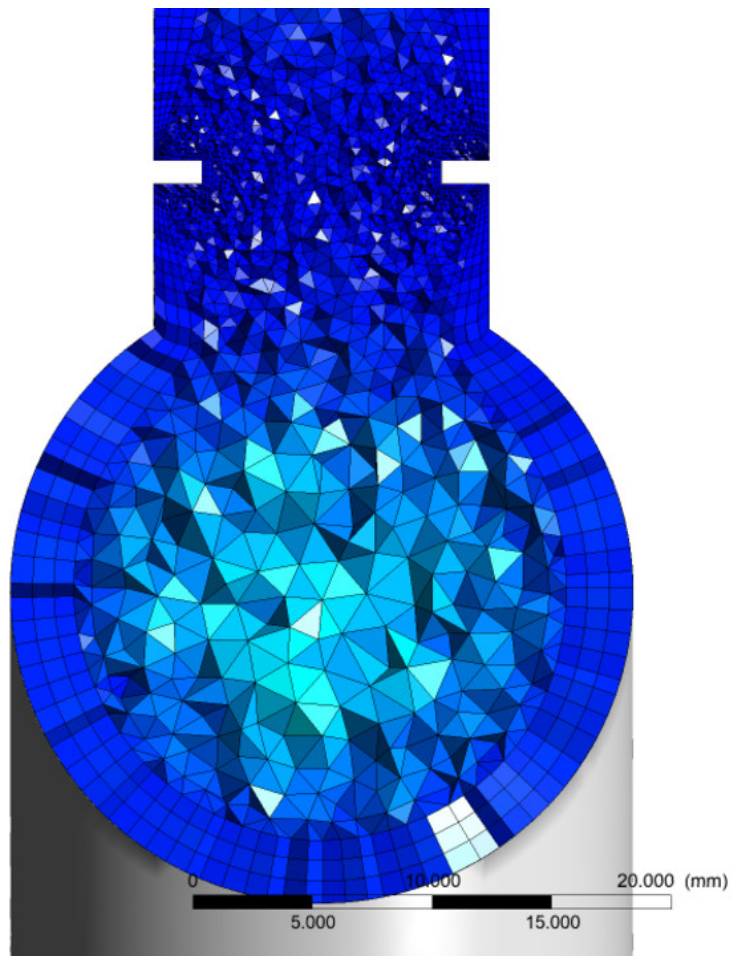


Figure D.4: Mesh of the experiment steam drum cut; Detail Orifice Pipe; Coloured by volume size; figure by the author